BEHAVIOUR OF HIGH-STRENGTH CONCRETE UNDER BIAXIAL LOADING CONDITIONS

by

© Amgad Ahmed Hussein, B.Sc. (Eng.), M.Eng.

A thesis submitted to the School of Graduate
Studies in partial fulfilment of the
requirements for the degree of
Doctor of Philosophy

Faculty of Engineering and Applied Science
Memorial University of Newfoundland
April 1998

St. John's Newfoundland Canada

National Library of Canada
Acquisitions and Bibliographic Services
395 Wellington Street
Ottawa ON K1A 0N4
Canada

Bibliothèque nationale du Canada
Acquisitions et services bibliographiques
395, rue Wellington
Ottawa ON K1A 0N4
Canada

Your file Votre référence

Our file Notre référence

The author has granted a non-exclusive licence allowing the National Library of Canada to reproduce, loan, distribute or sell copies of this thesis in microform, paper or electronic formats.

The author retains ownership of the copyright in this thesis. Neither the thesis nor substantial extracts from it may be printed or otherwise reproduced without the author's permission.

L'auteur a accordé une licence non exclusive permettant à la Bibliothèque nationale du Canada de reproduire, prêter, distribuer ou vendre des copies de cette thèse sous la forme de microfiche/film, de reproduction sur papier ou sur format électronique.

L'auteur conserve la propriété du droit d'auteur qui protège cette thèse. Ni la thèse ni des extraits substantiels de celle-ci ne doivent être imprimés ou autrement reproduits sans son autorisation.

0-612-34188-7

Canada

Abstract

With the increasing applications of high strength concrete in the construction industry, the understanding of its behaviour under multiaxial loading is essential for reliable analysis and safe design. This thesis encompasses an investigation of the behaviour of high strength concrete under biaxial loading conditions, and a constitutive modelling study to enable numerical prediction, through the finite element method, of such a behaviour.

The experimental phase included the evaluation and design of the loading platens. The test set-up and supports are very crucial to this type of testing due to the friction that exists between the testing platens and the specimen. A theoretical study using the finite element approach was conducted to investigate the effect of confinement on the displacement field in addition to the stress distribution in the loading direction. Three types of loading platens were examined: the dry solid platens, the brush support and teflon friction reducing pads. The results of the simulation indicated that the most homogeneous stress and displacement field are achieved through the brush platens. Based on the finite element investigation, the size and dimensions of the brush platens were recommended. They were used in the experimental study.

A test set-up was designed and manufactured. Modern control schemes and high-speed data acquisition system were be used to monitor the material response and collect the experimental results. Four different types of high strength concrete plate specimens were tested under different biaxial load combinations. The principal deformations in the specimen were recorded and the crack patterns and failure modes were examined. Based on the strength data, failure envelopes were developed for each type of concrete. The test results revealed that the failure envelopes of concrete depends on the concrete strength and on the type of aggregates. A pronounced difference was

found between the high strength light weight and the high strength normal weight concrete. The deformation characteristics indicated that high strength concrete shows a linear behaviour up to a higher stress than normal strength concrete. It also has a higher discontinuity limits. The observed failure modes showed that there is no fundamental difference in the crack patterns and failure modes due to the increase in the compressive strength of the concrete or due to the use of light weight aggregates under different biaxial loading combinations.

The test results were used to modify and calibrate a fracture energy-based non-associated model for high-strength concrete. The model was implemented in a general purpose finite element program and was verified against the test results. Using the proposed constitutive model, a finite element study was carried out to analyze the standard compression test on a concrete cylinder. The effects of the compressive strength, cylinder size, loading platens and sulphur capping were investigated. The study confirmed that a triaxial compressive stress state exists at the cylinder end, and a large stress concentration occurs at the corner. The simulation results revealed that the use of a standard bearing block is essential in testing high strength concrete. Moreover, in some cases, the use of a non standard bearing block can result in a lower strength, which was observed experimentally. The simulation provided an explanation for such a behaviour. Finally, the finite element analysis demonstrated that the use of soft materials, as friction reducers, could create drastic changes in the state of stress in the specimen as well as its compressive strength. The use of soft materials should, therefore, be carried out with caution.

Acknowledgements

I am greatly indebted to Dr. H. Marzouk, Professor of Civil Engineering, under whose guidance and supervision the project was carried out. His excellent guidance, support, and patience helped me to complete this thesis.

My special thanks to Drs. P. Morin and M. Booton, for their support and encouragement, and also for serving on the supervisory committee. Thanks are due to Dr. J. J. Sharp, Associate Dean of Engineering for Graduate Studies and Research, for his understanding, encouragement and the facilities provided. Furthermore, Dr. J. J. Sharp and Ms. M. Crocker, secretary of the Associate Dean's office, are acknowledged for ensuring smooth and efficient operation of the associated administrative tasks of my graduate program.

I would like to thank Dr. A. Elwi, Professor of Civil Engineering, University of Alberta, for his assistance and helpful discussion regarding the finite element implementation of the Leon Model. It formed the basis of the implementation of the Extended Leon Model that was carried out in this thesis.

Sincere thanks are due to the Technical Staff who made their services available at every stage of this project, especially Messrs A. Bursey, C. Ward and R. O'Driscoll. I express my warm appreciation to the members of the Technical Services of Memorial University, Mr. L. Spurrell for his invaluable assistance in manufacturing all the parts used in the test set-up, Mr. B. Burke for performing all the required welding. Thanks are also due to Mr. H. Dye, machine shop supervisor, and Mr. J. Andrews, welding shop supervisor, for their continuous accommodation and help during the manufacturing of the test set-up. The generous support from the Center for Computer Aided Engineering and its staff, especially Messrs D. Press, and T. Galaway and L. Little, on computing services is very much appreciated.

This thesis was completed at Memorial University of Newfoundland as part of a project funded by the Natural Sciences and Engineering Research Council of Canada. Funding in the form of graduate fellowship and graduate supplement from Memorial University is gratefully acknowledged.

I am grateful to the fellow graduate students for their encouragement and company. I would like to thank my friend S. Awadallah for his true friendship and his moral support to me throughout the course of my thesis.

I would like to take this chance to express my profound gratitude to all my family members for their continuing encouragement and affection.

Finally, a special word must go to my wife, Nancy, for the sacrifices she made and the privations she endured during the tenure of this thesis.

Contents

Abstract ii

Acknowledgements iv

List of Figures xii

List of Tables xxi

1 Introduction 1

1.1 Scope 4

1.2 Research Objectives 5

1.3 Thesis Outline 6

2 Review of Literature 8

2.1 Load Application System 8

2.2 Response of Concrete Under Biaxial Loading Conditions 14

2.2.1 Normal Strength Concrete 14

2.2.2 High-Strength Concrete 15

2.2.3 Light Weight Aggregate Concrete 17

2.2.4 Post Peak Behaviour in Uniaxial Compression 18

2.2.5 Post Peak Behaviour in Biaxial Compression 22

2.2.6 Loading Path 23
2.3 Constitutive Models 23
2.3.1 Elasticity Based Models 24
2.3.2 Plasticity Based Models 25
2.3.3 Endochronic models 27
2.3.4 Damage Models 27
2.3.5 Microplane Models 28
2.3.6 Adopted Model for the Current Study 28
2.4 Finite Element Simulation of Concrete Test Specimen in Compression 30
2.4.1 Analytical and Finite Element Studies of Uniaxial Testing of Concrete Cylinders 30
2.4.2 Finite Element Simulation of the Boundary Conditions used in Biaxial Testing of Concrete 32

3 Finite Element Evaluation of the Boundary Conditions used in Biaxial Testing of Concrete 34

3.1 Simulation of the Interaction Between the Test Specimen and the Loading Platens 35
3.2 Constitutive Material Model 36
3.2.1 Elastoplastic Behaviour 36
3.2.2 Behaviour under Compressive Stress State 38
3.2.3 Cracking 39
3.3 Specimen - Platen Interaction 40
3.4 Surface Constitutive Behaviour 43
3.5 Geometric Modelling 45
3.6 Material Properties 45

3.7 Results of the Numerical Evaluation of the Set-up 47
3.7.1 Uniaxial Loading 47
3.7.2 Linear Analysis Versus Nonlinear Analysis 55
3.7.3 Buckling Capacity of the Brush Rods 57
3.7.4 Biaxial Loading 58
3.8 Recommendations for the Test Set-Up 64

4 Experimental Program **65**

4.1 Biaxial Testing Apparatus 65
4.1.1 Loading Frame 65
4.1.2 Loading Platens 69
4.1.3 Hydraulic Actuators 72
4.1.4 Measurement Devices 72
4.1.5 Data Acquisition System 75
4.1.6 Control Scheme 76
4.2 Testing Procedure 79
4.2.1 Specimen Loading 79
4.2.2 Specimen Mounting 79
4.3 Test Specimens 80
4.4 Materials Used 81
4.4.1 Cementitious Materials 81
4.4.2 Aggregates 81
4.4.3 Chemical Admixtures 82
4.4.4 High-range Water Reducers 82
4.4.5 Retarder 85
4.5 Concrete Mixes 85

4.6 Mixing Procedure 87
4.7 Properties of Fresh Concrete 87
4.8 Specimen Fabrication 87
4.8.1 Casting 87
4.8.2 Curing 88
4.8.3 Grinding 88
4.9 Summary of Experiments 90

5 Test Results and Discussion **92**
5.1 Strength Data 92
5.1.1 Compressive Strength of the Different Mixtures 92
5.1.2 Biaxial Strength Data 95
5.2 Typical Stress Strain Curves 106
5.3 Post-Peak Behaviour 122
5.4 Failure Modes 127

6 A Constitutive Model for High Strength Concrete **136**
6.1 A Fracture-Energy-Based Plasticity Model 136
6.2 Leon's Triaxial Strength Failure Criterion 138
6.3 Extended Leon's Triaxial Strength Failure Criterion 140
6.4 Isotropic Hardening Model for Pre-Peak Behaviour 143
6.5 Nonlinear Hardening Response 146
6.6 Nonassociated Flow 147
6.7 Isotropic Softening Model for Post-Peak Behaviour 149
6.7.1 Mode I Type Fracture 149
6.7.2 Degradation of Triaxial Strength 153

6.7.3 Mixed Mode Fracture 155
6.8 The Basis of Numerical Implementation 157
6.8.1 Numerical Implementation of Plasticity 158
6.8.2 Elastic-Predictor Step 158
6.8.3 Plastic-Corrector Step 159
6.8.4 Crossing the Yield Surface 159
6.8.5 Returning to the Yield Surface 161
6.8.6 The plastic Multiplier $\Delta\lambda$ 162
6.9 Implementation of the Model 163
6.10 Calibration and Verification of the Model 163

7 Application of the Proposed Model: Evaluation of the Standard Uniaxial Compression Test **171**

7.1 Introduction 171
7.2 Standard Uniaxial Compression Test 172
7.3 Specifications for the Standard Cylinder Test 172
7.4 Standard Specimen Size 175
7.5 State of Stress in a Test Specimen 175
7.6 Finite Element Simulation 176
7.6.1 Geometric Modelling 178
7.7 Material Model 178
7.8 Simulation of the Compression Test 181
7.9 Effects of Different Test Variables 190
7.9.1 Concrete Compressive Strength 190
7.9.2 Specimen Size 197
7.9.3 Bearing Block Dimensions 203

7.10 End Preparation of the Specimen 210
7.11 Summary 216

8 Conclusions **219**

8.1 Summary 219
8.2 Evaluation of Different Loading Platens for Biaxial Testing of High-Strength Concrete 220
8.3 Experimental Findings 221
8.4 Finite Element Model 223
8.5 Application of the Finite Element Model: Evaluation of the Standard Uniaxial Compression Test 224
8.6 Contribution 226
8.7 Recommendations for Further Research 227

References **229**

List of Figures

2.1 Biaxial test methods [5] 10

2.2 Average shear stress-strain curves for different loading systems [20] . 12

2.3 Exploded view of fluid cushion cubical cell [22] 13

2.4 Biaxial strength envelope of concrete [14] 15

2.5 Schematic of the stress strain curves obtained form a uniaxial test specimen in compression 19

3.1 Constitutive model used in the FE analysis 37

3.2 Isoparametric interface element 41

3.3 Non-local interface friction model, for which the condition of no relative motion is approximated by stiff elastic behaviour, as shown by the dashes line. 44

3.4 The finite element mesh 46

3.5 Stress contours in the direction of loading (S22) and displacement contours in the orthogonal direction (U1) for the uniaxial cases (f'_c = 100 MPa), at ultimate load 48

3.6 Shear stresses induced in the specimen, due to the brush loading platens, for uniaxial case (f'_c = 100 MPa) 51

3.7 Shear stresses induced in the specimen, due to the lubricated teflon pads, for uniaxial case (f'_c = 100 MPa) 52

3.8 Shear stresses induced in the specimen. due to the solid loading platens. for uniaxial case (f'_c = 100 MPa) 53
3.9 Shear stresses induced in the specimen at the ultimate strength. due to the different loading systems. for uniaxial case (f'_c = 100 MPa). at ultimate load 54
3.10 Stress contours in the direction of loading (S22) and displacement contours in the orthogonal direction (U1) for the uniaxial elastic analysis 56
3.11 Contours of the principal stresses (SP1) and displacement contours in one of the orthogonal directions (U1) for the biaxial cases (f'_c = 100 MPa). at ultimate load 59
3.12 Shear stresses induced in the specimen. due to the brush loading platens. for biaxial case (f'_c = 100 MPa) 60
3.13 Shear stresses induced in the specimen. due to the lubricated teflon pads. for biaxial case (f'_c = 100 MPa) 61
3.14 Shear stresses induced in the specimen. due to the solid loading platens. for biaxial case (f'_c = 100 MPa) 62
3.15 Shear stresses induced in the specimen at the ultimate strength. due to the different loading systems. for biaxial case (f'_c = 100 MPa) . . 63

4.1 Test set-up (frontal view) 66
4.2 Test set-up (side view) 67
4.3 The brush loading platens 71
4.4 A test specimen mounted in the test set up 73
4.5 A test specimen with two orthogonal strain gauges mounted at the centre 74
4.6 A photograph of the data acquisition system and the MTS main control panel 77

4.7 Block diagram highlighting the details of the closed-loop test scheme 78
4.8 Grading of aggregates 84
4.9 Photograph of the grinder used for grinding the test specimen 89

5.1 A high strength concrete cylinder at failure 93
5.2 Biaxial strength envelopes for NSC under combined tension and compression, biaxial tension and biaxial compression 100
5.3 Biaxial strength envelopes for HSC under combined tension and compression, biaxial tension and biaxial compression 101
5.4 Biaxial strength envelopes for UHSC under combined tension and compression, biaxial tension and biaxial compression 102
5.5 Biaxial strength envelopes for HSLWC under combined tension and compression, biaxial tension and biaxial compression 103
5.6 Biaxial strength envelopes for the four different types of concrete under combined tension and compression, biaxial tension and biaxial compression 104
5.7 Stress-strain relationships for the normal strength concrete mix (NSC) under biaxial compression 108
5.8 Stress-strain relationships for the normal strength concrete mix (NSC) under combined tension and compression 109
5.9 Stress-strain relationships for the normal strength concrete mix (NSC) under biaxial tension 110
5.10 Stress-strain relationships for the high strength concrete mix (HSC) under biaxial compression 111
5.11 Stress-strain relationships for the high strength concrete mix (HSC) under combined tension and compression 112

5.12 Stress-strain relationships for the high strength concrete mix (HSC) under biaxial tension 113
5.13 Stress-strain relationships for the high strength concrete mix (UHSC) under biaxial compression 114
5.14 Stress-strain relationships for the high strength concrete mix (UHSC) under combined tension and compression 115
5.15 Stress-strain relationships for the high strength concrete mix (UHSC) under biaxial tension 116
5.16 Stress-strain relationships for the light weight concrete mix (HSLWC) under biaxial compression 117
5.17 Stress-strain relationships for the light weight concrete mix (HSLWC) under combined tension and compression 118
5.18 Stress-strain relationships for the light weight concrete mix (HSLWC) under biaxial tension 119
5.19 Poisson's ratio versus applied stress for the different types of concrete in uniaxial compression 123
5.20 Uniaxial stress-strain curve (σ_1 - ϵ_1) for a typical NSC specimen . . . 125
5.21 Failure modes of specimens subjected to uniaxial compression 131
5.22 Failure modes of specimens subjected to biaxial compression stresses $\sigma_2/\sigma_3 = 0.20$ 132
5.23 Failure modes of specimens subjected to biaxial compression stresses $\sigma_2/\sigma_3 = 1.0$ 133
5.24 Failure modes of specimens subjected to combined tension and compression (σ_3 / σ_1 = -1/0.10) 134
5.25 Failure modes of specimens subjected to uniaxial tension 135

6.1 Triaxial failure envelope, deviatoric sections, of the Pramono and Willam model [70]) 139
6.2 Deviatoric View of the ELM [71] 142
6.3 Plane stress sections of smooth (ELM) and polygonal (Leon) failure envelopes 142
6.4 Comparison of the model with the current biaxial test data 144
6.5 Loading surface of isotropic hardening model 146
6.6 Fictitious crack model [104] 150
6.7 Composite fracture model for tensile cracking 152
6.8 The forward-Euler procedure: (a) Locating the intersection point A: (b) Moving tangentially from A to C (and correcting to D). 160
6.9 Verification of plane stress elements 166
6.10 Comparison of the finite element results with the biaxial experimental data on normal strength concrete by H. Kupfer et al. [14] 167
6.11 Comparison of the finite element results with the experimental data for the UHSC mix 168
6.12 The finite element mesh for a cylindrical specimen subjected to triaxial loading 169
6.13 Comparison of the finite element results with the triaxial experimental data on high strength concrete by J. Xie et al. [90] 170

7.1 ASTM C 39-1993a standard bearing block for compression testing . . 173
7.2 State of stress on a compression test specimen 177
7.3 The finite element mesh 179
7.4 Forces acting on an axi-symmetric element 180

7.5 Principal stresses for a 150 × 300 mm cylinder, f'_c = 30 MPa, tested with a 152 mm bearing block at nominal axial stress = −12 MPa corresponding to 40 % loading 183
7.6 Principal stresses for a 150 × 300 mm cylinder, f'_c = 30 MPa, tested with a 152 mm bearing block at nominal axial stress = −27 MPa corresponding to 90 % loading 184
7.7 Principal stresses for a 150 × 300 mm cylinder, f'_c = 30 MPa, tested with a 152 mm bearing block at nominal axial stress = −30 MPa corresponding to 100 % loading 185
7.8 Shear stress induced in the specimen, at different loading levels, f'_c = 30 MPa, 150 × 300 mm cylinders that are tested with 150 mm bearing block 186
7.9 Displacement contours for a 150 × 300 mm cylinder, f'_c = 30 MPa, tested with a 152 mm bearing block at nominal axial stress = −30 MPa corresponding to 100 % loading 187
7.10 Principal stresses for a 150 × 300 mm cylinder, f'_c = 30 MPa, tested with a 152 mm bearing block at nominal axial stress = −30 MPa corresponding to 100 % loading and using interface element to simulate the interaction between the platen and the specimen 189
7.11 Shear stress induced in the specimen, along cylinder end, 150 × 300 mm cylinders that are tested with 150 mm bearing block, using different modelling assumptions 191

7.12 Displacement contours for a 150 × 300 mm cylinder. f'_c = 30 MPa. tested with a 152 mm bearing block at nominal axial stress = −30 MPa corresponding to 100 % loading and using interface element to simulate the interaction between the platen and the specimen 192

7.13 Principal stresses for a 150 × 300 mm cylinder. f'_c = 70 MPa. tested with a 152 mm bearing block at nominal axial stress = −70 MPa corresponding to 100 % loading 194

7.14 Principal stresses for a 150 × 300 mm cylinder. f'_c = 100 MPa. tested with a 152 mm bearing block at nominal axial stress = −100 MPa corresponding to 100 % loading 195

7.15 Shear stress induced in the specimen. along cylinder end. for different compressive strength. 150 × 300 mm cylinders that are tested with 150 mm bearing block 197

7.16 Principal stresses for a 100 × 200 mm cylinder. f'_c = 30 MPa. tested with a 102 mm bearing block at nominal axial stress = −30 MPa corresponding to 100 % loading 199

7.17 Principal stresses for a 100 × 200 mm cylinder. f'_c = 70 MPa. tested with a 102 mm bearing block at nominal axial stress = −70 MPa corresponding to 100 % loading 200

7.18 Principal stresses for a 100 × 200 mm cylinder. f'_c = 100 MPa. tested with a 102 mm bearing block at nominal axial stress = −100 MPa corresponding to 100 % loading 201

7.19 Shear stress induced in the specimen. along cylinder end. for different compressive strength. 100 × 200 mm cylinders that are tested with 102 mm bearing block 202

7.20 Principal stresses for a 150 × 300 mm cylinder, f'_c = 30 MPa, tested with a 102 mm bearing block at nominal axial stress = −30 MPa corresponding to 100 % loading 205
7.21 Principal stresses for a 150 × 300 mm cylinder, f'_c = 30 MPa, tested with a 102 mm bearing block at nominal axial stress = −30 MPa corresponding to 100 % loading and using interface element to simulate the interaction between the platen and the specimen 207
7.22 Shear stress induced in the specimen, along cylinder end, 150 × 300 mm cylinders that are tested with 102 mm bearing block, using different modelling assumptions 208
7.23 Principal stresses for a 100 × 200 mm cylinder, f'_c = 30 MPa, tested with a 152 mm bearing block at nominal axial stress = −30 MPa corresponding to 100 % loading 209
7.24 Shear stress induced in the specimen, along cylinder end, for different compressive strength, 100 × 200 mm cylinders that are tested with 150 mm bearing block 210
7.25 Principal stresses for a 150 × 300 mm cylinder, f'_c = 30 MPa, tested with a 152 mm bearing block at failure, specimen tested using a 1.5 mm rubber pad 213
7.26 Principal stresses for a 150 × 300 mm cylinder, f'_c = 30 MPa, tested with a 152 mm bearing block at failure, specimen tested using a 3 mm sulphur capping compound 214
7.27 Principal stresses for a 150 × 300 mm cylinder, f'_c = 30 MPa, tested with a 152 mm bearing block at failure, specimen tested using a 6 mm sulphur capping compound 215

7.28 Shear stress induced in the specimen capped with sulphur compound for 150 × 300 mm cylinders that are tested with 150 mm bearing block 217

List of Tables

3.1 Number of elements for different test set-ups 47

3.2 Shear stresses induced in the specimen 50

4.1 Grading of aggregates 82

4.2 Physical properties of normal weight aggregates 83

4.3 Physical properties of light weight aggregate 83

4.4 Mix proportions of 0.1 cubic meter of concrete 86

5.1 Uniaxial compressive strength for the different mixtures at different ages for the 100 × 200 mm cylinders 94

5.2 Splitting tensile strength (MPa) for the different mixtures at 91 days 94

5.3 Biaxial strength data for the normal strength concrete mix NSC . . . 96

5.4 Biaxial strength data for the high strength concrete mix HSC 97

5.5 Biaxial strength data for the high strength concrete mix UHSC . . . 98

5.6 Biaxial strength data for the light weight concrete mix HSLWC . . . 99

6.1 Material parameters for the different types of concrete 165

7.1 Different cases of the finite element simulation 178

7.2 Number of elements 181

7.3 Displacement values in the lateral direction (U1), and in the direction of loading (U2), at the ultimate load, for one-quarter of the test cylinder 202

Chapter 1

Introduction

In recent years, considerable attention has been given to the use of silica fume as a partial replacement for cement in the production of high strength concrete. High strength concrete possesses features that could be used advantageously in concrete structures; these features include: low creep characteristics, low permeability, low deflection of members resulting from high elastic modulus, and the reduced loss of prestress force because of lower creep deformation. Hence, the application of high strength concrete is rapidly gaining popularity in the concrete industry.

Concretes with strengths exceeding 60 MPa are produced commercially using conventional methods and materials and are not unusual in construction today. High strength concrete has been used for offshore platforms, marine structures, tall buildings and long span bridges. The construction of Chicago's Tower Place, would not have been possible without high strength concrete. High strength ready-mixed concrete was used on the First Pacific Centre in Seattle, Washington; in this case the design strength of the concrete was 97 MPa [1]. High strength concrete was also used for the world tallest building, the Malaysia's Twins.

The modern concrete offshore structures in the North Sea are built with high strength concrete, with a minimum compressive strength of 60 MPa [3]. Over twenty

concrete gravity platforms have been constructed in the North Sea, the Baltic Sea and offshore Brazil [4]. For example, the specified strength (56 MPa) for Gullfaks C platform (1986-87) concrete was 50 % higher than the strength of Beryl A platform (1973-75) concrete (36 MPa). The actual 28-day compressive strength of the Gullfaks concrete core samples was found to be approximately 70 MPa [3].

Recently, a gravity based structure utilizing high strength concrete was used for the Hibernia development off the eastern coast of Newfoundland. It is the first gravity base structure to be built in North America. High strength concrete, containing mineral admixture such as silica fume, is relatively impermeable. Hence, it offers great promise for the durability problem associated with marine and offshore structures situated in the harsh North Atlantic waters. The specified design strength for the Hibernia GBS was 74 MPa. The actual strength was found to be much higher. Normal weight aggregates as well as light weight aggregates were used in the high strength concrete mix. In the design of these type of structures many loading cases are considered. The state of stress in such a massive structure is quite complicated and finite element analysis had to be used.

The behaviour of reinforced concrete members and structural systems, specifically their response to loads and other actions, has been the subject of intensive investigations since the beginning of the present century. Because of the complexities associated with the development of rational analytical procedures, present-day design methods continue in many aspects to be based on the empirical approaches, which use the results of a large amount of experimental data.

Such an empirical approach has been necessary in the past, and may continue to be the most convenient method for ordinary design. However, the finite element method now offers a powerful and general analytical tool for studying the behaviour of

reinforced concrete. Cracking, tension softening, non-linear multiaxial material properties, complex steel-concrete interface behaviour, and other effects previously ignored or treated in a very approximate way can now be modelled rationally. Through such studies, in which the important parameters may be varied conveniently and systematically, new insights are gained that may provide a firmer basis for the codes and specifications on which ordinary design is based.

The finite element method has been used directly for the analysis and design of complex structures, such as offshore oil platforms and nuclear containment structures. These cannot be treated properly by the more approximate methods. However, the finite element method requires a good description of the actual material behaviour under different load combinations, in order to yield accurate and realistic results. For normal strength concrete, reasonable amounts of data are available. This is not the case for high strength concrete for which existing data are scarce.

Considerable experimental research has recently been directed towards applying new techniques in concrete testing. Special test set-ups and servo controlled testing have provided new experimental evidence which was not available earlier from predominantly load-controlled test data. For example, a stable descending portion of the stress-strain curve of concrete in compression and direct tension was observed. The uniaxial stress-strain curves obtained have provided an insight to the material's post-peak behaviour that was never known before.

Although concrete is subjected, in practice, to a wide range of complex states of stress, most of the available information on high strength concrete, elastic and inelastic deformational behaviour, has been obtained from simple uniaxial compression and bending tests. Such tests are usually carried out under short-term static loading. These experiments provide a small part of the vast amount of data required under all

possible combinations and types of stresses.

Very few experiments have been carried out to ascertain the behaviour of high strength concrete under biaxial and triaxial states of stress. Therefore, an extensive experimental program is required to investigate the behaviour of high strength concrete under biaxial loading.

1.1 Scope

The current study is carried out to examine the behaviour of high strength concrete when subjected to biaxial state of stress. The scope of the experimental program is as follows:

1. Investigate the behaviour of high strength concrete made with normal weight aggregates and light weight aggregates.
2. To examine and evaluate the test data.
3. Record the deformation characteristics.
4. Observe the failure modes.
5. Develop the failure envelopes.
6. Compare the behaviour of high strength concrete with that of normal strength concrete.

The experimental results can then be used to modify a suitable constitutive model for high strength concrete. By implementing the constitutive model in a general purpose finite element program, one can then predict the behaviour of different high strength concrete structures. Modelling of the reinforcement can be easily added to the finite element program. However, a bond characteristics study, for high strength concrete,

should be carried out first to produce proper modelling assumptions to yield good results.

1.2 Research Objectives

The main objective of the current research is to investigate the behaviour of high strength concrete under biaxial loading. The research objectives of this investigation can be summarized as follows:

1. To examine the available methods used in biaxial testing of normal strength concrete and to identify the suitable methods that can be used for high strength concrete.

2. To ensure that selected test set-ups will not impose any limitations when used for high strength concrete testing. To perform this task, a finite element evaluation of the existing test set-ups used in biaxial testing of concrete should be carried out.

3. To design an appropriate test set-up for biaxial testing of high strength concrete that can produce reliable test data.

4. To collect and analyze the strength data and the load-deformation behaviour of high strength concrete under biaxial loading conditions.

5. To examine the failure modes and crack patterns for different stress ratios.

6. To adopt a theoretical constitutive model suitable for the finite element analysis of high strength concrete and to calibrate it using the experimental test results.

7. To implement the proposed model in a general purpose finite element program capable of dealing with complex stress analysis problems. The validity of the

high strength concrete model should be established by appropriate comparisons with the test results.

8. To conduct a finite element analysis of the standard compression test in order to provide some insight into that important test. The parameters should be selected to simulate the actual ones used in the standard compression tests.

1.3 Thesis Outline

Chapter 2 is divided into four parts. The first part reviews the different methods of load application used in biaxial testing of concrete. The second part reviews previous research conducted on normal strength concrete under biaxial state of stress. The third part contains a brief review of the different constitutive models used in idealizing the behaviour of concrete. The fourth part is a literature review of previous analytical and finite element studies of uniaxial testing of cylindrical specimen.

Chapter 3 contains a non linear finite element study of the effect of different load application platens used in the biaxial testing of concrete. The findings of the study are used to recommend the loading platens for the test set-up.

Chapter 4 describes the experimental investigation. Details of experimental facilities, test procedures and instrumentation are presented.

Chapter 5 presents the test results and observations obtained from the experimental investigation, as well as the subsequent analysis of these results.

Chapter 6 deals with an adopted constitutive model and its application to high strength concrete. The implementation of this model in a general purpose finite element program is also described.

Chapter 7 presents a finite element study of the standard uniaxial compression test on concrete cylinders.

Finally, a summary of the current investigation and the conclusions reached are given in Chapter 7.

Chapter 2

Review of Literature

In this chapter, a short review of literature pertaining to the different aspects of the current research work is given. In the first section, a brief review of the existing test set-ups and the different methods of load application used in biaxial testing of normal strength concrete is presented. Secondly, the earlier work on biaxial testing of concrete, as reported by different researchers, is discussed. Highlights of different constitutive models used for idealizing the concrete behaviour are briefly summarized. Finally, previous work on finite element simulation of a test specimen under compressive loading is discussed.

2.1 Load Application System

Various variables of the test set-up can exert an influence on the specimen's response under biaxial state of stresses. Typically, the specimens used in biaxial tests are either concrete plates or concrete cubes loaded in two directions. Thus, the boundary conditions stand out as the most influential factor in a specimen's response, as the aspect ratio of a biaxial test specimen is equal to one. The interaction between the test specimen and the loading platens could influence the specimen's behaviour, strength and mode of failure.

Frictional forces develop between the concrete specimen and the loading platens as a result of the differences in lateral expansion between the concrete specimen and the steel platens. Friction constrains the specimen boundary against lateral displacements which leads to additional shear stresses on the surface, and thus induces forces in the concrete specimen which are added to the nominal test load. In addition, the stress distribution in the specimen is not uniform. As a result, the specimen is in a biaxial state of stress which is not well defined.

Various methods of load application have been proposed for biaxial testing of normal concrete to eliminate the friction problem (see Figure 2.1). A detailed and comprehensive classification of the loading systems is given by the international cooperative program carried out by Gerstle et al. [5]. The rationale of such methods is to reduce the effect of lateral confinement of the test specimen. The methods available in the literature can be classified into two main categories as follows:

a) The use of friction reducing pads to reduce the friction between the test specimen and the loading platens.

b) Flexible loading platens to allow for the specimen deformation without introducing any restraints such as the brush support and the fluid cushion system.

The simplest method for elimination of friction forces is the use of a lubricant between the loading platens and the test specimen. Sheppard [6] observed that such treatment may lead to the opposite effect: excessive lubrication may lead to outward-directed frictional forces caused by the squeezing out of the lubricant. The lateral extrusion of the lubricant will induce lateral tensile stresses and a nonuniform stress distribution in the specimen's end resulting in a reduction of its apparent strength.

In order to reduce friction, Sheppard [6] used friction-reducing pads composed of two layers of plastic film 0.0076 cm thick combined with a layer of axle grease. Hugues

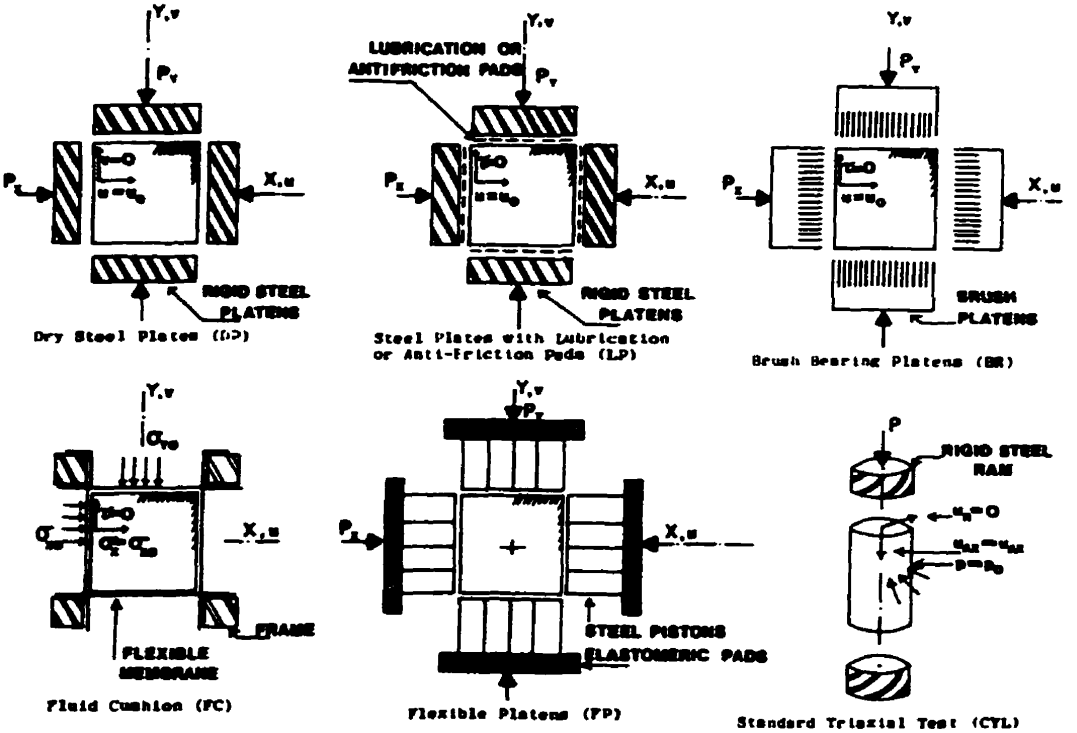

Figure 2.1: Biaxial test methods [5]

and Baharamian [7] examined those pads in uniaxial compression and noticed that the cube results were much lower than the expected strength values. They attributed that to the expansion of the plastic film between the grease and the concrete specimen which would have led to premature failure of the concrete.

Hugues and Baharamian [8] used a sandwich made of layers of aluminum sheets and grease to reduce the friction between the test specimen and the loading platens. Schickert [9] showed the limitation of this solution in the case of high applied stresses. The frictional forces were much stronger shortly before fracture occurred than at the start of load application.

Mills and Zimmerman [10] found that pads made with axle grease between 0.0075 cm teflon sheets had a very low coefficient of friction for normal stresses up to 350 MPa. Nojiri et al. [11] used two sheets of teflon (0.05 mm) lubricated with silicon grease as a friction reducing pad. The friction pads were able to reduce the coefficient of

friction between the testing platens and the specimens to a value of 0.04.

It should be noted that if intermediate layers are used, their thickness should be kept very small. Increasing the thickness will lead to a sign-reversal of the constraint at the interface between the specimen and the testing machine. This will lead to a splitting action at the specimen end. A comprehensive study on the use of intermediate layers is given by Newman [12].

Brush bearing platens were first introduced by Hilsdorf [13], and have been subsequently used by several researchers (for example [14, 15, 16, 17, 18], among others). The loading apparatus consists of assembled steel rods, with a cross section of 5 × 5 mm. The length of the rods varies from 100–140 mm, depending on the maximum concrete strength for which the particular brush platen can be used without buckling of the filaments. This support is laterally deformable to follow the concrete deformation and hence eliminate the lateral confinement. However, the applicability of this technique may be limited by the allowed maximum pressure load of only 69 MPa, above which the brush buckling may occur (Schickert [19]).

Vonk et al. [20] carried out a study to investigate the shear stresses induced in the specimen due to different support systems. In that investigation, three different systems were employed: solid platens, brush platens (short and long brushes) and teflon pads. The results of the study indicated that the shear stresses induced in the specimens were very high in the case of dry solid platens. With the brush bearing platens, the shear stresses increased at higher applied loads due to the bending of the brush rods. The use of teflon pads produced the opposite results. The induced shear stresses increased as the applied load was increased; it then started to decrease as the applied load was further increased (Figure 2.2). van Mier and Vonk [21] attributed this behaviour to the slip-stick behaviour exhibited by the teflon pads at

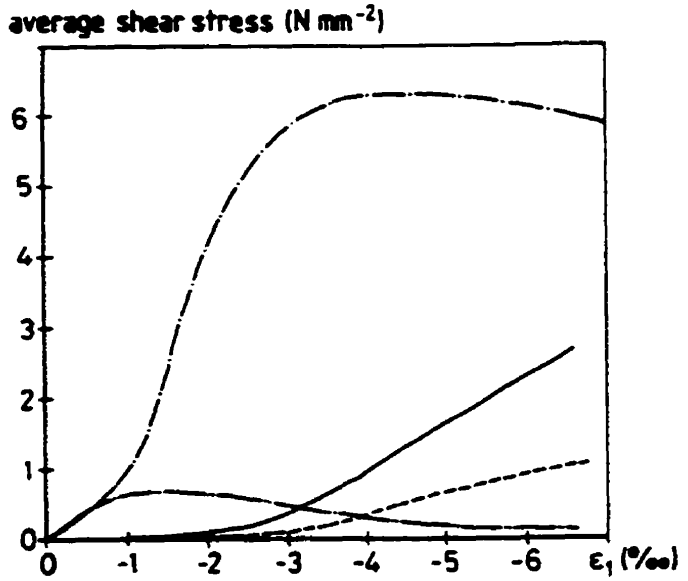

Figure 2.2: Average shear stress-strain curves for different loading systems: (— · —) dry platen, (——) short brush, (- - -) long brush, (— ·· —) teflon [20]

small deformations (high shear stresses).

The fluid cushion support system was developed by Andenaes et al. [22] at the University of Colorado. The specimen was loaded by means of flexible membranes under hydraulic pressure; and the fluid pressures were applied at the opposing surfaces of the test specimen so that the specimen floated within the load cell (Figure 2.3). This method eliminated any friction between the test specimen and the loading device. Fluid and fluid cushion (thin membrane) boundary devices, however, can lead to early failure due to interaction with the specimen microstructure [23]. In addition, they limit the nature of loading to compressive loadings only as they cannot produce tension loading. To perform tension tests, brush platens should be added [24].

As all of the above cases show, the loading devices used in biaxial testing of concrete impose some boundary constraints in the normal as well as the lateral directions.

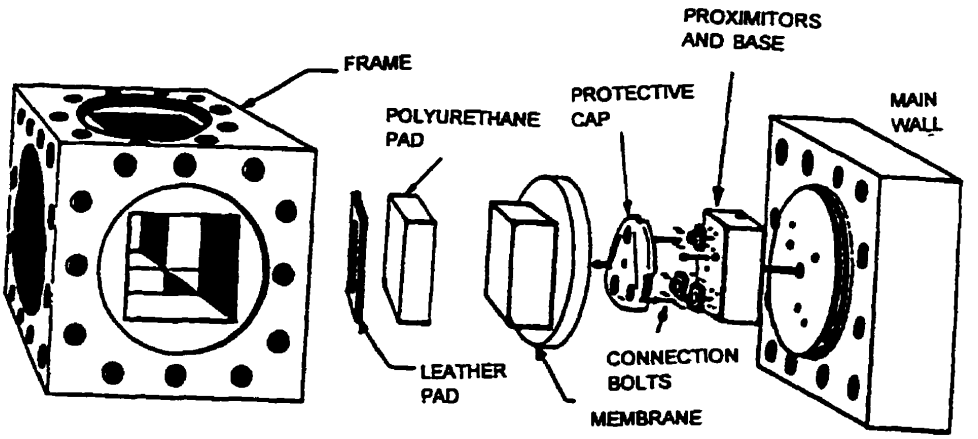

Figure 2.3: Exploded view of fluid cushion cubical cell [22]

For the lateral boundary constraint, the fluid cushions are sufficiently deformable so as to permit lateral displacements, with zero shear stresses on the surface. Rigid steel platens without surface lubrication produce sufficiently high friction to constrain the specimen boundary against lateral displacements, leading to shear stresses on the surface. To reduce lateral friction, different methods of lubrication or brush platens are used to allow lateral displacement.

As for normal boundary constraints, rigid steel platens, which cause uniform normal displacements but variable normal stresses may be grouped at one end of the scale; fluid cushions, which ensure uniform stresses but permit variable normal displacements, are at the opposite end. Other devices (such as brush platens or lubricant) produce an intermediate degree of boundary constraint.

2.2 Response of Concrete Under Biaxial Loading Conditions

2.2.1 Normal Strength Concrete

Several researchers have studied the behaviour of normal strength concrete subjected to biaxial stresses [14, 16, 17, 25, 26, 15]. Some of the much earlier information is questionable because of the technical difficulties involved in achieving the desired state of stress and in obtaining accurate measurements of the extremely small multiaxial strains. Iyengar et al. [25] reported biaxial strength values as high as 350 % of the uniaxial compression strength of an identical test specimen. This misleading result could be attributed to the three-dimensional state of stress existing in their tests due to friction between the testing platens and the test specimens. Applying different methods to reduce the friction between the test specimens and the testing platens yielded more accurate results. Nevertheless, the reported results had a large scatter [26].

The most effective method to alleviate the friction problem was the brush bearing platens developed by Hilsdorf [13]. The brush platens minimize the confinement due to friction and yield more reliable stress-strain and strength results. Kupfer et al. [14] utilized these platens and carried out an experimental investigation on the behaviour of concrete under biaxial loading. Their research provided some of the most complete and reliable experimentally determined information on the biaxial behaviour and ultimate strength of normal strength concrete. The results have been widely accepted and were verified by Liu et al. [16] and Tasuji et al. [17], using similar test set-ups. Moreover, the results of the fluid cushion tests carried out by Andenaes et al. [22] were in good agreements with Kupfer's observations.

The strength of concrete subjected to biaxial compression was found to be higher

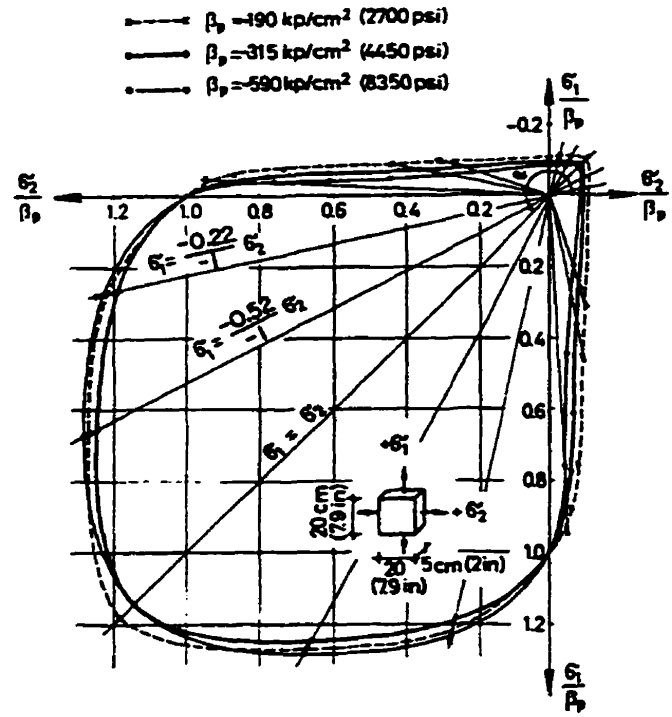

Figure 2.4: Biaxial strength envelope of concrete [14]

than the uniaxial strength [14, 16, 17]. A strength increase of approximately 16 % was achieved at an equal biaxial compression state ($\sigma_2/\sigma_3 = 1$). A maximum strength increase of about 25 % was reached at a stress ratio of $\sigma_2/\sigma_1 = 0.5$. The strength decreased almost linearly as the applied tensile strength was increased for the biaxial compression-tension case. The biaxial tensile strength was almost the same as that of uniaxial tensile strength (Figure 2.4).

2.2.2 High-Strength Concrete

Very few data is available on high-strength concrete under biaxial state of stress [11, 27, 28]. Nojiri et al. [11] carried out an experimental testing program on four concrete mixes with different compressive strength subjected only to biaxial compressive loading. The specimen used were 100 mm cubes. The highest concrete strength used in the study was 67.9 MPa. The authors concluded that failure envelopes for the

four different strength levels of concrete (in biaxial compression) were very similar. However, the whole range of the biaxial failure envelope was not covered.

Herrin [27] studied the behaviour of model concrete plate specimens, composed of nine aggregate discs embedded in a high-strength mortar matrix, when subjected to biaxial compression. Chen [28] tested the same model specimen as well as high-strength concrete plates (127 × 127 × 12.7 mm) made with different types of aggregates and subjected to biaxial loading. The maximum compressive strength of the tested plates was 60 MPa. Albeit the maximum strength of the control cylinders reached almost 95 MPa, no explanation was given for such discrepancy. Only compression-compression tests were performed and the whole range of biaxial failure envelope was again not covered.

The only available data in the literature that covers the entire behaviour of a relatively high-strength concrete mix, subjected to biaxial loading, was reported by Kupfer et al. [14]. In this experimental work, one set of the tested specimens had a compressive strength of 59 MPa. The specimens were subjected to three ranges of biaxial stresses: compression-compression (C-C), tension-tension (T-T), and compression-tension (C-T). The authors concluded that the neither the concrete composition nor the concrete strength has any effect on the biaxial strength, and that the strength characteristics are typical for any type of concrete. Nonetheless, some researchers noticed that the biaxial strength of concrete decreases with the increase of compressive strength [17, 29].

The behaviour of high-strength concrete could be different from normal strength concrete for different biaxial load combinations [31]. For the C-C case, the micro-cracking and the stress-strain characteristics of high-strength concrete under uniaxial loading is quite different than normal strength-concrete. As for the T-T case, a

decrease in the ratio of tensile strength to compressive strength may be observed for higher-strength concrete, as noted for uniaxial cases [30]. A large difference could be noted for the C-T case [31]. A small amount of tension would decrease the compressive capacity more radically for high-strength concrete than for normal strength one.

2.2.3 Light Weight Aggregate Concrete

Few experimental investigations of the behaviour of normal strength light weight aggregate concrete under biaxial stress were performed [32, 33, 34]. Taylor et al. [33] tested three different concrete mixes made with all light weight aggregate in biaxial compression. The specimens were 50 mm cubes and they were tested using brush loading platens. The results of the investigation indicated that the failure envelope of light weight concrete is different than that of normal weight concrete. This finding is in contrast to a previous investigation by Niwa et al. [32] (using greased bearing pads) which concluded that the shape of failure envelope (in biaxial compression) is similar to that of normal strength concrete. However, both investigations indicated that the maximum biaxial compression resistance, for light weight concrete, occurred at a ratio of applied loads equal to 0.8.

Atan and Slate [34] carried out a limited biaxial compression testing program on two types of light weight concrete (one with light weight fine aggregate and the other with natural sand). The experiments were performed on a 130 × 130 × 13 mm concrete plates using the brush platens. The results of the investigation indicated that, in contradiction to the above mentioned investigations, the shapes of the failure stress envelopes (in biaxial compression) for light weight and normal concrete are generally similar and the biaxial compression resistance, for light weight concrete, occurred at a ratio of applied loads equal to 0.4 - 0.5.

2.2.4 Post Peak Behaviour in Uniaxial Compression

In order to obtain a stable descending portion during a compression test, a closed-loop displacement control, of the test, has to be employed. Experiments carried out in load control (constant $\dot{\sigma}$) do not capture this phenomenon. In a displacement control compression test, some selected deformation in the specimen is used as a feed-back signal. Figure 2.5 provides a schematic of the stress strain curve which is obtained from such a test.

The post peak behaviour of a compression specimen is mainly affected by four interacting parameters [35]: (a) the strength of concrete; (b) the composition of the feedback signal that controls the test; (c) the friction restraint at the end zones; and (d) the areas of strain localization in the specimen.

Early research work [36, 20] revealed that as the support system is changed, the post peak behaviour of normal strength concrete becomes significantly different. In these tests, platen to platen displacement was used as the feedback signal. On the other hand, extensive experiments [37, 38, 39] have clearly demonstrated that using the platen to platen displacement, as a feedback signal, does not produce a stable descending portion of the stress strain curve for high strength concrete cylinders. It was suggested that a snap-back phenomenon occurs and that could be considered the reason for the absence of any post peak behaviour for high strength concrete. Several control techniques have been suggested to produce a stable control capable of capturing this phenomenon for high strength concrete cylindrical specimen. Among them is the use of circumferential strain as a feedback signal [40, 38, 41]. Post peak behaviour of high-strength concrete was obtained using a combination of cross-head displacement, axial and circumferential deformation of the specimen as the feed-back signal [42]. A similar method using a combination of axial and circumferential dis-

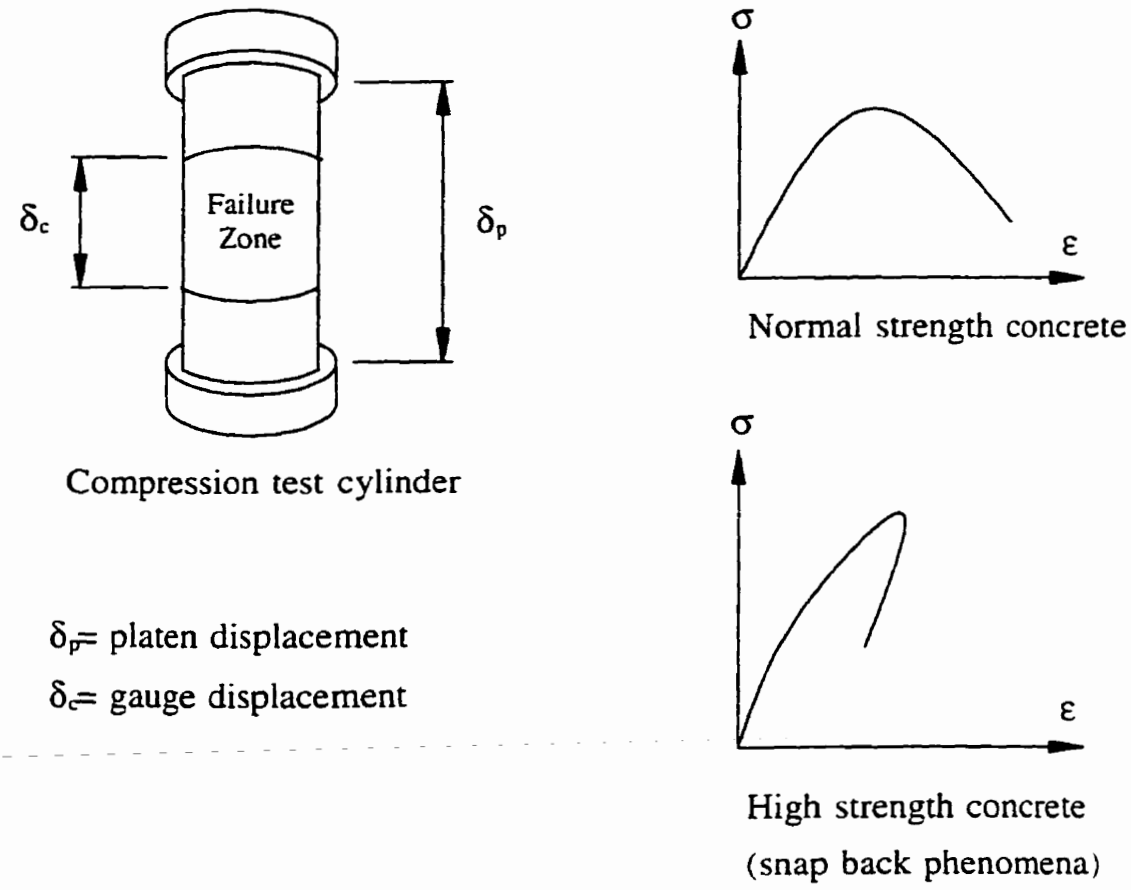

Figure 2.5: Schematic of the stress strain curves obtained form a uniaxial test specimen in compression (platen to platen displacement is used as a feedback signal)

placement as a feedback signal was used by Glavind and Stang [35]. Another method of feedback control using a linear combination of force and displacement was employed by [43, 39, 44]. This method was originally proposed for compression testing of rocks [45]. The factors that affect the post peak behaviour such as the specimen's end restraint exist for both high strength as well as normal strength concrete specimen. Using a platen to platen displacement as a feed back signal produces a stable descending portion for normal strength specimen but is not successful for high strength specimen. This was attributed to the so called snap-back phenomenon. The snap-back phenomenon was only observed, for high strength concrete specimen, when the circumferential strain is used as a feed back signal. A logical interpretation for such a phenomenon was given by [35]. In normal strength concrete, the cracks get arrested by the aggregate. In high strength concrete, the cement paste and the aggregate are similar in strength and stiffness. Thus, the crack extends through the aggregate. As a result, when a crack develops in high strength concrete, there is a sudden increase in circumferential strain, causing unloading to take place in the axial direction in order to regulate the error signal that controls the movement of the hydraulic actuator. On the other hand the research work by Jansen et al. [44] shows that the snap-back is a material phenomenon for high strength concrete. In that research program, the strain was still measured over a big portion of the specimen and close to the regions with end restraint due to the specimen- platen interaction. This could influence the results to some extent. In conclusion, it seems as more research work is needed before a solid conclusion can be reached regarding the issue of snap back phenomenon in high strength concrete.

Another outstanding issue is what does the compression post peak behaviour represent and over what portion of the specimen should it be measured? Also, does

this measurement reflect a true material behaviour or is it a structural response as the result of several factors including the stiffness of the loading platen and the regions of the test specimens that are affected by the end restraint?

The experimental results indicated that compression failure is subject to localization effects. The post peak behaviour was found to be dependent on the specimen geometry, boundary conditions, and the gauge length used to obtain the strains [18, 20, 46]. Consider the uniaxial compression cylindrical test specimen shown in Fig 2.5. Due to end restraint, the stress distribution in the specimen is not uniform. During the post peak behaviour, there exist two different zones in the specimen. The area that is adjacent to the platens with a smaller stress than the middle portion of the specimen and the failure zone located close to the centre of the specimen. The middle portion of the specimen, the failure zone, deforms in a way that is different than the end zone. Some expansion outside the failure zone will take place as unloading occurs. Thus the total deformation in the specimen is the combined deformation of the intact part as well as the localized failure zone. Thus the platen to platen deformation cannot be considered as the 'true' material behaviour. As a result, it is rational that the measurement of the strain should take place in the middle portion of the specimen. Also, this measurements should be used as the feedback signal to produce a stable descending portion of the stress strain curve. Otherwise, the measurements will represent a structural behaviour rather than a material behaviour.

In multiaxial testing, the nature of the test prevents mounting any sensor, in a secure way, directly on the specimen. Thus, unfortunately, it is only possible to measure the global deformations, that is, is platen to platen measurements. In biaxial testing, however, surface measurements, on the free surface of the specimen, can be attained. Still, these sensors are subjected to cracking and spalling under the

attachment points of the transducer in the post peak behaviour [35, 41, 46]. Thus, such a sensor cannot be used efficiently in the post peak regime as loss of control may occur and damage can occur to the loading actuators.

2.2.5 Post Peak Behaviour in Biaxial Compression

Post peak behaviour of concrete is of vital importance when nonlinear finite element analysis is used for accurate prediction of structural response. The existence of a descending branch of the stress-strain curves under biaxial stress states has not generally been observed. Nelissen [15] attempted to obtain the descending portion of the stress strain curve under biaxial loading. Constant rate of straining was used. However, Nelissen found that this part of the stress strain curve depended on the situation of the measurement instruments. As a result, the descending branch was not reported for any biaxial test.

van Mier [18] conducted a notable test program to study the softening behaviour of concrete under triaxial state of stress. The experimental program contained a very limited portion on biaxial compression loading. The descending portion, for a normal strength specimen, was reported for two low confinement stress ratios, $\sigma_2/\sigma_3 = 0.05$ and 0.10. Unfortunately, at a higher confinement ratio ($\sigma_2/\sigma_3 = 0.33$), the descending portions of the stress- strain curve, could not be successfully obtained. In addition, the specimen's response (stress strain curve) was calculated from the platen to platen displacement. Due to the bending of the brush rods, corrections to the stress strain curve had to be made using a similar aluminum specimen. It should be noted that such a correction may not be accurate. In the post peak regime, concrete will crack. As a result, the deformation, due to the bending of the brush rods, will be significantly different for a concrete specimen. Nonetheless, the triaxial test data obtained from that experimental program is considered to be fairly good and it is widely accepted.

2.2.6 Loading Path

Taylor et al. [47] investigated the effect of the loading path on the biaxial response of lightweight aggregate concrete. The findings of their study indicated that two-step sequential loadings resulted in strengths significantly lower than those obtained for proportional loadings. For normal strength concrete. Nelissen [15] observed that the maximum-strength envelope was independent of the load path. However. in his study. the effect of the loading path was not investigated for concrete with higher strength.

In conclusion. from the above mentioned reasoning, it appears that further investigations should be dedicated to study the behaviour of high-strength concrete under biaxial loading. In this thesis. an experimental investigation. covering the entire load path is carried out to determine the behaviour of high-strength concrete when subjected to biaxial state of stress.

2.3 Constitutive Models

Over the past 25 years. several constitutive models have been proposed and used for the finite element analysis of concrete structures. An extensive review of these models was undertaken by Chen and Saleeb [48]. Chen [49] and the ASCE Committee on Finite Element Analysis of Reinforced Concrete Structures [50]. Meanwhile. CEB report [51] provides a critical review of the constitutive laws used for modelling concrete under multiaxial state of stress. In this section. highlights of the available constitutive relationships for concrete and the advantages and disadvantages of these models are briefly summarized. Rather than reviewing each individual research separately. the main features of each family of models are presented.

2.3.1 Elasticity Based Models

The elasticity-based models can be divided into: a) linear elastic, b) nonlinear elastic, and c) incremental (hypoelastic) model.

Linear elastic models

The linear elastic models are based on the relation:

$$\sigma_{ij} = C_{ijkl}\epsilon_{kl}$$

where C_{ijkl} is material matrix $f(E, \nu)$, and σ_{ij} and ϵ_{ij} are the stress and strain vectors, respectively.

These models are simple and easy to formulate and use. However, such models are no longer used in the analysis of concrete structures. The main drawback of these models is that they fail to identify the inelastic deformation. Also, the state of stress depends only on the current state of strain.

Nonlinear elastic models

The nonlinear elastic (secant) model [52, 53, 54] can be expressed as:

$$\sigma_{ij} = F_{ij}(\epsilon_{kl})$$

where F_{ij} is the elastic-response function and σ_{ij} and ϵ_{ij} are the components of the stress and strain tensors, respectively.

These models provide a simple approach for problems in which monotonically proportional loads prevail. The disadvantage of these models is that the state of stress depends only on the current state of strain. These types of models are limited to structures subjected to specific types of loading (monotonic and proportional) [54].

The incremental (hypoelastic) models

The incremental (hypoelastic) models [55, 56, 57] are based on:

$$\dot{\sigma}_{ij} = D_{ijkl}\dot{\epsilon}_{kl}$$

where D_{ijkl} is a material property matrix, which is a function of stress or strain tensor, and $\dot{\sigma}_{ij}$ and $\dot{\epsilon}_{kl}$ are the stress and strain-increment tensors.

These models are capable of modelling many of the characteristics of concrete behaviour under monotonic loadings. In addition, they are simple to formulate in comparison to plastic and endochronic models. The main disadvantage of such models is that they do not apply in situations where the principal stress directions rotate [58]. In addition, they cannot account for the behaviour of concrete in the strain softening region. Also, these models do not accurately describe the behaviour of concrete under cyclic loading.

Recently, an orthotropic model was used by Link and Elwi [59]. The model was built on the equivalent uniaxial strain concept advocated in [55, 56, 57]. Link and Elwi [59], based on that model, carried out a finite element analysis (two dimensional) of composite ice resisting walls. Good agreement between the experimental and theoretical results were achieved. However, it was found that the model poorly predicted the behaviour of the walls subjected to significant longitudinal compressive loads. That was attributed to the overestimation of the confinement effects.

2.3.2 Plasticity Based Models

The traditional plasticity-based models can be classified as: a) elastic perfectly plastic, and b) elastic hardening plastic.

Elastic perfectly plastic

The elastic perfectly plastic models are incremental in nature and they can represent inelastic strains in concrete. However, the normality rule used in these models does not apply accurately to fractured concrete. The disadvantage of these models is that they predict higher volumetric expansion upon failure than observed in practice. Also, since the failure surface is fixed in the stress space, it cannot account for the behaviour of concrete in the strain softening region.

Elastic hardening plastic models

Earlier elastic hardening plastic models are based on a certain yield surface and the evolution of a subsequent loading surface ([60, 61, 62, 63], among others). They account for the plastic strains in concrete and they describe accurately many of the characteristics of concrete. The major disadvantage of these models is that they cannot account for the microcracking of concrete since the normality rule is used.

More recent elastoplastic models [64, 65, 66, 67] are often used to describe the behaviour of concrete in compression. These models may cover the stress history dependent behaviour. They allow, in connection with a nonassociated flow rule, the simulation of the nonlinear volume change. However, these elastoplastic models have some inadequacies in the tension and mixed compression-tension regions. The main disadvantage is their inability to model cracked concrete. Therefore, in these models the elastoplastic concept has to be abandoned totally when tensile cracks occurs.

Recently, the plasticity based models have made considerable progress. Such models incorporated the use of the recent concepts of fracture mechanics [68, 69], and continuum damage mechanics (in the form of elastic degradation) [70, 71]. Thus, plasticity-based constitutive laws are capable of modelling plain concrete in cracked

and un-cracked states with the same elastoplastic concept.

2.3.3 Endochronic models

The endochronic models are based on the concept of intrinsic time, which describes the inelastic strain accumulation [72, 73]. These models are capable of modelling a wide range of nonlinear behaviour of concrete. The use of such models requires a large number of material parameters that are incrementally nonlinear, resulting in heavy computational iteration in a finite element program.

2.3.4 Damage Models

A continuum damage mechanics approach is used to interrelate distributed defects and the macroscopic behaviour of concrete. Extensive research work on the application of damage mechanics to model concrete behaviour was carried out and numerous papers were published, for example [74, 75, 76, 77, 78]. A review of some of the available damage models used for concrete can be found in [78]. A state of the art review of damage mechanics can be found in [79, 80, 81]. Recent implementation of damage mechanics to study the behaviour of plain concrete dams was carried out by [82, 83].

The fundamental notion of these models is to represent the damage state of materials by an internal variable, which directly characterizes the distribution of microcracks formed during the loading process. Each damage model established mechanical equations to describe the evolution of the internal variables and the mechanical behaviour of damaged materials. Although there has been a profound disagreement among researchers regarding the proper choice for the characterization of damage, the further development of a more general, and unified, damage approach will provide a powerful tool in modelling concrete behaviour.

2.3.5 Microplane Models

The microplane model represents a micromechanics approach to modelling concrete behaviour. Originally presented by Bažant [84], the fundamental assumption is that the stress-strain relation can be specified independently on various planes in the material, assuming that the strain components on the plane are the resolved components of the strain tensor. The derivation of the incremental constitutive relationship is given in Bažant and Prat [85]. Incorporation of a nonlocal softening model into the microplane model was later performed by Bažant and Ozbolt [86].

Although the microplane model shows good promise for general multiaxial simulation of concrete constitutive response, much more development work needs to be undertaken. For example, in the research work by Bažant and Ozbolt [87] on cyclic triaxial behaviour of concrete, only uniaxial loading cases were considered. In addition, the decay parameters used to determine the constitutive moduli are not calibrated sufficiently. The spherical integrals used in the derivation of the constitutive relationship require the use of several integration points on the hemisphere per Gauss point, which increases solution time dramatically. These shortcomings make the microplane model unwieldy for the analysis of general concrete structures. Furthermore, the utilization of a microplane model to analyze full scale structures has yet to be tackled.

2.3.6 Adopted Model for the Current Study

Some may contest that the plasticity based models may be inadequate in representing the cracking of concrete, on the macro-level, as micromechanics would. Nevertheless, in the phenomenological approach to modelling a frictional material like concrete, it can be argued that all the essential response features can be represented in a tractable

model without the explanation that would be provided by micromechanics. Such an approach is justified by the need to provide engineering analysis of structural systems made with concrete. Thus the adequacy of a plasticity based model can be evaluated on a macromechanical basis, rather than on a micromechanical basis, as represented by the experiments on specimens on a laboratory.

The model adopted in this study is based on Etse and Willam [71] model. It is referred to as the Extended Leon Model. The development of that model occurred gradually over the years at the University of Colorado. The Leon model [88] was first employed by Willam et al. [89] to characterize the triaxial test data of medium strength concrete. Subsequently, it was extended by Pramono and Willam [70] to formulate an elasto-plastic constitutive model for hardening and softening behaviour of concrete when subjected to arbitrary triaxial loading. The model was further extended by Etse and Willam [71] to become the Extended Leon model.

The elasto-plastic constitutive model by Pramono and Willam [70] was implemented into the general purpose finite element program ABAQUS by Xie et al. [90]. It was used in a numerical investigation of high strength concrete columns. It is worth mentioning here that the implementation of the Etse and Willam [71] model, in the current thesis, is based on the Xie et al. [90] implementaion of the Pramono and Willam [70].

That particular model was chosen for the purposes of this study because it possesses different characteristics that make it attractive for use with finite element analysis. The development of the adopted model, together with the modification, calibration, and implementation in a general purpose finite element program is presented in Chapter 5.

2.4 Finite Element Simulation of Concrete Test Specimen in Compression

The finite element method can be applied to provide some insight into different types of basic testing of a concrete specimen. It can be used to provide some understanding of the stress state in the specimen as well as the interaction between the specimen and the testing machine. In the following sections, a literature review of some of the analytical and finite element work used in simulating a compression test cylinder, is presented. In addition, previous work involving the simulation of a brush platen support for biaxial testing is reported.

2.4.1 Analytical and Finite Element Studies of Uniaxial Testing of Concrete Cylinders

Analytical estimates of the stress distribution within a circular cylindrical specimen under compression, with perfectly constrained ends, were made as early as the beginning of this century in 1902 by Filon [91] using linear elasticity. Filon showed that the state of stress in the specimen is not perfectly uniform and a stress concentration exists at the corner ends. Other closed form solutions using the theory of elasticity have been proposed [92, 93, 94]. Al-Chalabi and Huang [95] provided a comparison of some of these predictions and showed that they differ significantly. Linear finite element analysis of a test cylinder have also been provided for unspecified rock and soil materials [96]. The effects of inserts on the behaviour of cylinders, in uniaxial compression, was studied by Brady [94]. Linear elastic analysis was performed on a cylinder with inserts used to minimize the end-plate-specimen interfacial friction. Three different moduli of inserts were examined. Because linear elastic model was used, such analysis can be considered useful for the elastic range only. The material

behaviour was not considered in the nonlinear range that actually occurs during an actual test.

Shrive [97] studied the state of stress in a concrete cylinder using linear elastic finite element analysis. The loading platens were not modelled in the simulation. Instead, the radial displacement of all nodes at the platen surface was restrained as those nodes were displaced equally in the loading direction.

Ottosen [98] carried out a non linear finite element analysis of a concrete cylinder under compression. The concrete cylinder was modelled together with the steel platens under the assumption that there is perfect bond between them. The loading platens had a radius of 160 mm and thickness of 93 mm with the elastic parameters assumed as E = 205 GPa and ν = 0.3, whereas the concrete had f_c' = 18.7 MPa, E = 28.9 GPa, ν=0.19 and f_t'/fc = 0.1. The results showed that the stress distribution in the specimen was not uniform, with stress concentration at the specimen's corners. The shear stresses induced at the specimen's edge were also calculated. The end blocks of the testing machine, used in the finite element simulation, did not conform to ASTM test standards [99]. Thus, the results obtained may differ from those obtained using the standard end block that is recommended by ASTM.

Bakht et al. [100] studied the variation of Young's modulus and Poisson's ratio across the width of a concrete cylinder using linear elastic finite element analysis. The steel loading platens and the concrete specimens were modelled together. The platens diameter was chosen as 406.4 mm, while the concrete specimen had a diameter of 203.2 mm and a height of 508 mm. Springs were used to numerically simulate the interaction (at the interface) between the specimen and the loading platens. Two extreme cases were studied, assuming no friction between the specimen and the platens, and assuming complete bond between the specimen and loading platens. The main

conclusion was that the values of Young's modulus and Poisson's ratio, as measured by the usual compression test, are reliable.

A better understanding of the behaviour of a concrete cylinder in compression test, using finite element simulation, should include actual test parameters. More studies that address such issues are needed so that the finite element simulation may represent actual testing.

2.4.2 Finite Element Simulation of the Boundary Conditions used in Biaxial Testing of Concrete

In a previous section, the different test set-ups used in biaxial testing of concrete were reviewed and examined. As discussed, the most commonly used methods are the use of a lubricant to minimize the friction, the use of the pressure platens developed by Hilsdorf; these are often referred to as brushes.

Recently, Torrenti and Royis [101] carried out a linear elastic finite element simulation of concrete cubes with an aspect ratio equal to one. The study was used to design the brush platens used for testing normal strength concrete subject to biaxial loading. In that study, the effectiveness of the brush platens was evaluated as opposed to dry solid platens. The analysis was performed assuming that the specimen was bonded to the loading platens. The performance of the supports was only evaluated for the case of uniaxial loading. The shear stresses induced in the specimen were reported to be at a minimum. However, no values for the shear stresses and the shear stress distribution at the specimens' edge were provided. In addition, the study did not include the maximum capacity of the brush supports. These factors are important if the brushes are used in testing high-strength concrete. For the case of testing high-strength concrete, the shear stresses induced in the specimens under high applied load should be quantified and the buckling capacity of the steel brushes

should be evaluated. In addition, the performance of the brush platens for biaxial loading should be examined.

Chapter 3

Finite Element Evaluation of the Boundary Conditions used in Biaxial Testing of Concrete

The present chapter reports a non linear finite element study of the effect of different load application platens used in the biaxial testing of concrete. Three methods are evaluated numerically: dry ordinary solid steel testing platens, brush platens, and friction reducing teflon sheets. The method of fluid support system was not evaluated because it limits the possibilities of experiment (no provisions for tension tests in particular).

The interaction between the concrete test specimen and the steel loading platens is modelled by introducing the friction that exists between the two different surfaces. This is achieved through an interface element with a friction coefficient that is measured from actual experimental tests. The effect of confinement on the displacement field in addition to the stress distribution in the loading direction are presented and discussed. The shear stresses induced in the specimen are evaluated. Finally, the buckling capacity of the brush platens is examined.

3.1 Simulation of the Interaction Between the Test Specimen and the Loading Platens

As mentioned in Section 2.4, previous studies on the simulation of a concrete test cylinder in compression either assumed full bond between the specimen and the loading platens, or used springs to numerically simulate the interaction (at the interface) between the specimen and the loading platens. As pointed out by Ottosen [98], the assumption that the specimen is glued to the loading platens could be fair for the concrete cylinders with an aspect ratio of two. However, Ottosen [98] concluded that when the aspect ratio of the specimen is one, slip must be expected as failure is approached. As for the case of using springs, normally two extreme cases are studied: either there is no friction between the specimen and the platens, or the specimens are completely stitched to the platens. Although the springs could be calibrated to simulate the friction between the specimen and the platens, finding a value for the spring stiffness is rather a difficult task.

A better representation of the interaction between the concrete test specimen and the steel loading platens is to introduce the friction that exists between the two different surfaces. This could be done through an interface element with a friction coefficient that is estimated from actual experimental tests. Hilsdorf [13] suggested that the coefficient of friction decreases from 0.6-0.15 with increasing normal stresses, and recommended a value of 0.10 for high normal stresses. Ottosen [98], after examining Hilsdorf's test results, concluded that the coefficient of friction (between the solid platens and the concrete specimens) decreased from 0.49 to 0.17-0.24 for large normal stresses. Recently, Vonk et al. [20], based on experimental testing, evaluated the coefficient of friction and reported that it varied from 15.5 % to 12.5 % at the beginning and at failure, respectively. Thus, a coefficient of friction equal to 0.30

seems to be reasonable for small normal stresses, while a value of 0.15 seems to be rational for large normal stresses. In this study, a coefficient of friction equal to 0.30 is used throughout the simulation as the friction model used could not include different friction coefficients at different loading stages.

In order to simulate the friction between the steel loading platens and the concrete specimen, interface elements are used. For the dry solid platens and the brush supports, the coefficient of friction is assumed to be equal to 25 %. The lubricated teflon pads have a thickness of 1 mm, a Young's modulus of 4 GPa and a Poisson's ratio equal to 0.42 and a coefficient of friction of 0.05.

3.2 Constitutive Material Model

For the finite element evaluation of the test set-up, the incremental elastic-plastic concrete model implemented in the general purpose finite element analysis code, ABAQUS, is adopted [102, 103]. The model utilizes the classical concepts of plasticity theory: a strain rate decomposition into elastic and inelastic strain rates; elasticity; yield flow; and hardening. In addition, the model uses a crack detection plasticity surface to determine when cracking takes place, and the orientation of the cracking.

3.2.1 Elastoplastic Behaviour

The initial yield surface defines the elastic limit (Fig 3.1). If the state of stress lies within the initial yield surface, linear-elastic constitutive equations are applied. As the material is stressed beyond the initial yield surface, a subsequent new yield (loading) surface is developed, which replaces the initial one. Moreover, any straining beyond the initial surface is accompanied by a new irrecoverable plastic deformation.

Isotropic hardening is used to define the post-yield response rather than kinematic

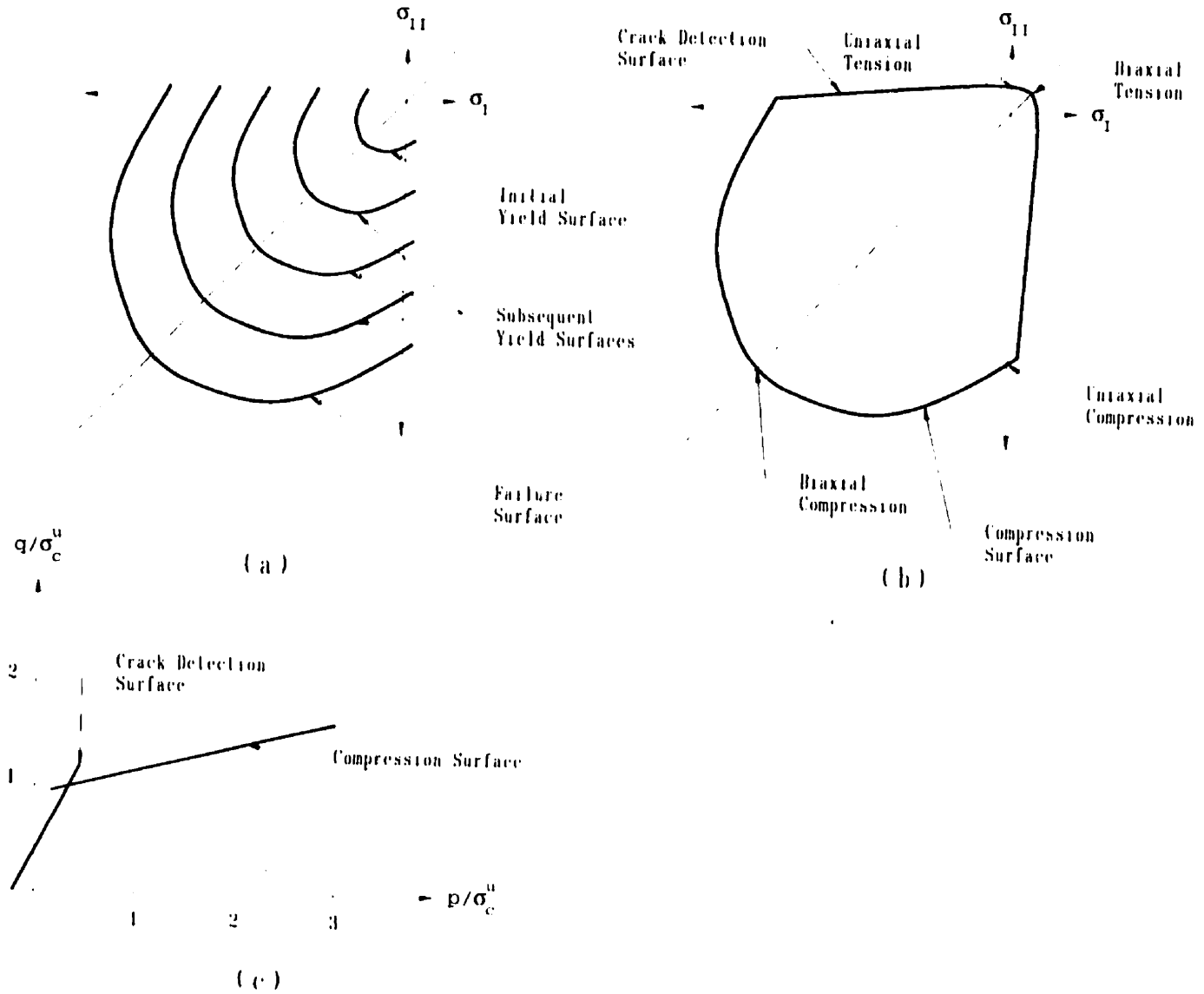

Figure 3.1: Constitutive model used in the FE analysis: (a) yield surface expansion; (b) failure surfaces in plane stress space; and (c) failure surface in the $p - q$ space

or mixed hardening due to its simplicity in the definition of subsequent yield surfaces; uniform expansion of the initial and subsequent surfaces is assumed. A hardening parameter relates the uniaxial material stress-strain relation to the multiaxial state of stress where an associated flow is assumed to govern the post-yielding stress-strain relationship.

3.2.2 Behaviour under Compressive Stress State

The model uses a simple yield surface that involves the first two stress invariants. This surface is defined in terms of the effective pressure p, von Mises equivalent stress q, and a hardening parameter $\tau_c(\lambda_c)$ as follows

$$f_c(p,q) = q - \sqrt{3}a_0 p - \sqrt{3}\tau_c(\lambda_c) = 0 \tag{3.1}$$

where a_0 = a constant, which depends on the relation between biaxial strength and uniaxial compressive strength.

The associated flow rule is used with the yield surface given by Eq. 3.1 to define the plastic strain increment ($d\epsilon_c^{pl}$) where

$$\begin{aligned} &\text{For } f_c = 0 \text{ and } d\lambda_c > 0 : d\epsilon_c^{pl} = d\lambda_c \left[1 + c_0\left(\frac{p}{\sigma_c}\right)^2\right] \frac{\partial f_c}{\partial \sigma} \\ &\text{otherwise: } d\epsilon_c^{pl} = 0 \end{aligned} \tag{3.2}$$

where $(\epsilon_c)^{pl}$ = plastic strain tensor; and $(\partial f_c/\partial\sigma)$ = gradient of the flow potential for the yield surface, which can be defined using Eq. 3.1. The constant c_0 depends on the relation between the ultimate plastic strain in the equal biaxial compression stress state and the ultimate plastic strain in the uniaxial compression stress state.

Failure in the compressive stress space is reached when the yield surface expands to a certain failure surface. This is expressed using an equation similar to Eq. 3.1, with τ_c equal to the yield stress in the case of pure shear (only $\sigma_{12} = \sigma_{21} = \tau_c$ exist

in the stress tensor σ). The compression surface is shown in (Fig 3.1) in both the $p-q$ plane and the plane stress space.

3.2.3 Cracking

Cracking is modelled using a smeared crack approach. Cracking occurs when the stress state reaches a failure "crack detection surface" (Fig 3.1), given by

$$f_t(\hat{p},\hat{q}) = \hat{q} - \Big[3 - b_0\frac{\sigma_t(\lambda_t)}{\sigma_t^u}\Big]\hat{p} - \Big[2 - \frac{b_0}{3}\frac{\sigma_t(\lambda_t)}{\sigma_t^u}\Big]\sigma_t(\lambda_t) = 0 \tag{3.3}$$

where b_0 = a constant, which depends on the relationship between the axial tensile and compressive strengths; σ_u^t = uniaxial tensile strength; $\sigma_t(\lambda_t)$ = hardening parameter; and $(\hat{p},\hat{q})$ = invariants in the subsection of stress space, which excludes the stress component $\sigma_{\alpha\beta}$ (α or β is a crack direction) associated with open cracks. After cracking, damage elasticity is used to model the cracked material where, at the increment at which crack detection surface is violated, "plastic" crack detection strains are calculated only once. They are defined using the associated flow by

$$\begin{aligned} &\text{For } f_t = 0 \text{ and } d\lambda_t > 0 : d\epsilon_t^{pl} = d\lambda_t\Big[\frac{\partial f_t}{\partial \sigma}\Big] \\ &\text{otherwise: } d\epsilon_t^{pl} = 0 \end{aligned} \tag{3.4}$$

The post-cracking behaviour, in tension, is based on the brittle fracture concepts introduced by Hillerborg et al. [104]. The fracture energy required to form a unit area of crack surface, G_f, is assumed to be a material property and can be calculated from

$$G_f = \int_0^{w_o} \sigma_t dw \tag{3.5}$$

where σ_t is the average stress over the area considered , w, is the crack width in the fracture process and w_o is the crack width when σ_t reaches zero at the end of the

softening branch. The cracking energy is then equal to the area under the stress-elongation curve.

The modified Riks algorithm (Crisfiled et al. [105]) is utilized to obtain a static equilibrium solution for the unstable response encountered in concrete due to concrete cracking in tension. or the post peak behaviour of concrete in compression. The Riks algorithm is based on attempting to step along the equilibrium path (the load-displacement response curve) by prescribing the path (arch) length along the curve to be traversed in each increment. with the load magnitude included as unknown.

3.3 Specimen - Platen Interaction

As mentioned in a Section 3.1. a rational simulation of a specimen during testing requires modelling of the interaction between the test specimen and the loading platens. A finite sliding formulation is adopted which allows for relative displacement of the contacting surfaces. The finite sliding capability is implemented by means of interface elements which model contact between an element face. attached to the test specimen. and the corresponding element on the loading platens. The elements used are compatible with the discretized domains and incorporate the corresponding nodes at the contact surfaces.

The behaviour of interface elements is characterized by the relation between the relative displacements of the surfaces in contact and shear and normal stresses at the interface. The isoparametric formulation with linear variation of both geometry and relative displacement is described by the 2 noded element shown in Fig 3.2. The shape functions $N_i(\xi)$associated with each node are given by:

$$N_1 = \frac{1}{2}(1-\xi) \qquad (3.6)$$
$$N_2 = \frac{1}{2}(1+\xi)$$

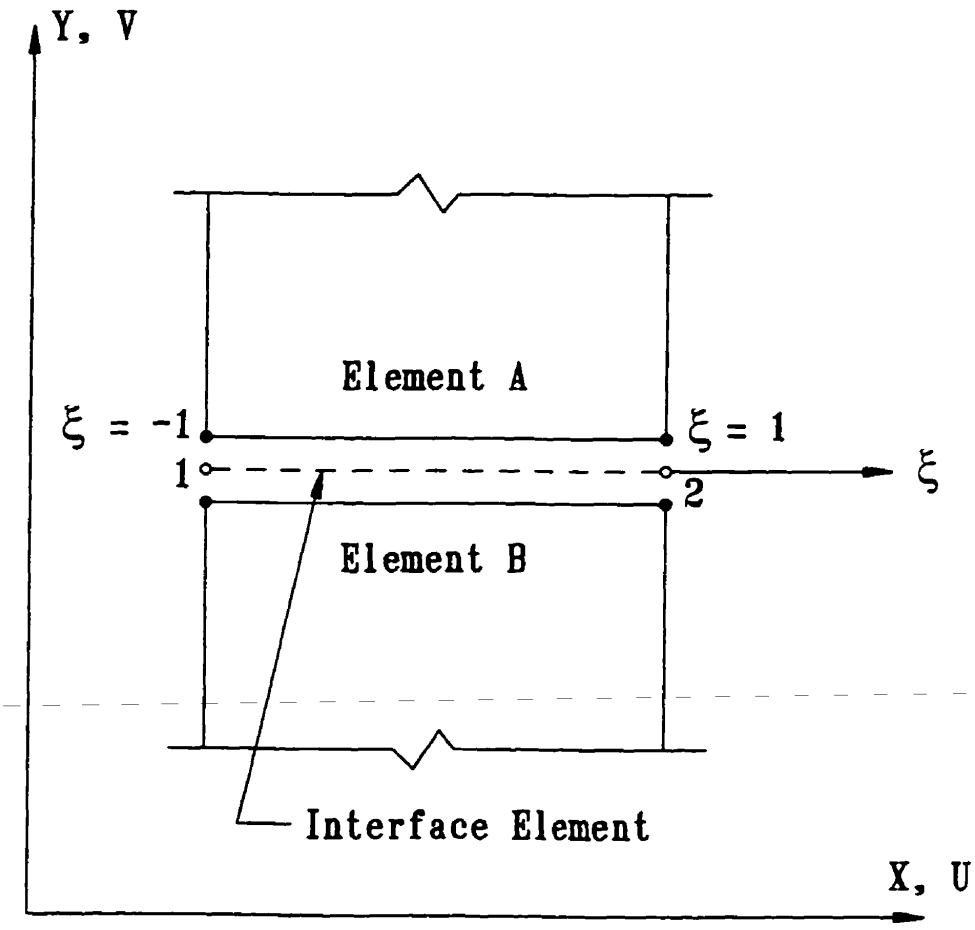

Figure 3.2: Isoparametric interface element

Thus,

$$x = \Sigma N_i x_i, \quad y = \Sigma N_i y_i, \tag{3.7}$$

and

$$\Delta u = \Sigma N_i \Delta u_i, \quad \Delta v = \Sigma N_i \Delta v_i \tag{3.8}$$

where, Δu and Δv are relative displacements in x and y directions respectively, and x_i, y_i, Δu_i and Δv_i are the nodal values of x, y, Δu and Δv respectively.

The relative displacements in the global coordinates x and y, at any point of the element can then be expressed in terms of nodal values of relative displacements as:

$$\delta = \begin{Bmatrix} \Delta u \\ \Delta v \end{Bmatrix} = \Sigma \begin{bmatrix} N_i & 0 \\ 0 & N_j \end{bmatrix} \begin{Bmatrix} \Delta u_i \\ \Delta v_i \end{Bmatrix} \tag{3.9}$$

Denoting the relative displacements in the element coordinates as δ^e, the displacements in the element and global systems can be written as

$$\delta^e = \begin{Bmatrix} \Delta u_s \\ \Delta u_n \end{Bmatrix} = T\delta \tag{3.10}$$

in which, Δu_s and Δu_n are relative displacements tangential and normal, respectively to the element axis, and T is the transformation matrix.

The tangential stress σ_s and the normal stress σ_n at any point in the element can be related to the corresponding displacements as

$$\begin{Bmatrix} \sigma_s \\ \sigma_n \end{Bmatrix} = \begin{bmatrix} k_s & 0 \\ 0 & k_n \end{bmatrix} \begin{Bmatrix} \Delta u_s \\ \Delta u_n \end{Bmatrix} \tag{3.11}$$

in which k_s and k_n are the interface stiffnesses tangential and normal to the interface, respectively.

3.4 Surface Constitutive Behaviour

The surfaces in contact transmit shear stress as well as normal pressure, and the contact traction depends upon the relative motion at the interface. The tangential shear traction is coupled to the normal pressure stress through frictional effects. The standard Coulomb friction model is used to describe the shear response at the interface. As illustrated in Fig 3.3, relative motion or slip is not permitted if the equivalent shear stress τ_{eq} is less than the critical stress τ_{cr}, or

$$\tau_{eq} = \{\tau_1^2 + \tau_2^2\}^{\frac{1}{2}} < \tau_{cr} \tag{3.12}$$

where the critical stress is proportional to the contact pressure σ_n, according to:

$$\tau_{cr} = \sigma_n \tan\delta = \mu\sigma_n \tag{3.13}$$

in which δ is the angle of friction at the interface, and μ is the corresponding Coulomb friction coefficient. Isotropic friction is assumed, such that the coefficient of friction is the same in both the local 1 - and 2 - directions. Frictional slip occurs when the equivalent stress reaches the critical stress value. For isotropic friction, the direction of the slip and the frictional shear stress coincide, which may be expressed in the form

$$\frac{\tau_i}{\tau_{eq}} = \frac{\delta\gamma_i}{\delta\gamma_{eq}} \tag{3.14}$$

where $\delta\gamma_i$ is the slip rate in the i - direction, and the $\delta\gamma_{eq}$ is the equivalent rate given by

$$\delta\gamma_{eq} = \{\delta\gamma_1^2 + \delta\gamma_2^2\}^{\frac{1}{2}} \tag{3.15}$$

In the numerical implementation of the friction model, the condition of no relative motion or sticking response, is approximated by stiff elastic behaviour. The

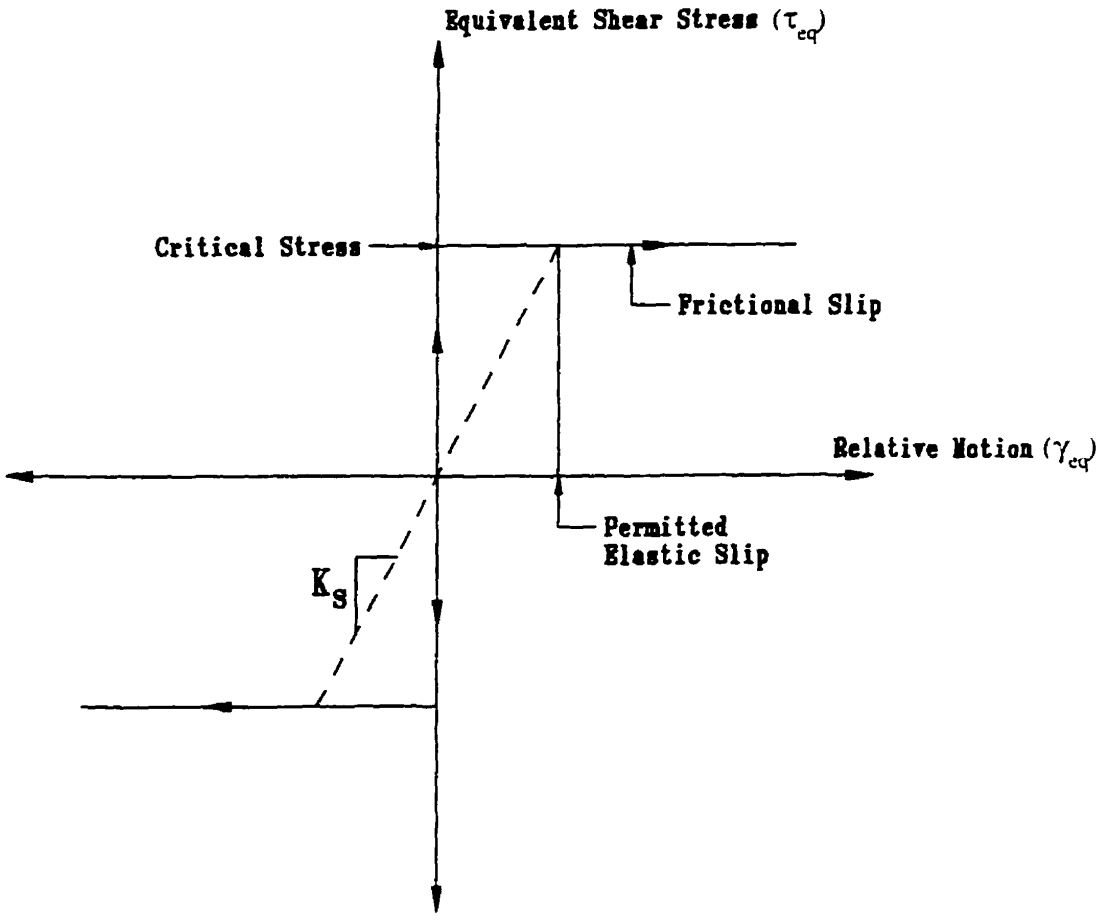

Figure 3.3: Non-local interface friction model, for which the condition of no relative motion is approximated by stiff elastic behaviour. as shown by the dashes line.

elastic stiffness k_s is defined such that the relative motion is bounded by an allowable maximum elastic slip, permitted before frictional slip would occur. This approximate approach may be viewed as an implementation of a non-local frictional model, in which the Coulomb condition is not applied at a point but is weighed over a small area of the interface [106].

3.5 Geometric Modelling

The test specimen and the loading platens are modeled using the mesh shown in Fig 3.4. The mesh shown is used for biaxial loading. The same mesh, without the lateral platens, is used for uniaxial loading. The element used is a four node bilinear plane stress element with 4 integration points. Note that there are no elements used for the gap between the brush rods. The maximum aspect ratio of any element is 2. Interface elements are used between the brush tips and the specimen's edge (refer to Section 3.3 for description). The mesh refinement of the first order elements is carried out by a standard multi-point constraint method: whereby a constraint is imposed to keep a node in a fixed position, on a straight line, between two nodes.

The specimen used has dimensions of 144 × 144 × 40 mm. The height of the solid platen is 76 mm. The solid part of the brush loading platen is assumed to be 76 mm, while the steel rods used in the brush are 5 × 5 mm in cross section, with a length of 76 mm. Details of the number of elements and nodes for the different loading systems are given in Table 3.1.

3.6 Material Properties

According to the material properties experimental program carried out at Memorial University (MUN) [107, 108, 30], the high-strength concrete used in the numerical

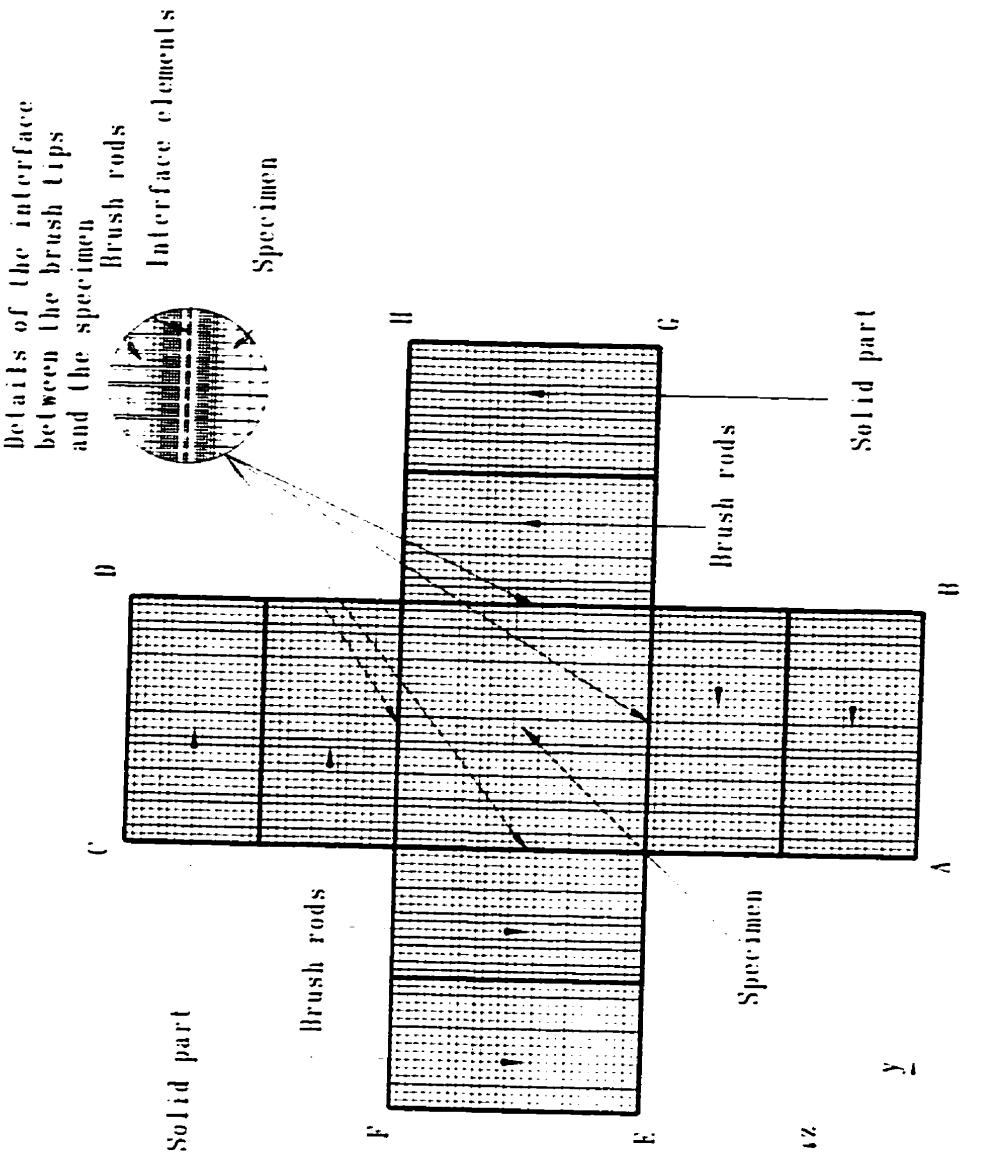

Figure 3.4: The finite element mesh

simulation has an ultimate uniaxial compressive strength, f'_c, of 100 MPa, with a modulus of elasticity, E_c, of 40 GPa, measured at 0.4 f'_c. The maximum recorded concrete strain, ϵ', is 0.0027. The uniaxial tensile strength of the high-strength concrete, f'_t, is approximately about 5.2 % f'_c. A special degradation function is assumed for the tension softening model, where a linear loss of tensile strength is assumed at the ultimate tensile strength, and a zero tensile strength at a displacement (w_o) of 0.10 mm as suggested by Marzouk and Chen [30]. The value of Poisson's ratio, ν, for high-strength concrete is 0.24 as reported by ACI Committee 363 [109]. It is worth mentioning here that the realistic behaviour of the materials used should be incorporated in the numerical model in order to achieve good results.

3.7 Results of the Numerical Evaluation of the Set-up

3.7.1 Uniaxial Loading

The stress contours of the uniaxial loading cases are given in Fig. 3.5. The stresses in the direction of loading, σ_{zz}, are identified as S22, and the displacement contours in the orthogonal direction, u_{yy}, are referred to as U1.

It is noted that plane stress elements are used. This assumption is valid only when the lateral confinement of the test specimens is minimized. In case of dry solid

Table 3.1: Number of elements for different test set-ups

Test set-up	Number of elements	
	Uniaxial loading	Biaxial loading
Solid dry platens	2824	5648
Pressure platens (brush)	6938	10182
Lubricated teflon pads	3288	6344

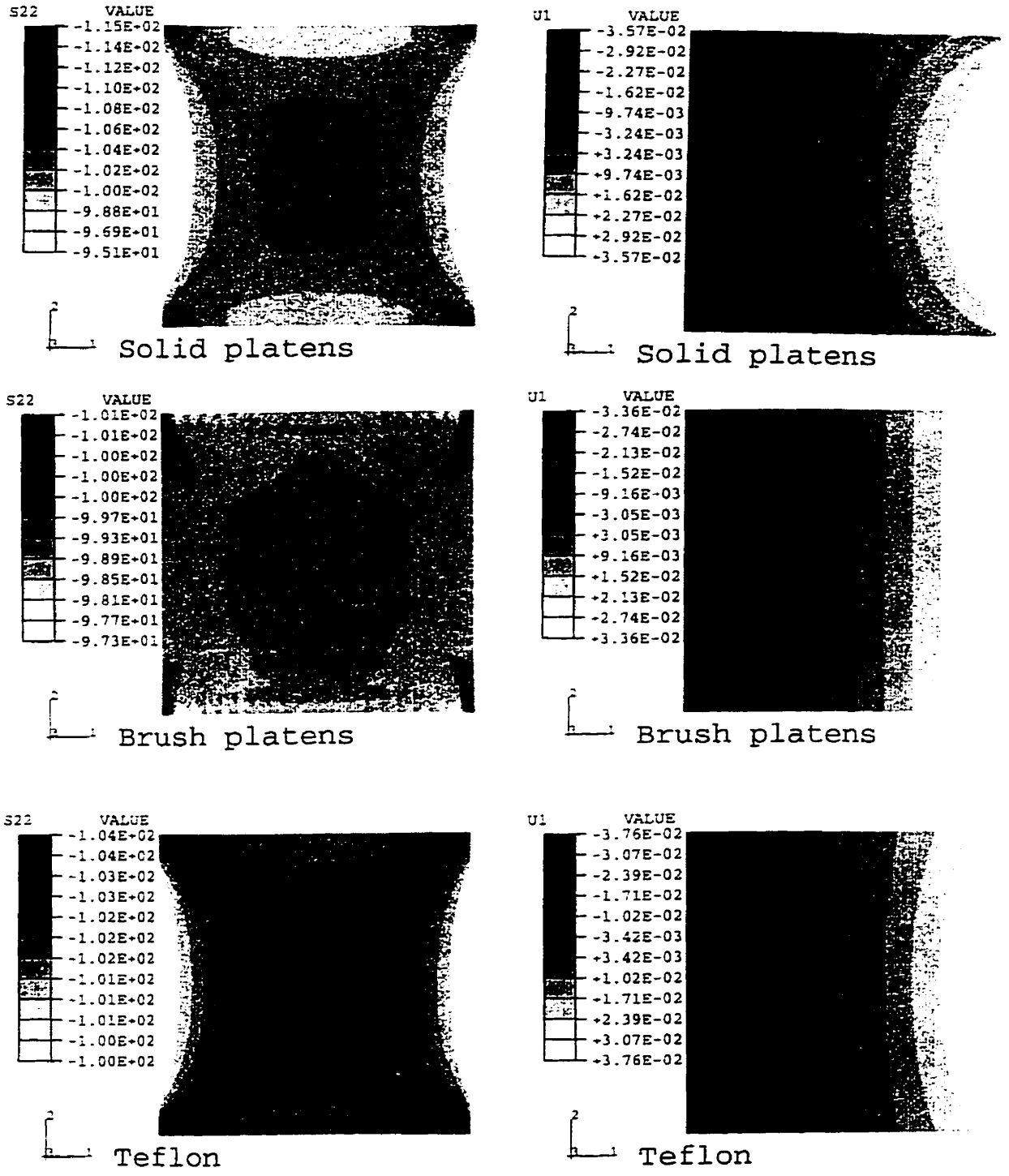

Figure 3.5: Stress contours in the direction of loading (S22) and displacement contours in the orthogonal direction (U1) for the uniaxial cases (f'_c = 100 MPa), at ultimate load

platens. the state of stress at the specimens' edge is highly triaxial. Thus a three dimensional analysis will be required to provide more accurate results. However. it is not within the scope of this work to investigate the stress distribution in a cube specimen. The assumption of plane stress is then a crude approximation for the solid platen case. and the obtained results could be used for comparison purposes.

Figure 3.5 clearly demonstrates that the brush platens provide more homogeneous stress and displacement fields compared to the results of solid platens or lubricated teflon pads. The solid steel platens provide the poorest stress and displacement distribution fields. The stresses in some parts of the specimen are below the ultimate strength as the applied stresses reach the assumed compressive strength of the specimen. The solid steel platens create a stress concentration at the corners of the specimen. The value of the stress concentration is about 14 % higher than the normal stresses. In this study, the loading platens are assumed to have the same side dimensions as the specimens. If the loading platens were assumed to be wider. the corresponding value of stress concentration would have been higher. In case of the brush supports and the lubricated teflon. the stresses are uniform and close to the ultimate strength. Note that although the stress distribution in the case of lubricated teflon pads may appear to be non-uniform (twelve contour intervals are used). the actual stress values are fairly homogenous.

Figures 3.6. 3.7 and 3.8 show the shear stresses induced along the edge of the specimen (f'_c = 100 MPa) due to different support systems at different axial loading stages. The shear stresses are shown at an axial loading level of 20. 40. 60. 80 and 100 % of the ultimate strength of the specimen. It is apparent from these figures that the induced shear strength increases as the axial load is increased. Figure 3.9 depicts the shear stresses (at the ultimate strength of the specimen) induced along the edge

of the specimen due to different support systems.

The shear stresses induced in the specimens are the highest for the case of dry solid platens. The shear stresses reach a maximum value of 14 % of the normal stresses. The shear stress distribution is fairly linear from the center of the specimen with some slight nonlinearity towards the corner. The slight irregularities in the shape of the shear stress distribution due to the brush supports is a result of the gap between the rods. Both the brush platens and the teflon pads decrease the shear stresses at the interface between the specimen and the loading platen (shear stresses values are 2.5 % and 3.5 %, respectively, of the maximum normal stresses).

To further investigate the shear stresses induced in the concrete specimens, three more specimens made with variable grades, namely 30, 70, and 140 MPa, respectively, are analyzed under uniaxial loading for the different loading systems. Table 3.2 shows the different properties of concrete, the maximum shear stresses (τ_{yz}), and the ratio of maximum shear stresses to normal stresses (τ_{yz}/σ_{zz}). For all the different concrete

Table 3.2: Shear stresses induced in the specimen

Concrete properties						shear stresses induced in the specimen					
						Dry platen		Teflon pads		Brush platens	
f'_c MPa	E_c GPa	μ	f'_t MPa	ϵ' $\times 10^{-3}$	w_o mm	τ_{yz} MPa	$\frac{\tau_{yz}}{\sigma_{zz}}$ %	τ_{yz} MPa	$\frac{\tau_{yz}}{\sigma_{zz}}$ %	τ_{rz} MPa	$\frac{\tau_{yz}}{\sigma_{zz}}$ %
30	25087	0.20	2.5	1.82	0.05	5.74	16.73	1.76	5.74	1.77	5.87
70	34667	0.24	4.2	2.36	0.08	10.40	12.83	3.00	4.13	2.56	3.58
100	40100	0.24	5.0	2.73	0.10	13.85	11.95	4.19	4.01	2.54	2.59
140	46183	0.24	7.0	3.41	0.12	18.16	11.26	5.66	3.79	3.10	2.33

grades, the values of shear stresses increase as the compressive strength increases. This is due to the higher failure loads on the specimens. However, the ratio of shear stresses to normal stresses decreases as the concrete compressive strength increases.

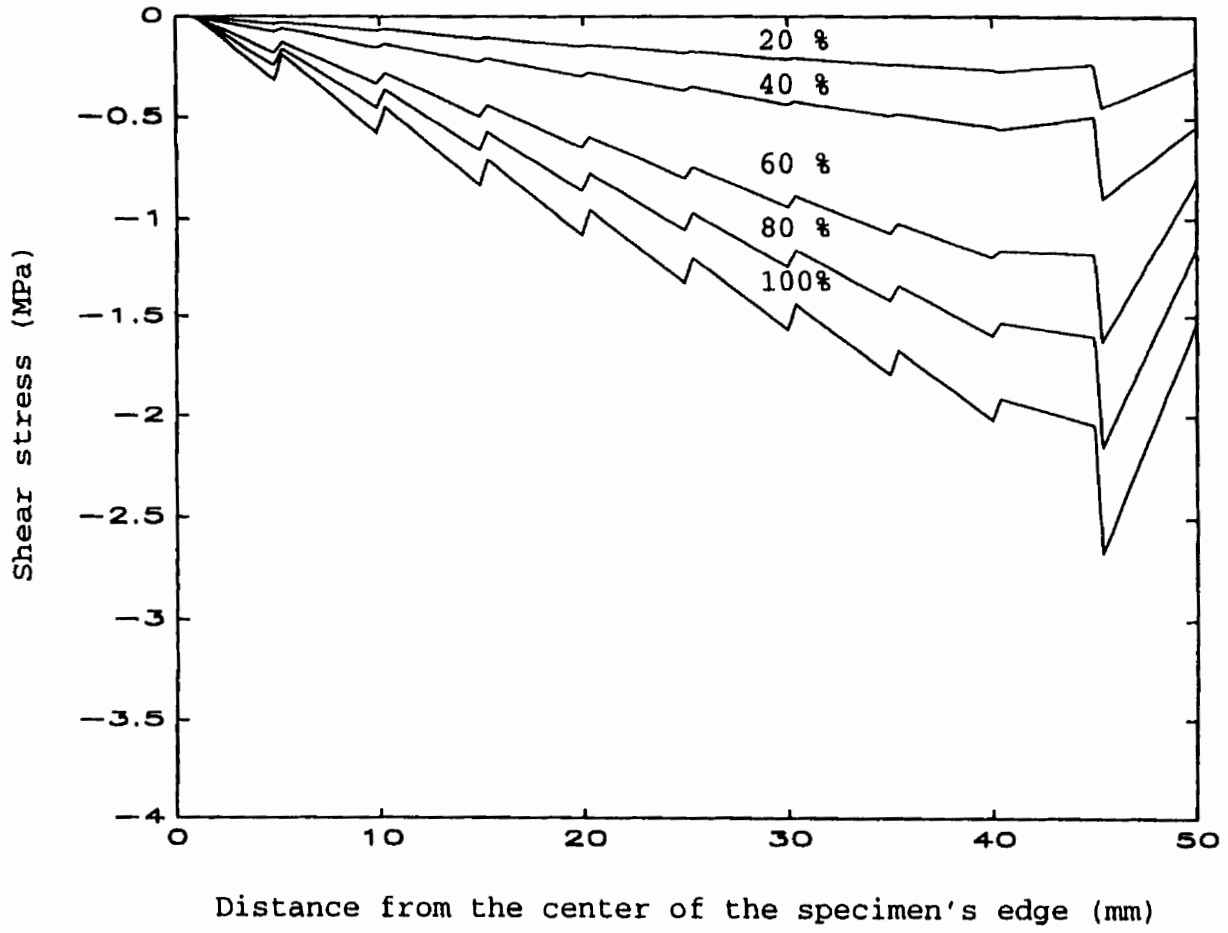

Figure 3.6: Shear stresses induced in the specimen, due to the brush loading platens, for uniaxial case (f'_c = 100 MPa). The axial loading level is 20, 40, 60, 80 and 100 % of the ultimate strength

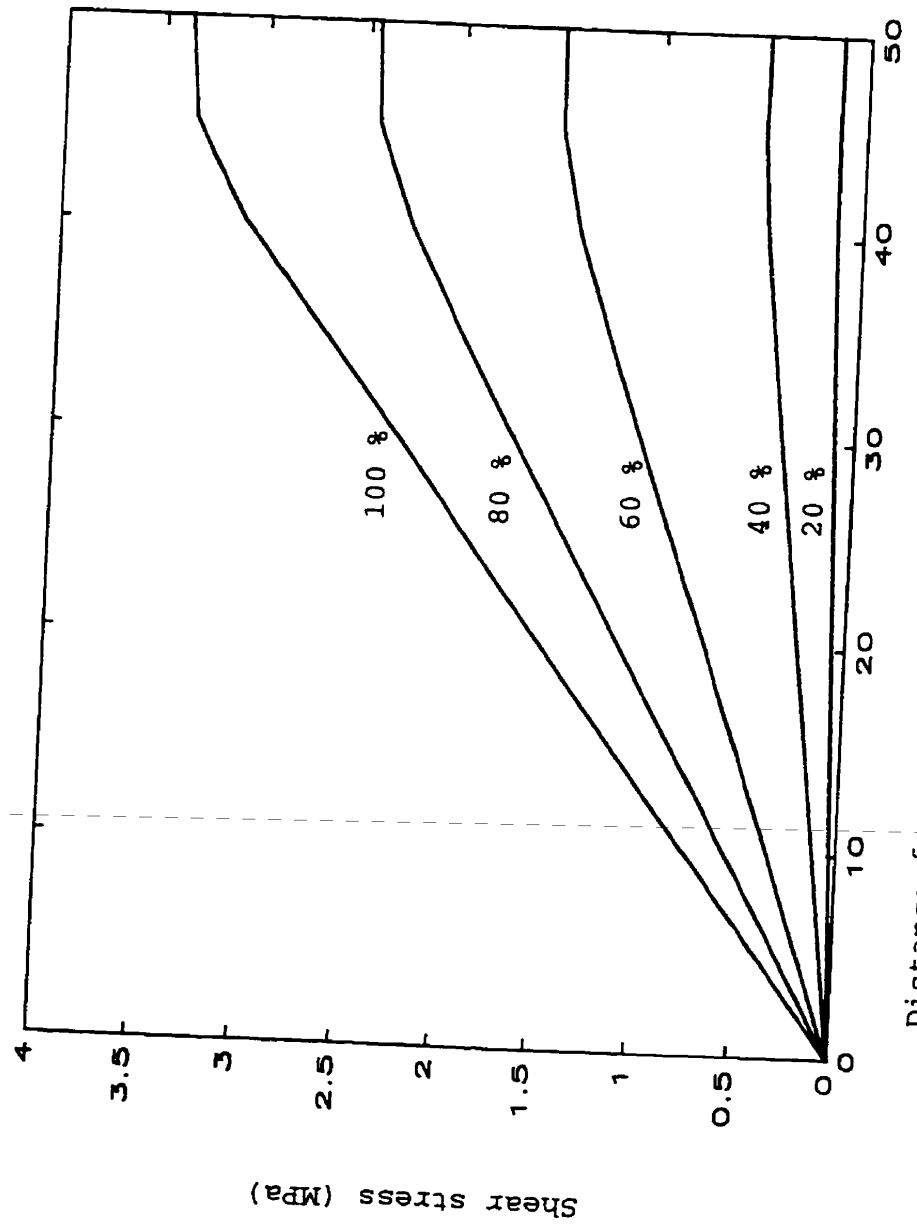

Figure 3.7: Shear stresses induced in the specimen, due to the lubricated teflon pads, for uniaxial case (f'_c = 100 MPa). The axial loading level is 20, 40, 60, 80 and 100 % of the ultimate strength of the specimen

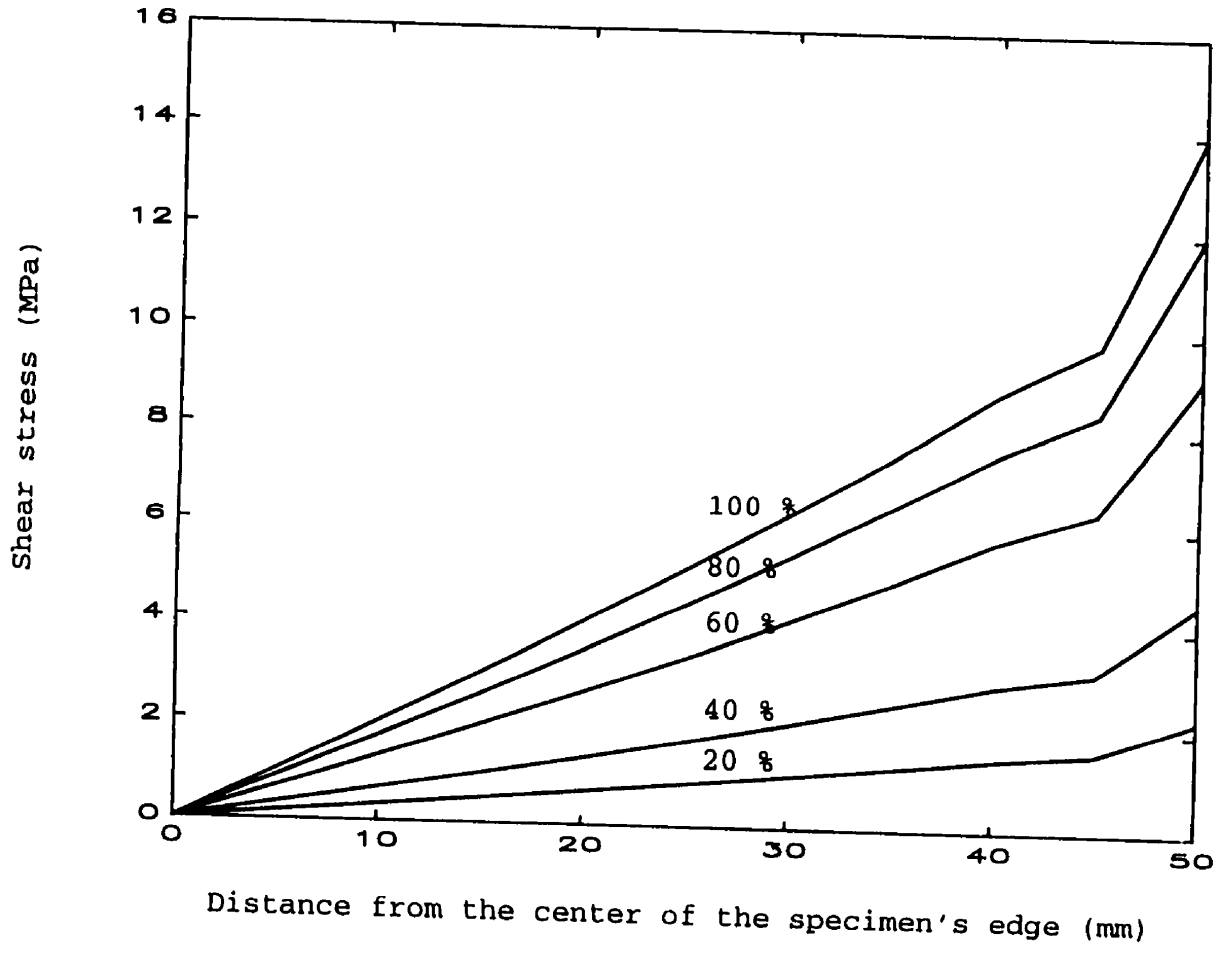

Figure 3.8: Shear stresses induced in the specimen, due to the solid loading platens, for uniaxial case (f'_c = 100 MPa). The axial loading level is 20, 40, 60, 80 and 100 % of the ultimate strength of the specimen

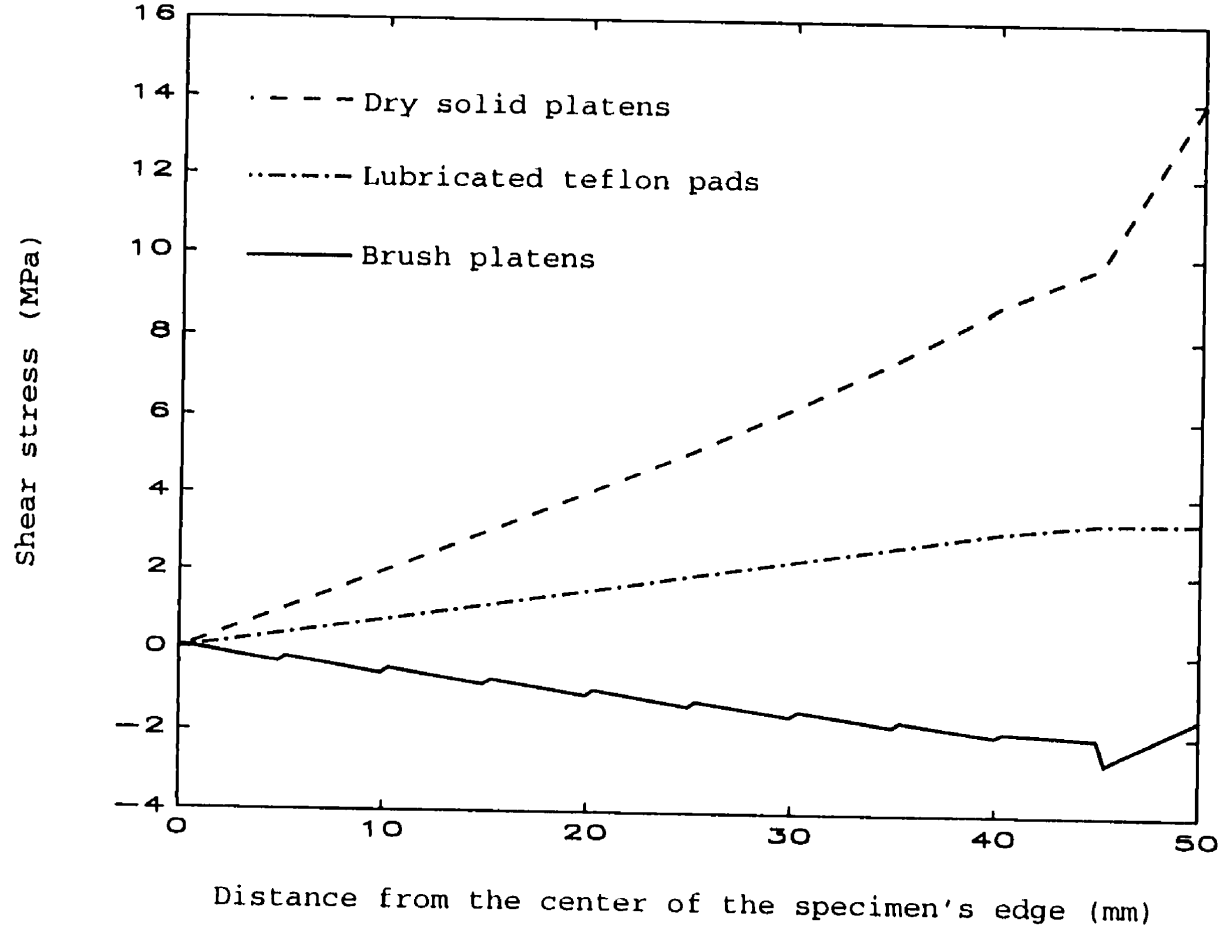

Figure 3.9: Shear stresses induced in the specimen at the ultimate strength, due to the different loading systems, for uniaxial case (f'_c = 100 MPa), at ultimate load

The shear stresses induced in the specimen are the highest for the dry solid platens, and decrease as teflon pads and brush platens are used.

To examine the effect of the compressive strength of the specimen on the induced shear strength, the corresponding cases are compared. Examining Table 3.2 show that increasing the compressive strength from 30 MPa to 70 MPa (i.e increasing f'_c by 133 %) changes the ratios of τ_{yz}/σ_{zz} from 16.73 %, 5.74 % and 6.52 % to 12.83 %, 4.13 % and 3.58 % for the cases of dry solid platens, teflon pads and brush supports, respectively. When the compressive strength for the high-strength concrete specimens is increased from 70 MPa to 140 MPa, the ratios of τ_{yz}/σ_{zz} change from 12.83 %, 4.13 % and 3.58 % to 11.26 %, 6.25 % and 2.33 % for the cases of dry solid platens, teflon pads and brush supports, respectively. In other words, increasing the compressive strength from 30 MPa to 70 MPa (i.e increasing f'_c by 133 %) decreases the ratio of τ_{yz}/σ_{zz} by 30 %, 39 % and 82 % for the cases of dry solid platens, teflon pads and brush supports, respectively. And if the compressive strength is increased from 70 MPa to 140 MPa (i.e increasing f'_c by 100 %) the ratio of τ_{yz}/σ_{zz} will decrease by 14 %, 9 % and 11 % for the cases of dry solid platens, teflon pads and brush supports, respectively. This shows that the ratio of τ_{yz}/σ_{zz} decreases very slightly as the compressive strength is increased for high-strength concrete tested with different loading systems.

3.7.2 Linear Analysis Versus Nonlinear Analysis

In order to ensure the accuracy of the finite element analysis, an elastic analysis of the uniaxial loading is first examined, then the non linear case is added to the problem. Figure 3.10 shows the stress contours of the uniaxial loading cases using linear analysis. The stresses in the direction of loading are identified as S22, and the displacement contours in the orthogonal direction are referred to as U1.

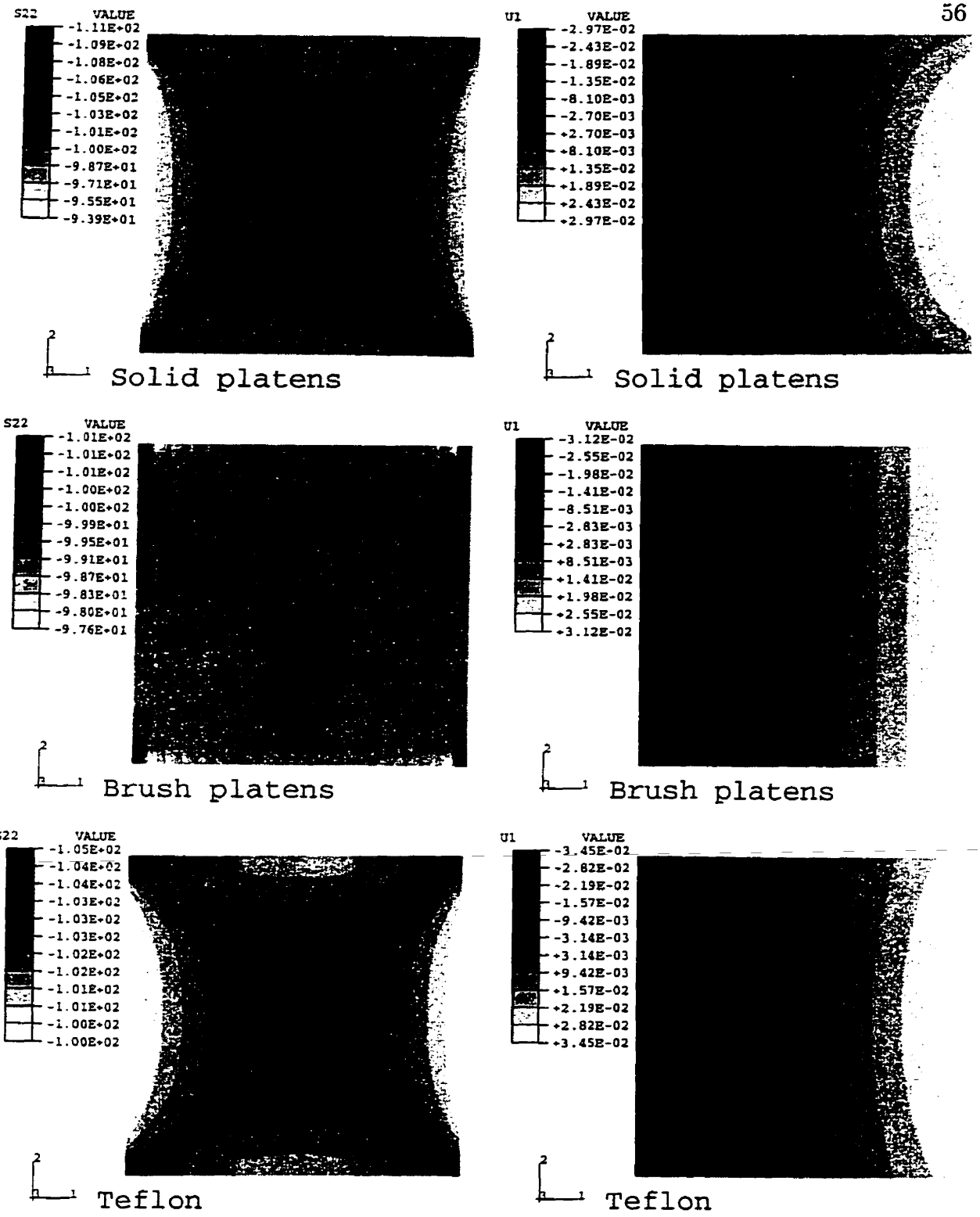

Figure 3.10: Stress contours in the direction of loading (S22) and displacement contours in the orthogonal direction (U1) for the uniaxial elastic analysis

Comparing the results of the nonlinear analysis to that of the elastic analysis indicates that the non-linearization leads to a redistribution of stresses. The main difference between the linear and nonlinear analysis is pronounced for the contours of the lateral deformation (U1) in the specimen. The lateral deformation are higher for the case of non linear analysis. Nevertheless, the difference between the stress fields obtained using a linear or non linear analysis remains small. This could be attributed to the more linear behaviour of high-strength concrete compared to normal strength concrete, and to the small plastic deformation of high-strength concrete prior to failure.

3.7.3 Buckling Capacity of the Brush Rods

In order to recommend the length of the brush rods, a preliminary buckling capacity evaluation of the brush rods is carried out using elastic analysis. To initiate the buckling in the rods, a very small initial imperfection (2×10^{-3} mm) is introduced at the mid-height of the rods. Two extreme cases are considered. The first case assumes that the brush rods are glued to the specimen. In the second case, the nodes are only connected for normal stresses; this is achieved through an interface element with no friction. Buckling is assumed to occur when there is a complete loss in the stiffness of the brush rods.

The results indicate that, for the first case, the brush rods will yield before buckling. This case corresponds to a complete fixing of the brush rods. This assumption is not entirely correct as there exists a relative slip between the rods and the specimen. The second case produces a buckling load that corresponds to a stress of 148 MPa. A third case, assuming friction between the brush rods and the specimen, results in a buckling load corresponding to a stress of 190 MPa. This produces a factor of safety between 1.5 and 2 for an applied stress of 100 MPa.

3.7.4 Biaxial Loading

The results of the biaxial loading for the steel solid platen, brush platen and lubricated teflon pads are shown in Fig. 3.11. The principal stresses in the specimen are identified as SP1. The displacement contours in the orthogonal direction are referred to as U1. It is clear that the solid platens do not provide homogeneous stress fields. In addition, the stresses induced in the specimen are far below the applied stresses. This will lead to overestimating the specimens's strength when using dry solid platens.

The use of the teflon pads and brush platens improves the stress fields drastically in the biaxial loading. However, the displacement contours for the brush support are slightly more uniform than those of the teflon pads. A concentration of stress with a disturbed area of about 5 mm at the edge of the specimen is always found when using the brush in biaxial case, while a concentration of stresses is always detected at the specimen corners for the teflon pads.

Figures 3.12, 3.13 and 3.14 show the shear stresses induced along the edge of the specimen (f'_c = 100 MPa) due to different support systems at different biaxial loading stages. The shear stresses are shown at loading levels of 20, 40, 60, 80 and 100 % of the ultimate biaxial strength. It is apparent from these figures that the induced shear strength increases as the biaxial loads are increased.

The shear stresses at the interface between the specimen and the testing machine, for the biaxial case, are shown in Fig. 3.15 at a load level that corresponds to the ultimate biaxial strength. This figure shows that the shear stresses induced in the specimen are much higher than the uniaxial case for the case of solid platens, the shear stresses reach a value of 45 % of the normal stresses. For the case of the brush supports, the shear stresses are 8 % of the normal stresses. The curve for shear stresses in the case of teflon pads changes its shape and become more distributed

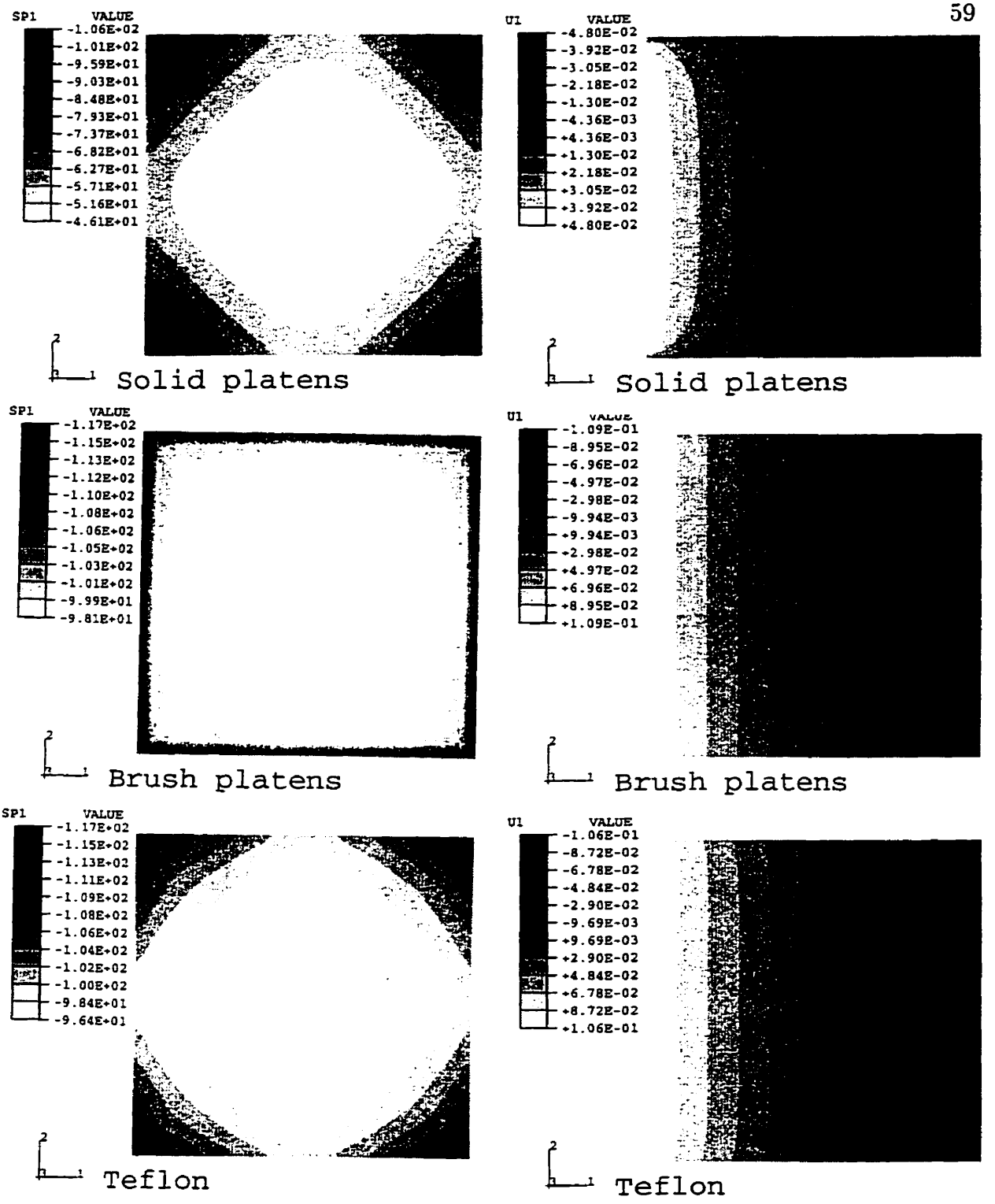

Figure 3.11: Contours of the principal stresses (SP1) and displacement contours in one of the orthogonal directions (U1) for the biaxial cases (f'_c = 100 MPa), at ultimate load

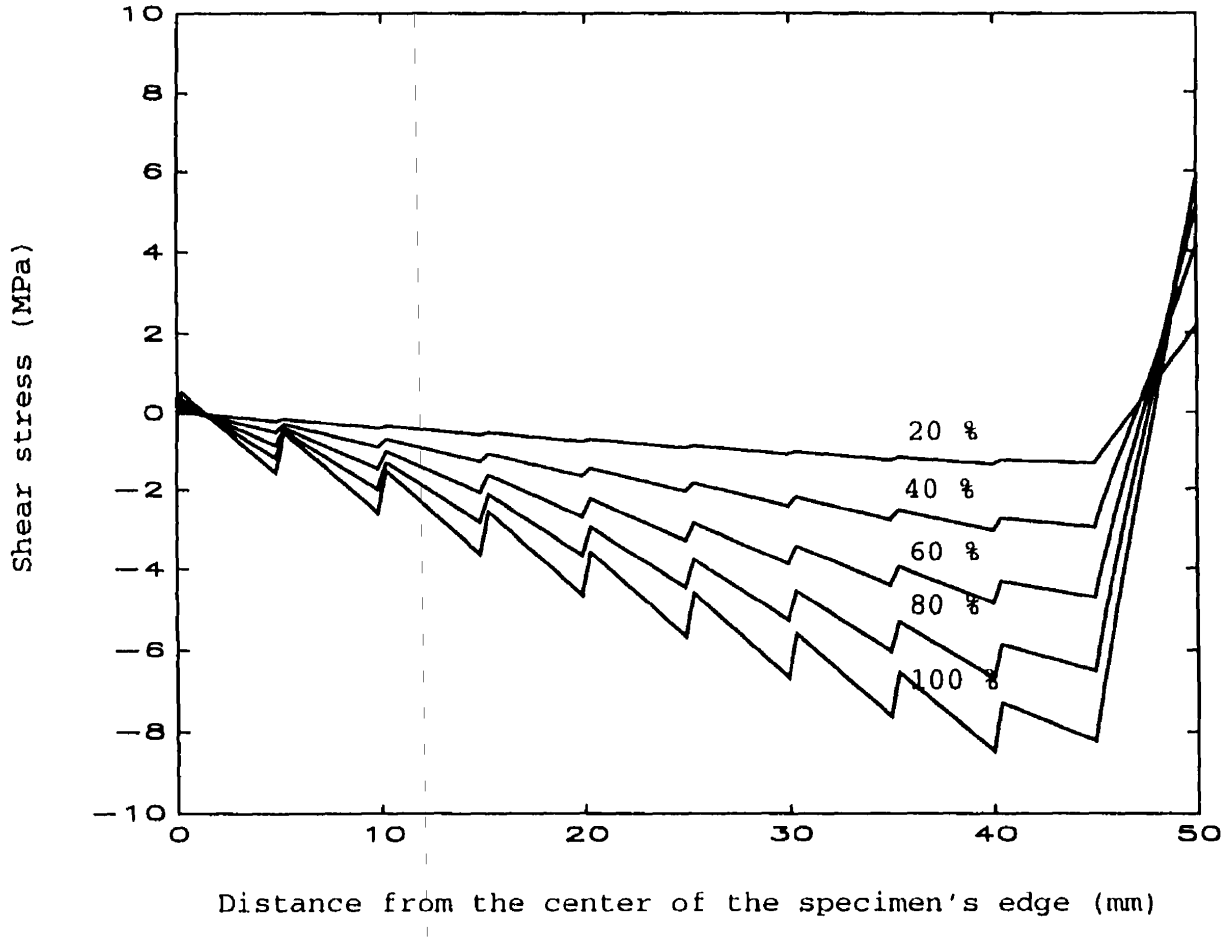

Figure 3.12: Shear stresses induced in the specimen, due to the brush loading platens, for biaxial case (f'_c = 100 MPa). The axial loading level is 20, 40, 60, 80 and 100 % of the ultimate load

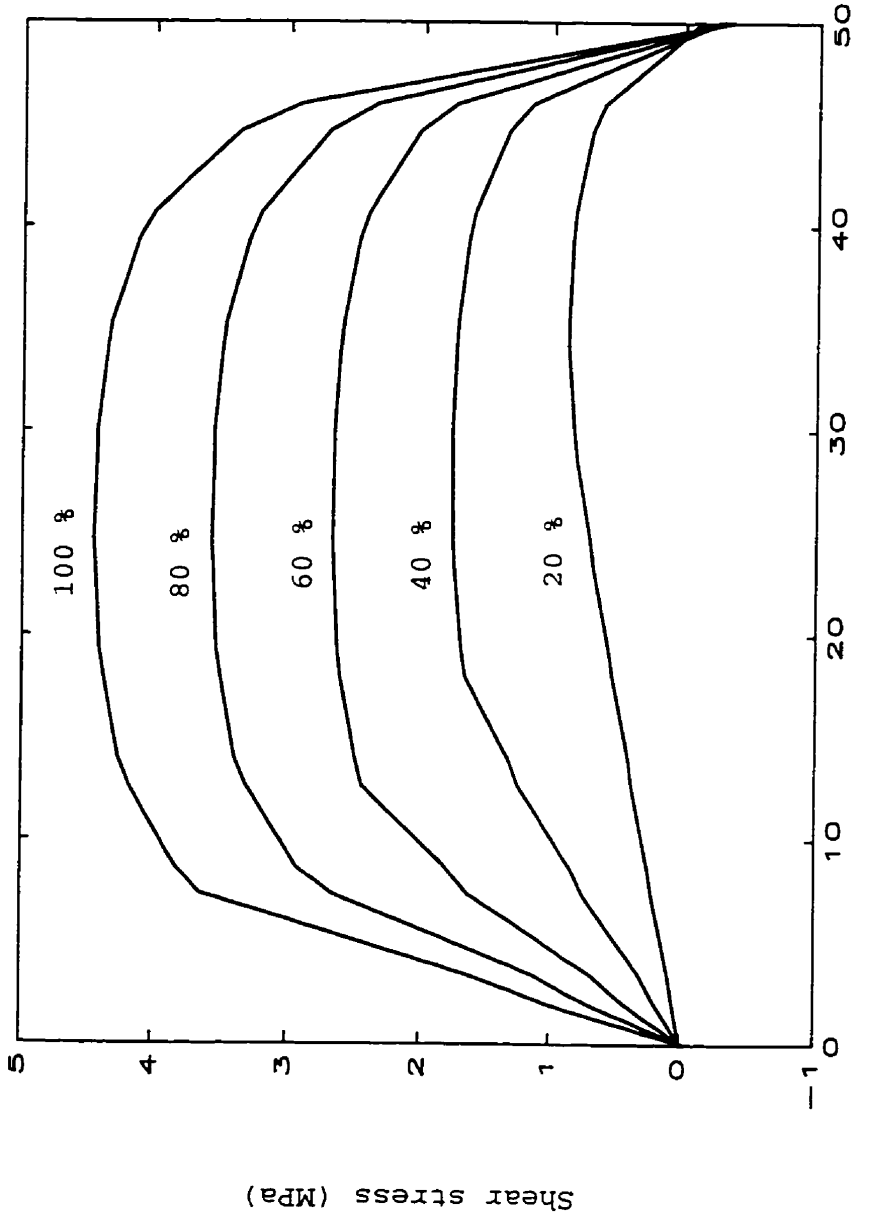

Figure 3.13: Shear stresses induced in the specimen, due to the lubricated teflon pads, for biaxial case (f'_c = 100 MPa). The axial loading level is 20, 40, 60, 80 and 100 % of the ultimate strength of the specimen

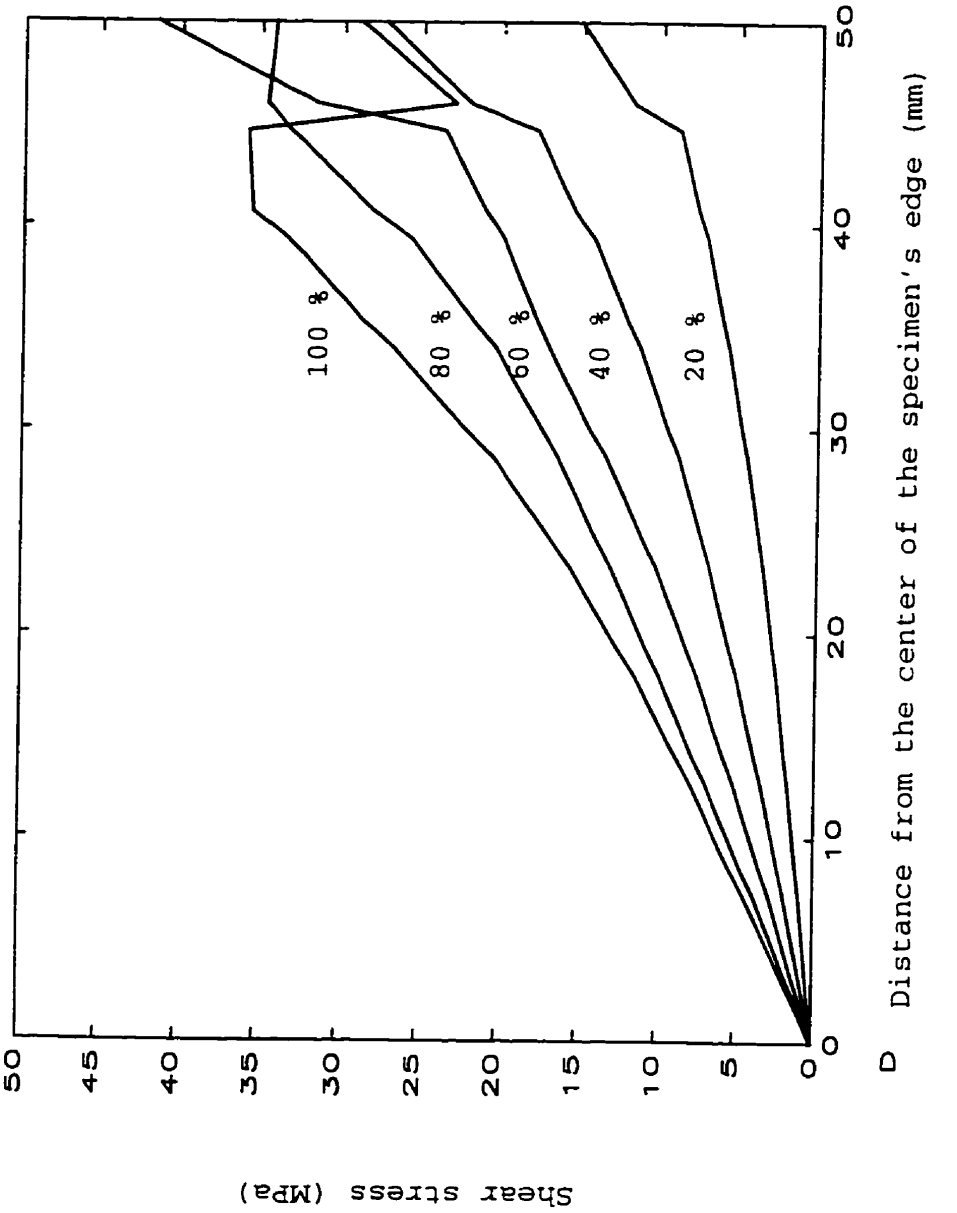

Figure 3.14: Shear stresses induced in the specimen, due to the solid loading platens, for biaxial case (f_r' = 100 MPa). The axial loading level is 20, 40, 60, 80 and 100 % of the ultimate load

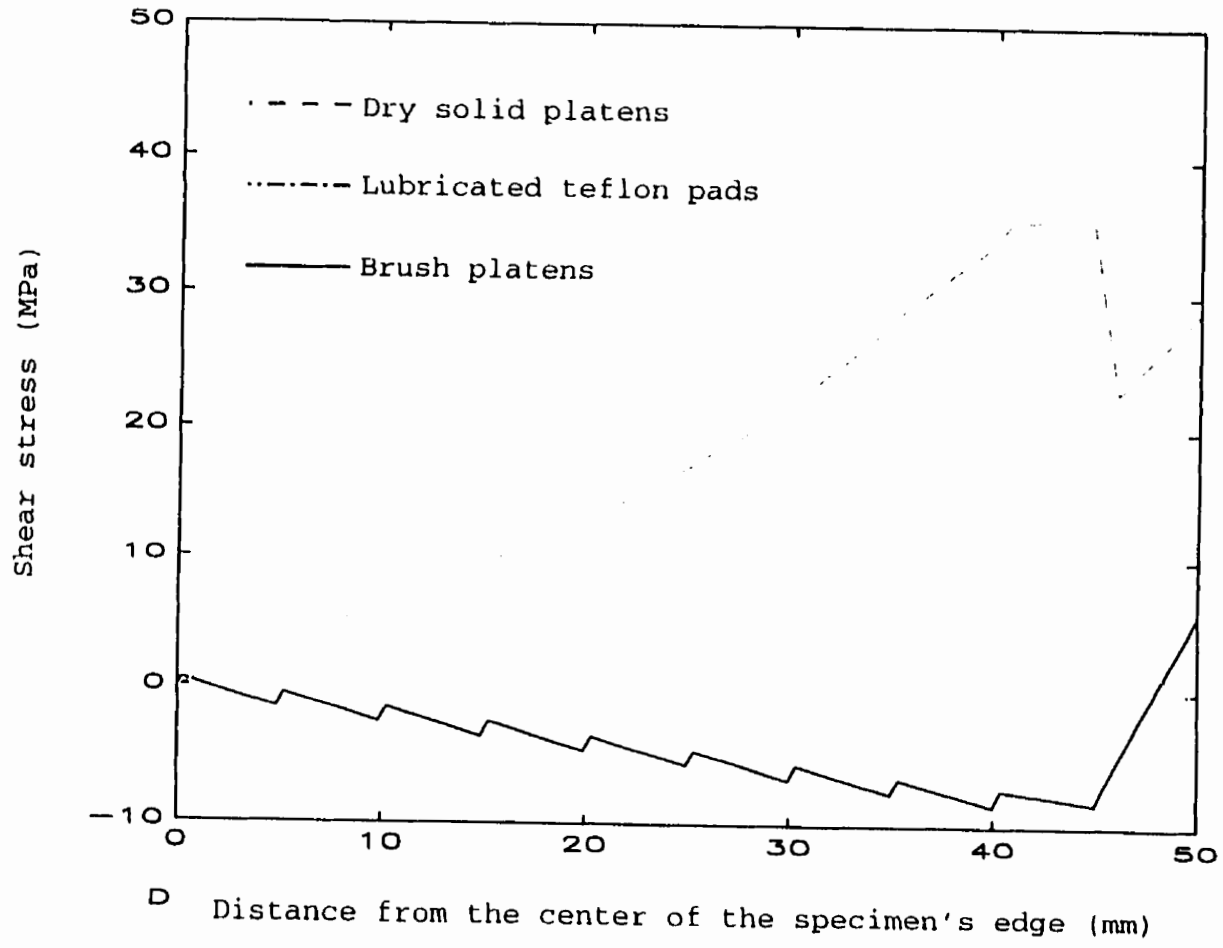

Figure 3.15: Shear stresses induced in the specimen at the ultimate strength, due to the different loading systems, for biaxial case (f'_c = 100 MPa)

over the edge. This is due to the effect of lateral loading on the lubricated surface.

3.8 Recommendations for the Test Set-Up

In this chapter, the results of the finite element investigation on the behaviour of the different support systems used in uniaxial and biaxial loading of concrete are presented. A four-node bilinear plane stress element with 4 integration points is used to model the concrete specimen and the test set-up. A non-linear concrete plasticity theory model including post-cracking behaviour with a linear degradation function for the concrete tensile crack softening is used. An interface friction element is utilized in the analysis to simulate the friction between the steel loading platens and the concrete specimen.

Three types of loading platens are used in the analysis to examine the effect of lateral confinement on the stress and displacement fields. The results indicated that the most homogeneous stress and displacement fields are achieved for the brush platen case. Also, a preliminary estimate of the buckling capacity of the brush rods indicate that a factor of safety between 1.5 and 2 can be obtained if the brush used in the study is employed to provide an applied stress of 100 MPa.

Chapter 4

Experimental Program

The primary objective of the experimental program is to study the behaviour of high-strength concrete when subjected to biaxial state of stress. Four different types of concretes were tested. This chapter contains the details of the experimental program. The test set up, the description of the experimental equipments and the methods used throughout the testing program, and the specimen preparation are presented in this chapter.

4.1 Biaxial Testing Apparatus

4.1.1 Loading Frame

A special test set-up was designed and manufactured by the technical services of M.U.N. for this study. The loading frame was placed in the structural laboratory at M.U.N. This laboratory contains a reinforced concrete floor with a thickness of one meter. Figures 4.1 and 4.2 show photographs of the test set-up.

The loading frame provided external loads in two orthogonal directions that were applied to the test specimen. It consisted of two loading frames. The vertical loading frame consisted of two vertical wide flange steel columns connected by two horizontal cross channels. The channels were braced together by means of a stiff box shaped

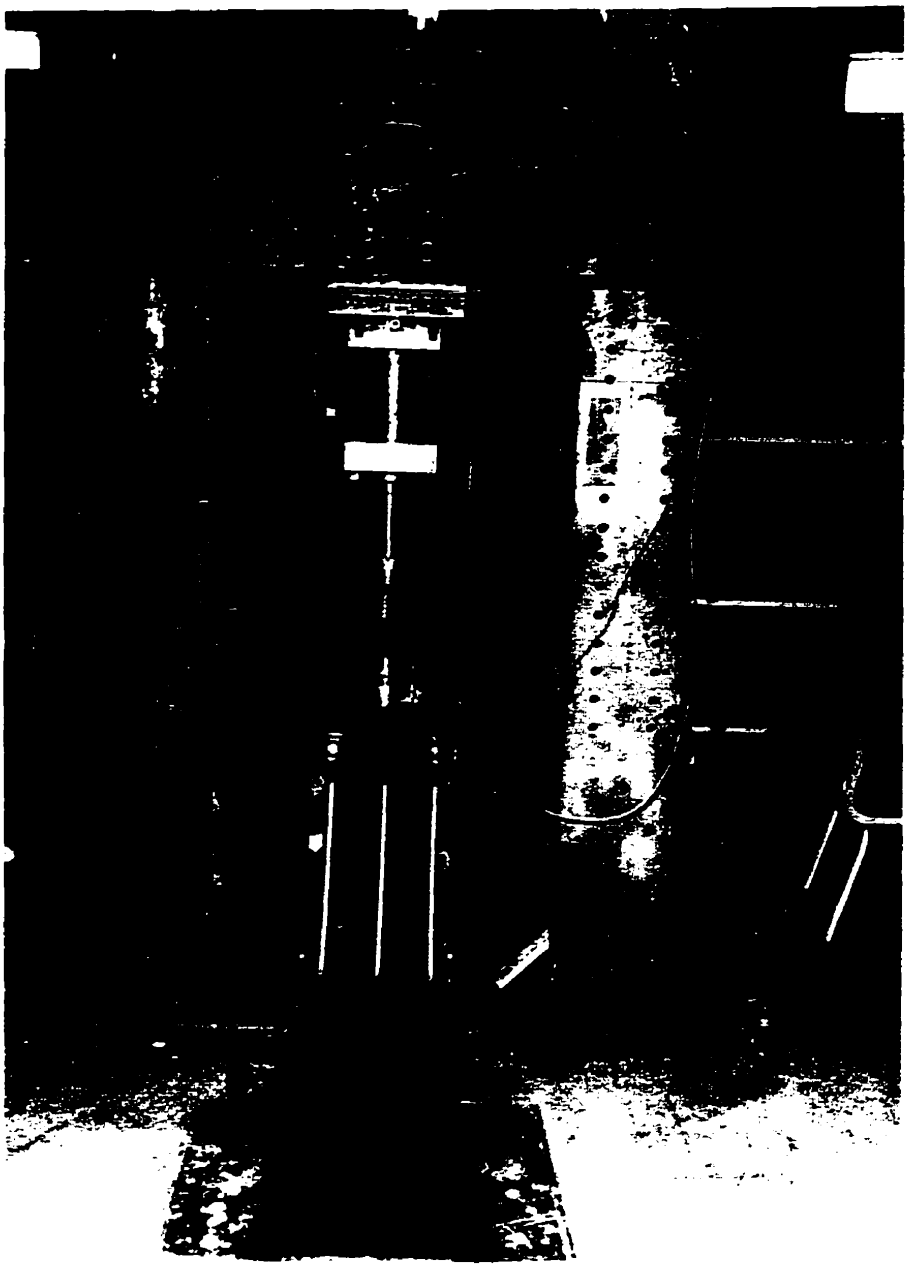

Figure 4.1: Test set-up (frontal view)

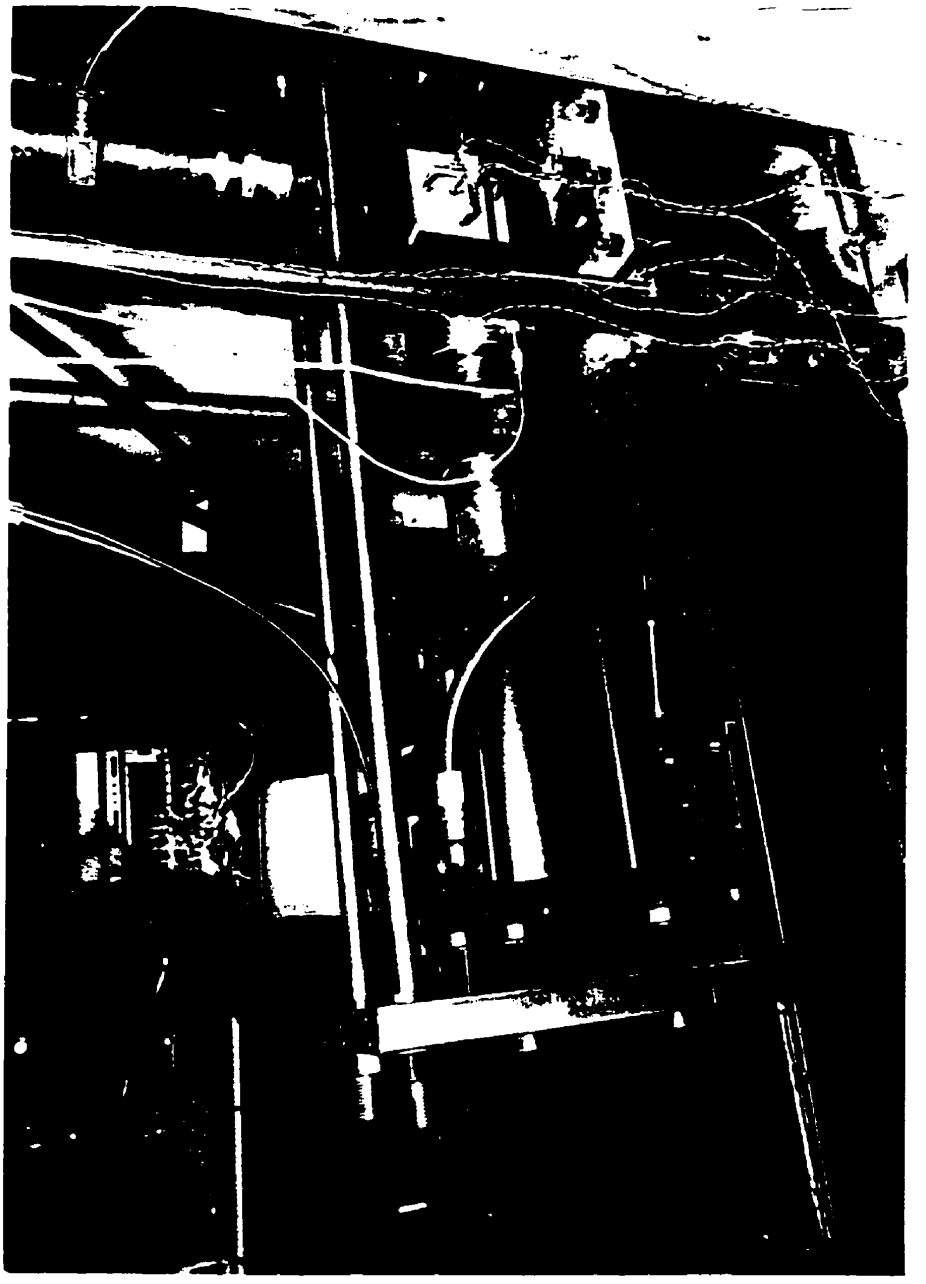

Figure 4.2: Test set-up (side view)

construction (a W-shape piece stiffened with top and bottom plates). The vertical columns were bolted to two inclined S-shape columns which acted as a horizontal brace to the frame. The two vertical columns were then bolted to the floor using a 38 mm base plate and 40 mm anchor bolts spaced at 600 mm apart. To increase the stiffness of the loading frame in the vertical direction, a 50 mm plate was placed on top of the horizontal channels and was securely bolted to the horizontal beam through four 50 mm solid rods. The horizontal frame consisted of a W-310 × 375 beam that rests horizontally on two 19 mm plates bolted to the structural floor. The horizontal actuator was attached to a vertical plate with a thickness of 38 mm. Another vertical plate was used at the opposite end to support the reaction force. The two vertical plates were connected at the top by means of two 25 mm rods. The plates were also supported by means of three 13 mm stiffeners that were welded to the horizontal beam. The two directions were aligned with an accuracy of 0.05 deg by a precision machinist. They were frequently checked to ensure that the alignment was always within the range of this required accuracy.

The constructed loading frame was in fact a non-symmetric one as opposed to the loading frame used by Kupfer et al. [14]. It was nearly similar to that used by Liu et al. [16] and Tasuji et al. [17]. Thus, it is expected that a non-symmetric specimen deformation would occur in the specimen's plane. A deviation between the measured specimen-load and true specimen-load may occur depending on the level of specimen deformation. However, the results of the experimental study by Winkler [110] suggested that no significant effect on strength and deformation results occurred when either a specimen was loaded through brush-bearing platens in a one part machine (that is with fixed loading axis), or in a multi-part machine.

4.1.2 Loading Platens

Chapter 3 presented a finite element simulation of the different end conditions used for the biaxial loading tests. The effectiveness of the brush loading platens was clearly demonstrated through the finite element analysis. As a result, brush type loading platens were used in this study. The platens were mounted on the hydraulic actuators by means of a spherical seat (swivel) and was used throughout the experimental program.

Different alternatives for manufacturing the brushes were considered. Among them was the use of different individual rods attached together at the base, and the use of laser cutting methods. Neither method was recommended. The first one was disregarded because of the high loads that would be applied to the high strength concrete specimen which would compromise the brush integrity during testing. The laser cutting method was dismissed as different manufacturers could not assure that the slots, cut to form the filaments of the brush in a solid block, would be straight. The reason for this was the depth of the slot (75 mm) was considered too big; as a result, some curvature in the slots near the end of the brush might occur.

The method that was used for manufacturing the brushes was the Electric Discharge Wire Cutting (EDWC). It is commonly called wire EDM, and is considered a special form of electric discharge machining that uses a small-diameter wire as the electrode to cut a narrow kerf in the workpiece. Each brush was manufactured from a solid steel block 150 mm thick, 40 mm wide and 150 mm high. The filaments of the brush (5 × 5 mm, in cross-section) were formed by cutting slots, with a 0.2 mm wire, in the solid block using wire EDM method. The height of each filament was 75 mm. Numerical control was specified to control the workpiece motions during cutting in order to achieve the desired cutting path. The flatness of the ends of the

rods were within ± 0.01 mm. The steel used for manufacturing the brush was SAE 4140 steel supplied by Atlas Alloys. Annealed condition heat treatment was used. The ultimate tensile strength of the steel was 700 MPa with yield strength (at 0.2 % offset) of 485 MPa with a hardness of 207 BHN. Figure 4.3 shows a photograph of the manufactured brush loading platens.

The brush loading platens were mounted on the hydraulic actuators by means of a spherical seat (swivel). It was not possible to purchase a swivel that would fit properly in the loading frame. The spherical swivel was manufactured at the machine shop of the technical services at M.U.N. The spherical seating was made of two parts, a concave part and a convex part. The sphere was discretized into different sections (using 0.05 mm intervals). Each interval , had a certain radius (in the cross-section) and a certain depth (from the edge). The values of the depth and radius were then calculated. A 200 mm solid circular shaft was used to make the swivels. This shaft was placed in the lathe. At each selected section, and at a specified depth, a circles was cut by means of a single pointed cutting tool (carbide), using the aid of a digital readout. The digital readout gave accurate movements to the carriage and cross-slide of the lathe to within 0.025 mm. After forming the part of the sphere the surface produced by removing the metal was then polished, manually, by means of emery paper. It was required that both concave and convex parts were to be lapped together. Lapping was achieved by mounting both mating parts in the lathe between centres and lapping the other. In other words, one part was revolving while the other was stationary. Using grinding compound, both parts were finally lapped by hand, to eliminate any high spots, along the diameters of the stationary part. The other end of the concave part of the swivel was formed into a U-shape where the brush was mounted. As for the other end of the convex part, it was machined down to a 25 mm

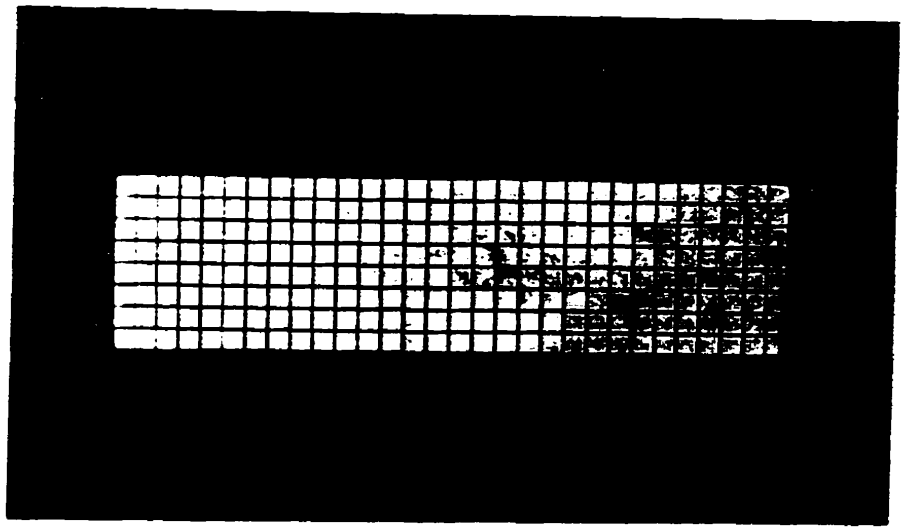

(Top view)

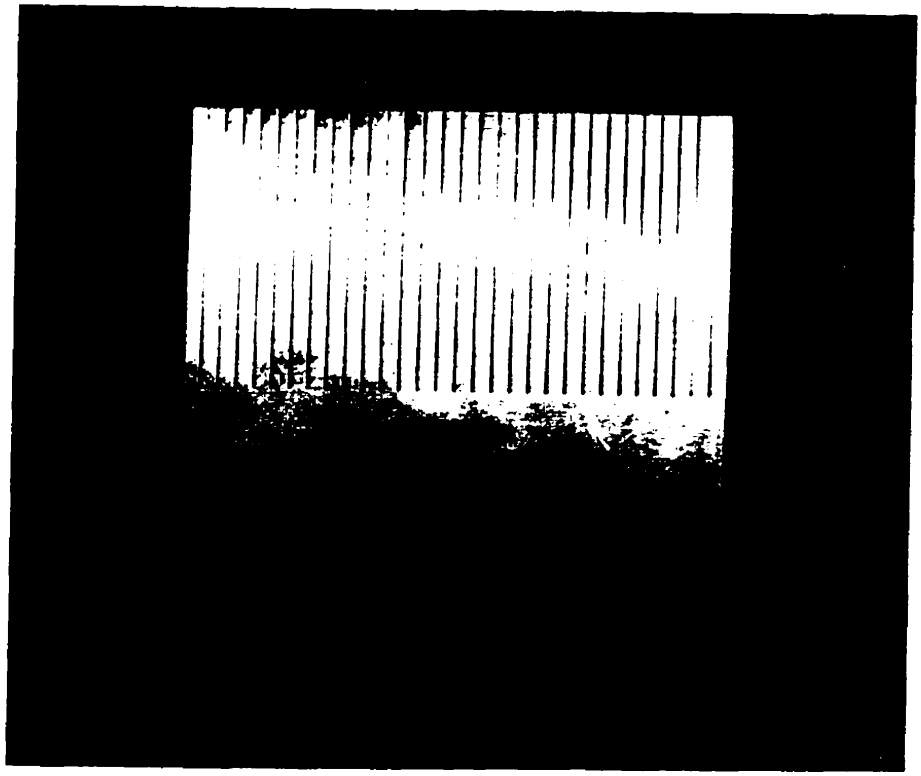

(Frontal view)

Figure 4.3: The brush loading platens

threaded part that was screwed into the MTS actuator. Both parts of the swivel were held together by means of two 20 mm bolts.

4.1.3 Hydraulic Actuators

The biaxial loading on the specimens was provided by means of two servo-controlled MTS compression-tension actuators with a maximum capacity of 710 kN (160 kips). Three modes of servo-control were available in terms of load, stroke or strain control. In the current testing program a closed loop system in displacement control was utilized. Since the measured deformations of the specimen were expected to be very small, the internal LVDT of the actuator would not have been sensitive enough to provide the feed back signal. Thus, the displacement control was provided by means of an external ultra-precision AC LVDT that was mounted on the platens. The closed loop control of the actuators was executed through an MTS 406 Controller. Figure 4.4 shows a close-up of a specimen mounted in the test set-up.

4.1.4 Measurement Devices

The load was measured by the load cell attached to the actuator. The load cell was connected via the controller's internal amplifier. The output voltage (10 V for 710 kN) from the controller was fed into the input channel of the data acquisition system. As mentioned in the previous section, the platen to platen deformation was measured by means of an ultra precision AC LVDT that was mounted on the loading platens. The LVDT had a sensitivity of 0.1 mm/volt. The output from the LVDT was used as the feed back signal used in the control scheme (Section 4.1.6).

The surface strains were measured at the centre of the specimen in the two loading directions by means of two extensometers. The extensometer was a cantilever type with two strain gauges mounted on each leg. The strain gauges were wired so that only

Figure 4.4: A test specimen mounted in the test set up

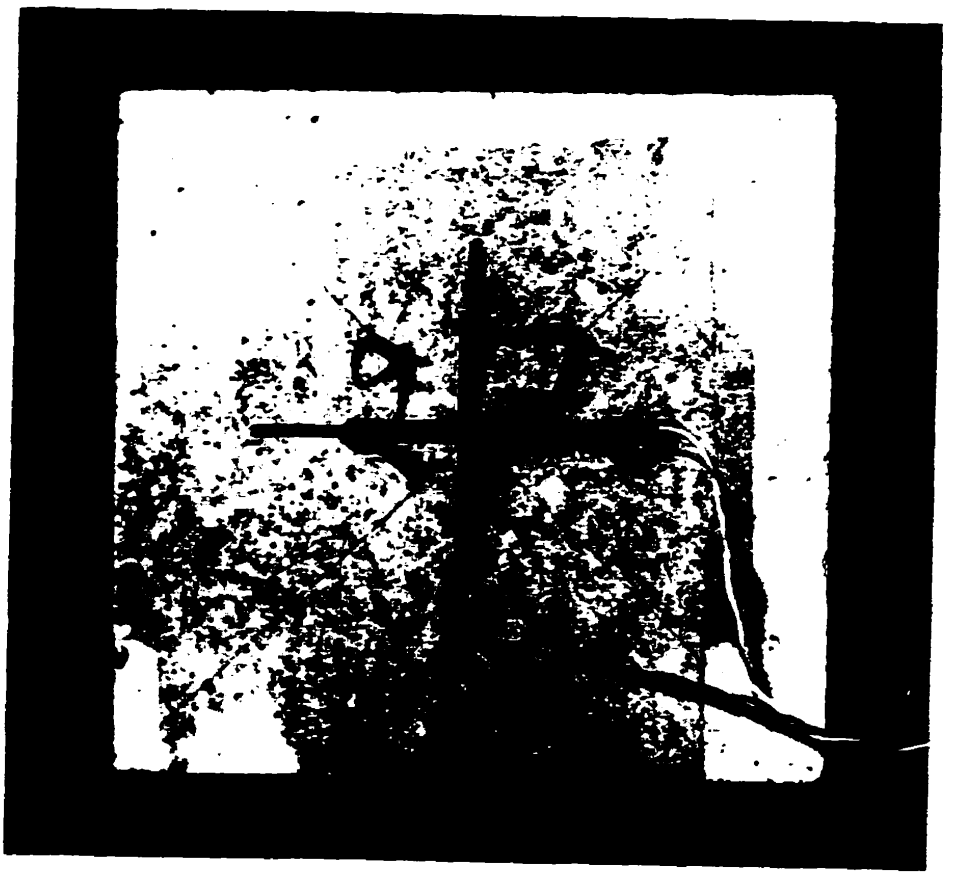

Figure 4.5: A test specimen with two orthogonal strain gauges mounted at the centre

flexural strains (in each leg) could be detected. The extensometers were calibrated by means of a vernier and the output was logged into the data acquisition system. The extensometers' legs were glued to the specimen by means of epoxy. The gauge length for each extensometer was 100 mm.

In addition, the strains were measured using electrical strain gauges. The strain gauges were used on one specimen, at each individual biaxial loading ratio. The concrete strain gauges were 50 mm long, with a resistance of 120 Ω and a gauge factor of 2.07 $\pm$ .5 %. Figure 4.5 shows a photograph of a test specimen with two strain gauges mounted at the centre.

The lateral displacement were measured via two short stroke Linear Potentiometer Differential Transformers (LPDT) mounted on both sides of the specimen. The LPDT's were first held by means of a magnetic stand. This method did not provide

satisfactory results. Thus, a special stand that was fastened to the horizontal beam was manufactured. The stand was provided with fitting to hold the LPDT's. The LPDT's were then mounted on the stand and they were secured to the special fitting by means of three screws. This method provided satisfactory readings.

4.1.5 Data Acquisition System

The data for all experiments was monitored by a high speed data acquisition and control system. The modules of the system consisted of an input module, a digital to analog module, and an analog to digital module. The modules were connected to a host processor which was an IBM personal computer through an interface card. The input module had up to 32 available input channels. The module was used to measure the analog signals that were produced by devices. It also served as a bridge/strain gauge conditioning module. The bridge conditioning module had the capability of handling different bridge configurations (quarter, half and full scale bridge). The input channels had a maximum scanning speed of 1000 measurement per second. The high speed A/D converter performed conversions in 25 μs. It also contained a 2nd order, operational amplifier-based active filter. Eight different input ranges of voltage input (0 to 10 V) could be used with the system. This enabled a high resolution of the measurements that were obtained from the different equipments used in the current testing program, especially those devices that produced small output voltage. The D/A module had four output channels. It primarily served, in the current study, as a function generator that had a very high output sensitivity.

The analog output signals from the different measuring devices were connected to different input channels of the data acquisition system. Menu driven software was used to drive the different modules of the data acquisition system. In each measuring step, all the connected devices, and the elapsed time (in sec), were scanned and the

data was stored on the hard disk of the IBM PC. In addition, different x-y plots were displayed on the screen of the computer for visual control of load versus deformation. A constant scanning rate of one-quarter second was used for displaying the different graphs on the screen, and a saving time of one-half second was used for all the experiments. An average of ten readings was used for each measurement. Figure 4.6 shows a photograph of the data acquisition system and the MTS main control panel.

4.1.6 Control Scheme

The control scheme for the biaxial testing program was composed of two closed control loops. The first control loop was in displacement control in the major loaded direction. The command signal was supplied using the digital function generator and fed into the MTS controller. The AC LVDT that was mounted near the specimen supplied the feedback signal. Through the controller both signals were compared and if necessary an error signal was created. The correcting signal was then given to the servo-valve at the hydraulic actuator. The output from the load cell, in the major direction, was used as a command signal for the other actuator that operated in a load control closed loop. The proportionality of the two loads was maintained through the MTS controller. A block diagram highlighting the details of the used closed-loop test scheme is shown in Figure 4.7.

The major loading direction was specified as the one with the highest absolute value of the load. That choice was dictated by the capabilities of the MTS controller. At the beginning, an attempt was made to control the system through the data acquisition system. This method slowed down the system response time and sometimes led to total loss of control. This effect was undesirable as it could allow the two actuators to hit each other; this would have caused them severe damage. In addition, the slow

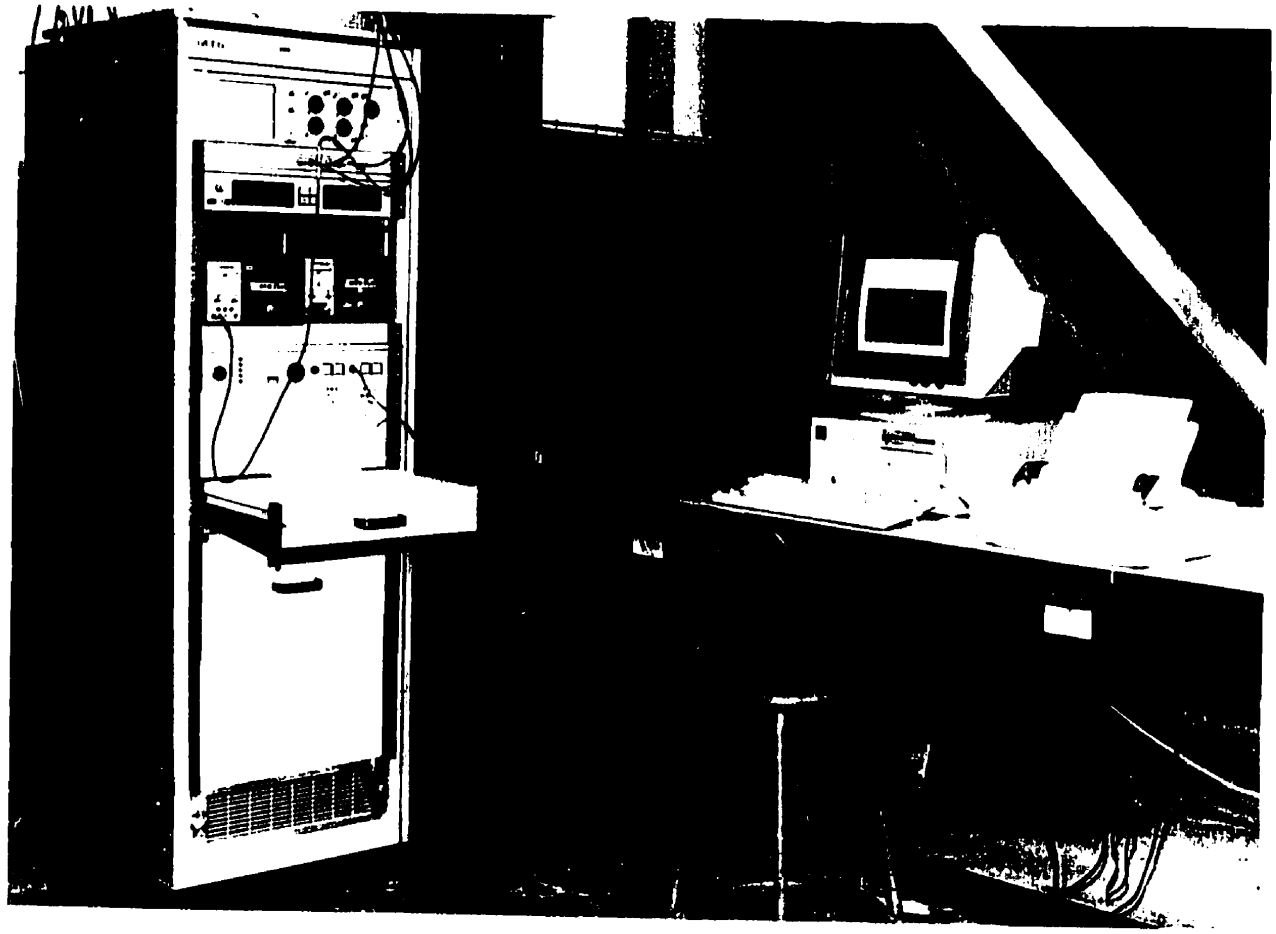

Figure 4.6: A photograph of the data acquisition system and the MTS main control panel

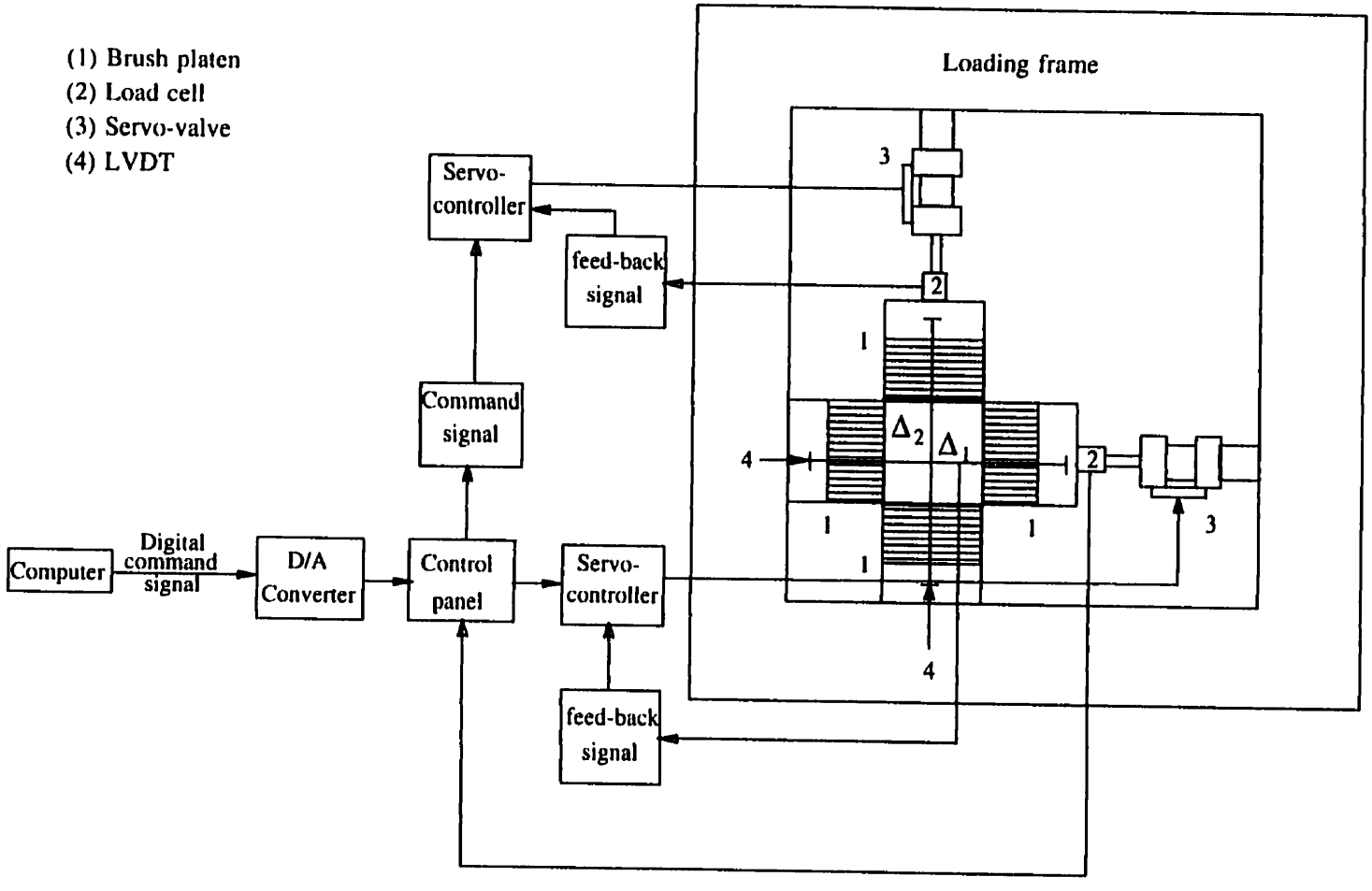

Figure 4.7: Block diagram highlighting the details of the closed-loop test scheme

system response would prevent the measurement of a stable descending branch. Thus the MTS controller was used. The MTS controller could only scale down the signal by a factor between 0 and 1. Thus the only choice for the major direction was that with the absolute maximum value of the load.

4.2 Testing Procedure

The plate specimens used in this study were 150 × 150 × 40 mm in dimensions. The details of the fabrication and preparation of the specimen are mentioned in section 4.8.

4.2.1 Specimen Loading

Proportional loading was used for all the tests. The ratio of the two applied loads was kept constant throughout the test. All combinations of biaxial stress, compression-compression, compression-tension, and tension-tension, were investigated. For compression-compression, stress ratios were $\sigma_2/\sigma_3 = 0$ (uniaxial compression), 0.2, 0.5 and 1.0; for compression-tension, stress ratios were σ_1/σ_3 = -0.05, -01.0 and -0.25; and for tension-tension, stress ratios were σ_1/σ_2 = 1.0, 2.0 and ∞ (uniaxial tension).

The loading rate of all the experiments was kept constant. A specimen was always loaded with a constant displacement rate in the major direction as mentioned in Section 4.1.6. This constant strain rate was equal to $\dot{\epsilon} = 5.0 \times 10^{-6}$/ s.

4.2.2 Specimen Mounting

The specimen was mounted with the sides that were ground first resting on the support loading platens (at right angles). The reason was that the first two ground sides provided the most accurate right angles between any two edges of the specimen. For tension tests, the specimen was glued to the loading platens by means of epoxy

resin. The resin was left to cure for at least fifteen hours and it performed its function in a satisfactory manner.

4.3 Test Specimens

The experimental program was undertaken to investigate the behaviour of high-strength concrete under biaxial loading. Four different types of concrete were tested:

a) A normal strength normal weight concrete mix (NSC) with a target strength of 40 MPa.

b) Two high strength concrete mixes with a target strength of 70 MPa: the first mix is made with normal weight aggregates (HSC) while the second one is almost identical in composition except light weight aggregates were used (HSLWC). The purpose of these two mixes is to study the effect of aggregate type on the behaviour of high strength concrete under biaxial loading conditions.

c) A very high strength concrete mix (UHSC) with a target strength of 100 MPa.

Note that the different mixes were designed to provide the targeted strength after 91 days. As the experimental program was scheduled to take at least six months of testing, it was necessary to ensure that the effect of maturity on the strength results is minimized.

In addition to the 150 × 150 × 40 mm plate specimen, eighteen 100 × 200 cylinders were cast from each concrete batch. The specimens were cast in three layers and compacted by means of a standard rod. Those specimen served as control specimen. They were used to obtain the compressive strength of each batch at 14, 28, 56 and 91 days. In addition, the splitting tensile strength of each batch was determined after 56 days.

4.4 Materials Used

In this section, the details of the different materials used in the concrete mixes, the mixing procedure, and the specimen fabrication are discussed.

4.4.1 Cementitious Materials

The term "cementitious materials" refers to the combined total weight of Portland cement and pozzolanic materials (silica fume) for the production of high-strength concrete. Ordinary Portland cement (Type 10) CSA3-AS5, as produced in Newfoundland, was used. The silica fume was supplied from the only Canadian source in Quebec.

4.4.2 Aggregates

The normal weight coarse aggregate was mostly crushed granite with a maximum nominal size of 6 mm. The fine aggregate had identical composition as the coarse aggregate, with a fineness modulus (FM) of 3.02. Both types of aggregates were locally available. For the light weight concrete mix, a slate-based light weight aggregate, known commercially as STALITE, was used as coarse aggregate. The light weight aggregate was brought from the construction site for the Hibernia offshore oil platform project. This aggregate had a maximum nominal size of 19 mm. Thus, it had to be separated and recombined to a desirable grading. A specified maximum nominal size of 9 mm was achieved.

Sieve analysis of the aggregates was conducted according to ASTM C 135. Tests for determination of specific gravity and absorption percentage were done according to ASTM C 127 and ASTM C 128, respectively. The results of sieve analysis are plotted as shown in Fig 4.8. The grading and the physical properties of both the fine

Table 4.1: Grading of aggregates

Sieve size		Cumulative percentage retained		
Metric	Imperial (US units)	Coarse (Granite)	Coarse (Light weight)	Fine
12.7 mm	1/2		0	
11.2 mm	7/16	0	8	
9.61 mm	3/8	1	56	
6.3 mm	1/4	38	90	
4.76 mm	No. 4	69	96	0
2.36 mm	No. 8	94		22
1.18 mm	No. 16			40
600 μm	No. 30			62
300 μm	No. 50			84
150 μm	No. 100			94

and coarse aggregates are given in Tables 4.1, 4.2, and 4.3, respectively.

4.4.3 Chemical Admixtures

All chemical admixtures met the requirement of ASTM C 494. The compatibility of the admixtures with the choice of cement is a very important consideration so that no slump loss or any undesirable effects in the concrete are created. This can be achieved through trial mixtures to ensure that the targeted workability and strength are satisfied.

4.4.4 High-range Water Reducers

The use of high range water reducing agents, also known as superplasticizers, in high strength concrete may serve the purpose of increasing strength at a specified slump or increasing slump. Throughout the whole experimental program, a superplasticizer

Table 4.2: Physical properties of normal weight aggregates

	Coarse aggregate	Fine aggregate
Bulk specific gravity, SSD	2.56	2.61
Apparent specific gravity	2.67	2.71
Absorption, percentage	0.45	0.43

Table 4.3: Physical properties of light weight aggregate

Bulk density (dry loose)	830 kg/m^3
Maximum dry density	960 kg/m^3
Apparent specific gravity (dry)	1.50
Bulk specific gravity (SSD)	1.58
Absorption (%)	6

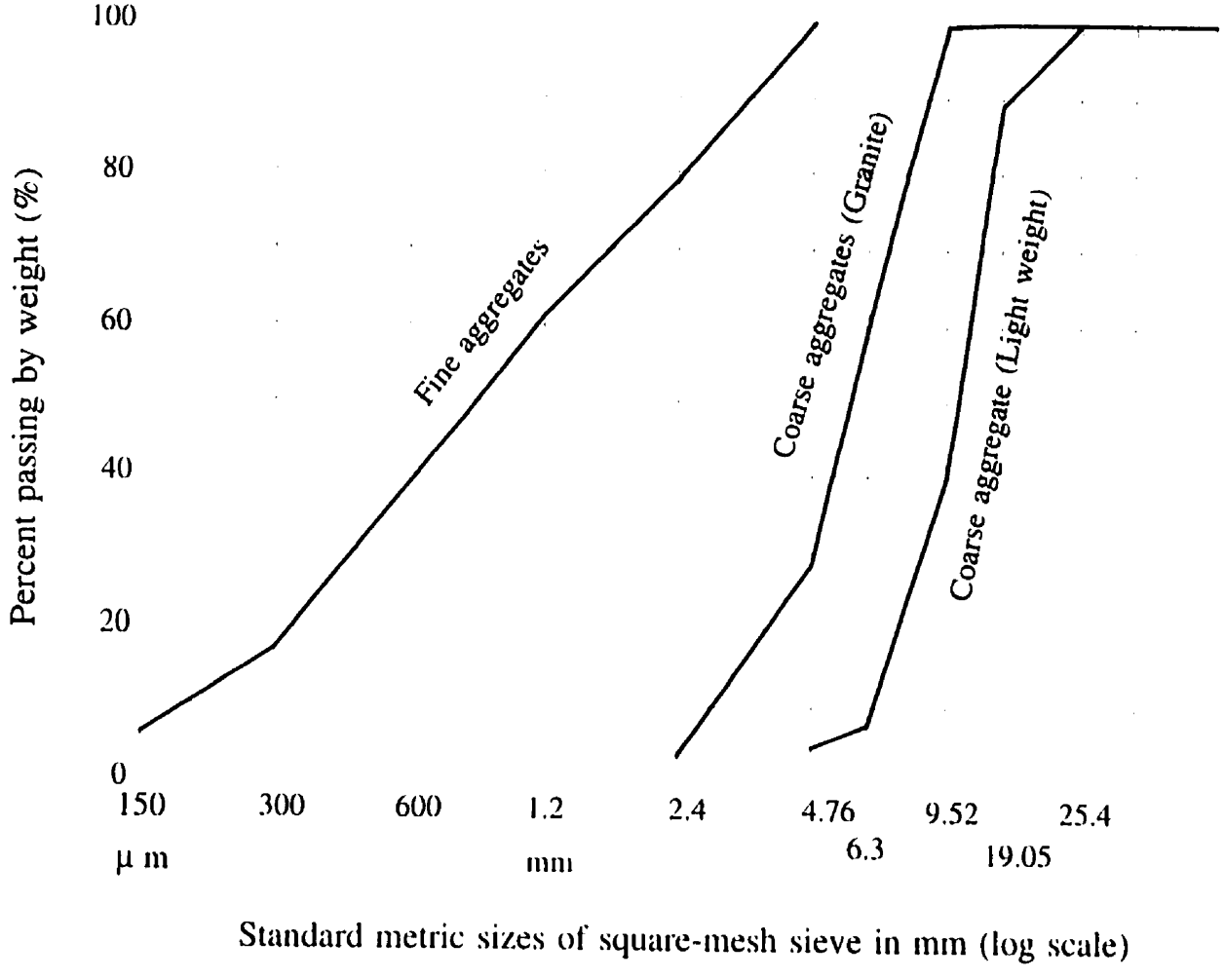

Figure 4.8: Grading of aggregates

of sulfonated naphthalene formaldehyde base. conforming to ASTM C 494 Type F. was employed.

4.4.5 Retarder

High-strength concrete mix designs incorporate high cement factors and low water cement ratios which are not common to normal concrete. A retarder is beneficial in controlling early hydration. The retarder is also useful in delaying the setting time so that the same consistency is achieved for all the specimen prepared from each batch. A non chloride water reducing agent of poly-hydroxy-carboxylic base. conforming to ASTM C 494 Type B and D. was used.

4.5 Concrete Mixes

The final mix design was reached after carrying out twenty trial mixes. The targeted strength and workability were ensured and the proper mixing procedure was established. The trial mixes also served in establishing the proper vibrating time and procedure used in manufacturing the specimen so that the variability between the specimen was minimized.

Based on the trial mixes. high strength-concrete mix was produced using conventional cement and aggregates from Newfoundland. The incorporation of silica fume and high-range water reducers makes it possible to achieve high strengths at early ages. A compressive strength of 100 MPa at 91 days was achieved for the concrete containing 6 % condensed silica fume and a high-range water reducing agent of naphthalene formaldehyde base. The concrete mix proportions for the different mixes are given in Table 4.4.

Table 4.4: Mix proportions of 0.1 cubic meter of concrete

Constituent	Unit	Normal strength mix	High strength mix (No. 1)	High strength mix (No. 2)	Light weight mix
Cement	kg	35	40	40	40
Silica Fume	kg	-	3.4	3.4	3.4
Cement & silica fume	kg	35	43.4	43.4	43.4
Fine aggregate	kg	65	60	53	61
Coarse aggregate	kg	110	100	85	67
Retarder	ml	-	75	100	75
Superplasticizer	ml	-	1000	1300	1000
w/(c+sf)		0.46	0.28	0.23	0.33
Mix density	kg/m^3	2350	2410	2385	1950

4.6 Mixing Procedure

The following mixing procedure was developed for the production of a workable high-strength concrete mix:

1) Charge 100 % of coarse aggregate.

2) Batch 100 % of cement.

3) Batch 100 % of sand.

4) Batch 100 % of silica fume while dry mixing all the constituents.

5) Mix for 3-5 minutes after adding 70 % of estimated water with superplasticizer.

5) Add 30 % of mix water together with air entraining admixture.

7) Re-temper with extra superplasticizer dose to target slump if necessary.

4.7 Properties of Fresh Concrete

The fresh density of the high-strength normal weight concrete mix was almost constant with an average value of 2400 kg/m^3. Slump values for the normal strength concrete mix were generally at the 100 mm target. For the high-strength concrete mixtures, including a superplasticizer and a retarder, flowing concrete was attained.

4.8 Specimen Fabrication

4.8.1 Casting

Special plexiglass moulds were manufactured for casting the biaxial test specimens. Each mould was used to cast four specimens. The mould consisted of a base, four walls and four internal partitions. The walls were secured in the base by means of

screws spaced at 50 mm. Also, the vertical walls were embedded in a 5 mm groove, in the base, to ensure that no distortion in the specimen occurred during casting.

During casting, compaction was achieved by placing the mould on a vibrating table and vibrating it at a frequency of 40 Hz for 60 seconds. The casting surfaces were finished, and the specimen were placed under a plastic cover to avoid drying out.

4.8.2 Curing

Two days after casting, the specimens were de-moulded and placed in a fresh water basin. At 56 days, the specimen were transported to a humidity room with a 99 % relative humidity and a constant temperature of 20° C. The specimen were taken out of the humidity room two days before testing and were then ground and prepared for testing.

4.8.3 Grinding

The biaxial testing machine was prepared for specimens with side dimension of 150 mm. As a result of the right angles between the two fixed supports, very accurate manufacturing of the specimen was demanded. Therefore, great attention was paid to ensure that each specimen has a plane and square end surfaces.

The four sides of the specimens were ground in order to ensure that the specimen had flat edges and right angle corners. The available grinder for concrete specimen in the concrete lab was equipped to handle cylinders only. Thus, a special jig was designed and manufactured for the rectangular specimen used. Figure 4.9 shows a photograph of the grinder and the grinding jig, respectively.

On one side of the jig, a flat guide was attached to the base. At the other side, a stiffened angle was used to hold the specimen against the side guide. At one end of

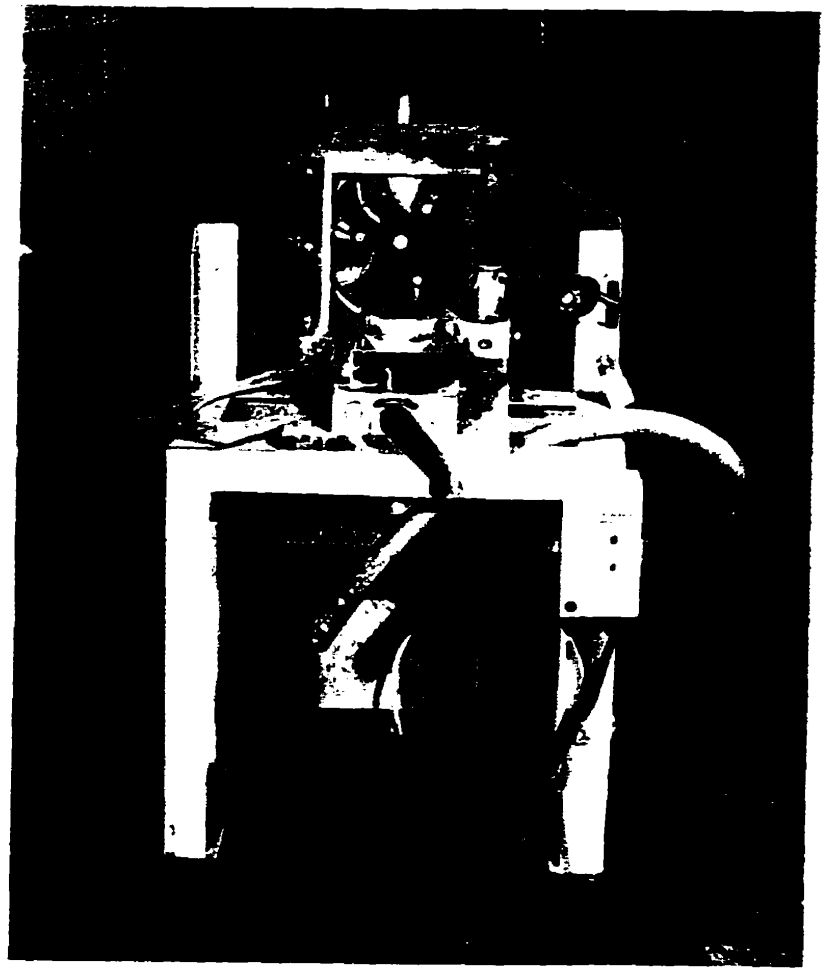

(a) The grinder

(b) The grinding Jig

Figure 4.9: Photograph of the grinder used for grinding the test specimen

the jig, a pin was fastened to the base to provide the reaction force when the other free end of the specimen was being ground. The jig was mounted on the grinder by means of four bolts by a precision machinist. Special care was given to ensure that the specimen was always normal to the grinding wheel and was checked and re-adjusted after every week of usage.

The grinder employed a wet-type grinding method using a diamond grinding wheel. The final ground surface finish was within $\pm$ 0.05 mm. The grinding of the specimen was achieved at the rate of 0.5 mm/60 seconds. One millimetre was ground from each side of the specimen. The grinding process started by grinding one side of the specimen. The ground side was then placed against the side guard and the specimen was rotated until all four sides were ground. The two surfaces of the specimen were also ground to eliminate any non uniformity in the free casting surface using a hand held grinder with a masonry cutting stone. The specimens were ground one day prior to testing.

4.9 Summary of Experiments

Three specimen were tested for each biaxial compression loading ratio. Due to time limitation only two specimen were tested for the biaxial-compression and tension-tension tests. Note that the epoxy glue used to take at least sixteen hours to harden and that limited it to one test a day. However, three specimen were used for the uniaxial tension tests.

Two days before each test, the specimen was removed from the humidity room. It was ground and then left in room temperature for one day to dry. The extensometer was then glued to the specimen, or in case of strain gauges they were attached to the specimen. On the test date, the specimen was mounted in the test set up and the

experiment was carried out. In the case of tension tests, a very small compression load (around 200 lbs) was applied to the specimen while the glue was setting. The test was then carried out on the next day.

Chapter 5

Test Results and Discussion

In this chapter, the experimental results and observations obtained from the biaxial testing program are reported and analyzed. Firstly, the strength data and biaxial strength envelopes for the different types of concrete are presented. Secondly, the stress and strain measurements obtained from various measuring systems are characterized. Finally, the crack patterns and failure modes of the test specimens are examined.

5.1 Strength Data

5.1.1 Compressive Strength of the Different Mixtures

The ultimate uniaxial compressive strength, for each mix, was determined from testing 100 × 200 mm control cylinders. The specimen were tested using a 2670 kN (600 kips) Soiltest compression testing machine. Due to the anticipated duration of the testing program, the strength gain with time had to be measured for all the mixtures. The test cylinders were capped with a high strength sulphur compound on both ends. For each mix, three cylinders were tested in accordance with ASTM C 39 at 7, 28, 91 and 180 days. Table 5.1 provides the compressive strength values for the different concrete mixes at different ages. All the high strength concrete specimen

Figure 5.1: A high strength concrete cylinder at failure

formed a cup and cone type of failure (Fig 5.1).

The splitting tensile strength for the different mixtures at the age of 91 days, is given in Table 5.2. Due to the shortage of cylinders, only two 100 × 200 mm cylinders were tested. The tests were carried out in accordance with ASTM testing procedures.

In order to ensure that there was no significant gain in the compressive strength, it was decided that the biaxial test program on the concrete plates should start at 91 days from casting of the specimen. It should be noted that the uniaxial compressive strength, obtained from testing the concrete cylinders, is slightly different than the uniaxial strength obtained from testing the plate specimen (refer to Section 5.1.2).

Table 5.1: Uniaxial compressive strength for the different mixtures at different ages for the 100 × 200 mm cylinders

Mix No.	Specimen No	Compressive strength (MPa)			
		28 days	56 days	91 days	180 days
NSC	1	39.19	43.70	45.31	45.95
	2	36.94	40.10	42.62	44.16
	3	38.17	42.80	44.97	45.50
	Average	38.10	42.20	44.30	45.20
HSC	1	71.10	76.52	75.04	75.16
	2	69.68	73.88	76.14	80.72
	3	72.52	73.70	78.62	78.72
	Average	71.10	74.70	76.60	78.20
UHSC	1	91.59	98.36	101.25	105.49
	2	96.94	96.64	97.59	101.07
	3	99.62	99.30	101.41	102.14
	Average	96.05	98.10	100.08	102.90
HSLWC	1	61.76	66.59	67.84	72.43
	2	60.59	63.34	65.13	66.25
	3	63.06	65.96	73.13	70.72
	Average	61.80	65.30	68.70	69.80

Table 5.2: Splitting tensile strength (MPa) for the different mixtures at 91 days

Mix No.	Specimen 1	Specimen 2
NSC	3.56	3.63
HSC	5.07	5.48
UHSC	6.03	6.58
HSLWC	3.45	3.96

Such a difference can be attributed to the difference in sizes between the two specimen and to the effect of end conditions in the two different tests. It is noted that in this study, only 100 × 200 mm cylinders were used.

The experimental program was carried out using the steel brushes in all the tests. Accordingly, the same end conditions, used for testing remain the same. Thus, it seems rational to use the uniaxial compressive strength of the concrete plates as the representative uniaxial compressive strength for the different types of concrete specimen throughout this chapter. It is referred to as σ_{co}.

5.1.2 Biaxial Strength Data

The plate specimen were tested under different combinations of biaxial loading as mentioned in Section 4.2.1. For all the experiments, the tests were performed under constant stress-ratio ($\sigma_1 > \sigma_2 > \sigma_3$, σ_i negative in compression). In the presentation of the data, and the subsequent discussion, all strength data are normalized with respect to the unconfined uniaxial compressive strength σ_{co} which was obtained from the plate specimen presented next ($\sigma_{co} = \sigma_3$ when $\sigma_2 = \sigma_1 = 0$).

The ultimate compressive strength of the concrete plate specimens, under different load combinations, are reported in Tables 5.3, 5.4, 5.5, and Table 5.6, for the NSC, HSC, UHSC and HSLWC mixes, respectively. Figures 5.2, 5.3, 5.4, and 5.5, show the relationship between the normalized (w.r.t. σ_{co}) principal stresses at failure. The graphical representation of this relationship is also referred to as the strength envelopes. The biaxial strength envelopes for all the four types of concrete, combined, are presented in Fig 5.6.

In general, the ultimate strength of concrete under biaxial compression is higher than under uniaxial compression. The strength increase under biaxial compression is dependent on the biaxial stress ratio. The maximum biaxial strength occurs at a

Table 5.3: Biaxial strength data for the normal strength concrete mix NSC

(a) Compression-Compression

σ_2 MPa	σ_3 MPa	σ_2/σ_3	σ_2/σ_{co}	σ_3/σ_{co}	Average	
					σ_2/σ_{co}	σ_3/σ_{co}
0	-41.86	0	0	-0.988		
0	-42.96	0	0	-1.014		
0	-42.32	0	0	-0.999	0	-1.00
-10.90	-51.91	-0.210	-0.257	-1.225		
-10.09	-51.25	-0.197	-0.238	-1.209		
-10.30	-51.98	-0.198	-0.243	-1.227	-0.246	-1.220
-27.90	-54.57	-0.511	-0.658	-1.288		
-28.20	-55.76	-0.506	-0.665	-1.316		
-28.47	-56.48	-0.504	-0.672	-1.333	-0.665	-1.312
-50.78	-51.86	-0.979	-1.198	-1.224		
-50.47	-48.07	-1.050	-1.191	-1.134	-1.195	-1.179

(b) Compression-Tension

σ_1 MPa	σ_3 MPa	σ_1/σ_3	σ_1/σ_{co}	σ_3/σ_{co}
0.924	-38.608	-0.024	0.022	-0.911
1.598	-34.116	-0.047	0.038	-0.805
1.534	-31.404	-0.049	0.036	-0.741
1.822	-25.894	-0.070	0.043	-0.611
1.695	-24.114	-0.070	0.040	-0.569
2.276	-22.928	-0.099	0.054	-0.541
1.975	-21.020	-0.094	0.047	-0.496
2.645	-14.028	-0.189	0.062	-0.331

(c) Tension-Tension

σ_1 MPa	σ_2 MPa	σ_1/σ_2	σ_1/σ_{co}	σ_2/σ_{co}
3.43	0.00	∞	0.081	0.000
3.16	0.00	∞	0.075	0.000
3.14	1.54	2.043	0.074	0.036
3.72	1.91	1.944	0.088	0.045
3.34	3.55	0.939	0.079	0.084
3.13	3.02	1.036	0.074	0.071

Table 5.4: Biaxial strength data for the high strength concrete mix HSC

(a) Compression-Compression

σ_2 MPa	σ_3 MPa	σ_2/σ_3	σ_2/σ_{co}	σ_3/σ_{co}	Average	
					σ_2/σ_{co}	σ_2/σ_{co}
0	-77.88	0	0	-1.057		
0	-72.91	0	0	-0.990		
0	-70.16	0	0	-0.953	0	-1.00
-19.29	-84.19	-0.229	-0.262	-1.143		
-19.52	-94.76	-0.206	-0.265	-1.287		
-18.87	-89.87	-0.210	-0.256	-1.220	-0.261	-1.217
-49.57	-93.06	-0.533	-0.673	-1.264		
-48.41	-101.39	-0.477	-0.657	-1.377		
-49.53	-98.09	-0.505	-0.673	-1.332	-0.668	-1.324
-84.21	-85.76	-0.982	-1.143	-1.164		
-84.10	-81.57	-1.031	-1.142	-1.108	-1.143	-1.136

(b) Compression-Tension

σ_1 MPa	σ_3 MPa	σ_1/σ_3	σ_1/σ_{co}	σ_3/σ_{co}
1.318	-53.470	-0.025	0.018	-0.726
1.974	-41.170	-0.048	0.027	-0.559
1.723	-38.887	-0.044	0.023	-0.528
1.804	-38.077	-0.047	0.025	-0.517
2.025	-26.956	-0.075	0.028	-0.366
2.076	-29.239	-0.071	0.028	-0.397
2.651	-25.998	-0.102	0.036	-0.353
2.445	-23.568	-0.104	0.033	-0.320
2.983	-15.467	-0.193	0.041	-0.210
2.998	-15.246	-0.197	0.041	-0.207
2.902	-14.435	-0.201	0.039	-0.196

(c) Tension-Tension

σ_1 MPa	σ_2 MPa	σ_1/σ_2	σ_1/σ_{co}	σ_2/σ_{co}
4.12	0.00	∞	0.056	0.000
4.43	0.00	∞	0.060	0.000
3.90	0.00	∞	0.053	0.000
4.73	2.45	1.928	0.064	0.033
4.15	2.04	2.035	0.056	0.028
3.91	3.85	1.016	0.053	0.052
4.05	4.01	1.011	0.055	0.054

Table 5.5: Biaxial strength data for the high strength concrete mix UHSC

(a) Compression-Compression

σ_2 MPa	σ_3 MPa	σ_2/σ_3	σ_2/σ_{co}	σ_3/σ_{co}	Average	
					σ_2/σ_{co}	σ_2/σ_{co}
0	-99.98	0	0	-1.036		
0	-93.90	0	0	-0.973		
0	-95.74	0	0	-0.992	0	-1.00
- 22.85	-122.68	-0.186	-0.237	-1.271		
- 24.95	-115.86	-0.215	-0.258	-1.200		
- 25.60	-122.04	-0.210	-0.265	-1.264	-0.253	-1.245
-61.58	-132.42	-0.465	-0.638	-1.372		
-61.54	-130.33	-0.472	-0.637	-1.350		
-61.98	-128.53	-0.482	-0.642	-1.331	-0.639	-1.351
-104.65	-108.71	-0.963	-1.084	-1.126		
-108.80	-107.65	-1.011	-1.127	-1.115		
-99.62	-103.07	-0.967	-1.032	-1.068	-1.081	-1.103

(b) Compression-Tension

σ_1 MPa	σ_3 MPa	σ_1/σ_3	σ_1/σ_{co}	σ_3/σ_{co}
1.718	-63.330	-0.027	0.018	-0.656
2.259	-47.594	-0.047	0.023	-0.493
2.269	-44.988	-0.050	0.024	-0.466
2.056	-39.292	-0.052	0.021	-0.407
2.066	-29.831	-0.069	0.021	-0.309
2.269	-31.955	-0.071	0.024	-0.331
2.858	-29.541	-0.097	0.030	-0.306
2.809	-28.286	-0.099	0.029	-0.293
3.775	-18.729	-0.202	0.039	-0.194
3.669	-18.536	-0.198	0.038	-0.192

(c) Tension-Tension

σ_1 MPa	σ_2 MPa	σ_1/σ_2	σ_1/σ_{co}	σ_2/σ_{co}
4.90	0.00	∞	0.051	0.000
4.70	0.00	∞	0.049	0.000
4.86	0.00	∞	0.050	0.000
5.25	2.77	1.899	0.054	0.029
4.86	2.30	2.112	0.050	0.024
4.61	4.69	0.982	0.048	0.049
5.12	5.27	0.972	0.053	0.055

Table 5.6: Biaxial strength data for the light weight concrete mix HSLWC

(a) Compression-Compression

σ_2 MPa	σ_3 MPa	σ_2/σ_3	σ_2/σ_{co}	σ_3/σ_{co}	Average	
					σ_2/σ_{co}	σ_2/σ_{co}
0	-64.97	0	0	-0.975		
0	-66.82	0	0	-1.002		
0	-68.19	0	0	-1.023	0	-1.00
-18.12	-77.19	-0.235	-0.272	-1.158		
-17.74	-84.47	-0.210	-0.266	-1.267		
-17.56	-81.51	-0.215	-0.263	-1.223	-0.267	-1.216
-45.85	-91.15	-0.503	-0.688	-1.367		
-45.67	-86.34	-0.529	-0.685	-1.295		
-46.45	-98.48	-0.472	-0.697	-1.477	-0.690	-1.380
-86.85	-90.22	-0.963	-1.303	-1.353		
-89.86	-88.91	-1.011	-1.348	-1.334		
-80.85	-83.65	-0.967	-1.213	-1.255	-1.288	-1.314

(b) Compression-Tension

σ_1 MPa	σ_3 MPa	σ_1/σ_3	σ_1/σ_{co}	σ_3/σ_{co}
1.100	-40.856	-0.027	0.017	-0.613
1.340	-36.143	-0.037	0.020	-0.542
1.813	-35.643	-0.051	0.027	-0.535
1.713	-34.410	-0.050	0.026	-0.516
1.793	-33.910	-0.053	0.027	-0.509
1.913	-25.664	-0.075	0.029	-0.385
1.983	-27.931	-0.071	0.030	-0.419
2.186	-21.944	-0.100	0.033	-0.329
1.953	-20.891	-0.093	0.029	-0.313
2.366	-11.839	-0.200	0.036	-0.178
2.120	-10.479	-0.202	0.032	-0.157

(c) Tension-Tension

σ_1 MPa	σ_2 MPa	σ_1/σ_2	σ_1/σ_{co}	σ_2/σ_{co}
3.05	0.00	∞	0.046	0.000
3.65	0.00	∞	0.055	0.000
3.46	0.00	∞	0.052	0.000
3.59	1.79	2.005	0.054	0.027
3.25	1.63	1.995	0.049	0.024
3.61	3.46	1.043	0.054	0.052
3.43	3.71	0.925	0.051	0.056

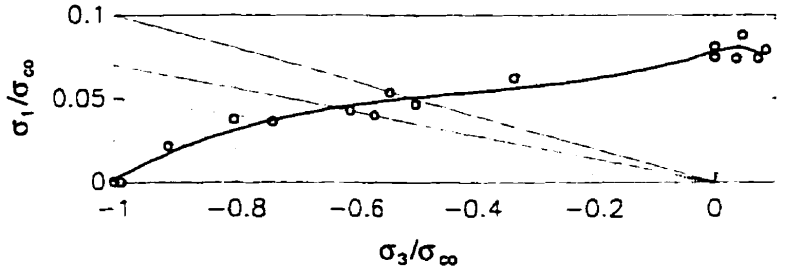

(a) Compression-tension and tension-tension

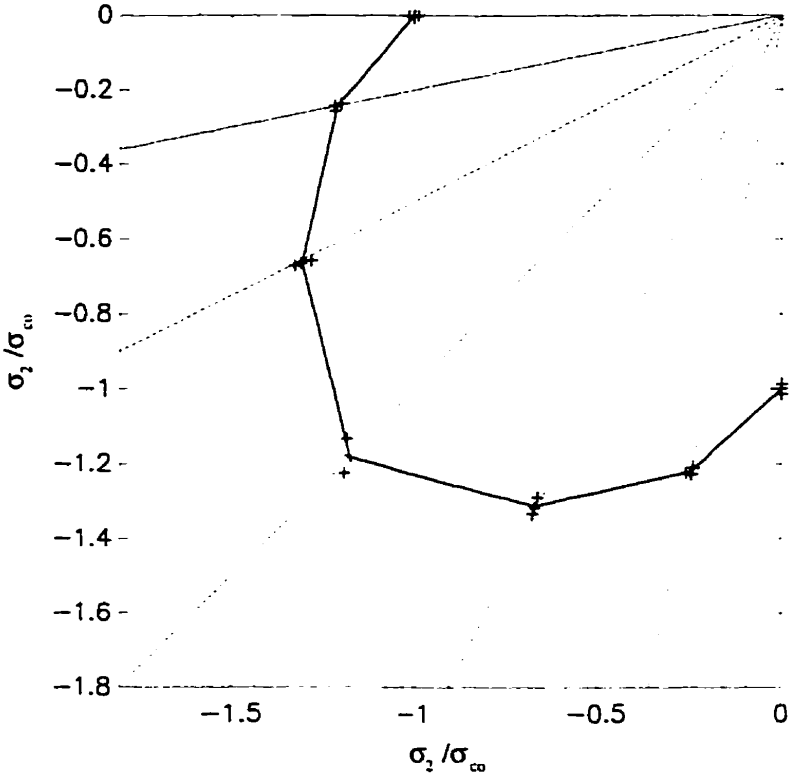

(b) Compression-Compression

Figure 5.2: Biaxial strength envelopes for NSC under combined tension and compression, biaxial tension and biaxial compression

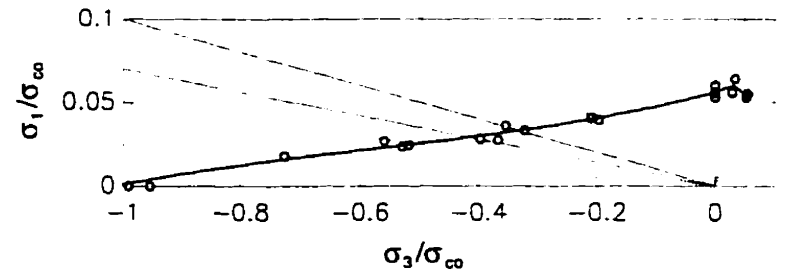

(a) Compression-tension and tension-tension

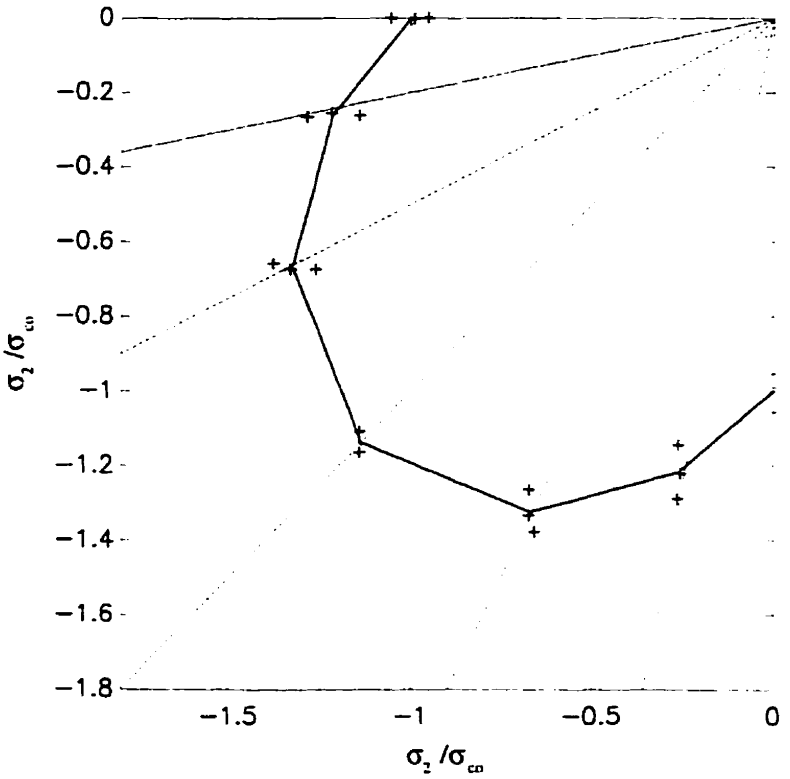

(b) Compression-Compression

Figure 5.3: Biaxial strength envelopes for HSC under combined tension and compression, biaxial tension and biaxial compression

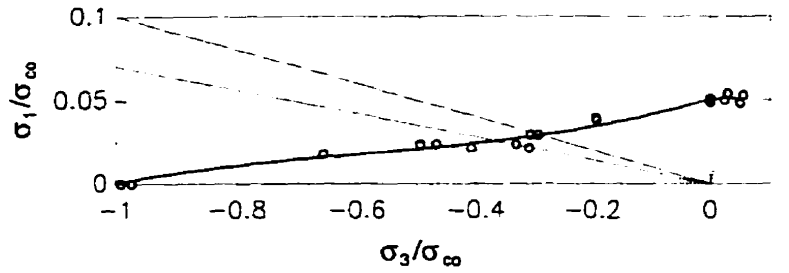

(a) Compression-tension and tension-tension

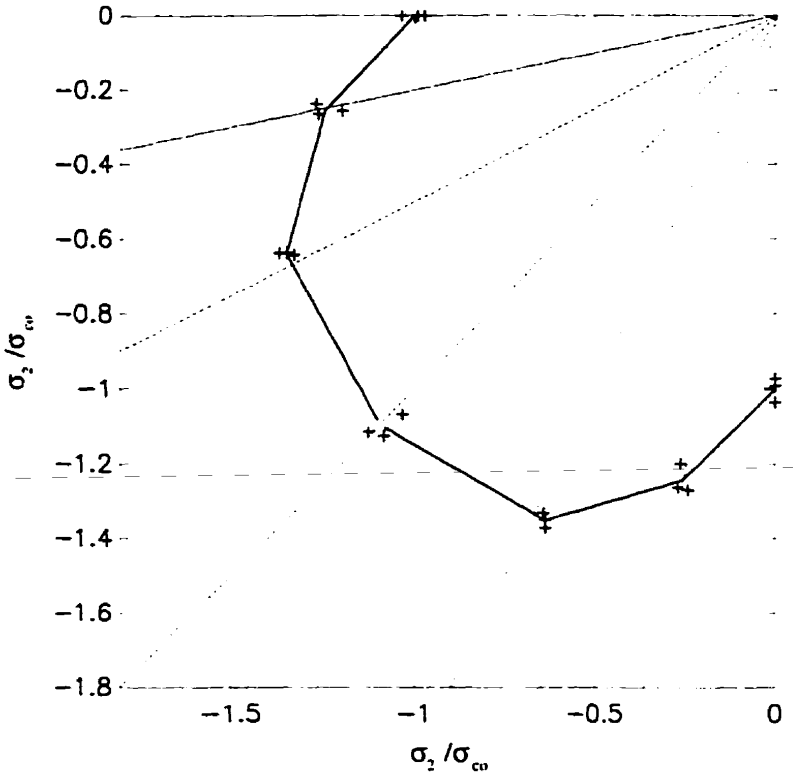

(b) Compression-Compression

Figure 5.4: Biaxial strength envelopes for UHSC under combined tension and compression, biaxial tension and biaxial compression

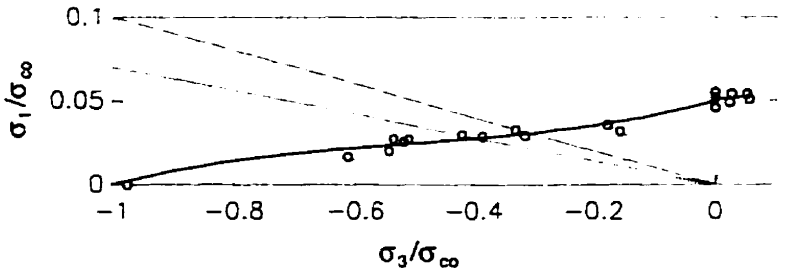

(a) Compression-tension and tension-tension

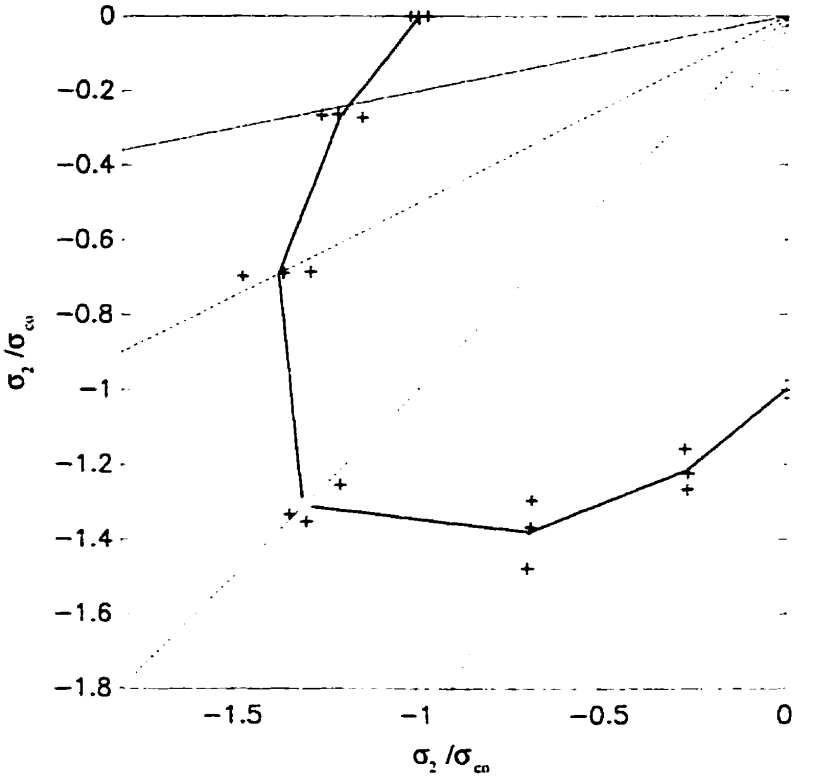

(b) Compression-Compression

Figure 5.5: Biaxial strength envelopes for HSLWC under combined tension and compression, biaxial tension and biaxial compression

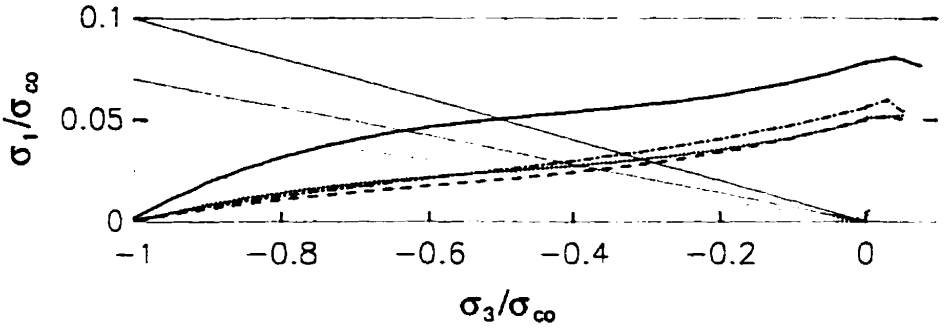

(a) Compression-tension and tension-tension

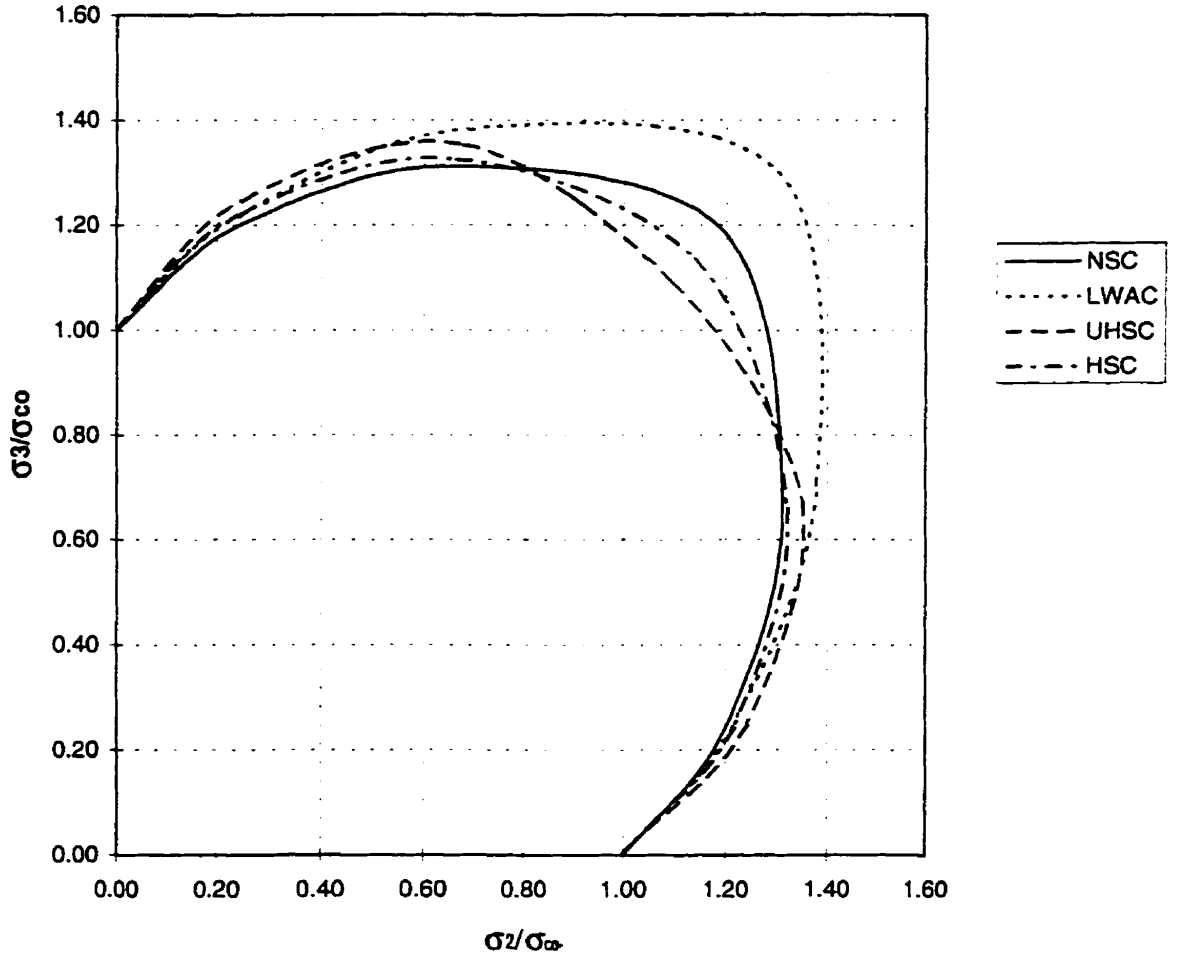

(b) Compression-Compression

Figure 5.6: Biaxial strength envelopes for the four different types of concrete under combined tension and compression, biaxial tension and biaxial compression

biaxial stress ratio of 0.5 , for all specimens tested. At this stress ratio, a strength increase of about 31 % for the NSC specimen, 32 %, 35 % and 38 % for the HSC, UHSC and HSLWC was observed

At equal biaxial compression ($\sigma_2/\sigma_3 = 1.0$), the relative strength increase becomes smaller as the compressive strength is increased for all the normal weight mixes. The strength increase is 19, 14 and 9 % for the NSC, HSC and UHSC mixes, respectively.

The effect of aggregate type on the biaxial behaviour of concrete can be demonstrated by comparing the lightweight concrete mix HSLWC with the corresponding HSC mix which is relatively similar except for the slight difference in compressive strength and the type of aggregate used. The HSLWC indicated a higher strength gain, at all stress ratios, than the HSC (refer to Fig 5.6(b)). This contradicts the findings by Yin et al. [111] for normal weight aggregates. The results of that study suggested that the biaxial strength of concrete increases as the strength of the aggregates is increased. The discrepancy can be attributed to the nature of lightweight aggregate concrete. When lightweight aggregate concrete is subjected to a uniaxial compressive load, the aggregate is subjected to a lateral confinement of the surrounding matrix [112]. Thus, the lightweight aggregates benefit from the confinement effects that occur in multiaxial stress conditions. Moreover, light weight aggregates possess higher bond (with cement mortar) than normal weight aggregates. Accordingly, these factors can lead to the enhancement of the behaviour of high strength lightweight concrete over the high strength normal weight concrete under biaxial compression.

The uniaxial tensile strength, f'_t was found to be 3.30, 4.15, 4.82 and 3.38 MPa for the NSC, HSC, UHSC and HSLWC, respectively, resulting in a ratio of f'_t/f'_c that is equal to 0.078, 0.056, 0.050, and 0.051. Note the f'_t/f'_c ratio decreases as the compressive strength increases. It is noted here that the uniaxial tensile strength is

in good agreement with previous research work on high strength concrete [30, 113]. The tensile strength of the HSLWC is less than the corresponding HSC mix. The different combinations of the biaxial tension-tension test resulted in a strength that was almost equal to the uniaxial tensile strength.

In previous studies on normal strength concrete, and in the biaxial tension region, Tasuji et al. [17] have noticed a slight increase in the tensile strength when the two principal tensile stresses are equal whereas Kupfer et al. [14] have observed that there is no difference. However, it should be noted that in both cases the differences of concrete tensile failure strength with f'_t is not significant enough to necessitate a more accurate verification in this region. It should be noted here that the values of f'_t/f'_c that were reported by Kupfer et. al [14] for the 59 MPa concrete appears to be slightly high. Comparing the values of the uniaxial tensile strength and the splitting tensile strength, in this study, indicate that the tensile splitting strength was found to be always higher than the uniaxial tensile strength for high strength concrete.

In the biaxial compression-tension region, there is a significant difference in the behaviour between high strength and normal strength concrete. Introducing a small amount of tension decreases the compressive capacity more radically for high strength concrete than for normal strength concrete. This is clear from inspection of Fig 5.6(a). This was suggested by [31], as a difference between normal strength and high strength concrete, and it is apparently true. Note also that the same trend was reported by Kupfer et al. [14].

5.2 Typical Stress Strain Curves

The loads and deformations in the three principal directions were measured for all the tests using the devices mentioned in the previous chapter. The stress strain curves,

presented in this section, show the relationships of normalized stress to actual strain. The conventions for the principal strains are such that $\epsilon_1 > \epsilon_2 > \epsilon_3$ with tensile stress being positive. The stress strain curves are reported up to the peak value of the load. The post peak behaviour is discussed in the next section.

Figures 5.7 to 5.18 show typical stress strain curves, under different load combinations, for each concrete mix. In uniaxial compression, the average value of the principal compressive strain at the ultimate stress (ϵ_3) increases as the compressive strength was increased (for the normal weight aggregate concretes). The strain at ultimate stress was 2076 and 2600 microstrain for the normal strength concrete NSC and the high strength concrete UHSC (Figs. 5.7 and 5.13). As shown in Figs. 5.10 and 5.16, the light weight concrete mix (HSLWC) showed a higher value of ϵ_3 (3080 microstrain) than the corresponding high strength normal weight mix HSC (2200 microstrain). An average value of the modulus of elasticity, E, was found to be 27.7, 39, 42, and 25.3 GPa for the NSC, HSC, UHS and UHSC specimens, respectively.

Under different biaxial compression loading combinations, the results show that the introduction of a second principal stress significantly affects the effective elastic modulus of concrete specimen in the direction of the first principal stress (Figures 5.7, 5.10, 5.13 and 5.16). The strain, at a given stress, in the major principal stress, σ_3, is reduced by the presence of a minor principal stress, σ_2. This indicates that the stiffness of the concrete specimen increases in the major principal direction as the minor principal stress is applied. It is important to emphasize that the change in the elastic moduli is not solely due to the Poisson's effect: it is also related to microcrack confinement [17]. This was observed for all the different types of concrete. Also, in the direction of larger principal stress, the strains at ultimate load increase as the failure stress increases. The maximum ϵ_3 was observed at a stress ratio of 0.5.

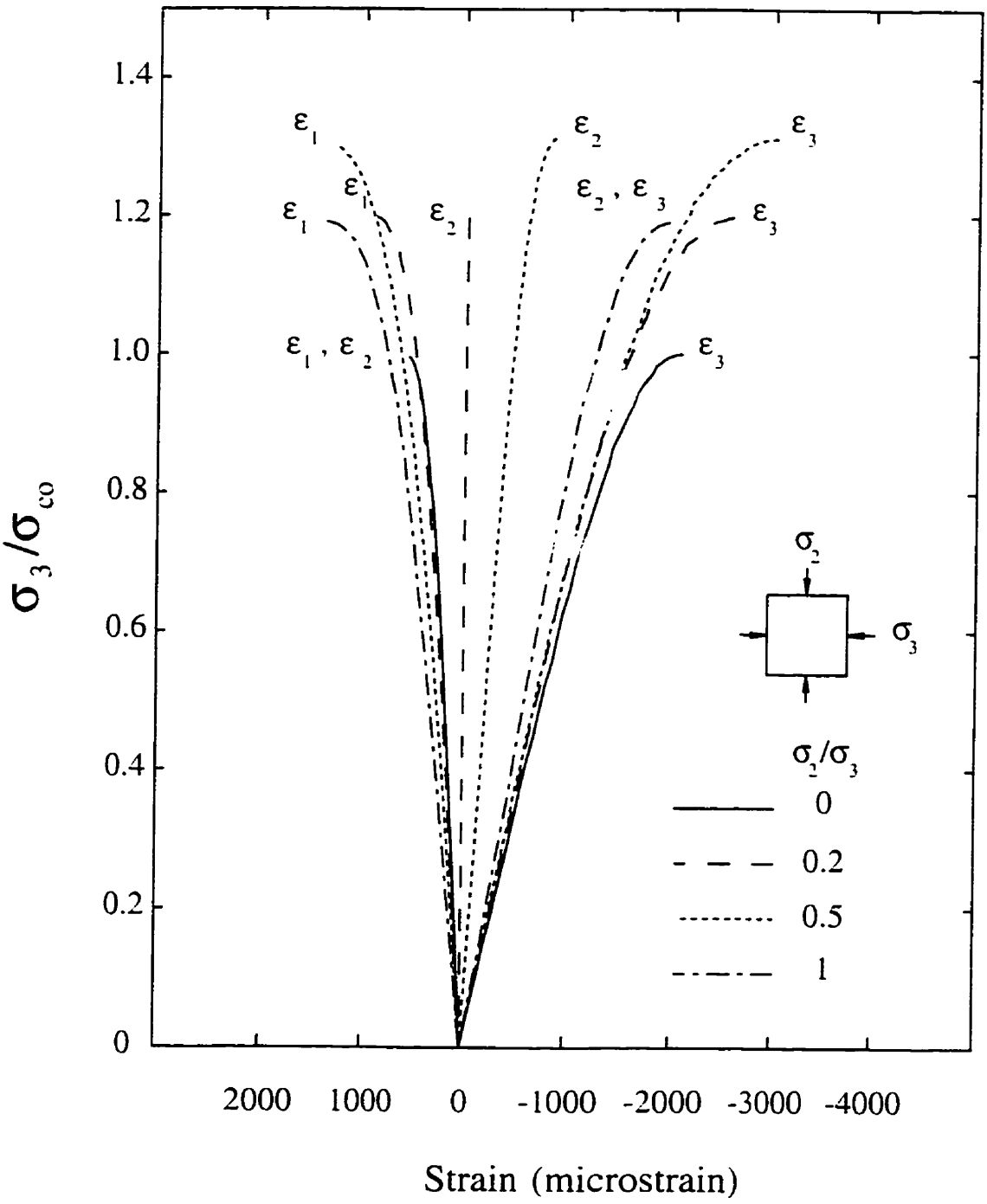

Figure 5.7: Stress-strain relationships for the normal strength concrete mix (NSC) under biaxial compression

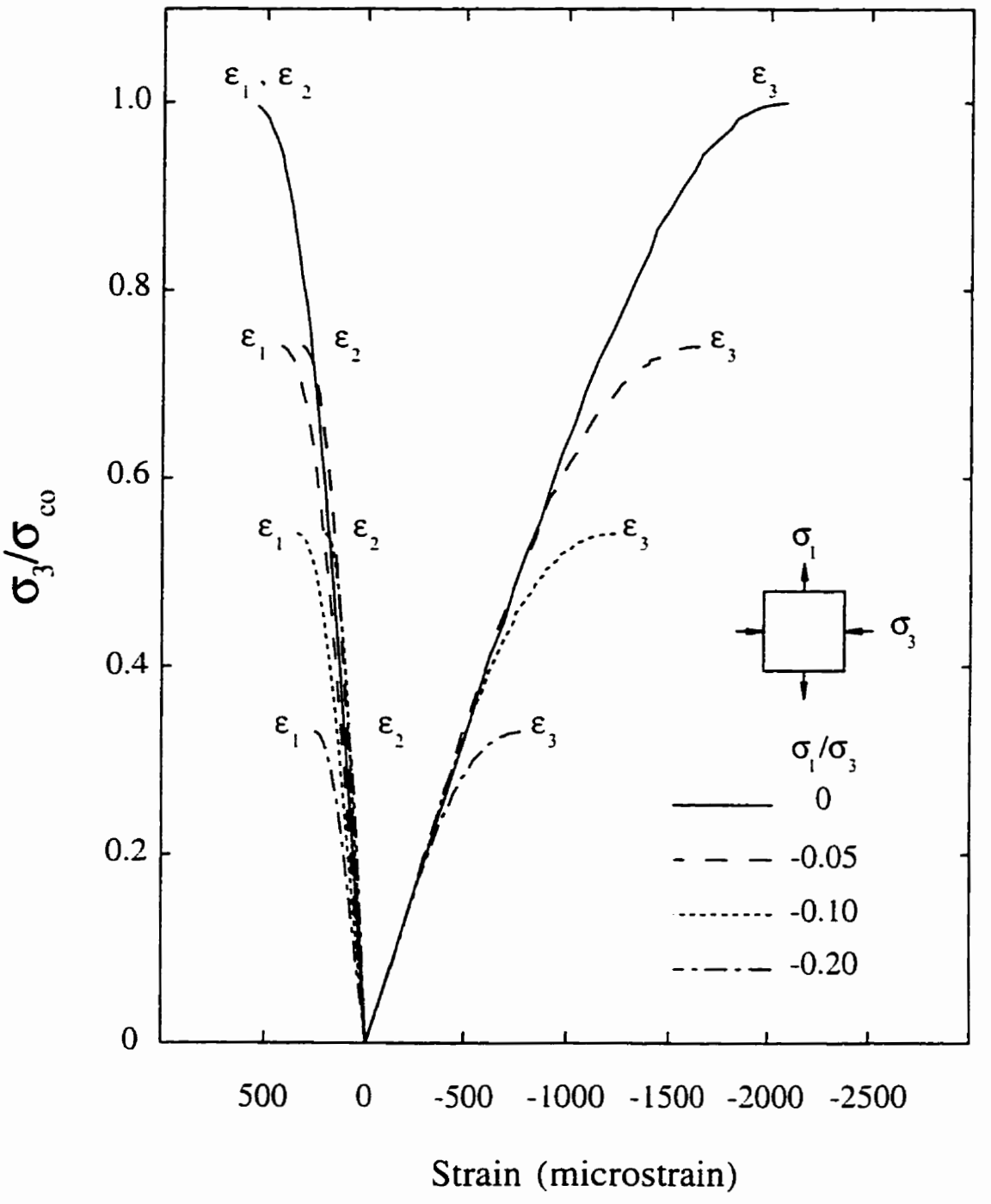

Figure 5.8: Stress-strain relationships for the normal strength concrete mix (NSC) under combined tension and compression

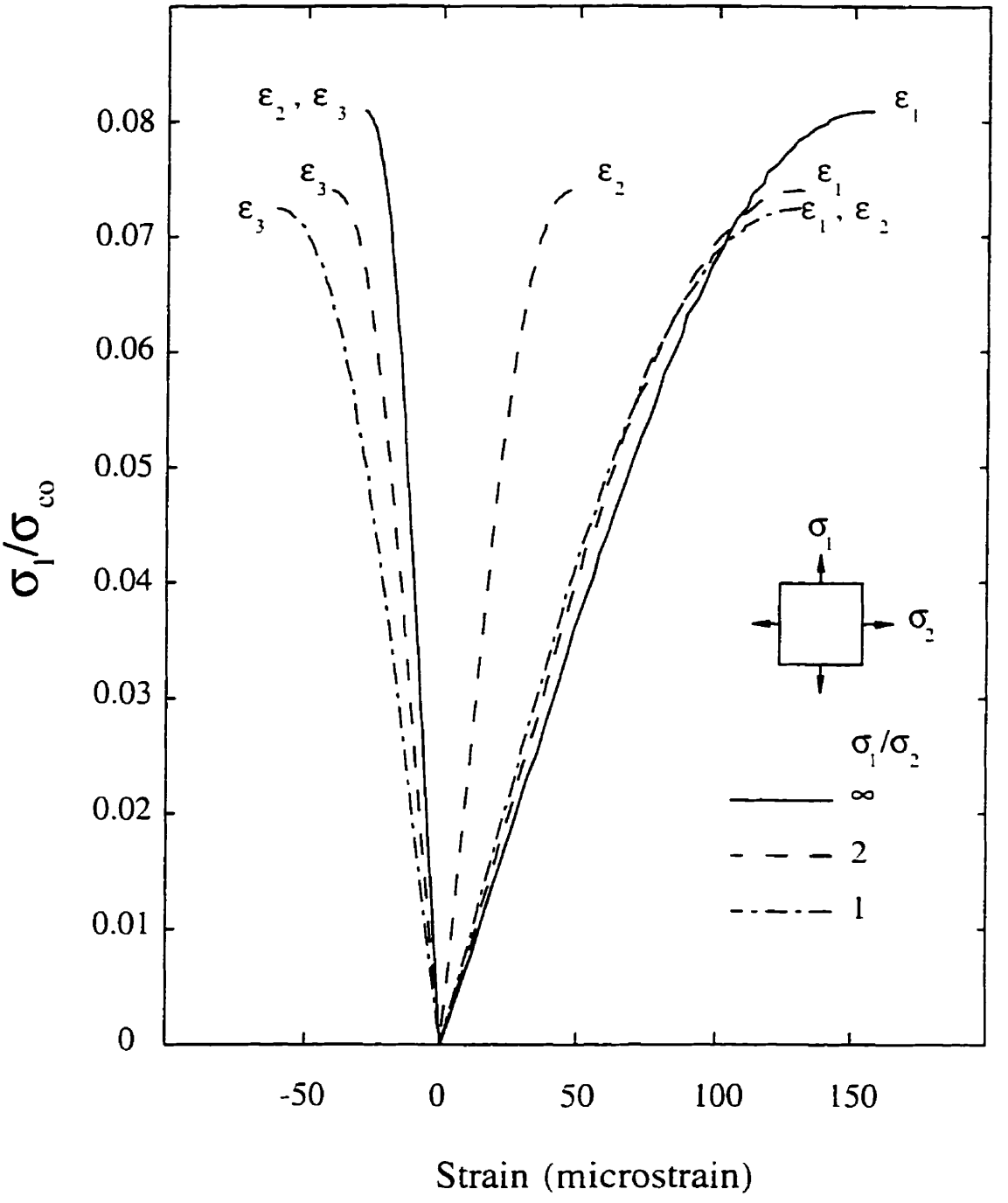

Figure 5.9: Stress-strain relationships for the normal strength concrete mix (NSC) under biaxial tension

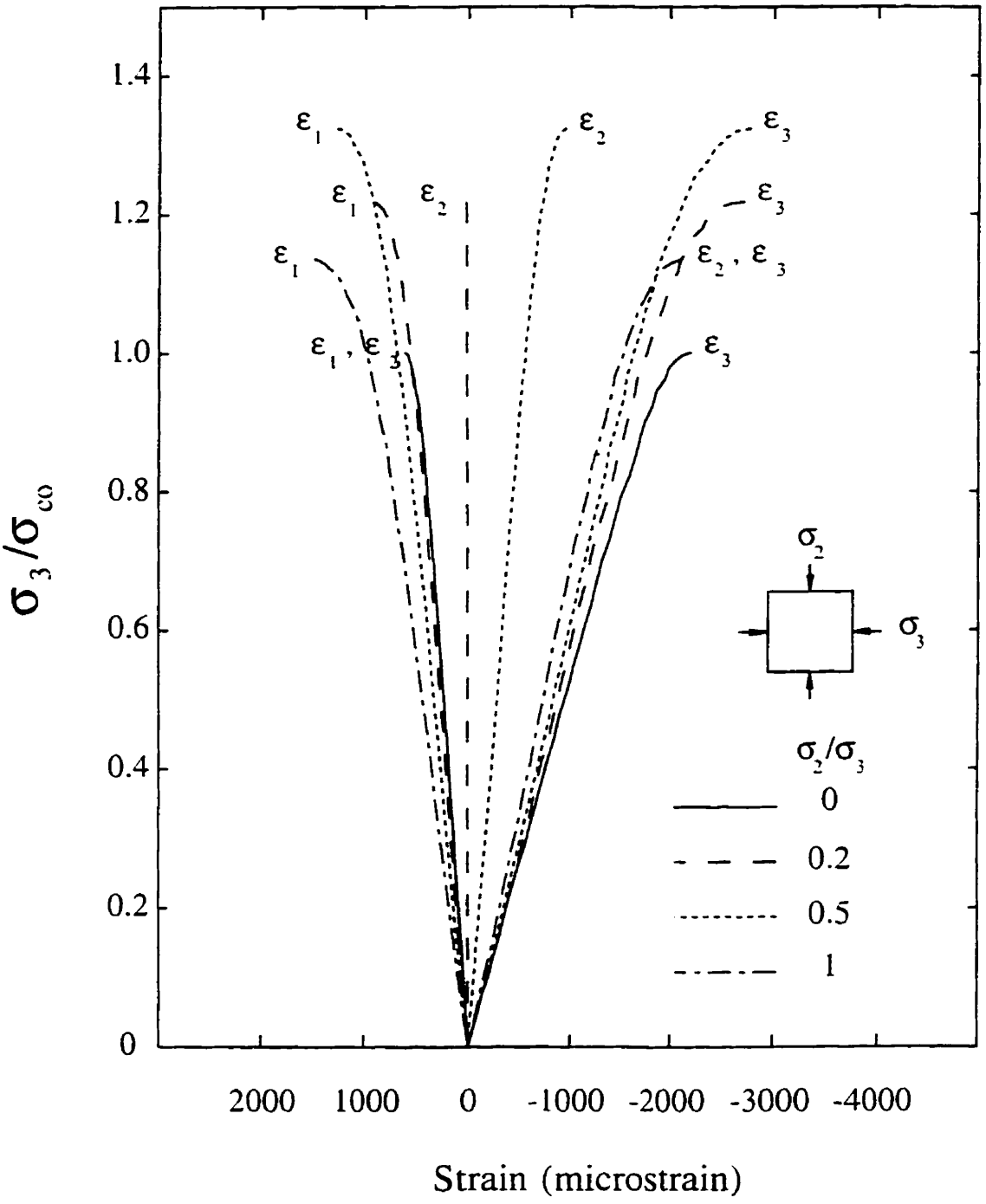

Figure 5.10: Stress-strain relationships for the high strength concrete mix (HSC) under biaxial compression

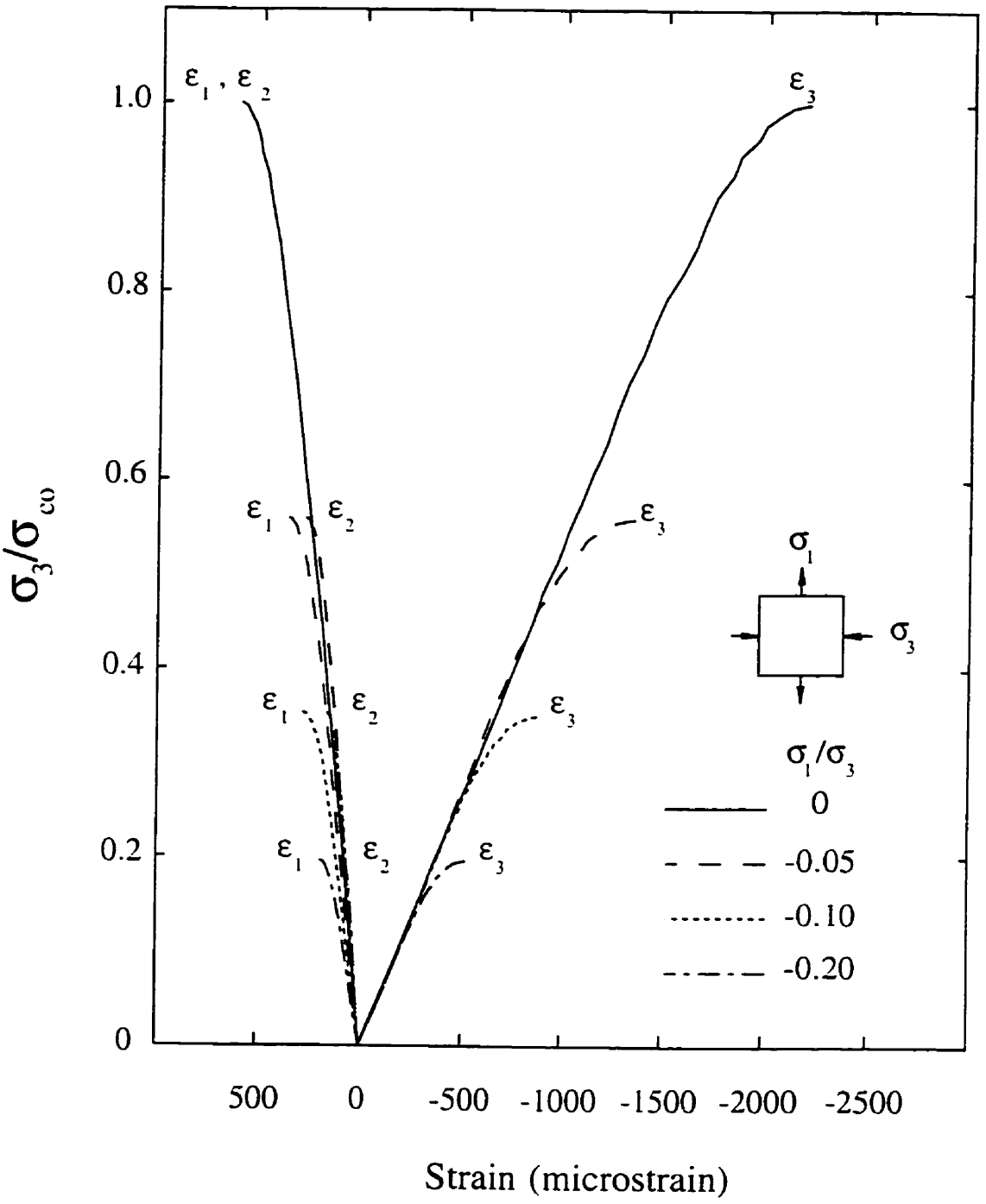

Figure 5.11: Stress-strain relationships for the high strength concrete mix (HSC) under combined tension and compression

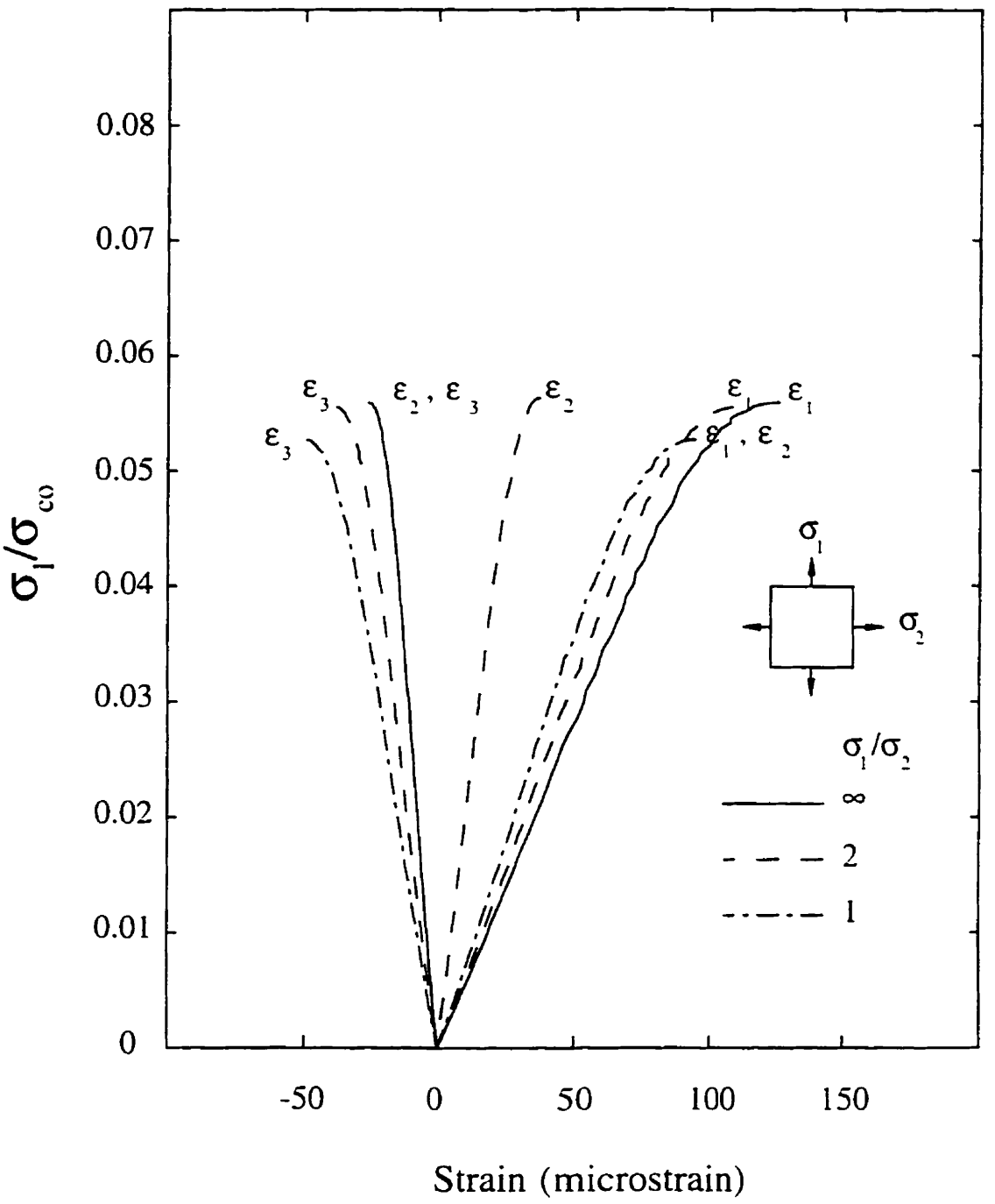

Figure 5.12: Stress-strain relationships for the high strength concrete mix (HSC) under biaxial tension

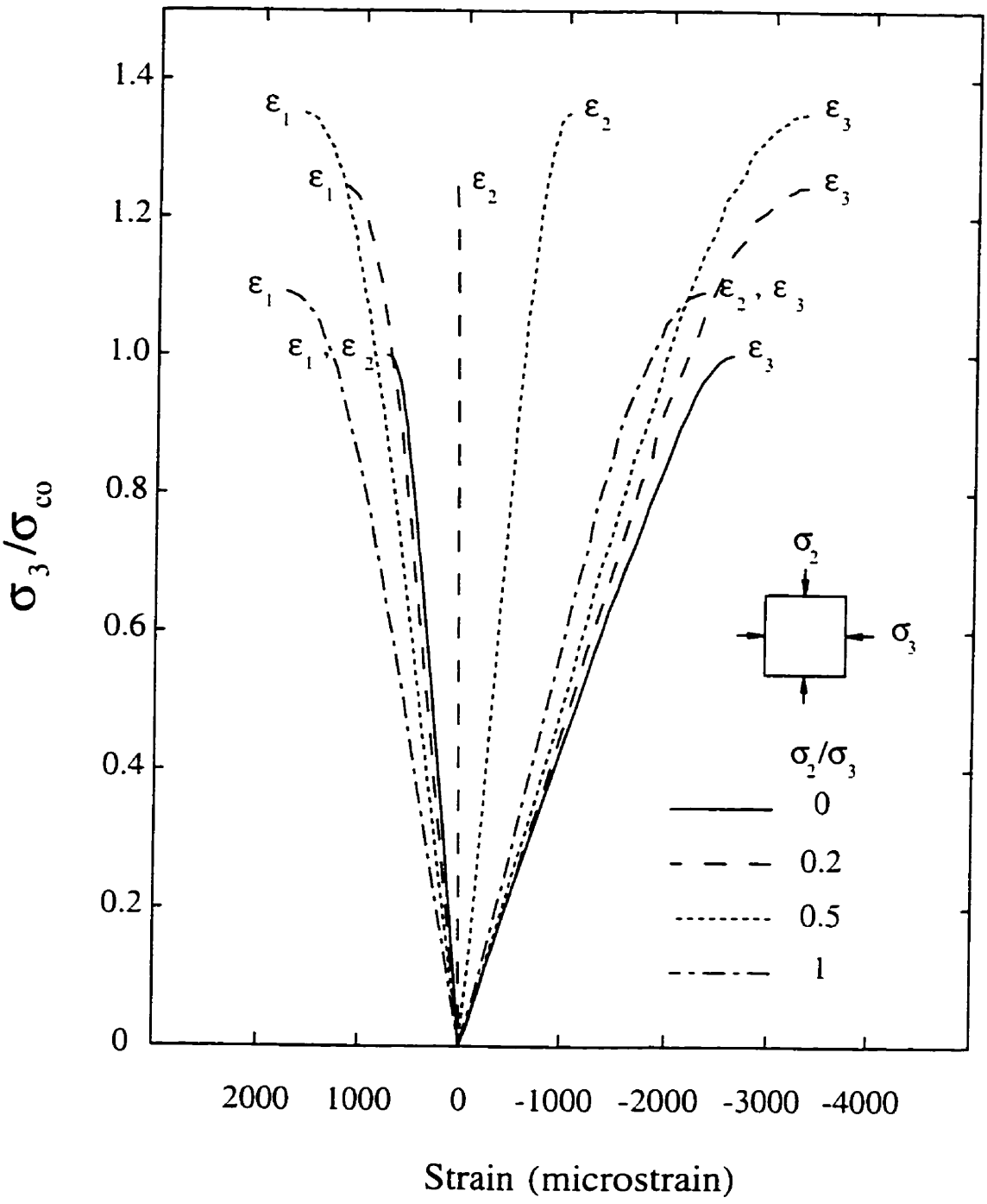

Figure 5.13: Stress-strain relationships for the high strength concrete mix (UHSC) under biaxial compression

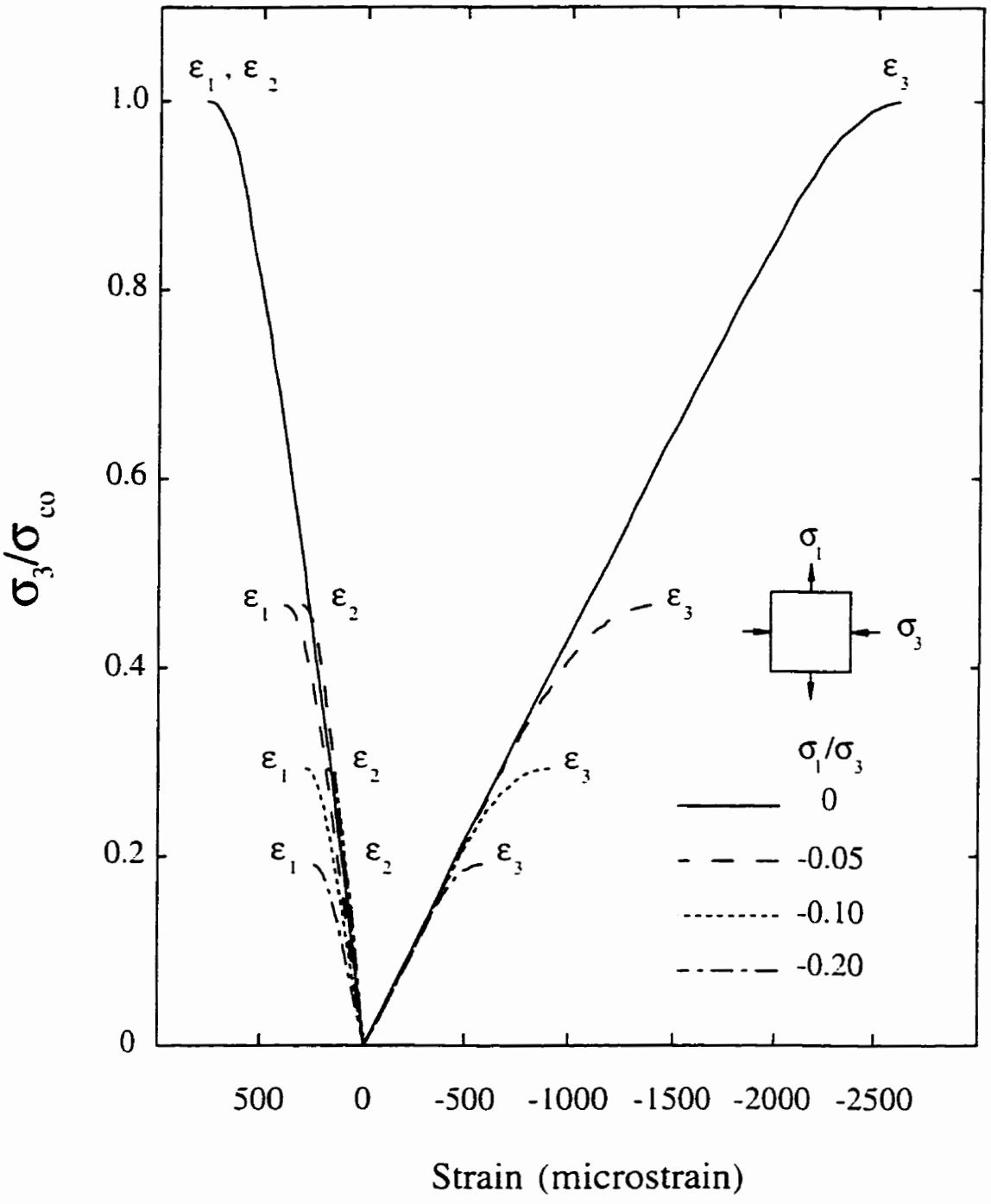

Figure 5.14: Stress-strain relationships for the high strength concrete mix (UHSC) under combined tension and compression

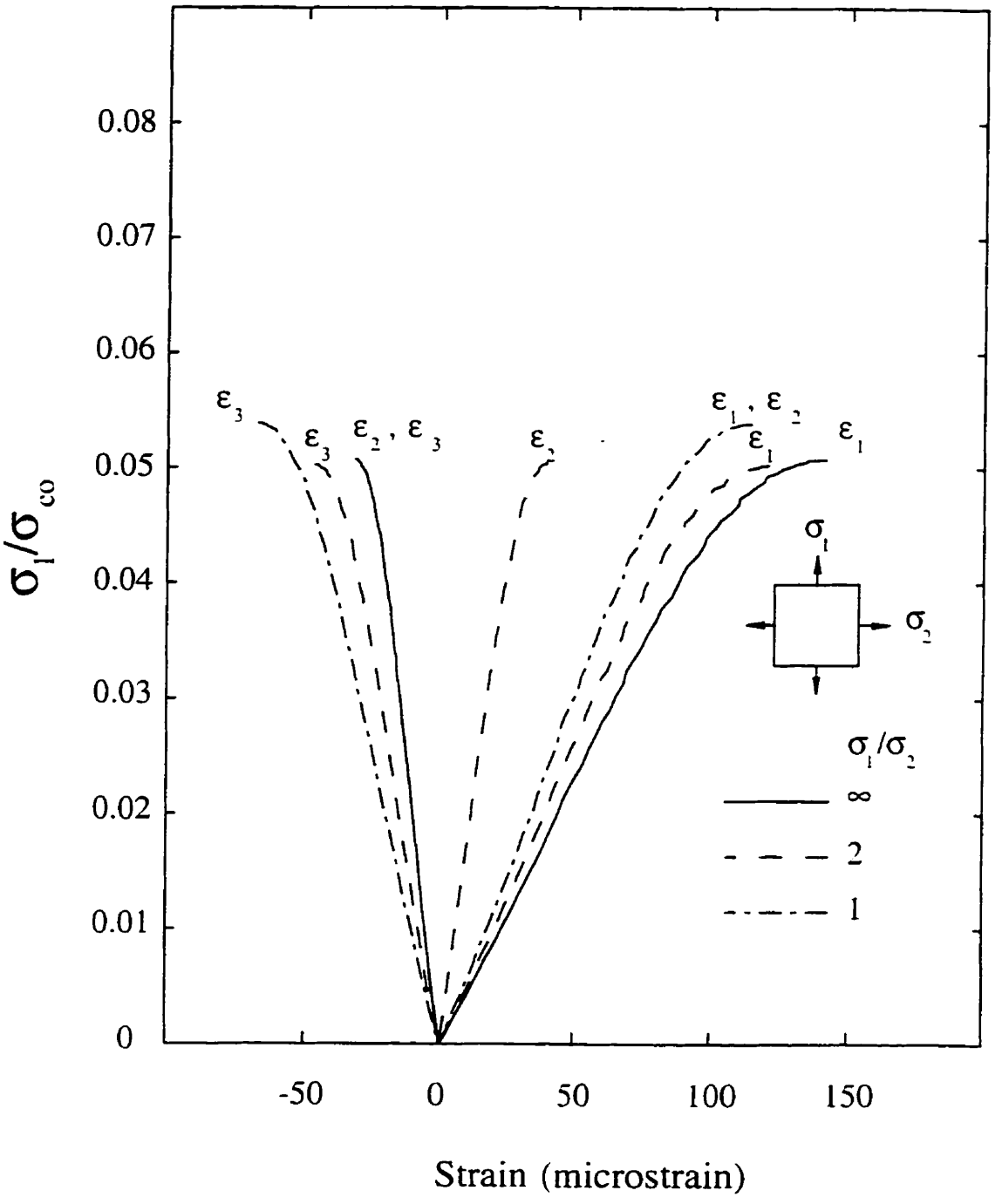

Figure 5.15: Stress-strain relationships for the high strength concrete mix (UHSC) under biaxial tension

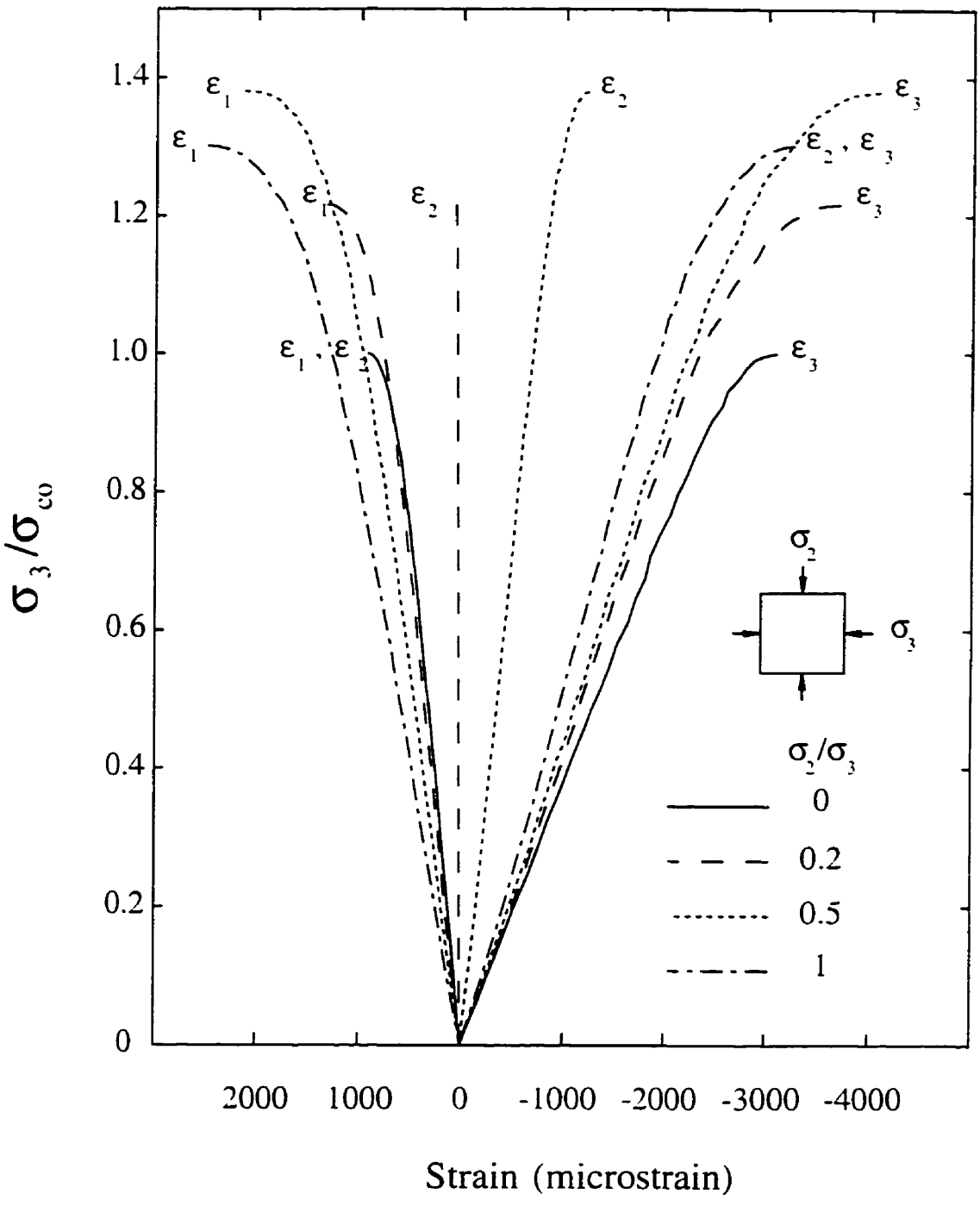

Figure 5.16: Stress-strain relationships for the light weight concrete mix (HSLWC) under biaxial compression

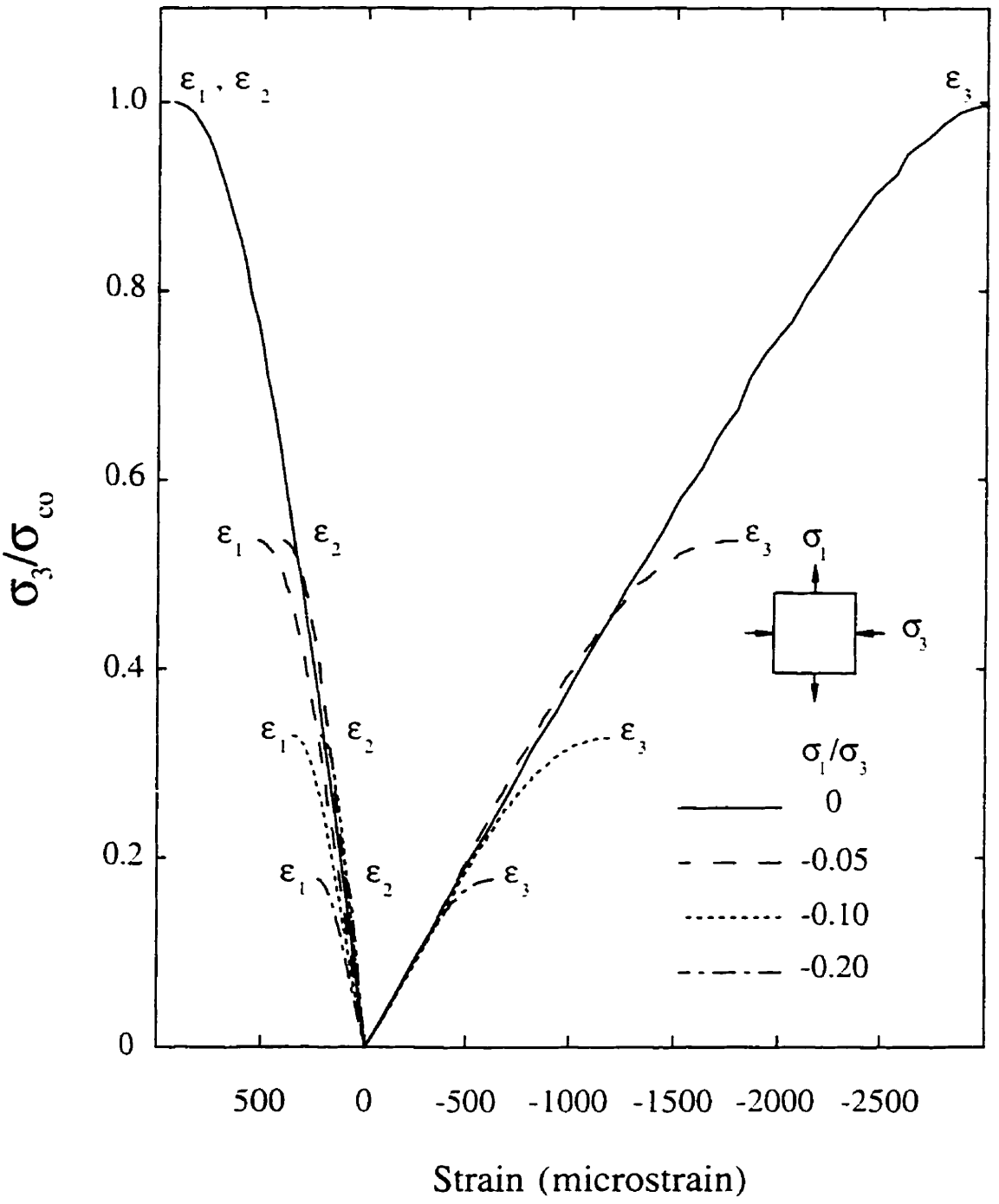

Figure 5.17: Stress-strain relationships for the light weight concrete mix (HSLWC) under combined tension and compression

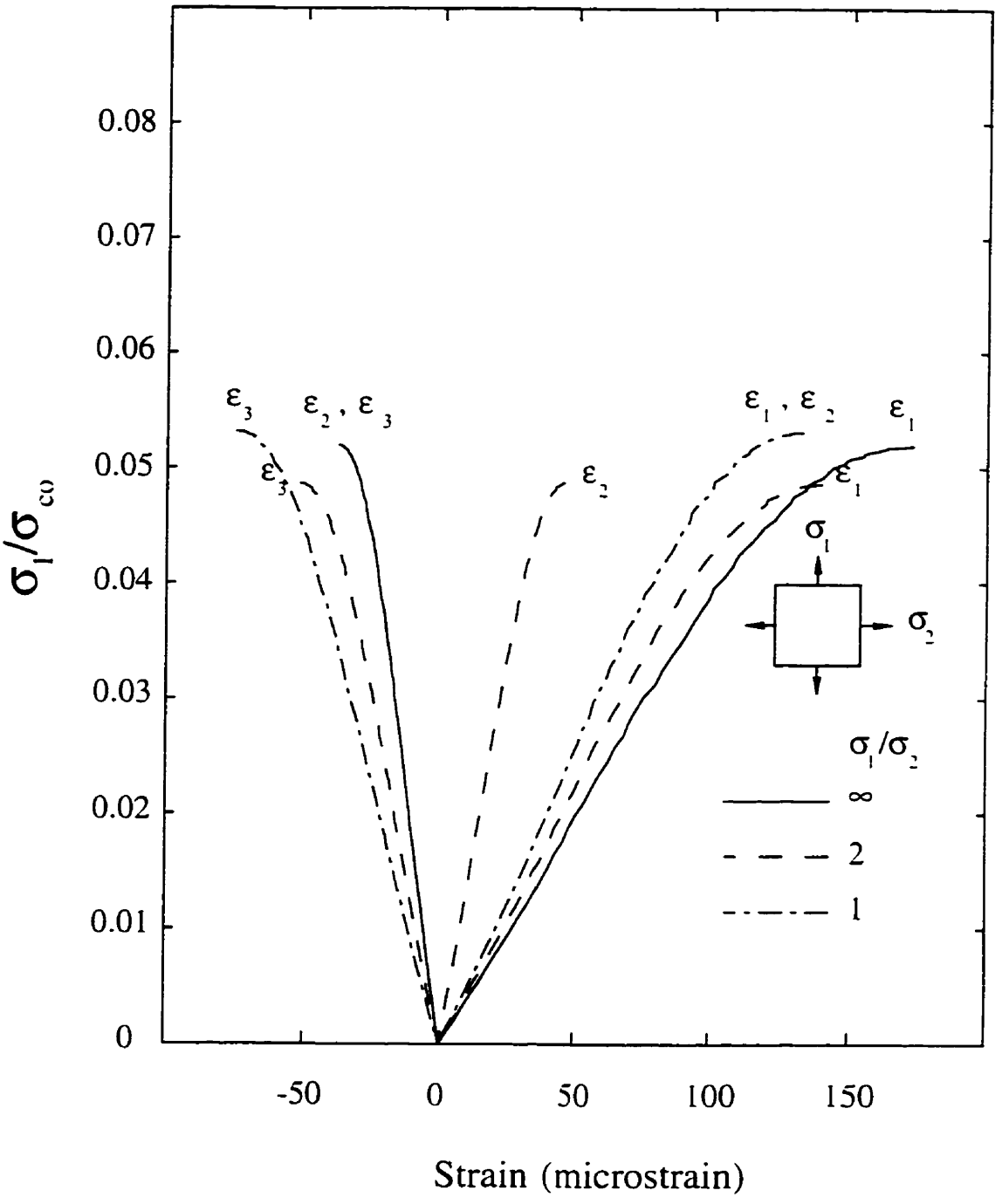

Figure 5.18: Stress-strain relationships for the light weight concrete mix (HSLWC) under biaxial tension

The average increase in stiffness under biaxial compression is higher for the HSC mix and less for the corresponding HSLWC specimen. This is due to the higher modulus of elasticity of the granite, and the lower modulus of elasticity of the light weight aggregates.

In biaxial compression-tension, the magnitude, at failure, of the principal compressive strain decrease as the tensile stress is applied.

Figurers 5.9, 5.12, 5.15 and 5.18 show the stress strain relationship of the different types of concrete under tension-tension stresses. In uniaxial tension, the principal strain ϵ_1 at failure was found to be 156, 126, 141, and 172 microstrain for the NSC, HSC, UHSC and HSLWC, respectively. In uniaxial and biaxial tension, the variation of the average value of the principal tensile strain at ultimate stress (ϵ_1) was not significant, for each individual mix, under different load combination. Note that the light weight aggregate concrete (HSLWC) had higher values than those of the corresponding HSC mix. It was noted that the material constants obtained in the experimental study were somewhat different in uniaxial compression and uniaxial tension for all the mixes. The modulus of elasticity, in uniaxial tension, was found to be 30, 42.6, 46, and 28.5 GPa, respectively. Those values are slightly higher than those in compression. This is in good agreement with previous research on high strength concrete [114].

The proportional limit values can be defined as the as the point at which the stress-strain curve deviates from linearity. In uniaxial compression, the high strength concrete specimens, HSC and UHSC showed a linear behaviour up to a higher stress than normal strength concrete. Also, HSC specimen showed a more linear behaviour than the corresponding HSLWC (Figs. 5.7 5.10 5.13, and 5.16).

Also, in biaxial compression, as the minor principal stress, σ_2, is increased, the

proportional limit is also increased. A major cause for the non-linearity of the stress strain curve for concrete is internal microcracking. The microcracks begin as bond cracks at the aggregate-mortar interface, and propagate through the mortar matrix to cause failure. A stress σ_2 preventing these microcracks from propagating, results in a stiffer, more linear stress strain response in the major principal direction. A manifestation of this explanation can be seen from the HSLWC specimen. It seems that the lightweight aggregates benefit from the confinement effects that occur in multiaxial stress conditions. The stress strain curves were more linear over a higher range as the confining stress was increased.

The behaviour of the concrete specimen was considered at the discontinuity level as well as at the ultimate strength. The discontinuity level represents the onset of major microcracking of concrete as defined by Newman [115] and used by Tasuji et al. [17] in interpreting the biaxial behaviour of normal strength concrete. It is apparently related to the beginning of extensive mortar cracking. For the uniaxial and biaxial compression tests, discontinuity was defined as the point at which the ratio of principal tensile strain to the principal compressive strain began to increase. For uniaxial compression, this is equivalent to the point at which Poisson's ratio started to increase. For biaxial tests involving direct tension, discontinuity was defined as the point at which the tensile strain began to deviate from linearity. Tasuji et al. [17] found that the discontinuity occurred at about 70 % of the ultimate load in uniaxial and biaxial compression tests; and at about 60 percent of the ultimate load in tests involving direct tension for normal strength concrete.

In the current study, no reasonable value could be obtained for the discontinuity level in tension. In fact, the results were quite scattered. On the other hand, the results of the compression specimens produced more reliable values for the dis-

continuity limit. Figure 5.19 shows a plot of Poisson's ratio versus applied stress for the different mixes under uniaxial loading. From this figure, the discontinuity limits can be estimated to be 70, 85, 90 and 76 percent for the NSC, HSC, UHSC and HSLWC, respectively. Close values were also obtained under different biaxial compression loading combinations and thus those values can be used as discontinuity levels for the different types of concrete.

It can be also seen from Fig 5.19 that the Poisson's-ratio curves were not almost vertical to a certain level. Thus a definitive value of Poisson's ratio could not obtained. Rather, an average value can be used. The scatter of the ratio of longitudinal to lateral stress were very large at the beginning of the loading and up to 10 % of the ultimate load.

5.3 Post-Peak Behaviour

In Section 2.2.4, the post peak response of a concrete cylinder was discussed in details as well as the results and recommendations of earlier research work. The conclusions reached were that compression failure was localized and that the measurements should be taken from the specimen's deformation; this type of measurement should be used as the feed back signal in order to obtain a stable post peak behaviour.

It should be noted that in multiaxial testing, the nature of the test prevents mounting any sensor, in a secure way, directly on the specimen. Thus, unfortunately, it is only possible to measure the global deformations, that is, platen to platen measurements. In biaxial testing, however, surface measurements, on the free surface of the specimen, can be attained. Still, those sensors are subjected to spalling and cracking of concrete. Thus they can not be used efficiently to produce a feedback signal in the post peak range. Also, unlike uniaxial loading, any loss of control that

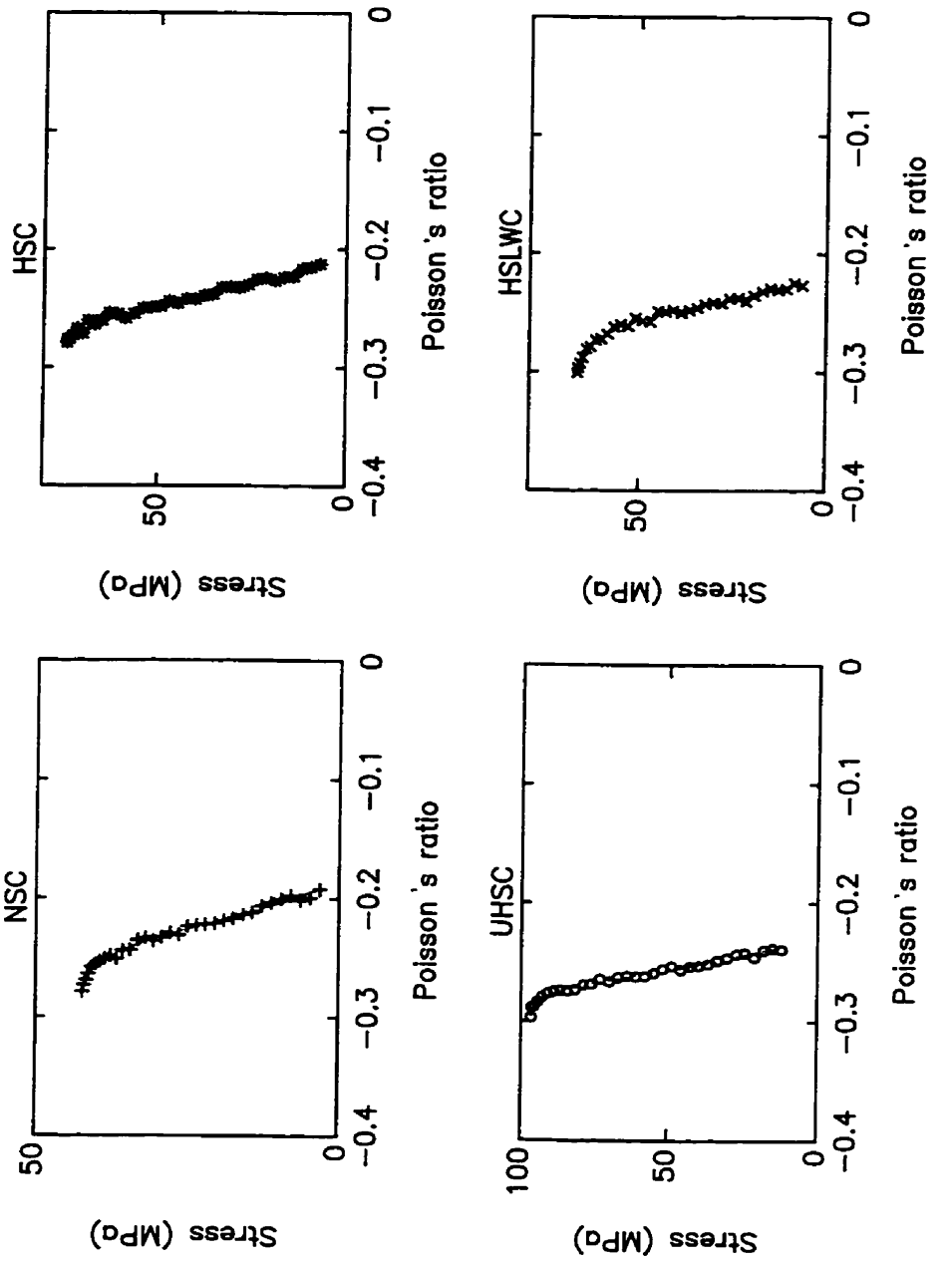

Figure 5.19: Poisson's ratio versus applied stress for the different types of concrete in uniaxial compression

may occur will damage the loading actuators as they could hit each other.

In the current research work, the control scheme (Section 4.1.6) was designed such that the main loading was carried out in closed-loop displacement control while the other loading was in closed-loop force control. The main objective of selecting such control scheme was to obtain the post-peak behaviour of the specimen. The results from a uniaxial compression test, for an NSC specimen is shown in Fig 5.20. The solid lines in this figure represent the stress-strain curve obtained from the overall LVDT-measurement (between the two opposite loading platens), while the dashed line is the stress-strain curve obtained from the surface strain measured by means of the extensometer mounted on the free surface of the specimen. The relative loading platen displacement was corrected for the total brush deformations from a calibration test on an aluminum specimen in the same manner that was suggested by van Mier [18].

From this figure, a considerable difference in post-peak behaviour, is observed when surface and platen-to-platen strains are compared. Just beyond peak, the surface strain increases at a lower rate when compared with the platen-to-platen strain. Eventually, the surface strain starts to decrease. The same behaviour was observed by van Mier [18] on cubic specimens tested with brush loading platens. van Mier concluded that unloading takes place in the outer layers of the specimen, and the residual carrying capacity (of the now highly fractured specimen) seems to be the result of the more or less intact core.

Another possible explanation is that the difference between the surface strain and the platen to platen strain is mainly a result of the load application system and disturbances at the specimen - load application interface. The use of brush platens causes bulging of the specimen free surfaces. This was observed through the use of proximity sensors and the use of strain gauges [18, 9]. This behaviour can

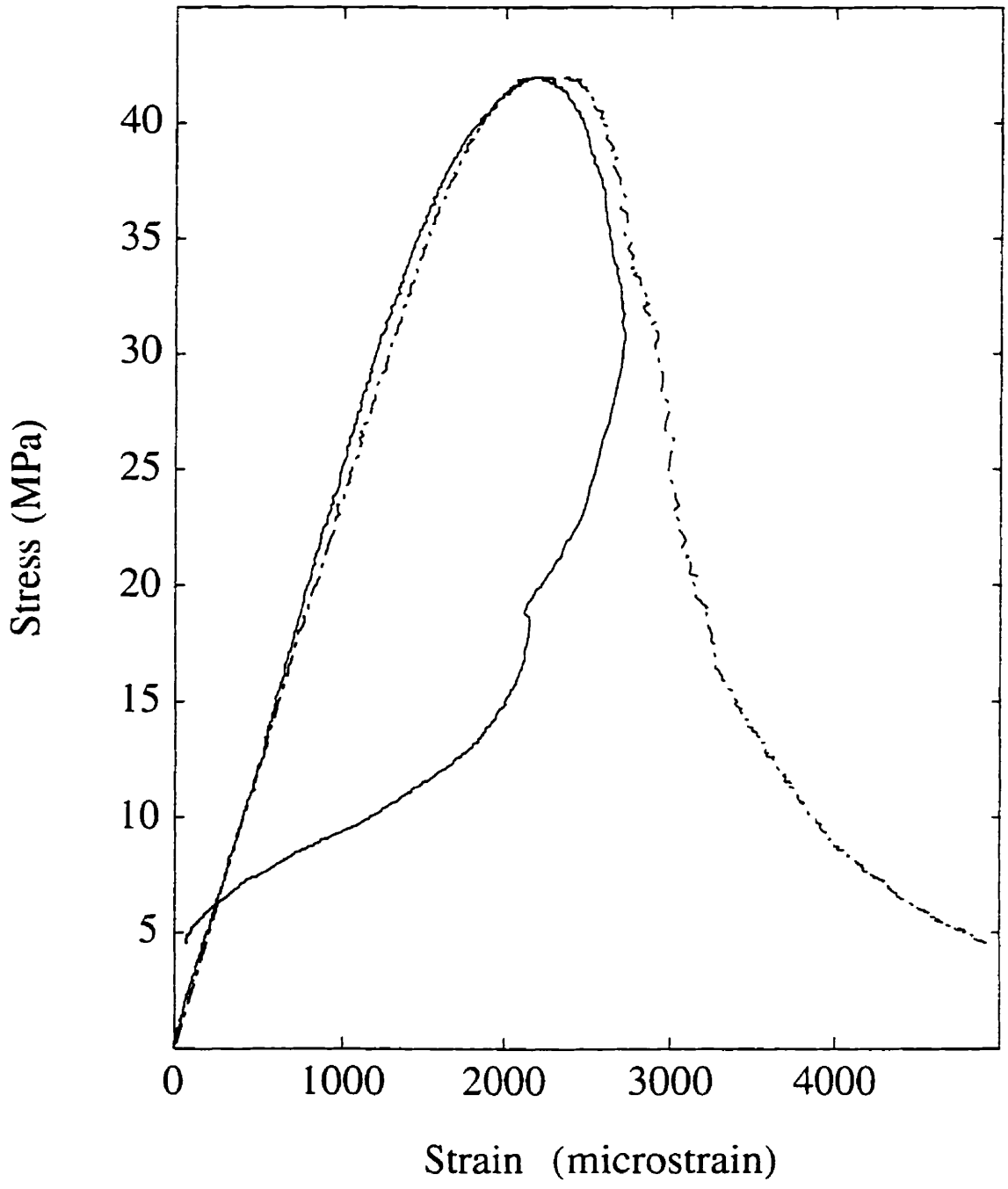

Figure 5.20: Uniaxial stress-strain curve (σ_1 - ϵ_1) for a typical NSC specimen. (- · - ·) platen to platen displacement and (- - -) extensometer

be attributed to the rotation of the brush rods. The lowest rotation occurs at the middle brush rod and the highest at the end rods. Thus, the use of brush platens will reduce the specimen-platen interaction but it will not completely eliminate it. Any global measurements can thus be considered as a structural behaviour rather than a material property. This is a serious issue that needs be addressed in future studies as the deformations of a triaxial specimen, either cube or cylinder, can be only measured globally (i.e. platen to platen movements). Hence, it is important to identify whether this measurements represents a material behaviour or a structural response as a result of the platen-specimen interaction. In the case of high strength concrete (HSC and UHSC), no descending portion was obtained from either measurements. However, the stresses did go slightly over the top. This could be attributed to the snap back phenomenon. This phenomenon was described in detail in Section 2.2.4.

In the biaxial compression-compression tests, it was observed that failure of the specimen was due to formation of tensile splitting cracks in a plane parallel to the unconfined planes of the specimen (refer to Section 5.4). Thus, in the unconfined direction, large lateral tensile strain occurred after the peak was reached. The test was controlled in the in-plane direction (direction of loading). Thus, it seems that the displacement control (in the principal direction) could not fully control the crack propagation in the unconfined direction and thus a complete descending portion could not be obtained. It seems that a feedback signal from the unconfined direction could result in a more stable behaviour. Nonetheless, due to the current configuration of the test set-up and the associated control methods, this type of control was very hard to achieve and it had to be abandoned.

In uniaxial tension tests, the descending portions of load deformation curves were recorded for a few specimens. However, replication of these tests showed that the

post peak behaviour had a large scatter. Also, the rate of success of those tests were very low. This can be attributed to the nature of the specimen as well as the control technique. The specimens can be classified as un-notched type. Thus a crack can start anywhere in the specimen. In the notched specimen, the crack is forced to proceed between the notched parts. With proper measurement device, such as LVDT or extensometer, the crack opening displacement can thus be used as a feedback signal to produce stable behaviour. Finally, the elastic component that is included in the platen to platen deformation is very high (refer to Section 6.6.2). Those factors hindered the production of a stable load-deformation curves. It should be noted here that an earlier experimental program on the behaviour of high strength concrete, under uniaxial tension, was successfully carried out at MUN [30]. Notched specimens were used and the crack opening displacement was used as a feedback signal.

Based on the above mentioned arguments, the recorded post-peak response of the specimen (platen to platen displacement) seems to represent more of a structural response rather than a material behaviour. Thus, it was decided to report the stress strain curves up to the peak loads only.

5.4 Failure Modes

The crack patterns and failure modes were observed for all the test specimens. In general, the failure modes observed in the high strength concrete (HSC and UHSC) and the high strength light weight (HSLWC) tests, were similar to those obtained for normal strength concrete (NSC). There was no fundamental difference in the crack patterns and failure modes due to the increase in the compressive strength of the concrete or due to the use of light weight aggregates under different biaxial loading combinations.

The crack patterns observed in the normal strength concrete specimens (NSC) were in good agreement with those obtained in previous investigations [14, 15, 16, 17, 18]. Under uniaxial compression, fracture of the specimens occurred by the formation of cracks that were inclined at an angle of 20 to 30 deg to the direction of the applied load and perpendicular to the larger unloaded surface of the specimen. This type of failure can be referred to as faulting failure [111] as opposed to the splitting type of failure (where the splitting occurs along the direction of loading). Figure 5.21 (a) shows photographs of the typical cracking patterns of an NSC specimen under uniaxial loading.

The high strength concrete specimens HSC and UHSC as well as the high strength light weight specimens HSLWC showed a splitting type of failure. The cracks were formed in a direction parallel to the applied load. Figures 5.21 show a typical specimen, at failure, under uniaxial compression for the different high strength concrete types.

Examination of the failure surfaces of normal strength concrete (NSC) specimens showed that no cracks passed directly through the coarse aggregate, the cracks passed through the mortar. The failure surfaces of the high strength specimens (HSC and UHSC) passed through some of the aggregates, with a larger portion of the failure surface passing through the coarse particles for the UHSC type. The failure surfaces of high strength light weight (HSLWC) specimens revealed that the cracks passed through the coarse aggregate and the mortar. It should be noted here that mix UHSC had a uniaxial compressive strength (f'_c) of 96 MPa. This value is close to the compressive strength of the coarse aggregate (crushed granite). Thus, a better compatibility of the strength and elastic properties between the mortar and the coarse aggregate is achieved. This, in turn, leads to a more homogeneous-type of behaviour

and influences the cracks to pass through the aggregate as well as the mortar.

Under biaxial compression, and at the low stress ratio of 0.2, the specimen showed formation of microcracks parallel to the free surface of the specimen. However, failure occurred by the formation of a major crack that had an angle of 18 - 25 deg to the free surfaces of the specimen. This failure mode was observed for all the different types of concrete (Fig 5.22).

For the specimens subjected to biaxial compression ratios of 0.5 and 1, failure progressed due to tensile splitting cracks that occurred along the direction of loading and in a plane parallel to the free surfaces of the specimen ($\sigma_1 - \sigma_2$ plane). It was also observed that the light weight aggregate specimen HSLWC developed more microcracks along the loaded surfaces and parallel to the loaded surfaces of the specimen than in the case of normal weight specimen Figure 5.23 show the failure modes for the different types of concrete under equal biaxial compression.

The tests under combined compression and tension revealed that only one continuous crack normal to the principal tensile stress was formed. However, for the smaller ratio of tension to compression (σ_1/σ_3 = - 0.05), several cracks were observed, in the direction of compressive loading, before failure for the NSC specimen. The high strength specimen showed a somewhat different behaviour. Failure always occurred with one crack normal to the principal tensile stress at such small stress ratio of σ_1/σ_3 = - 0.05. Figure 5.24 shows the failure modes for some of the concrete specimen under combined compression and tension.

Under uniaxial tension, fracture of the specimen and failure occurred by the formation of a single crack perpendicular to the direction of loading and normal to the plane of the specimen. Examination of the failure surfaces of the test specimens for the concrete type NSC showed there were no cracks that passed directly through

the coarse aggregate. The fracture surface of the HSC and UHSC specimen showed that failure surface progressed through some coarse aggregates. A crude comparison between the failures surface in uniaxial tension and uniaxial compression indicated that the percentage of broken aggregates were higher in tension than in compression. Inspection of the failure surfaces of high strength light weight (HSLWC) specimens revealed that the cracks passed through the coarse aggregate as well as the mortar. Figure 5.25 shows the failure modes for some of the concrete specimen under uniaxial tension.

Under biaxial tension loading, a single crack was formed in a direction normal to the unloaded surface of the specimen and perpendicular to the maximum principal stresses. In the case of equal biaxial tension, there was no preferred direction for the fracture surface and the cracks were always normal to the unloaded surface.

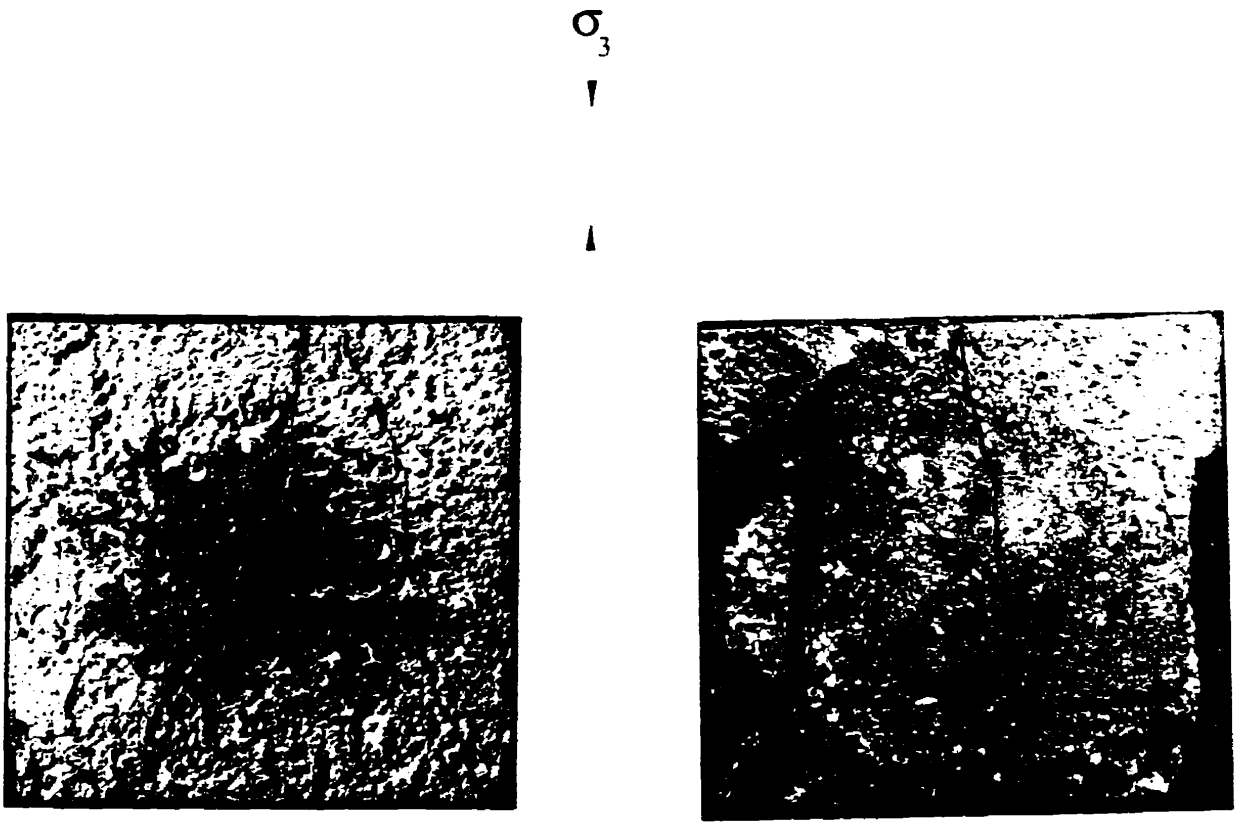

Figure 5.21: Failure modes of specimens subjected to uniaxial compression

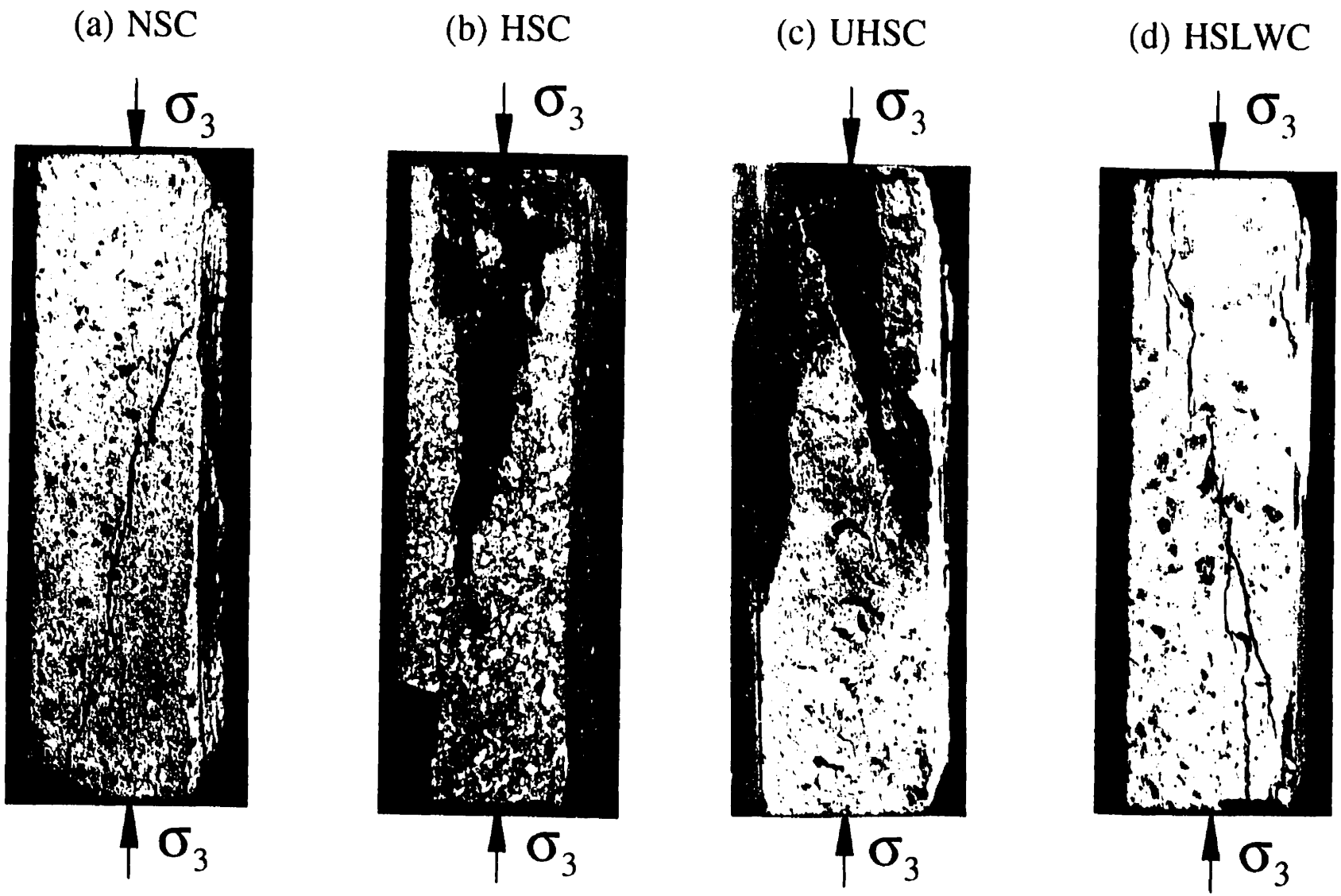

Figure 5.22: Failure modes of specimens subjected to biaxial compression stresses $\sigma_2/\sigma_3 = 0.20$

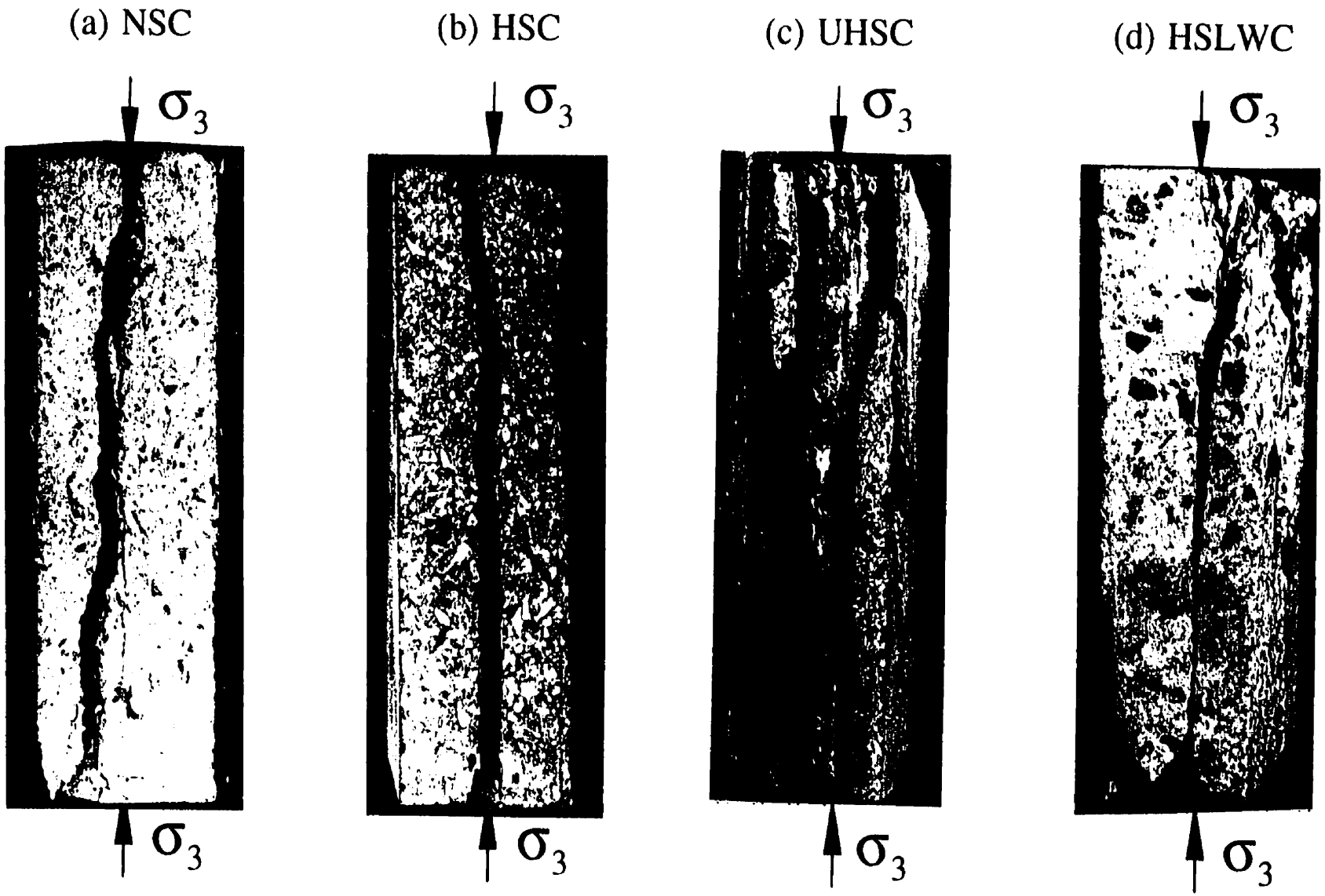

Figure 5.23: Failure modes of specimens subjected to biaxial compression stresses $\sigma_2/\sigma_3 = 1.0$

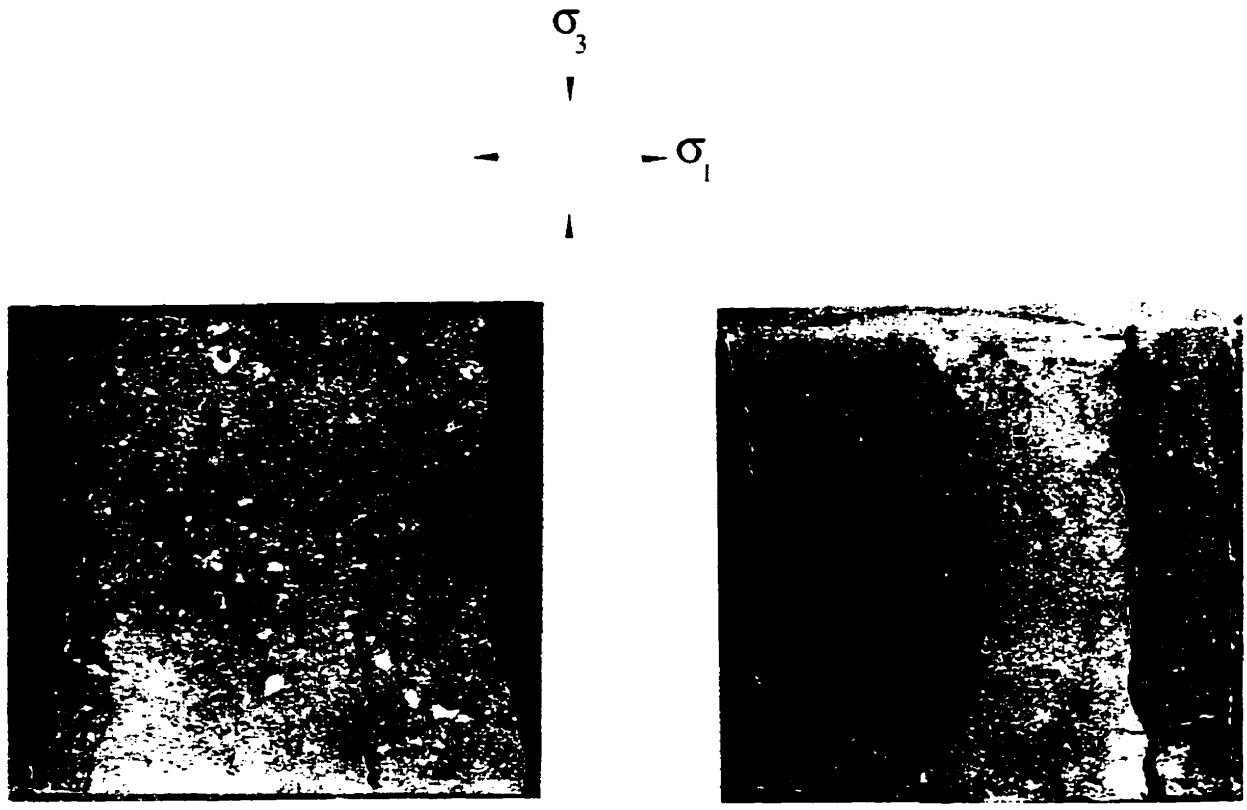

(a) HSC

(b) UHSC

(c) HSLWC

Figure 5.24: Failure modes of specimens subjected to combined tension and compression (σ_3 / σ_1 = -1/0.10)

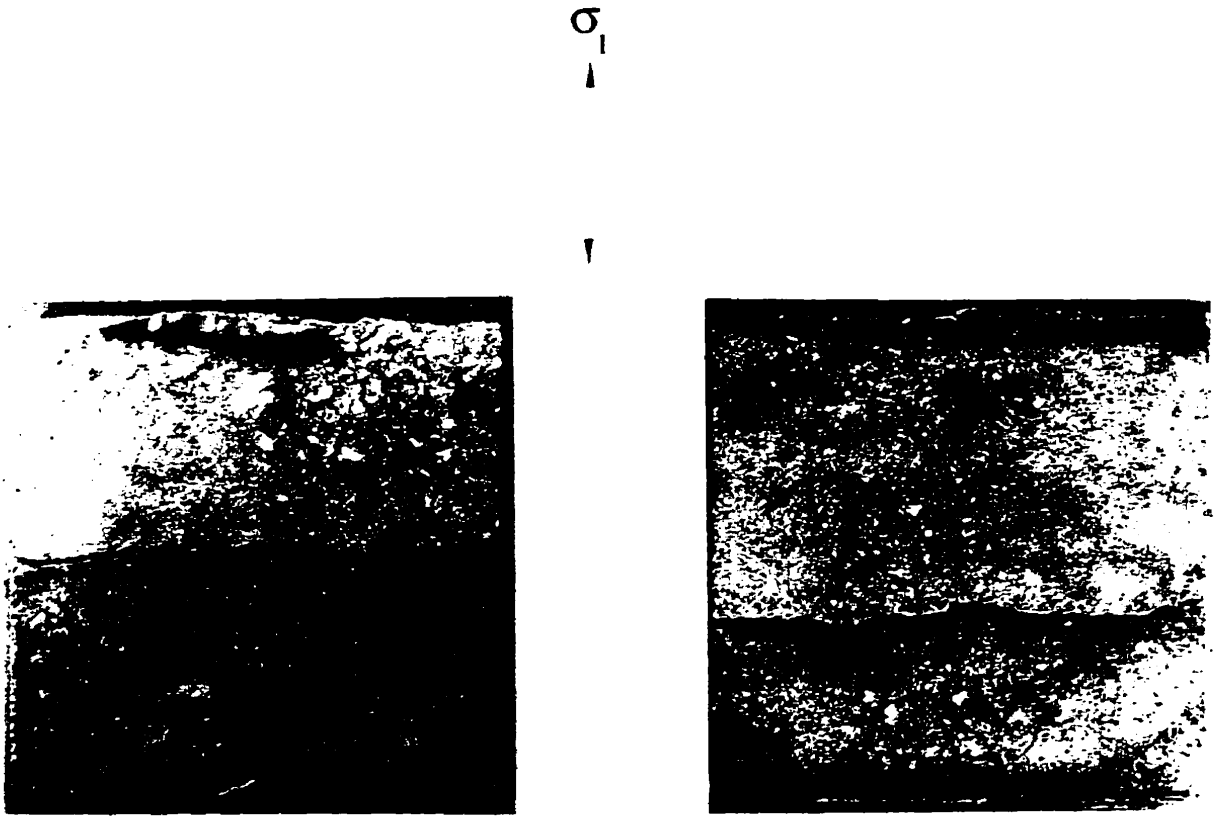

(a) HSC

(b) UHSC

(c) HSLWC

Figure 5.25: Failure modes of specimens subjected to uniaxial tension

Chapter 6

A Constitutive Model for High Strength Concrete

In this chapter, a constitutive model is adopted and modified for high strength concrete application. A brief description of the model is presented. The implementation of the model in a general purpose finite element program is described. Finally, the calibration of the model and the verification are reported.

6.1 A Fracture-Energy-Based Plasticity Model

The adopted constitutive model for high-strength concrete is based on Etse and Willam [71] model. This particular model was chosen because it possesses characteristics that makes it attractive for use with finite element analysis. The model uses a unified formulation for both tension and compression. A non-associated plastic flow is used to account for the volume changes. This gives the model added flexibility and allows a better fit of concrete behaviour. The strain-softening concept is included for concrete in tension and compression. The model allows a realistic and comprehensive representation of various aspects of concrete behaviour. In particular, the model has the ability to fit the group of uniaxial, biaxial, and triaxial test data.

The model utilises the Extended Leon Model that combines the Leon-Pramono

description (Pramono and Willam [70]) with the five parameter model (Willam and Warnke [116]) using the Haigh-Westergaard stress coordinates. The following items characterize the concrete model which are further presented in the subsequent sections

- The **yield surface** is based on the original work by Leon [88]. This model combines the two-parameters Mohr-Coulomb friction law and the one-parameter tension cut-off condition of Rankine. The continuity between the two yield criteria is enforced.

- The **hardening behaviour** is modeled by an isotropic growth of the yield surface in the pre-peak regime. This growth is controlled by the amount of plastic work. The yield surface which grows isotropically, will reach the failure envelope whenever the peak strength is reached.

- The **softening behaviour** is modelled by an isotropic decrease of the yield surface using the fracture mechanics approach. The softening regime is initiated, when the stress path reaches the failure envelope in tension or low confined compression below the transition point of ductile fracture. In that case, the material can no longer be assumed intact and the de-cohesion parameter controls the degradation of tensile strength.

- The **non-associated flow** is modeled by a plastic potential function that differs from the yield surface by an hydrostatic component.

In the following sections, the above-mentioned concepts are presented. It should be noted that the development of the Etse and Willam model [71] occurred gradually over the years at the University of Colorado. The Leon model was first used by Willam, Hurlbut and Sture [89] to characterize the triaxial test data of medium strength concrete. Subsequently, it was extended by Pramono and Willam [70] to

formulate an elasto-plastic constitutive model for hardening and softening behaviour of concrete when subjected to arbitrary triaxial loading. The model was further extended by Etse and Willam [71] to compose the Extended Leon model. The following presentation is largely based on these publications. The necessary procedures followed in adapting the model to high-strength concrete are introduced and the finite element implementation is then discussed at the end of the chapter.

6.2 Leon's Triaxial Strength Failure Criterion

The failure criterion proposed by Leon (Romano [88]) was proposed originally for the shear strength of concrete under combined tension-compression. This failure criteria is also widely used in the field of rock mechanics, where it is known under the names of Hoek and Brown [117]). This strength formula combines the two-parameter Mohr-Coulomb friction law and the one-parameter tension cut-off condition of Rankine. The isotropic failure criterion is conveniently expressed in terms of the major, and minor principal stresses, σ_1 and σ_3, respectively, as:

$$F(\sigma_1, \sigma_3) = \left(\frac{\sigma_1 - \sigma_3}{f'_c}\right)^2 + m_0 \frac{\sigma_1}{f'_c} - c_0 = 0 \tag{6.1}$$

The influence of the intermediate principal stress, σ_2, is omitted, similar to the Tresca and Coulomb conditions of maximum shear.

The triaxial failure criteria in Eq. (6.1) is characterized by the uniaxial compressive strength f'_c, the frictional parameter m_0, and the cohesion parameter c_0. At ultimate strength, c_0 has a value of 1.

The friction parameter m_0 is calibrated in terms of the uniaxial tensile strength, f'_t, due to the importance of that parameter and its role in the fracture energy for-

mulation. A uniaxial state of stress ($\sigma_3 = 0$, and $\sigma_1 = f_t'$) results in

$$m_0 = \frac{f_c'^2 - f_t'^2}{f_c' f_t'} \tag{6.2}$$

The triaxial failure surface proposed by Leon was used by Pramono and Willam [70] and is depicted in Fig 6.1. This figure shows the main disadvantage of Pramono and Willam [70] failure criteria of having corners in the deviatoric trace. The corners complicate the numerical implementation and oversimplify the failure envelope because of their lack of dependence on the intermediate principal stress.

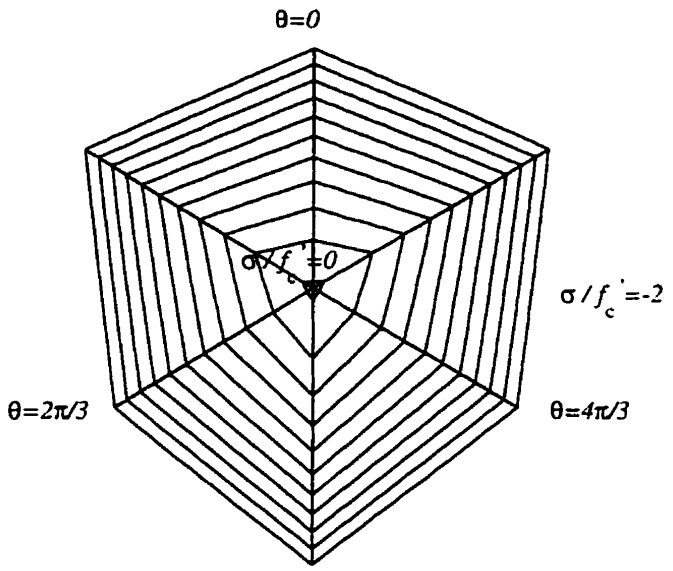

Figure 6.1: Triaxial failure envelope, deviatoric sections, of the Pramono and Willam model [70])

6.3 Extended Leon's Triaxial Strength Failure Criterion

The Extended Leon Model (ELM) combines the Leon-Pramono characterization (Pramono and Willam [70]) with the five parameter model (Willam and Warnke [116]). That produces an elliptical approximation of the failure surface. Consequently, the corners in the deviatoric trace are eliminated and a C^1-continuous failure surface is produced.

Using the three scalar invariants σ, the mean normal stress, ρ, the deviatoric stress, and the polar angle θ, where

$$\sigma = \frac{I_1}{3} \tag{6.3}$$

$$\rho = \sqrt{2J_2} \tag{6.4}$$

$$\cos 3\theta = \frac{\sqrt{27}J_3}{2J_2^{\frac{3}{2}}} \tag{6.5}$$

the relationship between the principal stresses and the Haigh-Westergaard coordinates can be given by:

$$\begin{Bmatrix} \sigma_1 \\ \sigma_2 \\ \sigma_3 \end{Bmatrix} = \sigma \begin{Bmatrix} 1 \\ 1 \\ 1 \end{Bmatrix} + \sqrt{\frac{2}{3}}\rho \begin{Bmatrix} \cos\theta \\ \cos(\theta - \frac{2\pi}{3}) \\ \cos(\theta + \frac{2\pi}{3}) \end{Bmatrix} \tag{6.6}$$

this relationship is valid for $0 \leq \theta \leq \frac{\pi}{3}$ and consequently for $\sigma_1 \geq \sigma_2 \geq \sigma_3$. Substituting the principal stresses into Eq. (6.1) leads to

$$F(\sigma, \rho, \theta) = \left[\sqrt{2}\frac{\rho}{f'_c}\sin(\theta + \frac{\pi}{3})\right]^2 + m_0\left[\sqrt{\frac{2}{3}}\frac{\rho}{f'_c}\cos\theta + \frac{\sigma}{f'_c}\right] - c_0 = 0 \tag{6.7}$$

In order to remove the corners, in the deviatoric section, from the Leon's model, the following approximations are introduced into Eq. (6.7)

$$\begin{aligned} \sqrt{2}\sin(\theta + \frac{\pi}{3}) &\approx \sqrt{1.5}\, r(\theta) \\ \sqrt{\frac{2}{3}}\cos(\theta) &\approx \sqrt{\frac{1}{6}}\, r(\theta) \end{aligned} \tag{6.8}$$

This leads to the failure criteria of the ELM with a C^1-continuous failure surface.

$$F(\sigma, \rho, \theta) = \frac{3}{2}\left[\frac{\rho r(\theta)}{f_c'}\right]^2 + \frac{m_0}{f_c'}\left[\sigma + \frac{\rho r(\theta)}{\sqrt{6}}\right] - c_0 = 0 \tag{6.9}$$

The elliptic variation of the five parameter model by Willam and Warnke [116], $r(\theta)$, is given by Eq. (6.10). Note that the yield surface is a function of the three scalar invariants σ, the mean normal stress, ρ, the deviatoric stress, and the polar angle θ.

The elliptic variation of the five parameter model $r(\theta)$ is given by the following equation

$$r(\theta) = \frac{4(1-e^2)\cos^2\theta + (2e-1)^2}{2(1-e^2\cos(\theta) + (2e-1)\sqrt{4(1-e^2\cos^2\theta + 5e^2 - 4e}} \tag{6.10}$$

where the eccentricity e is defined by the ratio ρ_t/ρ_c. The values of ρ_t and ρ_c can be found by considering the tensile ($\theta = 0$), and compressive meridians ($\theta = \pi/3$) in Eq. (6.9), respectively.

The deviatoric view of the ELM is shown in Fig 6.2. Figure 6.3 shows the original Leon model and the ELM failure criteria in the principal stress plane σ_1 - σ_2 for the plane stress case. The elliptic variation of the deviatoric strength includes the effect of the intermediate principal stress,σ_2, and thus a C^1-continuous curvilinear trace is observed in the ELM. A highly idealized polygonal shape of the failure envelope is observed in the original Leon model as the effect of intermediate principal stress is not included.

The friction parameter, m_0, for the original Leon model can be calculated from Eq. (6.2). In order to calculate m_0 for the ELM, the uniaxial state of stress ($\sigma_3 = 0$, and $\sigma_1 = f_t'$) is used again

$$m_0 = 3\frac{1}{e(e+1)}\frac{f_c'^2 e^2 - f_t'^2}{f_c' f_t'} \tag{6.11}$$

From this equation it is clear that m_0 is not coupled from the stress function as it includes a term with the eccentricity e. In order to overcome this shortcoming, the

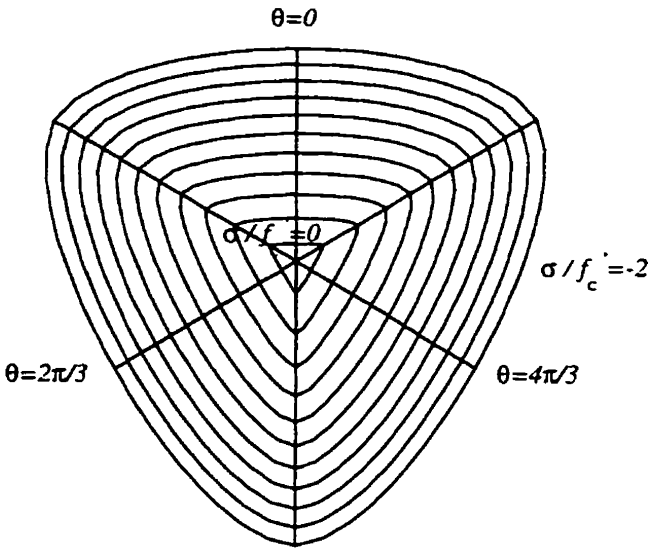

Figure 6.2: Deviatoric View of the ELM [71]

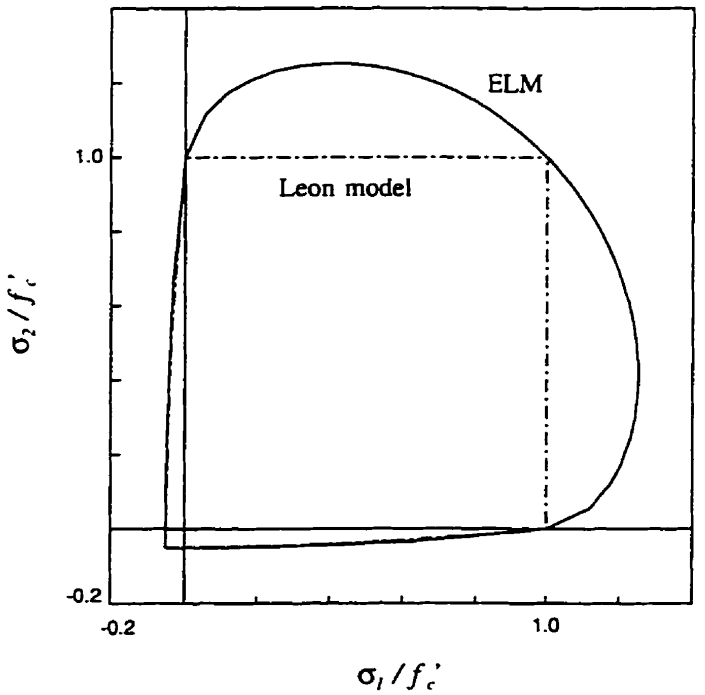

Figure 6.3: Plane stress sections of smooth (ELM) and polygonal (Leon) failure envelopes

friction parameter of the original Leon model is used. Consequently, the meridional sections (at $\theta = 0$ and at $\theta = \pi/3$) will be identical for both the Leon and the ELM models.

The comparison between the experimental data and the failure criteria, for the original Leon model, was carried out by Pramono an Willam [70] for the various data available in the literature. Another verification, for the original Leon model, was done by Xie et al. [90] for high strength concrete using the triaxial test results obtained from their experimental program. Both comparisons indicated good agreement between the model and the triaxial test data.

The ELM model was verified against the biaxial test data obtained from the current study. Figure 6.4 shows the verification along the compression meridians ($\theta = 0$) and the tension meridians ($\theta = \pi/3$) for the three types of concrete (NSC, HSC and UHSC).

6.4 Isotropic Hardening Model for Pre-Peak Behaviour

The hardening rule defines the motion of the subsequent yield surfaces during plastic loading. The expansion of the yield surface is called hardening, conversely a contracting yield surface denotes softening, and a stationary yield surface designates perfect plasticity.

A number of hardening rules have been proposed such as isotropic hardening, kinematic hardening, and mixed hardening rules (Chen [49]). Among these three hardening rules, the assumption of isotropic hardening is the simplest one to formulate mathematically, and it is used in this model. Isotropic rule requires only one parameter κ to define the subsequent yield surface after plastic deformation oc-

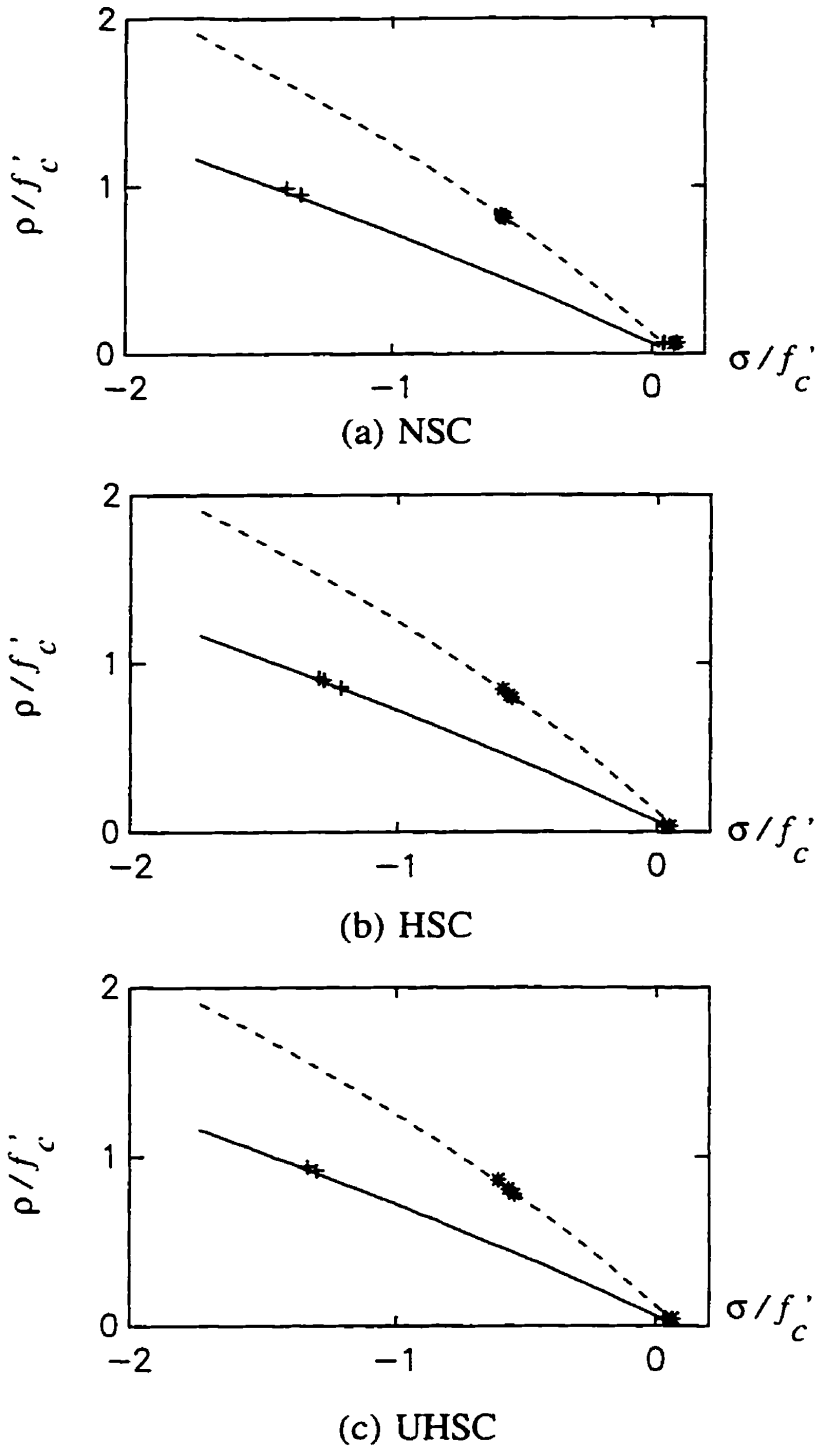

Figure 6.4: Comparison of the model with the current biaxial test data: (*) test data along the compressive meridians of the ELM (- - -), and (+) test data along the tensile meridians of the ELM (——)

curs. This hardening rule assumes that the yield surface expands uniformly without distortion as plastic deformation occurs.

It should be noted that Bauschinger effect cannot be modelled by the isotropic hardening rule. Nevertheless, under the monotonic loading condition, the Bauschinger effect is not crucial as in situations where reverse loading takes place. As a consequence, the isotropic hardening rule is adequate in modelling the behaviour of concrete under monotonic loading conditions.

The isotropic hardening mechanism involves, in this case, an initial loading surface that expands uniformly when a hardening parameter, k, increases monotonic from an initial value $k = k_0 > 0$ to a final value at peak $k = k_p = 1$

$$F(\boldsymbol{\sigma}, \rho, \theta, k, c) = \left\{(1-k)\left[\frac{\boldsymbol{\sigma}}{f_c'} + \frac{\rho r(\theta)}{\sqrt{6} f_c'}\right]^2 + \sqrt{\frac{3}{2}}\right\}^2 + \frac{k^2 m}{f_c'}\left[\sigma + \frac{\rho r(\theta)}{\sqrt{6}}\right] - k^2 c = 0 \tag{6.12}$$

Different loading stages in a meridian plane, for the UHSC mix, are depicted in Fig 6.5.

The constitutive model assumes that the material is initially isotropic and remains isotropic during the entire deformation history irrespective of the orientation and magnitude of the principal stress components and inelastic deformations. The total strain increment can thus be decomposed into independent elastic and plastic components

$$d\epsilon = d\epsilon_e + d\epsilon_p \tag{6.13}$$

where $d\epsilon$ is the total mechanical strain rate, $d\epsilon_e$ is the elastic strain rate and $d\epsilon_p$ is the plastic strain rate. The elastic or recoverable response is governed by the linear isotropic material operator E

$$d\sigma = E d\epsilon_e \tag{6.14}$$

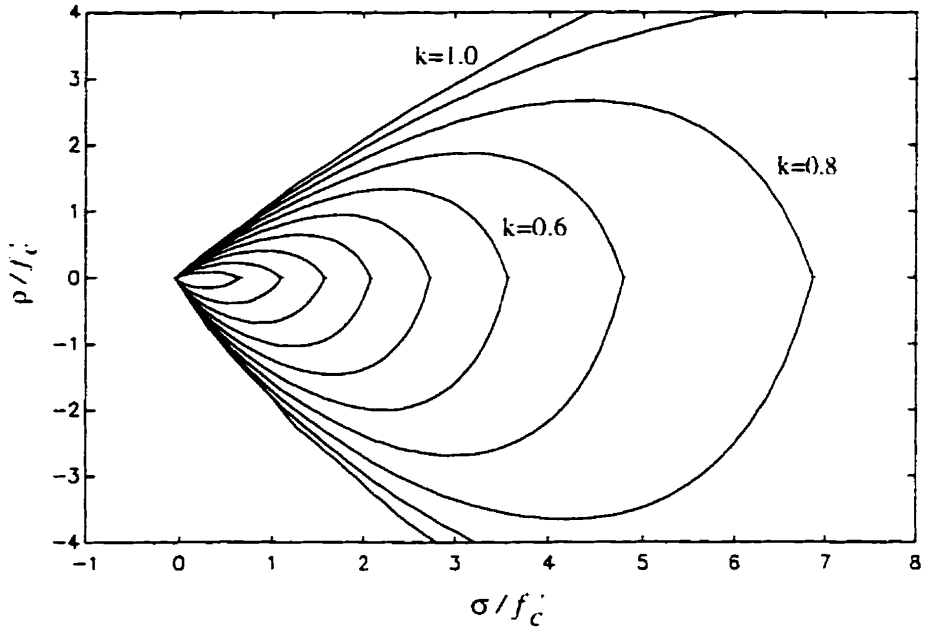

Figure 6.5: Loading surface of isotropic hardening model

6.5 Nonlinear Hardening Response

The strain-hardening hypothesis describes the current state of the inelastic deformation process in terms of a scalar-valued kinematic variable, ε_p, which defines the length of the plastic strain trajectory. During progressive plastic deformations, the value of the hardening parameter increases according to an elliptical function of ε_p. The influence of confinement on the rate of hardening is introduced in terms of a ductility measure χ_p, which defines the accumulated plastic strain at peak in terms of the lateral confinement. As a result, the hardening parameter $k = k(\varepsilon_p, \chi_p)$ is expressed as a monotonically increasing elliptic function of the plastic strain:

$$k = k_0 + \frac{1 + k}{\varepsilon_p}\sqrt{2\varepsilon_p\chi_p - \varepsilon_p^2} \tag{6.15}$$

The equivalent plastic strain rate is defined as the Euclidean norm of the plastic

strain increment:

$$d\bar{\varepsilon}_p = \sqrt{d\bar{\epsilon}_p^T . d\bar{\epsilon}_p} \tag{6.16}$$

where $d\bar{\epsilon}_p$ is the vector of principal plastic strain increments. The ductility measure γ_p introduces the effect of confining pressure on the rate of hardening in terms of a quadratic polynomial of the mean normal stress, σ.

$$\gamma_p = \gamma_p(\sigma) = A_h \left(\frac{\sigma}{f_c'}\right)^2 + B_h \left(\frac{\sigma}{f_c'}\right) + C_h \tag{6.17}$$

The ductility parameters A_h, B_h and C_h are dimensionless deformation parameters that are calibrated from laboratory experiments.

6.6 Nonassociated Flow

When the concrete deforms plastically, it is convenient to assume that, based on the normality condition, the incremental plastic strain, $d\epsilon_p$, can be related to a plastic potential function, Q, by the following equation

$$d\epsilon_p = d\lambda \mathbf{m} = d\lambda \frac{\partial Q}{\partial \sigma} \tag{6.18}$$

where $d\lambda$ is a plastic multiplier, and it is a positive scalar factor that may vary through the hardening process. It has a non-zero value only when plastic deformation occurs. The gradient of the potential surface, $\mathbf{m} = \partial Q/\partial\sigma$, defines the direction of the incremental plastic strain vector $d\epsilon_p$, and the length is determined by the factor $d\lambda$. Because the vector $\partial Q/\partial\sigma$ is normal to the potential surface, the plastic strain is also normal to the surface defined by the plastic potential function Q. This condition is referred to as the normality law. In the simplest case when the plastic potential function and the yield function coincide ($Q = F$), then

$$d\epsilon_p = d\lambda \frac{\partial F}{\partial \sigma} = d\lambda \frac{\partial Q}{\partial \sigma} \tag{6.19}$$

this is called the associated flow rule because the incremental plastic strains are associated with the yield function. If $Q \neq F$, Eq. (6.19) is termed a nonassociated flow rule.

Use of the associated flow rule has been implemented in concrete material models by many investigators [50]. For pressure-sensitive materials, it is widely accepted that the use of an associated flow results in the prediction of too much dilatancy (Vermeer and de Borst [120]). Thus, the associated flow rule does not hold for the whole range of the response spectrum of concrete and it sometimes leads to great discrepancies between predicted and measured response, as well as load carrying capacities.

In the current model, a nonassociated flow rule is adopted. The plastic potential for nonassociated flow is based on a modification of the loading surface given in Eq. (6.12)

$$Q(\boldsymbol{\sigma}, \rho, \theta, k, c, m_Q) = \left\{(1-k)\left[\frac{\boldsymbol{\sigma}}{f_c'} + \frac{\rho r(\theta)}{\sqrt{6} f_c'}\right]^2 + \sqrt{\frac{3}{2}}\frac{\rho r(\theta)}{f_c'}\right\}^2 + \frac{k^2}{f_c'}\left[m_Q + m\frac{\rho r(\theta)}{\sqrt{6}}\right] - k^2 c = 0 \tag{6.20}$$

except for the friction parameter $m \rightarrow m_Q(\boldsymbol{\sigma})$ which is redefined in terms of its gradient

$$\frac{\partial m_q}{\partial \boldsymbol{\sigma}} = D\exp(Ex^2) + G; \qquad \text{where } x = \frac{-\boldsymbol{\sigma} + f_t'/3}{f_c'} \tag{6.21}$$

The material parameters D, E, and G are calibrated from test results. The gradient of the plastic potential is evaluated by the chain rule of differentiation

$$\mathbf{m} = \frac{\partial Q}{\partial \sigma} = \frac{\partial Q}{\partial \boldsymbol{\sigma}}\frac{\partial \boldsymbol{\sigma}}{\partial \sigma_{ij}} + \frac{\partial Q}{\partial \rho}\frac{\partial \rho}{\partial \sigma_{ij}} + \frac{\partial Q}{\partial \theta}\frac{\partial \theta}{\partial \sigma_{ij}} \tag{6.22}$$

where

$$\frac{\partial Q}{\partial \boldsymbol{\sigma}} = \frac{\partial F}{\partial \boldsymbol{\sigma}} + \frac{k^2}{f_c'}\left(\frac{\partial m_Q}{\partial \sigma} - m\right); \qquad \frac{\partial Q}{\partial \rho} = \frac{\partial F}{\partial \rho}; \qquad \frac{\partial Q}{\partial \theta} = \frac{\partial F}{\partial \theta} \tag{6.23}$$

Calculating these is lengthy and the derivatives obtained will be long expressions. Thus the symbolic package MAPLE was employed to determine the derivatives. A distinct feature of MAPLE that produces the output in the form of Fortran language was used. The output was then used in the user defined subroutine was used.

6.7 Isotropic Softening Model for Post-Peak Behaviour

The softening response is initiated when the concrete starts cracking, due to increasing loading, in tension or low confined compression in triaxial tests. In direct tension, (Mode I type cracking), the fracture process is based on the fictitious crack model by Hillerborg [104]. This failure concept is then extended to model Mode II (shear) type of failure.

In the current model, a smeared crack description was used in which microscopic as well as macroscopic discontinuities in the from of discrete cracks are distributed and represented by equivalent continuum concepts.

6.7.1 Mode I Type Fracture

The micro-crack and the crack propagation phenomena in case of uniaxial tension test are well described by Hillerborg [104], and will be briefly restated here. Consider the tension test specimen shown in Fig 6.6. The deformation is measured along two equal gauge lengths A and B. These curves coincide until the maximum load is reached. On further deformation, a fracture zone develops somewhere in the specimen. As the fracture zone develops, the load will decrease due to the formation of microcracks.

Consequently, the deformation will decrease everywhere outside the fracture zone. This corresponds to the unloading curve in the stress strain diagram. In addition, no further fracture zone can be formed anywhere else in the specimen. The deformation

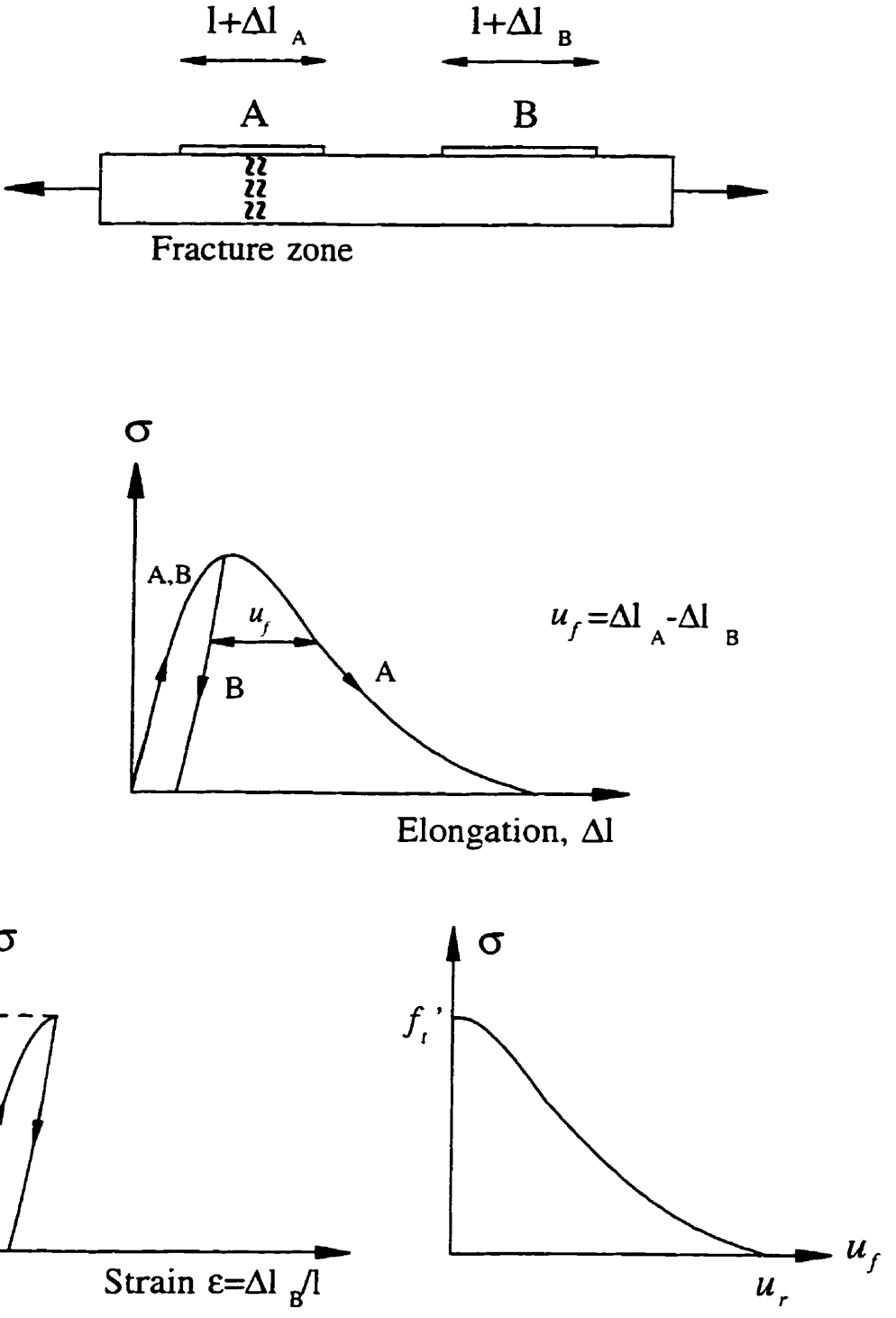

Figure 6.6: Fictitious crack model [104]

can be coupled into two contributions, as illustrated in Fig 6.6:

- The deformation within gauge B which is the elastic deformation of the specimen. The material could be assumed homogeneous, and it can be described by a stress strain curve including unloading branch.

- The deformation of the fracture zone. The additional deformation, u_f, is the difference between the descending branches of curves A and B.

During the tensile test that is carried out to complete separation, energy is absorbed inside and outside the fracture zone. The fictitious crack model defines the energy absorbed in the fracture zone or fictitious crack as

$$G_f = \int_0^{u_r} \sigma_t du_f \tag{6.24}$$

where G_f is the absorbed energy per unit crack area for complete separation of the crack surfaces. This absorbed energy is constant for different specimen heights in the σ_t - u_f space.

The softening is monitored in terms of the fracture modulus E_d which is the slope of the of the σ_t - u_f diagram Fig 6.7. The mapping between the crack opening displacement rate, du_f, and the equivalent tensile fracture strain rate, $d\epsilon_f$, is carried out with the aid of the parameter h_t. The value of h_t denotes the height of the elementary volume normal to the crack band as shown in Fig 6.7. The degradation of the tensile strength, σ_t, is then controlled by the fracture strain, ϵ_f, which is expressed in terms of $du_f = h_t d\epsilon_f$. The definition of the fracture-energy based strain-softening modulus is:

$$E_f = \frac{\partial \sigma_t}{\partial u_f} \frac{\partial u_f}{\partial \epsilon_f} \|\mathbf{m}\| \tag{6.25}$$

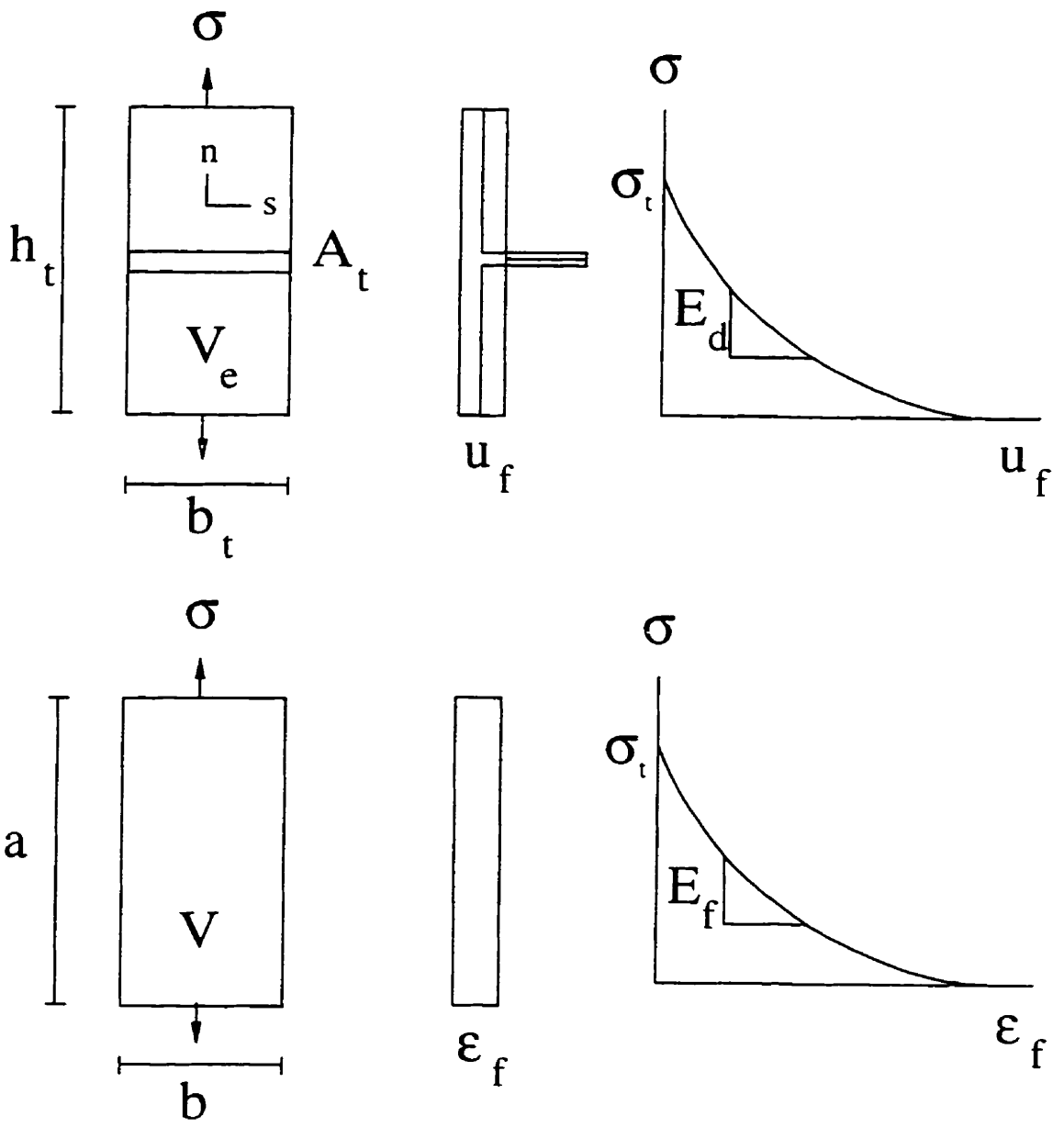

Figure 6.7: Composite fracture model for tensile cracking

In this case, h_t is used for the evaluation of the softening modulus:

$$E_f = E_d h_t \quad \text{where} \quad E_d = \frac{\partial \sigma_t}{\partial u_f}, \quad h_t = \frac{\partial u_f}{\partial \epsilon_f} \tag{6.26}$$

Consequently, the definition of the strain-softening modulus, E_f, depends on the geometry of the elementary volume.

There are different types of description for the uniaxial strength degradation in the post peak zone, including linear and bi-linear expressions. In all expressions, the area underneath the stress versus crack opening displacement curve, in direct tension, is constant and it is referred to as the fracture energy G_f^I. The fracture energy, in direct tension, was established as a material property.

In the Etse and Willam model [71], an exponential expression is adopted with a best fit of the Hurlbut [118] direct tension test. The expression related the crack width, defined as total change of length in the crack process zone, to the crack width at complete rupture

$$\sigma_t = f_t' \exp\left(-5\frac{u_f}{u_r}\right) \tag{6.27}$$

where u_r is the rupture displacement and u_f is the crack opening displacement.

6.7.2 Degradation of Triaxial Strength

As mentioned before, the softening response is initiated when the concrete starts cracking, due to increasing loading, in tension or low confined compression in triaxial tests. At this stage, the material can no longer be assumed intact. This mechanism, at low confining pressure, can be assumed to be controlled by the degradation of the cohesion parameter, c, where $0 \leq c \leq 1$. When $c = 0$, the material is considered to be completely fractured and it exhibits only residual friction similar to cohesionless materials. Etse and Willam [71] used the model proposed by Willam et al. [89] to model the post-peak behaviour of concrete. This model is used in the current

work. The model assumes that the failure mode is strongly dependant on the level of confinement. For example, the case of direct tension test produces a single discrete crack with a fairly brittle post-peak response with the strength dropping to zero at the end of the load displacement curve. On the other hand, triaxial compression tests with high level of confinement (Hurlbut [118], and Xie et al. [90]) develops distributed micro-cracks within the specimen and the strength does not drop to a zero level. Thus, the specimen exhibits ductile hardening or, in the limit, perfectly plastic response. Therefore, we can assume that there is a zone in stress space which defines the transition between brittle and ductile failure behaviour.

It should be noted that in the triaxial loading cases, the strain softening becomes more complicated. However, there is still common features in the strength degradation. Based on the triaxial test results of high strength concrete conducted by Xie et al. [90], the concrete under triaxial compression experiences strain-softening after the minor stress reach the peak. The slope of the descending curve becomes smaller and smaller as the strain increases. There is a stress level at which the slope of the descending curve becomes insignificant. It is called the residual strength. Etse and Willam [71] assumed that the residual strength is reached when, the strength is dominated purely by frictional resistance, which corresponds to a zero residual value of the cohesive parameter $c_r = 0$. Thus the residual strength envelope becomes:

$$F(\sigma, \rho, \theta, c) = \frac{3}{2}\left[\frac{\rho r(\theta)}{f_c'}\right]^2 + \frac{m_r}{f_c'}\left[\sigma + \frac{\rho r(\theta)}{\sqrt{6}}\right] = 0 \tag{6.28}$$

The governing mechanism that controls the degradation of strength, is the decohesion measure that is independent strength parameter, which is accompanied by the friction hardening as a dependent strength parameter. The relation between the

decohesion and the uniaxial tensile strength f_t' is expressed as:

$$c_s = \frac{\sigma_t}{f_t'} \tag{6.29}$$

where σ_t is the degrading tensile strength. The associated frictional hardening parameter is related to the value of decohesion as:

$$m_s = m_r - (m_r - m_0)c_s \tag{6.30}$$

This expression is derived from the condition that for $c = 1 \rightarrow m = m_0$, and for $c = 0 \rightarrow m = m_r$. As a result, the intermediate softening surface is defined by

$$F(\boldsymbol{\sigma}, \rho, \theta, c) = \frac{3}{2}\left[\frac{\rho r(\theta)}{f_c'}\right]^2 + \frac{m_s}{f_c'}\left[\sigma + \frac{\rho r(\theta)}{\sqrt{6}}\right] - c_s = 0 \tag{6.31}$$

In order to capture the pronounced softening response at low compression, the fracture model for Mode I type tensile cracking is extended to the Mode II type shear fracture.

6.7.3 Mixed Mode Fracture

The fracture model for Mode I type tensile cracking is extended to the Mode II type shear fracture. From experiments, it is known that tensile splitting in compression as well as shear is preceded by distributed microcracking, and that this microcracking is more important for Mode II than for Mode I. Hence, the crack surface in Mode II can be interpreted as a multiple of the one in direct tension case. A fracture energy similar to the one developed for tensile cracking can be used in order to maintain constant fracture energy release between the surface and volume of the failure process:

$$du_f = \frac{V}{A_c} d\epsilon_f = h_c d\epsilon_f \tag{6.32}$$

where the fraction A_c/V represents the microcrack density in compression. Here, h_c is called 'gauge length' or the 'equivalent crack spacing' for cases other than direct

tension. ϵ_f is called the 'equivalent tensile fracture strain', and is used to monitor the degradation of the triaxial strength envelopes. The measure of the incremental equivalent tensile fracture strain is suggested as

$$d\epsilon_f = \sqrt{< d\bar{\epsilon}_f >^T . < d\bar{\epsilon}_f >} \tag{6.33}$$

where the McCauley brackets <>, extract the tensile components of the principal fracture strain increments $d\bar{\epsilon}_f$.

The crack spacing, h_c can be evaluated approximately in terms of the ratio between the fracture energy release rate in tension G_f^I and that in shear G_{fI}^I. From the equivalence of strain energy in splitting compression it can be assumed that

$$G_f^I \Delta A_t = G_f^{II} \Delta A_c \quad \text{or} \quad \Delta A_t = \frac{G_f^I}{G_f^{II}} \Delta A_t \tag{6.34}$$

The crack spacing in compression and in tension h_c and h_t can thus be related by:

$$h_c = \frac{V}{A_c} = \frac{G_f^I}{G_f^{II}} \frac{V}{A_t} = \frac{G_f^I}{G_f^{II}} h_t \tag{6.35}$$

The ratio G_f^I/G_f^{II} represents the ratio between equivalent compressive crack surface and the direct tension test crack surface. As adopted by Etse and Willam [71], this ratio can be described with a quadratic polynomial in terms of the hydrostatic stress as

$$\frac{G_f^{II}}{G_f^I} = A[\frac{\sigma - f_t'/3}{f_c'}]^4 + B[\frac{\sigma - f_t'/3}{f_c'}]^2 + 1 \tag{6.36}$$

where A and B are calibrated from the low and high confined compression tests.

According to the nonassociated flow rule, the failure potential Q_s is obtained by volumetric modification of the yield surface in the softening regime in Eq. (6.31)

$$Q(\sigma, \rho, \theta, c_s, Q) = \frac{3}{2}\left[\frac{\rho r(\theta)}{f_c'}\right]^2 + \frac{1}{f_c'}\left[m_Q + m\frac{\rho r(\theta)}{\sqrt{6}}\right] - c_s = 0 \tag{6.37}$$

6.8 The Basis of Numerical Implementation

Before proceeding to the numerical implementation of the plasticity based constitutive model into the finite element program, it may be useful to reiterate the basic assumptions of the flow theory of plasticity. In general, the flow theory of plasticity is based on three assumptions as mentioned in the previous sections

- *Decomposition of strain rate* into elastic and plastic response with complete decoupling of both components

$$d\epsilon = d\epsilon_e + d\epsilon_p \tag{6.38}$$

  This assumption is normally justified for small or infinitesimal deformation.

- *Yield criterion* that delimits the elastic portion of the material response under combined state of stress. The yield criterion is generally expressed as a function of the state of stress $\boldsymbol{\sigma}$ and the internal variables $\boldsymbol{q}$ (Lubliner [119]). The internal variables $\boldsymbol{q}$, in vector form, are used to describe the past history of the state of stress. Thus, the general form of the yield function can be written as

$$F(\boldsymbol{\sigma}, \boldsymbol{q}) = 0 \tag{6.39}$$

  For a the case of isotropic behaviour, the yield surface can be expressed in terms of the principal stresses or in terms of the invariants of the stress tensor.

- The *flow rule* describes the evolution of the plastic strain rate when the material undergoes plastic deformation. The plastic flow equation takes the form

$$d\epsilon = d\lambda \frac{\partial Q}{\partial \sigma} = d\lambda \mathbf{m} \tag{6.40}$$

  where Q designates the plastic potential, $\mathbf{m}$ describes the direction of the plastic flow, and $d\lambda$ is a positive scalar factor called the plastic multiplier. The value of $d\lambda$ is non-zero only when plastic deformations occur.

- Many *material stability postulates* were proposed by different researchers, for example Hill's, Il'yushin and Drucker postulates. However, Bazant [121] proved that those postulates are neither necessary nor sufficient for stability. As a result no stability postulate is used in the current model.

6.8.1 Numerical Implementation of Plasticity

The elastic-predictor plastic-corrector method is used [123, 122]. It is simply on an assumed trial stress vector (elastic-predictor), and a correcting procedure (plastic-corrector) in case the trial vector violates the yield condition. The problem can be summarized as follows:

- At time $t = t_n$, the initial values σ, ϵ, $\boldsymbol{q}$ are known
- An increment of stress $\Delta\sigma$ is applied
- It is required to find the new state of stress and strain

6.8.2 Elastic-Predictor Step

The elastic-predictor defines the trial stress state as:

$$\sigma_t = \sigma_n + E\Delta\epsilon \tag{6.41}$$

From this step, one of three situations will arise

- Elastic loading: $F(\sigma_t, \boldsymbol{q}_n) < 0$
- Neutral loading: $F(\sigma_t, \boldsymbol{q}_n) = 0$
- Plastic loading: $F(\sigma_t, \boldsymbol{q}_n) > 0$

The case of elastic loading and neutral loading is handled within the elastic constitutive relation. The case of the plastic loading a plastic-corrector will be required as presented in the next section.

6.8.3 Plastic-Corrector Step

When the state of stress exceeds the elastic limit, the stresses cross the yield surface. The purpose of the plastic-corrector is to return the trial stress vector σ_t to the yield surface. In order to obtain an efficient return strategy, two conditions have to be satisfied:

- The stress state σ_{n-1} must be on the loading surface.
- The constitutive law for hardening/softening must be satisfied.

For the case of plastic loading, the elastic-predictor step is followed by a plastic-corrector step. This can be expressed as:

$$\Delta\sigma = \Delta\sigma_t - \Delta\sigma_p \tag{6.42}$$

The elastic stress and the plastic stress, as mentioned before, are expressed as

$$\Delta\sigma = E\Delta\epsilon_e \tag{6.43}$$

$$\Delta\epsilon_p = \Delta\lambda\mathbf{m}$$

Thus, Eq. (6.42) can be written as

$$\Delta\sigma = E\Delta\epsilon - \Delta\lambda E\mathbf{m} \tag{6.44}$$

6.8.4 Crossing the Yield Surface

The integration procedure used here requires the location of the intersection of the elastic stress vector with the yield surface (Fig 6.8(a)). In such circumstances, we have [123]

$$f(\sigma_x + \alpha\Delta\sigma_e) = 0 \tag{6.45}$$

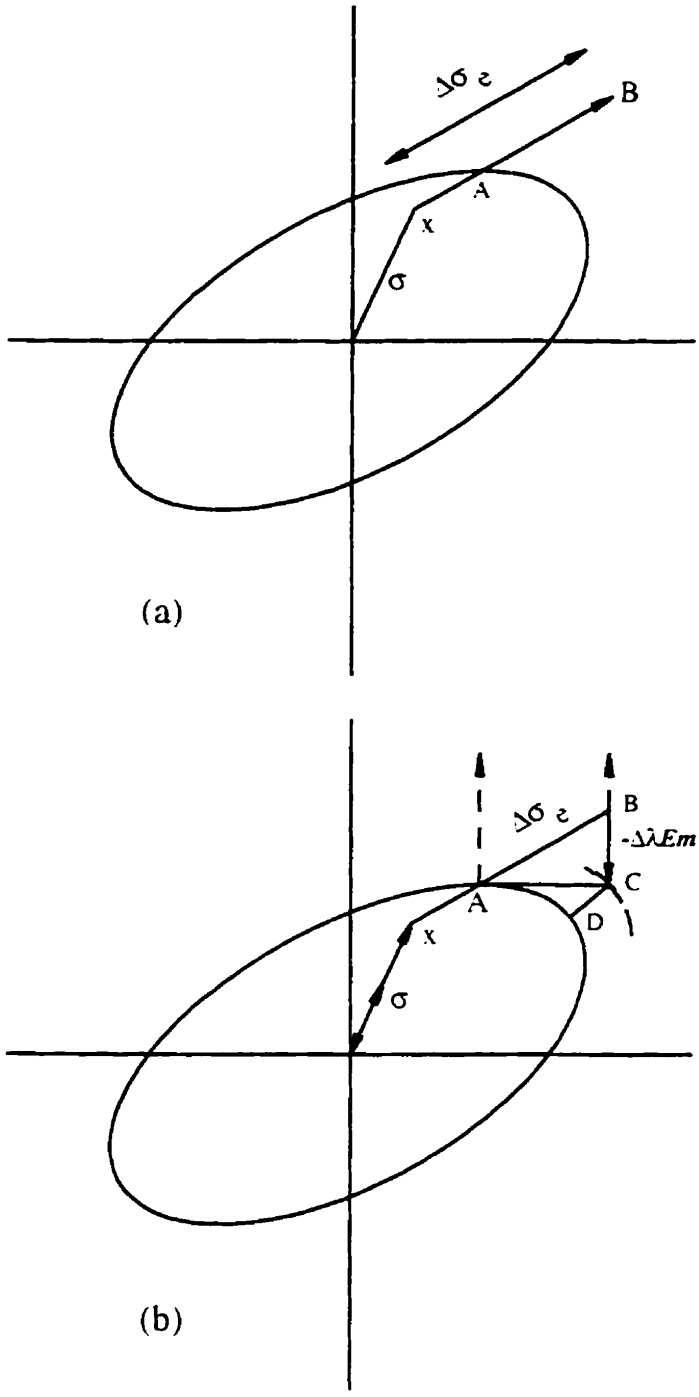

Figure 6.8: The forward-Euler procedure: (a) Locating the intersection point A: (b) Moving tangentially from A to C (and correcting to D).

where the original stresses, σ_x are such that

$$f(\sigma_x) = f_x < 0 \tag{6.46}$$

while, with $\alpha = 1$, the elastic stresses $\sigma_x + \sigma_e$ give

$$f(\sigma_B) = f(\sigma + \Delta\sigma_e) > 0 \tag{6.47}$$

For some yield surfaces, this problem can be solved exactly. In the current work, an iterative scheme is used to determine the point of intersection with the yield surface.

As mentioned before, a scheme is needed to return the stresses to the yield surface following an initial predictor. The procedure used in the current work is a standard predictor in the form of forward-Euler procedure, such that

$$\Delta\sigma = E\Delta\epsilon - \Delta\lambda E\frac{\partial f}{\partial\sigma} = \Delta\sigma_e - \Delta\lambda E\frac{\partial f}{\partial\sigma} \tag{6.48}$$

Moving from the intersection point A (Fig 6.8(b)), $\Delta\sigma_e$ is now the elastic increment after reaching the yield surface. In relation to Fig 6.8

$$\sigma_C = \sigma_A + \Delta\sigma_e - \Delta\lambda E\frac{\partial f}{\partial\sigma} = \sigma_B - \Delta\lambda E\frac{\partial f}{\partial\sigma} \tag{6.49}$$

and the step can be interpreted as giving an elastic step from the intersection point A to B followed by a plastic return that is orthogonal to the yield surface at A.

6.8.5 Returning to the Yield Surface

In general, the previous method produces stresses that lie outside the yield surface. It is now possible to simply scale the stresses at C (Fig 6.8(b)) by a factor r until the yield surface f becomes zero (Ortiz and Popov [124]). However, this technique will generally involve an elastic component and thus it is not encouraged to use it. An alternative technique (Ortiz and Simo [125]) suggests that the total strains are kept

fixed while additional plastic strains are introduced in order to relax the stresses to the yield surface. Consequently Eq. (6.49) can be repeated at point C Fig 6.8(b) so that

$$\sigma_D = \sigma_C - \Delta\lambda E \frac{\partial f}{\partial \sigma}\bigg|_C \tag{6.50}$$

If the resulting yield function at D Fig 6.8(b) is insufficiently small, further relaxation can be applied.

6.8.6 The plastic Multiplier $\Delta\lambda$

The evaluation of the plastic multiplier was first suggested by Willam et al. [89] and it was subsequently used by Pramono and Willam [70]. It is used in the current implementation of the ELM.

Consider a load increment of finite size in which the strain increment $\Delta\epsilon$ is prescribed. Assuming that the previous stress state $F_n = 0$ is satisfied, the subsequent stress state $\sigma_{n+1} = \sigma_n + \Delta\sigma$ must remain on the loading surface and must satisfy the yield condition at step $n+1$, i.e. $F_{n+1}(\sigma_{n+1}, \boldsymbol{q}_{n+1})$=0. The $\boldsymbol{q}_{n+1}$ designates the plastic control variables for hardening/softening at step n+1. The linearized consistency condition is used to evaluate the plastic multiplier $\Delta\lambda$.

The linearized consistency condition is derived by expanding the yield criterion into a first order of the truncated Taylor series around the previous converged state.

$$F_{n+1} = F_n + \frac{\partial F}{\partial \sigma}(\sigma_{n+1} - \sigma_n) + \frac{\partial F}{\partial \boldsymbol{q}}(\boldsymbol{q}_{n+1} - \boldsymbol{q}_n) = 0 \tag{6.51}$$

Thus, the classical linearized consistency condition can be written as:

$$\Delta F = \frac{\partial F}{\partial \sigma}\Delta\boldsymbol{\sigma} + \frac{\partial F}{\partial \boldsymbol{q}}\Delta\boldsymbol{q} = 0 \tag{6.52}$$

It can be seen that the full consistency condition is not satisfied since $F_{n+1} \neq F_n + \Delta F_n$ except for linear yield surfaces and hardening/softening rules. In case of

isotropic softening/hardening the internal variables degenerate into a single variable function of the plastic strain. The plastic multiplier can be expressed in an explicit form [89, 70] as:

$$\delta\lambda = \frac{nE\Delta\epsilon}{-\frac{\partial F}{\partial q}|m| + nEm} \tag{6.53}$$

6.9 Implementation of the Model

Etse and Willam's model requires a solver for non-symmetric system to account for non-associated plastic flow. The finite element program 'ABAQUS' has such a capacity. ABAQUS is a general purpose finite element program that can be used to solve a variety of non-linear problems. It provides different choices for the solution strategy.

Version 5.4 was mounted on the DEC workstations in the Centre for Computed Aided Engineering at the Faculty of Engineering, Memorial University of Newfoundland. Etse and Willam model was coded in FORTRAN 77 language and it was implemented as a user defined subroutine 'UMAT' into ABAQUS. The implementation was carried out to handle plane stress elements, axisymmetric elements and 3-D solid elements. It can also be extended to handle other types of elements.

6.10 Calibration and Verification of the Model

The material parameters required for the calibration of the model were calculated from the current experimental program, whenever this was possible. The hardening parameters A_h, B_h, and C_h can be calculated from three sets of tests. However, a best fit of all the experimental results was used to obtain these parameters. The parameters were calculated for the three different type of concrete, namely: NSC and HSC and UHSC. They are given in Table 6.1. The mechanical properties of each mix are also provided in this table.

The softening parameters A_s and B_s could not be calculated from the current experimental work. Because of the configuration of the test set-up no reliable descending portion, that represent the true material behaviour, could be measured. Thus, a simple expression that was suggested by Xie et al. [90] was used instead of Eq. (6.36). They proposed a different definition that depends on whether the confining stress, σ_1, is compressive or tensile:

$$\frac{h_t}{h_c} = A_s\sqrt{1+B_s\frac{\sigma_1}{f'_c}} \qquad \text{when } \sigma_1 < 0 \tag{6.54}$$

$$\frac{h_t}{h_c} = 1-(1-A_s)(1-\frac{\sigma_1}{f'_t}) \qquad \text{when } 0 \leq \sigma_1 \leq f'_t \tag{6.55}$$

the softening parameters were calculated based on the results of their study on the triaxial behaviour of high strength concrete. These parameters were used here. It was not possible to confirm the validity of these parameters due to the absence of the post peak part in the current experimental data.

Performance of the calibrated model was examined by simulating a plane stress element and a cylindrical specimen. To avoid the problems associated with the interaction between the platens and the test specimen, only a test specimen was considered. The loads were applied to the specimen's end. This is done so that a true material response, of the specimen, could be evaluated.

Figure 6.9 shows the geometry of the plane stress model used for verification purposes. The geometric model is a single 8-node plane stress isoparametric element with 4 integration points (reduced integration). Two edges have simple supports. The load is applied proportionally on the other two edges. The nodes along each loaded edge are constrained to have the same displacement in the direction of the applied load. Figure 6.10 shows a comparison of the finite element results with the biaxial experimental data on normal strength concrete by H. Kupfer et al. [14]. The

Table 6.1: Material parameters for the different types of concrete

Concrete Mix	NSC	HSC	UHSC
E (GPa)	27.7	39	42
f'_c (MPa)	42.4	73.65	96.54
f'_t (MPa)	3.30	4.15	4.82
A_h	-0.0011499	-0.0008926	-0.0008626
B_h	-0.0023142	-0.0018178	-0.0016532
C_h	0.0001115	0.0000778	0.0000696
A_s	24	24	24
B_s	-4	-4	-4

results of the analysis are presented in Fig 6.11 for the UHSC mix.

The verification case for the triaxial tests was carried out using the experimental results of Xie et al. [90]. The specimen's size was 55 mm × 111 mm. Due to the symmetry of the geometry and the loading condition, only a quarter of the specimen is chosen. The elements used are 8-node axisymmetric isoparametric elements with 4 integration points (reduced integration). Figure 6.12 shows the finite element mesh used in the model verification. The loading of the specimen is carried out in the same fashion as the experiment was conducted. The confining stress is applied first to the specimen. Once the confining stress reached its prescribed value, the axial load is applied. The finite element results are shown in Fig 6.13.

From the simulation results, it seems that the finite element model, generally speaking, is able to capture the specimen's behaviour under the uniaxial, biaxial and triaxial stress states.

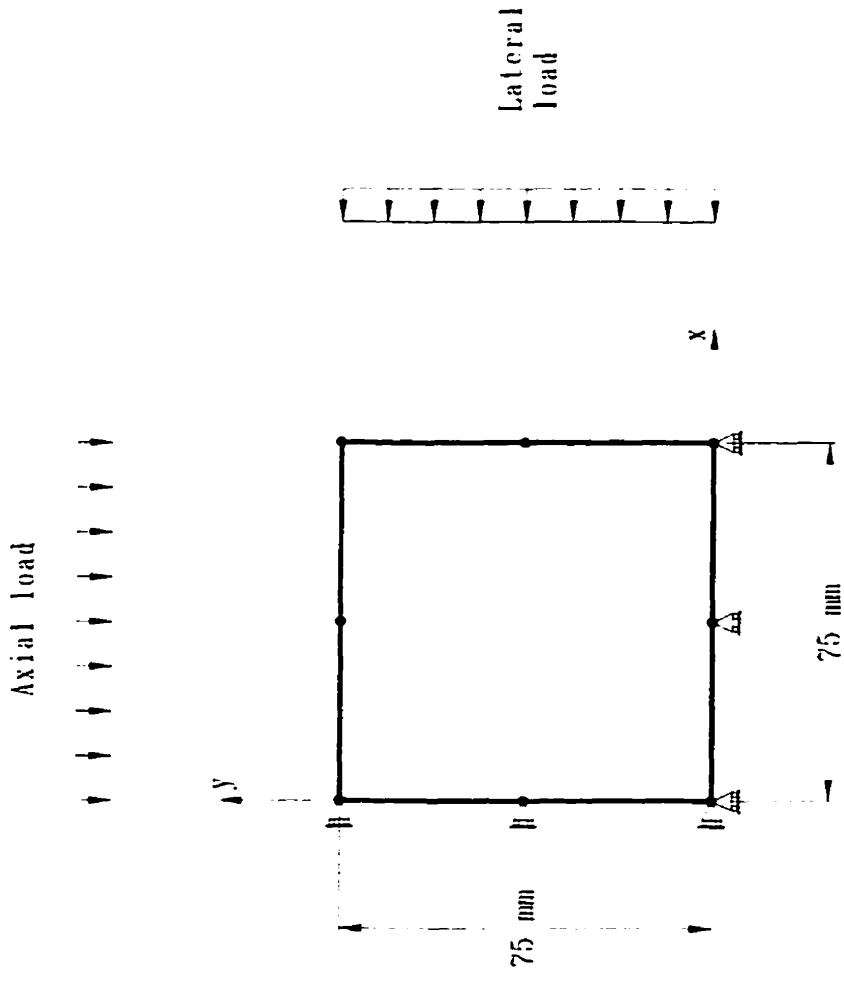

Figure 6.9: Verification of plane stress elements

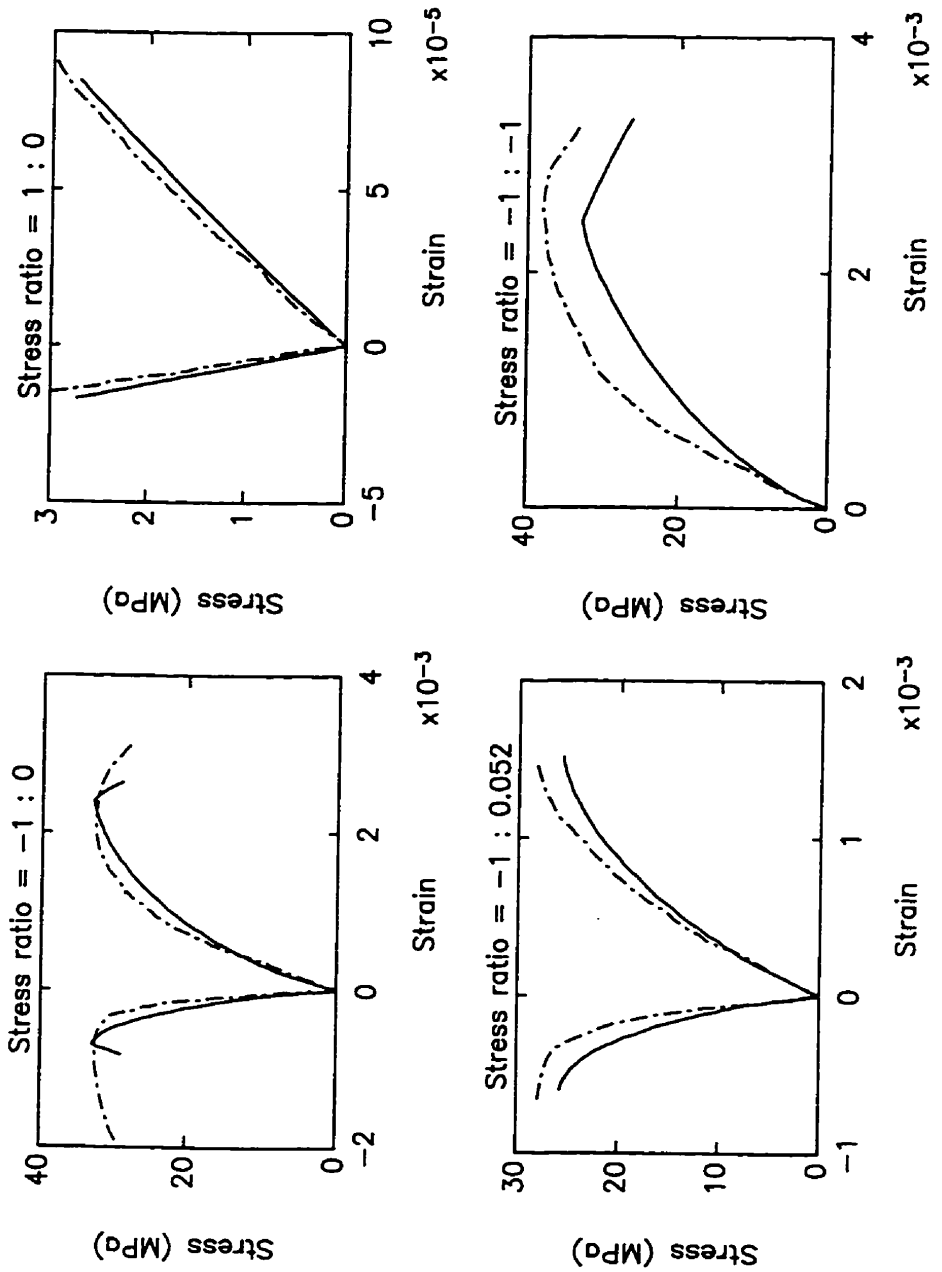

Figure 6.10: Comparison of the finite element results with the biaxial experimental data on normal strength concrete by H. Kupfer et al. [14]: (· · · ·) experimental data, and (——) finite element results

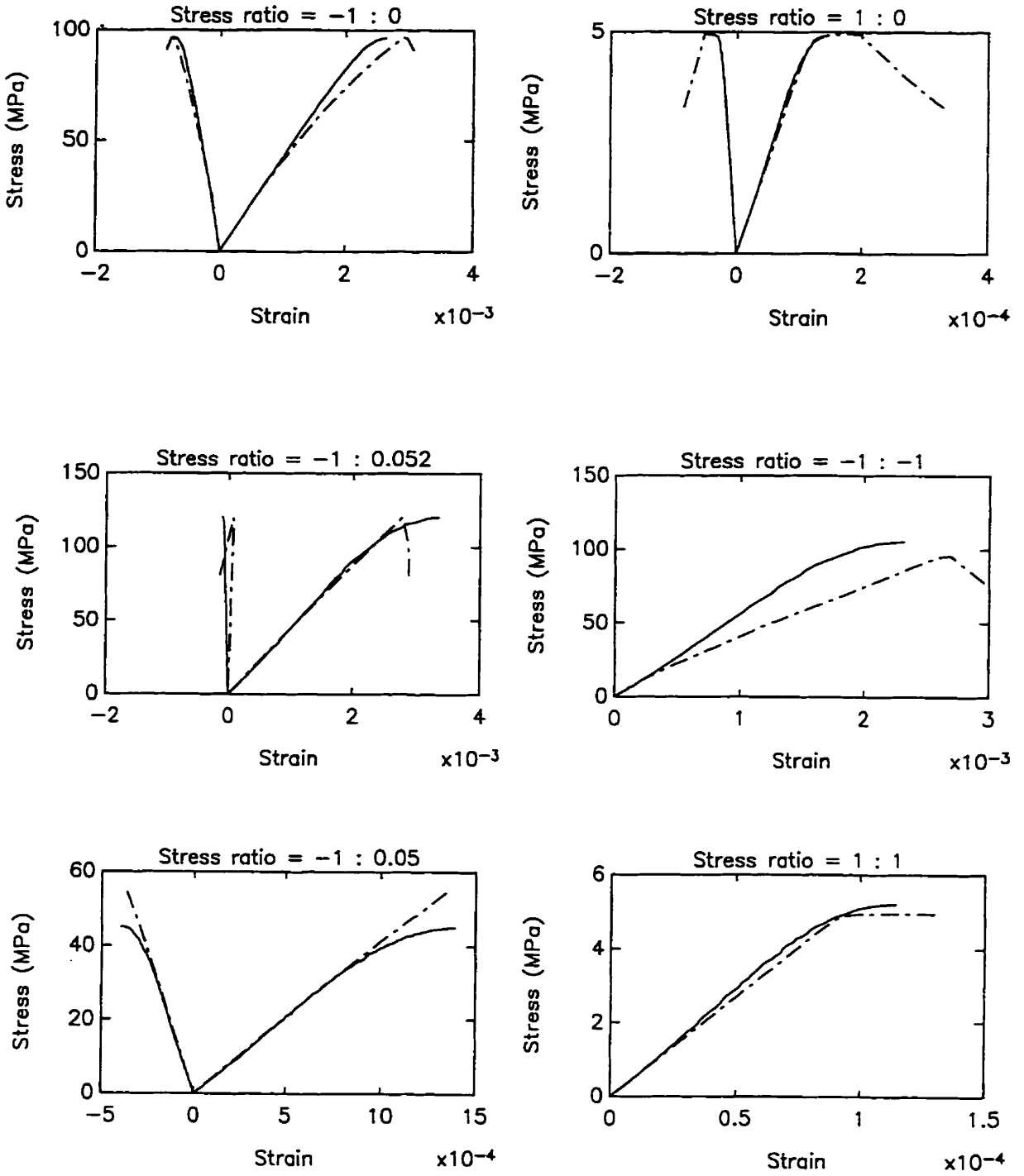

Figure 6.11: Comparison of the finite element results with the experimental data for the UHSC mix: (——) experimental data, and (- · - · ·) finite element results

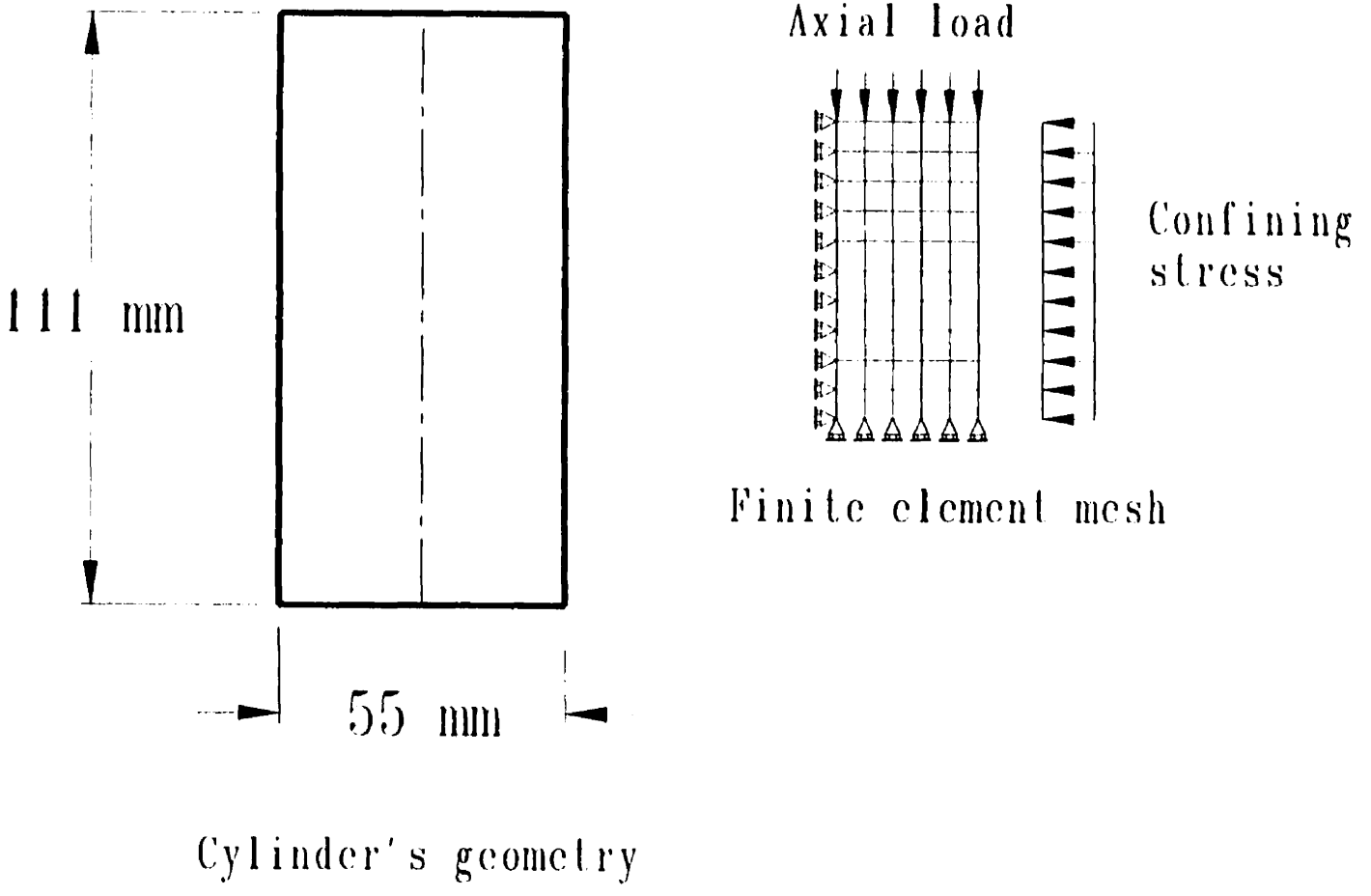

Figure 6.12: The finite element mesh for a cylindrical specimen subjected to triaxial loading

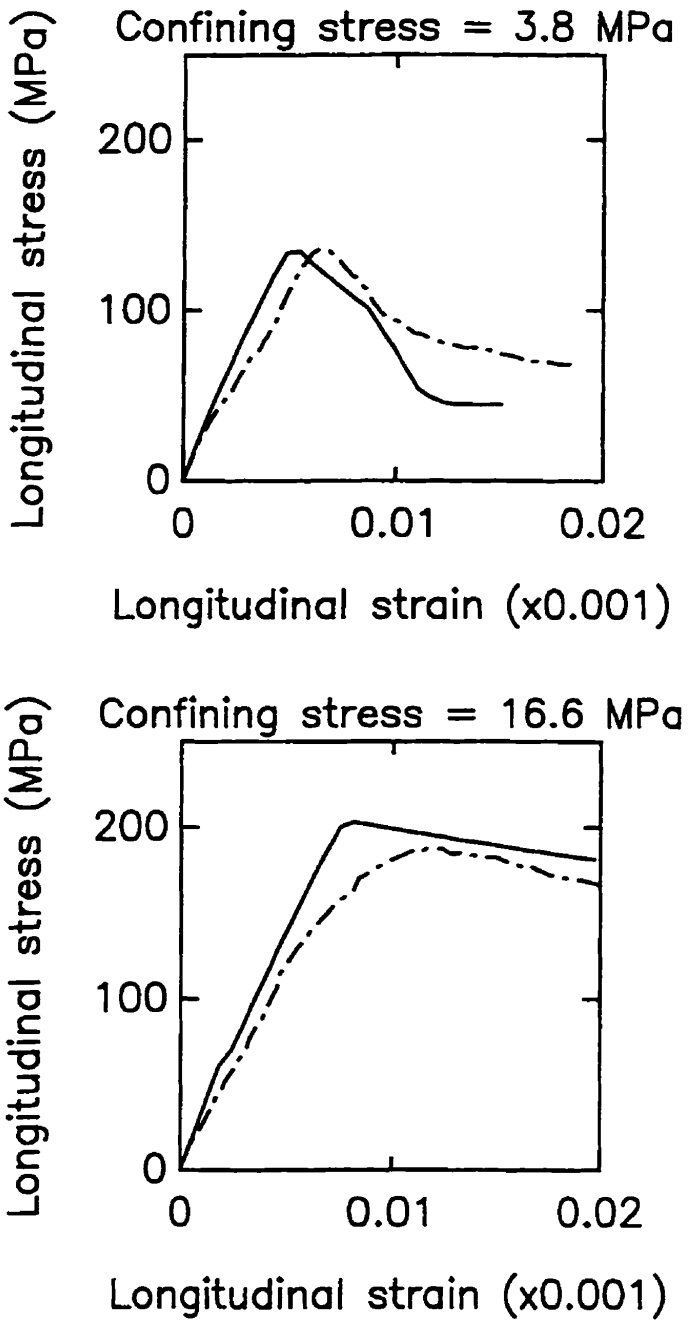

Figure 6.13: Comparison of the finite element results with the triaxial experimental data on high strength concrete by J. Xie et al. [90]: (- · - ·) experimental data, and (——) finite element results

Chapter 7

Application of the Proposed Model: Evaluation of the Standard Uniaxial Compression Test

7.1 Introduction

In the present chapter, the finite element model presented in the previous chapter is employed to model the standard uniaxial test of a concrete cylinder. The parameters investigated are the concrete compressive strength, specimen dimensions, bearing block dimensions, and the specimen's end preparation (effect of mechanical properties of the capping material). These parameters are selected to simulate the actual ones used in the standard compression tests. The study utilizes the finite element model to investigate the state of stress in a cylindrical specimen (with an actual test parameters) as well as the shear stresses induced in the specimen's edge at the interface with the steel loading platens.

7.2 Standard Uniaxial Compression Test

Concrete quality is generally governed by its compressive strength. In the design process, this property is the key parameter although other strength properties must also be considered. Concrete cylinders are used in North America to find the uniaxial compressive strength of concrete whereas test cubes are used in the United Kingdom to obtain the same parameter.

The current standard practices and test methods for testing high strength concrete (60 - 120 MPa) are based mainly on the recommendations from earlier research work conducted on conventional normal strength concrete (30 MPa). Thus, the testing methods should be re-evaluated to determine how suitable they would be for testing high-strength concrete. The various factors that affect the compressive strength of a concrete cylinder during testing are: the size of the specimen, the end preparation of the specimen, and the dimension of the bearing block. Also, the stiffness of the testing machine and the loading rate are of significant importance. An extensive literature review of the effect of different testing variables that influence the concrete cylinder test is given by Carino et al. [126].

7.3 Specifications for the Standard Cylinder Test

ASTM Test Method C 39-1993a [99] recommends that the dimensions of the bearing block should be changed if the specimen dimensions are changed in order to maintain the same mode of failure. Figure 7.1 depicts a schematic drawing of a typical spherical bearing block as recommended by ASTM C 39-1993a.

The Université de Sherbrooke, Québec, Canada, has carried out an extensive program on high-strength concrete testing. In one of their recent publications [127], a study was reported based on 378 compression tests on 150 × 300 mm and 100 × 200

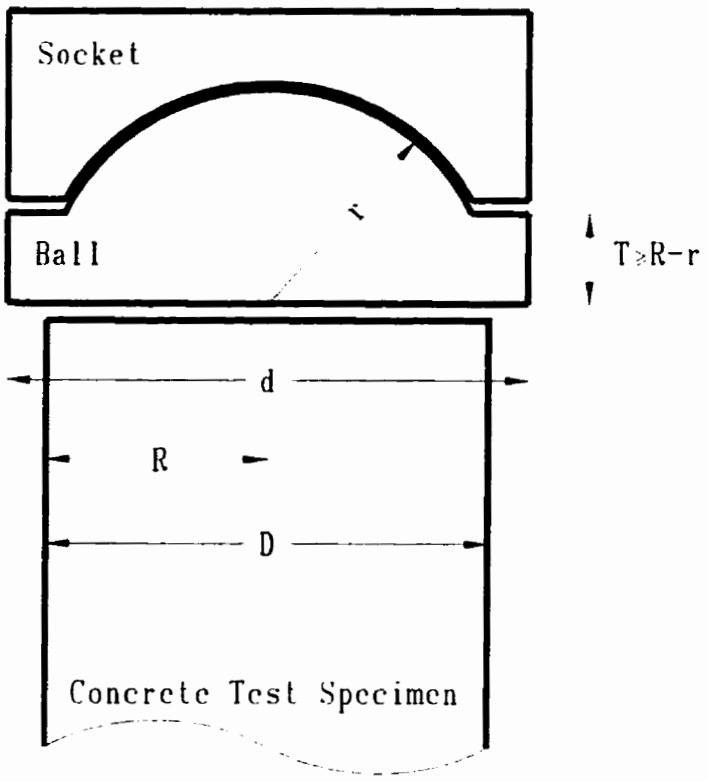

D	Maximum d
102 mm	165 mm
152 mm	254 mm

Figure 7.1: ASTM C 39-1993a standard bearing block for compression testing

mm high-strength concrete specimens made of a total of 14 different laboratory and field concretes. A bearing block with a diameter (2r) of 152 mm was used for testing 150 × 300 mm whereas a 102 mm block was used for testing 100 × 200 mm. Both blocks conformed to ASTM C 39-1993a. The results of the study revealed that the compressive strength slightly increases as the specimen size decreases. In addition, the compressive strength of the standard 150 × 300 mm specimens obtained using a 102 mm diameter block was found to be 83 percent of that obtained using a standard 152 mm diameter bearing block. Also, a splitting type of rupture was observed for the 150 × 300 mm specimens tested using a 102 mm diameter bearing block.

With the wide use of high-strength concrete, new criteria have evolved regarding the compression test requirements [128], such as the specimen size, end preparation, dimensions of bearing block, etc. The evaluation and calibration of such new methods are based solely on obtaining compressive strength values. These values are then compared to the results of the standard cylinders tested in accordance with ASTM C 39-1993a. The standard practice for testing cylindrical concrete specimens requires a cylinder with a dimension of 150 × 300 mm (6 × 12 in); this size is almost universally accepted for the compressive strength test.

Most experimental studies are only concerned with the effect of different test variables on the compressive strength of the specimen. It also should be noted that, in addition to the specimen's strength, the mechanical property values, such as Young's modulus, E, and Poisson's ratio, ν, will be influenced by the different variables in the compression test. A quantitative stress analysis of this problem can provide useful information both in understanding the different state of stresses in the concrete specimen and in serving as a guide to designing a test specimen in which a somewhat corresponding state of stress exists throughout the specimen during the test. That will

enable accurate measurements of the intrinsic mechanical properties of the specimen under different conditions.

7.4 Standard Specimen Size

Most laboratories are equipped with testing machines that have the capacity for normal concrete (30 MPa) cylinder compression test. To test a concrete specimen with the standard dimensions and a compressive strength of 100 MPa, more than triple the load will be needed. Such a load could be beyond the machine capacity not to mention the machine stiffness. Recently, as a result of numerous research work (reported in [126] and [127]), a cylinder dimension of 100 × 200 mm (4 × 8 in) was recommended for testing high-strength concrete. Such a size makes it possible to use conventional testing machines available in most laboratories. However, extensive calibration is required to relate the strength obtained from such specimens to the standard specimen (150 × 300 mm).

7.5 State of Stress in a Test Specimen

The different lateral stiffness of the loading platens and the concrete specimen create a complicated stress state, in particular near the end of the specimen. Due to the differences in lateral expansion between the concrete specimen and the loading platens, frictional forces will develop between them. Friction constrains the specimen boundary against lateral displacements which leads to additional shear stresses on the surface. In addition, the stress distribution in the specimen will not be uniform. Figure 7.2 shows the stress distribution along the loaded side of a specimen. The normal compressive stress distribution at the platen-specimen interface indicate that the compressive stress is higher near the perimeter than at the centre of the specimen.

The induced friction forces in the end of the specimen influence the specimen's failure mode. The end restraint normally produce a cup and cone failure in the cylinder. The developed friction forces have a significant effect on the strength of the specimen if its aspect ratio is equal to one. To eliminate this, the present ASTM testing method recommends the use of a specimen with an aspect ratio of two.

7.6 Finite Element Simulation

In an attempt to provide some insight to the standard compression test, a finite element simulation of the test is carried out. The concrete test specimen is modeled with the bearing block using actual test parameters. A portion of the finite element investigation is designed to simulate the experimental program conducted at the Université de Sherbrooke, Québec, Canada [127]. Thus, the test parameters are the same as those used in the experimental study. The diameters of the analyzed standard blocks are 102 and 152 mm. Two different sizes of specimens are investigated. They are the standard 150 × 300 mm mm cylinder and the 100 × 200 mm cylinder (which is currently popular for testing high strength concrete). The 100 and 150 mm test specimen are tested using each standard block. Thus, the numerical simulation falls into four main cases as shown in Table 7.1. In order to examine the effect of the compressive strength of the specimen, each simulation is carried out for three different grades of concrete, namely: 30, 70 and 100 MPa. Finally, the effects of the different end preparations of the specimen are investigated.

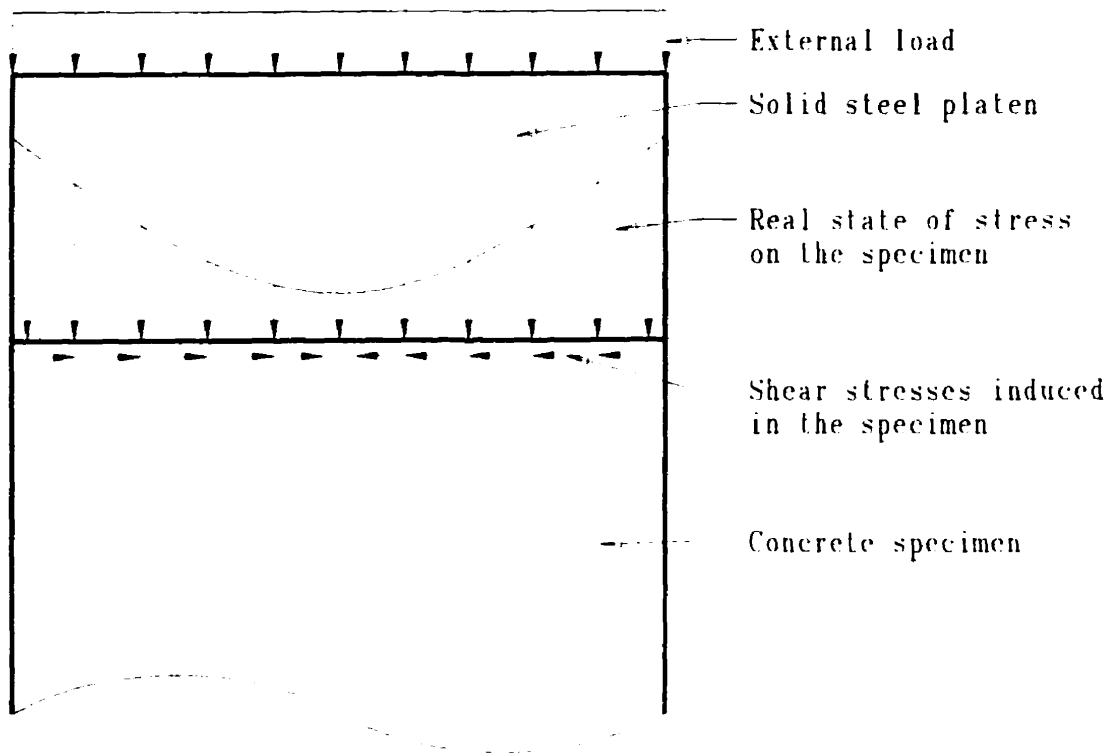

Figure 7.2: State of stress on a compression test specimen

Table 7.1: Different cases of the finite element simulation

	Case 1	Case 2	Case 3	Case 4
Dimensions of specimen (mm)	150 × 300	150 × 300	100 × 200	100 × 200
Bearing block diameter (mm)	152	102	152	102

7.6.1 Geometric Modelling

The test specimen and the end bearing blocks are modeled using the mesh shown in Fig. 7.3. The element used is an eight-node axisymmetric element with 4 integration points (reduced integration). Due to symmetry, only one quarter of the cylinder and one bearing block is simulated. Details of the number of elements for the different systems are given in Table 7.2. Figure 7.4 illustrates the coordinate system and nomenclature used in this study. This figure also shows the forces acting on an axi-symmetric element. Distributed loads are used to simulate the action of the swivel. Such type of loads remains perpendicular to the element side (in the local coordinates) as opposed to concentrated loads that are fixed in one direction in the global coordinates at any loading stage.

7.7 Material Model

The analysis presented in the following sections was carried out using the finite element program 'ABAQUS'. The constitutive model is the Etse and Willam [71] model as modified and described in Chapter 6. The steel platens have a modulus of Elasticity of 200 GPa and Poisson's ratio of 0.30.

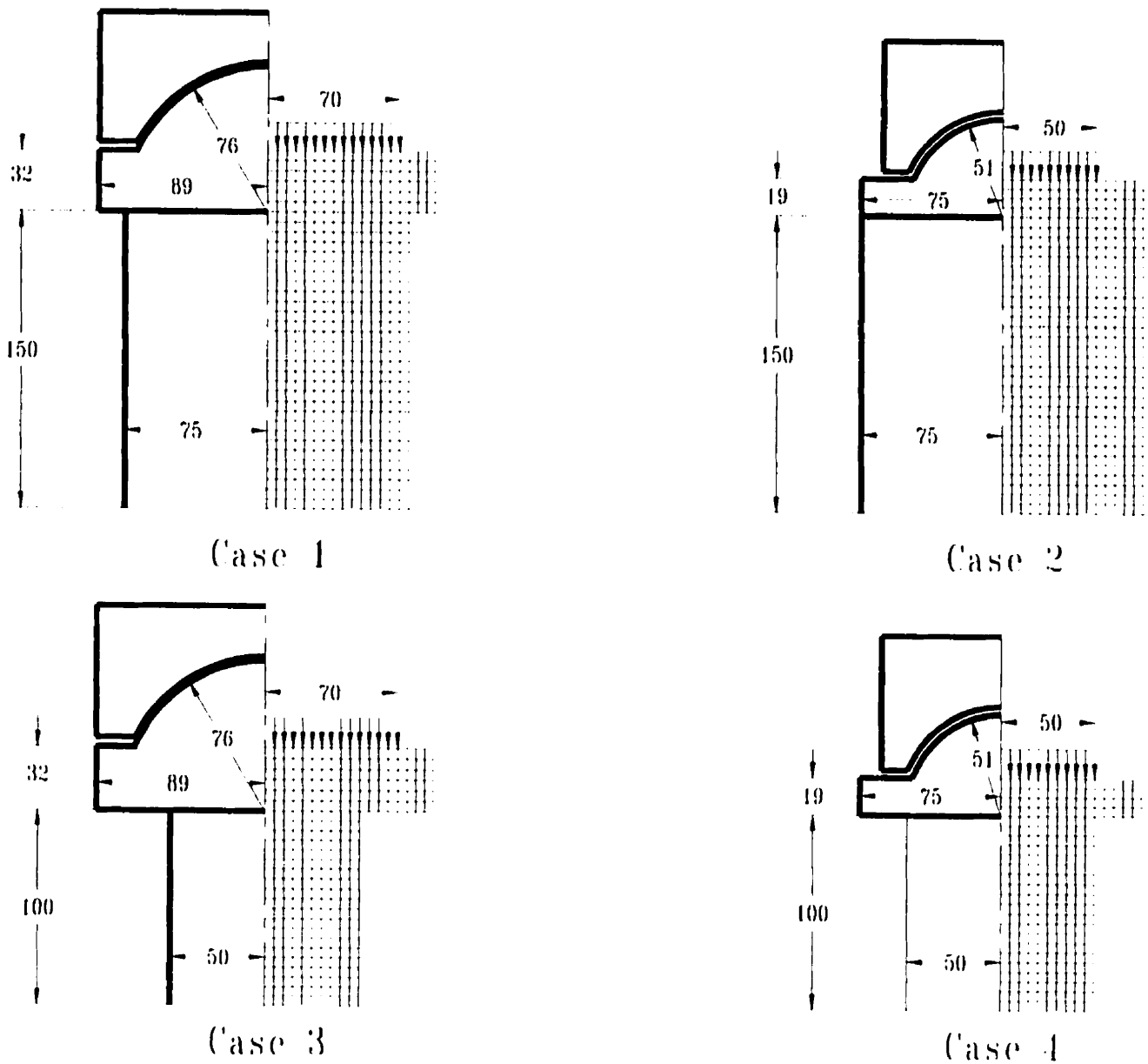

Figure 7.3: The finite element mesh

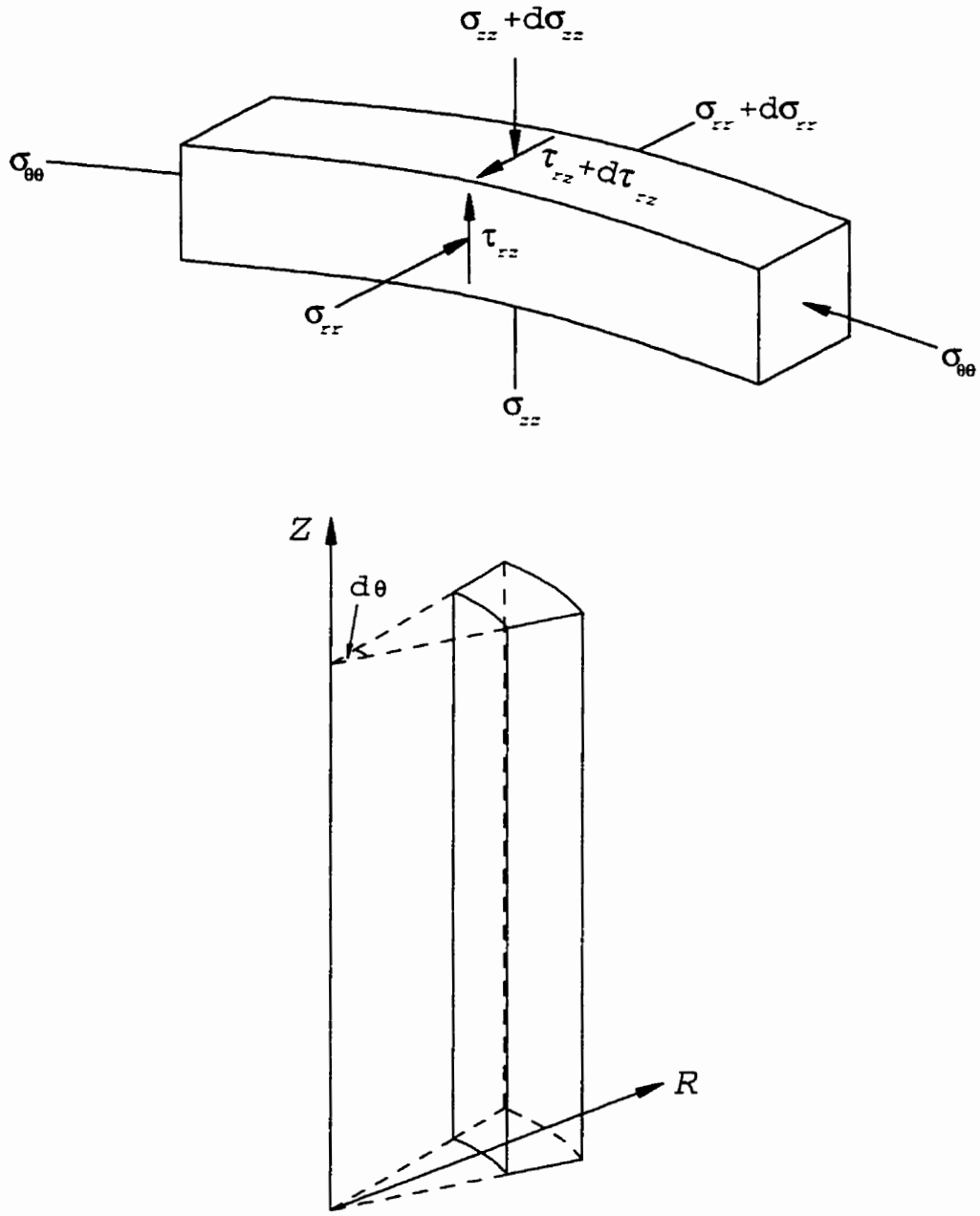

Figure 7.4: Forces acting on an axi-symmetric element

Table 7.2: Number of elements

No. of elements	Case 1	Case 2	Case 3	Case 4
Specimen	450	450	200	200
Loading block	108	60	108	60
Total	558	510	308	260

7.8 Simulation of the Compression Test

The standard compression test is normally carried out using a stiff testing machine. The specimen is mounted in the machine and the load is applied at a specified constant rate until the specimen fails. The ultimate load at which the specimen fails is then used to find the maximum stress. The value obtained is the compressive strength of the concrete, f'_c. Thus, in the current analysis of the standard compression test, the load is applied using load control to simulate the actual test. Hence, the post peak behaviour of the specimen is not considered. In the following discussion, the load at which the specimen reaches its ultimate calculated strength is referred to as 100 % loading.

To examine the specimen behaviour at the different loading stages, a standard concrete cylinder is considered. The cylinder has a compressive strength $f'_c = 30$ MPa and is loaded with a 152 mm bearing block. The stresses in the specimen are evaluated at a load level corresponding to 40 %, 90 %, and 100 % of the ultimate load. Figures 7.5, 7.6, and 7.7 show the circumferential (hoop) stresses, $\sigma_{\theta\theta}$, referred to as S33, the maximum principal stress in a radial plane (SP3), and the minimum principal

stress in a radial plane (SP1), in the test specimen at a load level corresponding to 40 %, 90 %, and 100 % of the ultimate load, respectively.

The distribution of the three principal stresses in the cylinder are shown in Fig. 7.5 for a loading equal to 40 % of the ultimate load. Figure 7.5(c) shows almost linear behaviour of the specimen. However, it appears that a triaxial compressive stress state exists at the cylinder end, and a large stress concentration occurs at the corner. This finding is in good agreement to that of an earlier study by Ottosen [98]. However, Ottosen's study resulted in some compressive stress (maximum principal stresses in a radial plane) in the middle of the cylinder in the elastic range. Nevertheless, a uniaxial compressive stress can be closely approximated in the middle of the cylinder (Fig. 7.5(c)) despite the presence of small tensile stresses (Figs. 7.5(a) and (b)) in this region. This is in accordance with Saint-Venant principle of linear elasticity that the axial stress is approximately uniform at a distance equal to the cylinder's diameter from the cylinder edge [129].

Figure 7.6 shows the stress distribution in the cylinder at 90 % of the ultimate load. A comparison of Figs. 7.5(a) and (b) with Figs. 7.6(a) and (b) shows that , with increased loading, the regions with tensile stresses in the middle of the cylinder decrease in size and the stresses becomes less uniform. Comparing Fig. 7.5(c) with 7.6(c) indicate that the axial stress becomes less homogeneous.

The stress distribution in the cylinder at 100 % loading, i.e. failure load, is shown in Fig. 7.7. Note that the regions with tensile stresses change and they become located closer to the outer surface of the cylinder middle (comparing Figs. 7.6(a) and (b) with Figs. 7.7(a) and (b)). In addition, the axial stress in the cylinder becomes inhomogenously disturbed (Fig. 7.7(c)). It is clear that the stress distribution deviates from Saint-Venant principle. This also suggest that the influence of end restraint

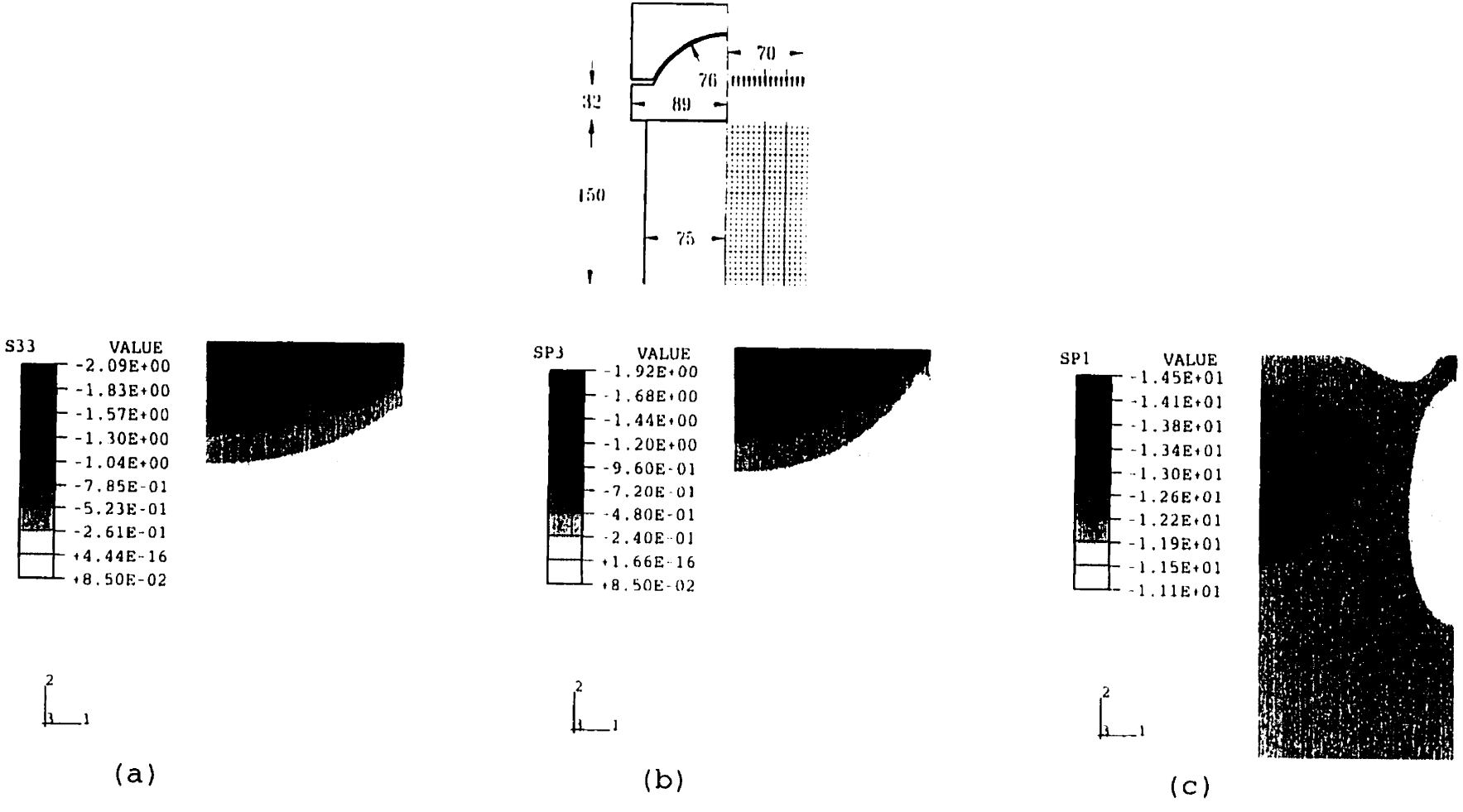

Figure 7.5: Principal stresses for a 150 × 300 mm cylinder, f'_c = 30 MPa, tested with a 152 mm bearing block at nominal axial stress = −12 MPa corresponding to 40 % loading: (a) circumferential stress (S33); (b) maximum principal stress (SP3) in a radial plane; and (c) minimum principal stress (SP1) in a radial plane

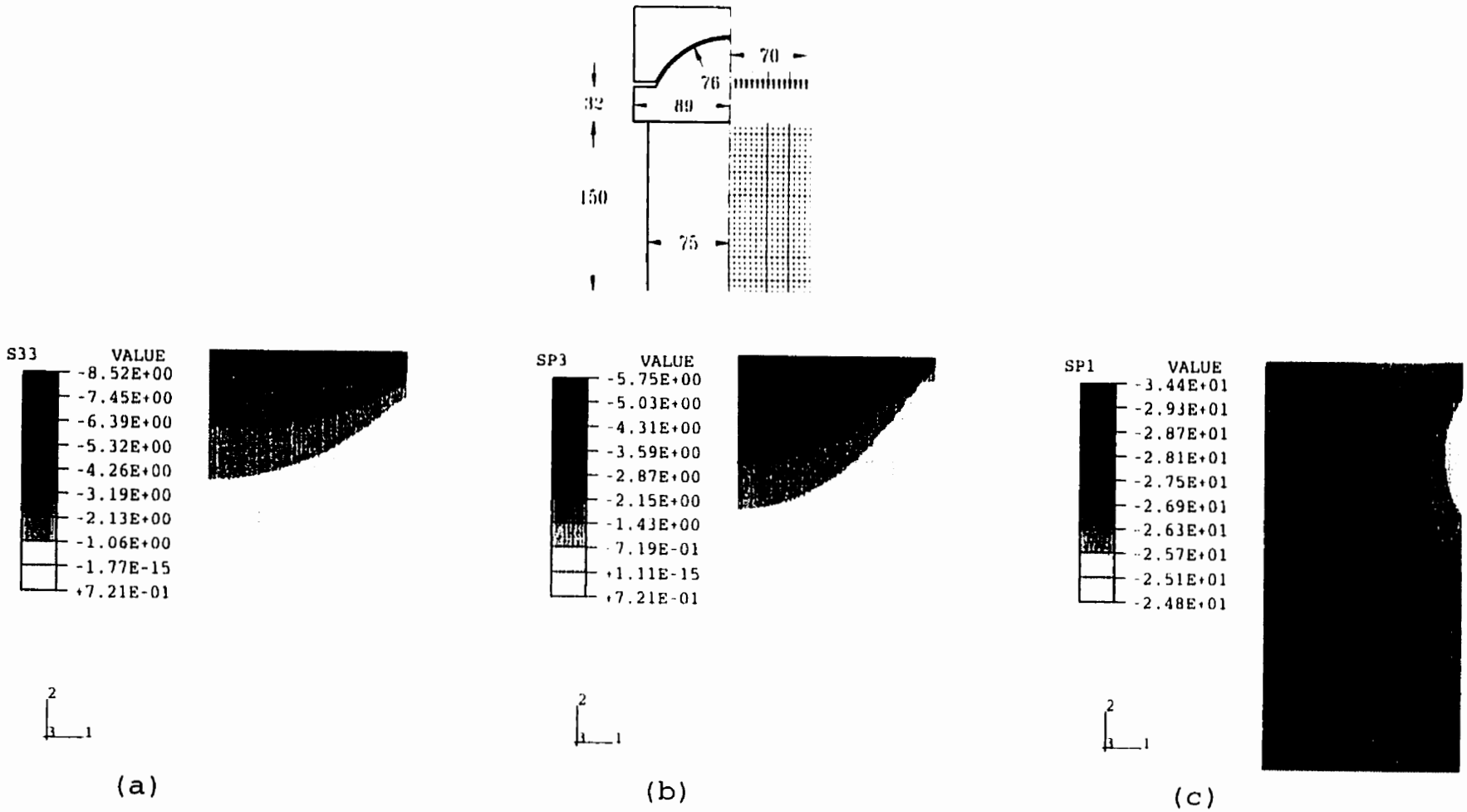

Figure 7.6: Principal stresses for a 150 × 300 mm cylinder, f'_c = 30 MPa, tested with a 152 mm bearing block at nominal axial stress = −27 MPa corresponding to 90 % loading: (a) circumferential stress (S33); (b) maximum principal stress (SP3) in a radial plane; and (c) minimum principal stress (SP1) in a radial plane

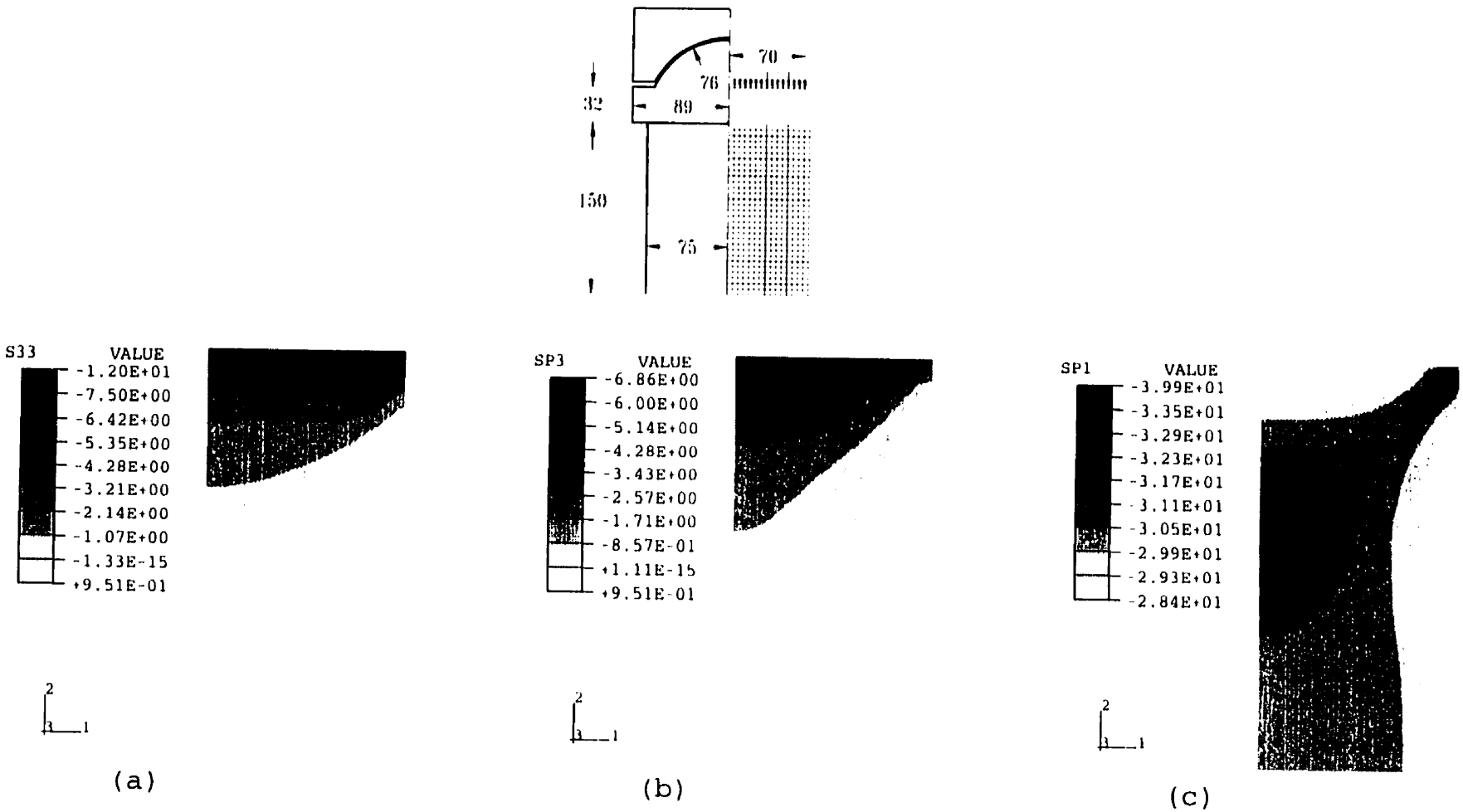

Figure 7.7: Principal stresses for a 150 × 300 mm cylinder, f'_c = 30 MPa, tested with a 152 mm bearing block at nominal axial stress = −30 MPa corresponding to 100 % loading: (a) circumferential stress (S33); (b) maximum principal stress (SP3) in a radial plane; and (c) minimum principal stress (SP1) in a radial plane

becomes more significant as the load on the specimen is increased.

The shear stress, τ_{rz}, and the normal stress, σ_{zz} along the cylinder's edge, at the different load levels, are depicted in Fig. 7.8. The figure shows that the shear stress increases as the applied load is increased. Also, as the load is increased, the axial stress values, close to the edge's centre, drops to a value less than the nominal stress. Moreover, at the specimen's corner, the stress concentration increase as the load level is increased.

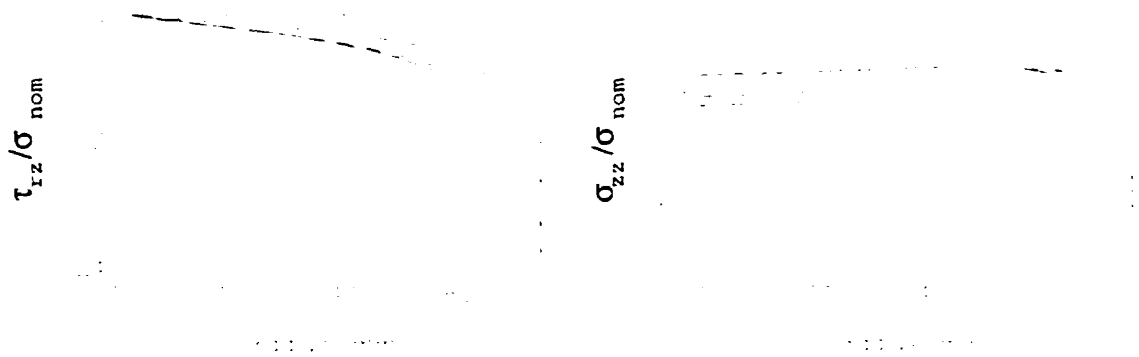

Figure 7.8: Shear stress induced in the specimen, at different loading levels, f'_c = 30 MPa, 150 × 300 mm cylinders that are tested with 150 mm bearing block: (- · - · -) at nominal axial stress = −12 MPa corresponding to 40 % loading, (- - -) at nominal axial stress = −27 MPa corresponding to 90 % loading, (——) at nominal axial stress = −30 MPa corresponding to 100 % loading

The displacement contours in the direction of loading (U2), and in the lateral direction (U1) are shown in Fig. 7.9 at the ultimate load. This figure clearly shows the effect of confinement exerted by the platen on the test specimen in the vicinity of the region of the interface between them. The specimen is restrained in this region. In the middle of the specimen there is confinement. Hence, the displacement contours become uniform. This simulation is based on the assumption that there is no slip between the specimen and the loading block. As concluded by Ottosen [98], the assumption of no slip between the specimen and loading platens seems to be fair

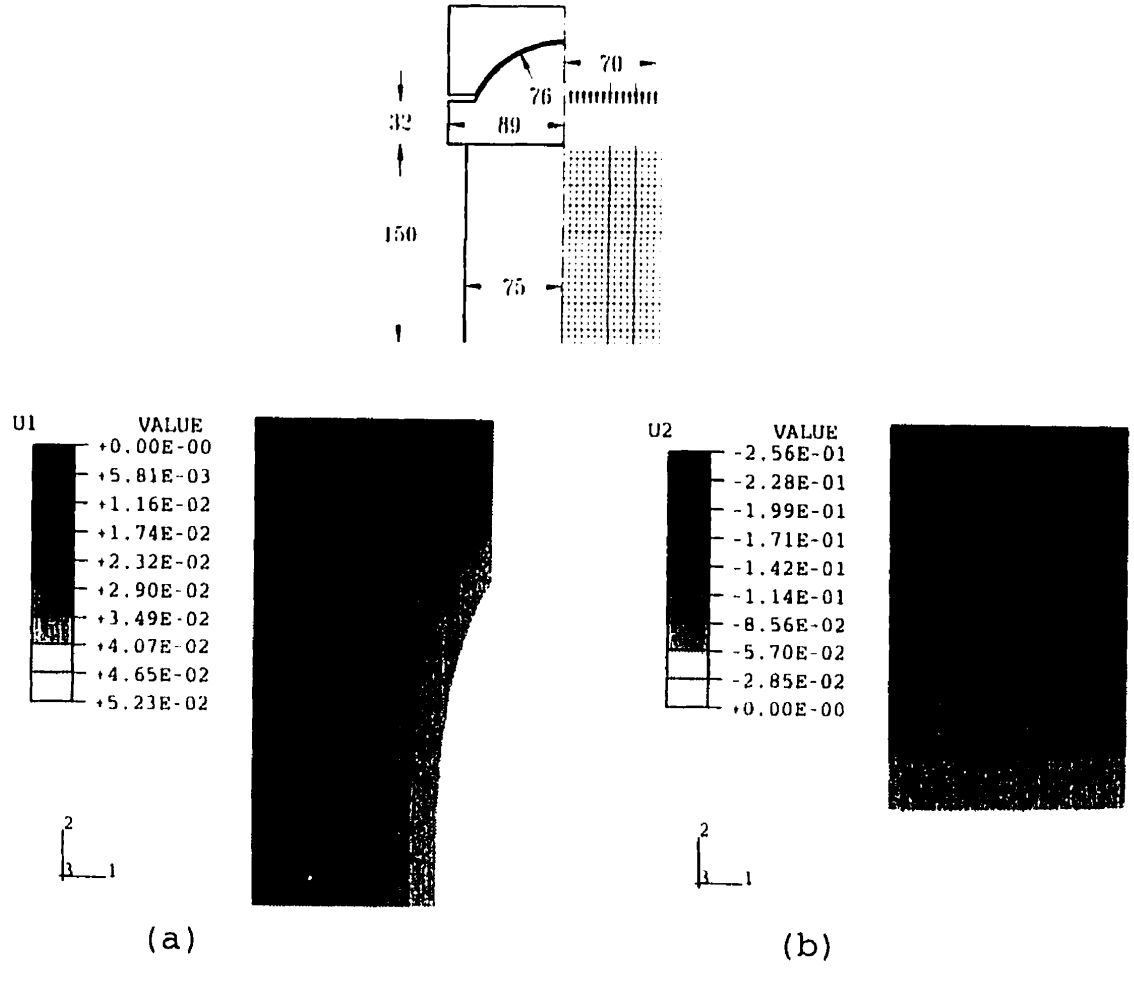

Figure 7.9: Displacement contours for a 150 × 300 mm cylinder, f'_c = 30 MPa, tested with a 152 mm bearing block at nominal axial stress = −30 MPa corresponding to 100 % loading: (a) lateral direction (U1); and (b) axial direction (U2)

for concrete cylinders (as the aspect ratio of the specimen is two). Another method to simulate the interaction between the specimen and the loading blocks can be accomplished by simulating the friction between the two different surfaces. This is achieved through an interface element between the specimen and the bearing block. Such method of modelling is discussed in Chapter 3.

An alternate analysis using this interface element is carried out to examine the differences between the two different types of modelling (slip or no slip). The interface elements used are the same as those presented in Section 3.3. Also, the same friction model (Section 3.4) is employed. Based on the discussion in Section 3.1, a reasonable value for the coefficient of friction is assumed to be 0.25.

The distribution of the three principal stresses in the cylinder, simulated using interface elements, are shown in Fig. 7.10. A comparison between Figs. 7.7 and 7.10 suggest that the axial and hoop stress distribution are almost identical, for both cases, except that using interface element decreases the stress concentration at the specimen's corner. However, the values of the maximum principal stresses in a radial plane, close to the specimen's end, are much higher if a full bond between the specimen and loading block is assumed. The shear stress, τ_{rz}, and the normal stress, σ_{zz}, along the cylinder's edge, for the two modelling assumptions are depicted in Fig. 7.11. The different stress distribution is presented for three different grades of concrete, namely 30, 70 and 100 MPa. The figure shows that the shear stress distribution is almost the same except near the specimen's corner. As anticipated, the use of interface elements result in lower values for shear. This also suggest that some slip may occur at this region. The axial stresses are also very similar. Furthermore, comparing the displacement contours (Fig. 7.9 and Fig. 7.12) shows that the two methods yield almost identical results. However, the displacement contours, in the

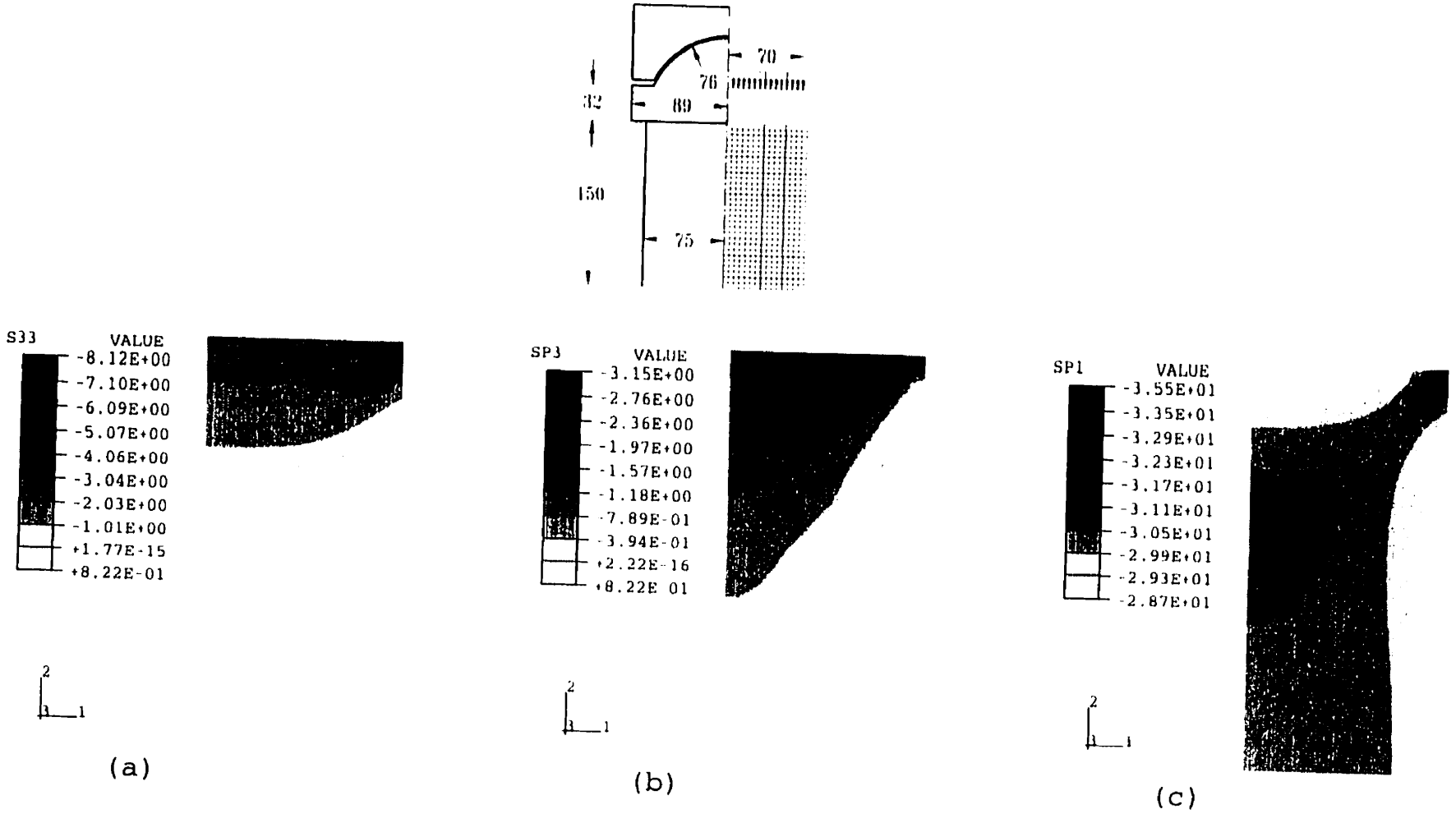

Figure 7.10: Principal stresses for a 150 × 300 mm cylinder, f'_c = 30 MPa, tested with a 152 mm bearing block at nominal axial stress = −30 MPa corresponding to 100 % loading and using interface element to simulate the interaction between the platen and the specimen: (a) circumferential stress (S33); (b) maximum principal stress (SP3) in a radial plane; and (c) minimum principal stress (SP1) in a radial plane

lateral direction. indicate a slightly less restraint at the specimen's edge for the case of interface elements.

Thus. it seems the assumption of a full bond between the specimen (with an aspect ratio of 2) and the loading block provides similar results as those produced using interface elements. It should be noted that the analysis is carried out using a friction coefficient of 0.25 and it is assumed constant throughout the test. Using different values of the coefficient of friction could change the results. Nonetheless. more experimental evidence is warranted in this area. In the following sections. the analysis is carried out assuming full bond between the specimen and the loading blocks.

7.9 Effects of Different Test Variables

In this section. the effects of different variables on the standard compression test are presented and discussed. The parameters investigated are the concrete compressive strength. specimen dimensions. bearing block dimensions. and the specimen's end preparation (effect of mechanical properties of the capping material). Those parameters are selected to simulate the actual ones used in the standard compression tests.

7.9.1 Concrete Compressive Strength

In order to study the influence of the compressive strength on the behaviour of a compression test specimen. three cylinders are analyzed. The cylinders have compressive strengths of 30. 70 and 100 MPa. The cylinders are selected to represent the common standard case. that is a 150 × 300 mm specimen tested with a 152 mm end block (Case 1 in Fig. 7.4).

Figures 7.13 and 7.14 show the stress fields in a test specimen with a compressive

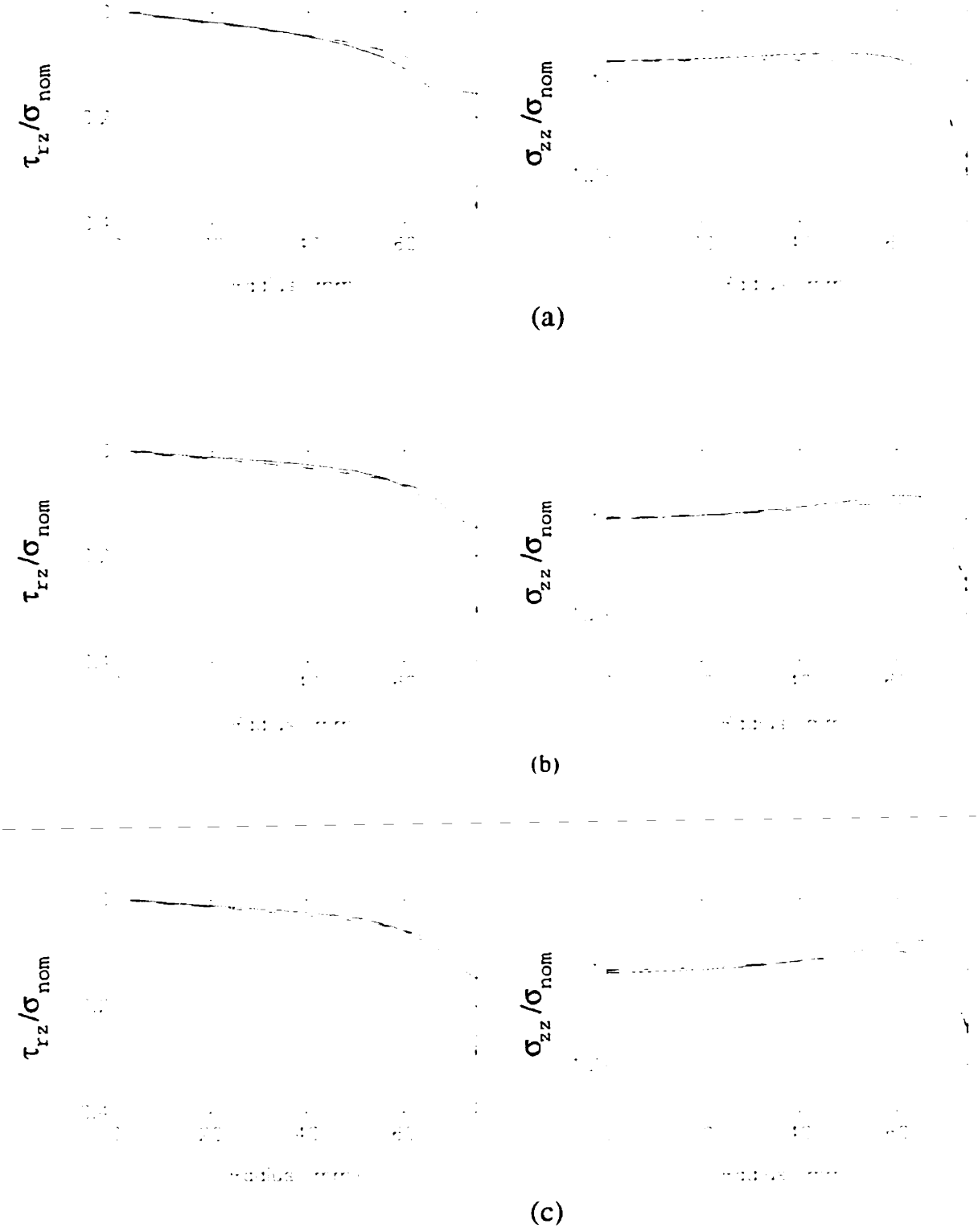

Figure 7.11: Shear stress induced in the specimen, along cylinder end. 150 × 300 mm cylinders that are tested with 150 mm bearing block, using different modelling assumptions, (——) assuming full bond between the platen and the specimen, (- - -) using interface elements: (a) f'_c = 30 MPa; (b) f'_c = 70 MPa and (c) f'_c = 100 MPa

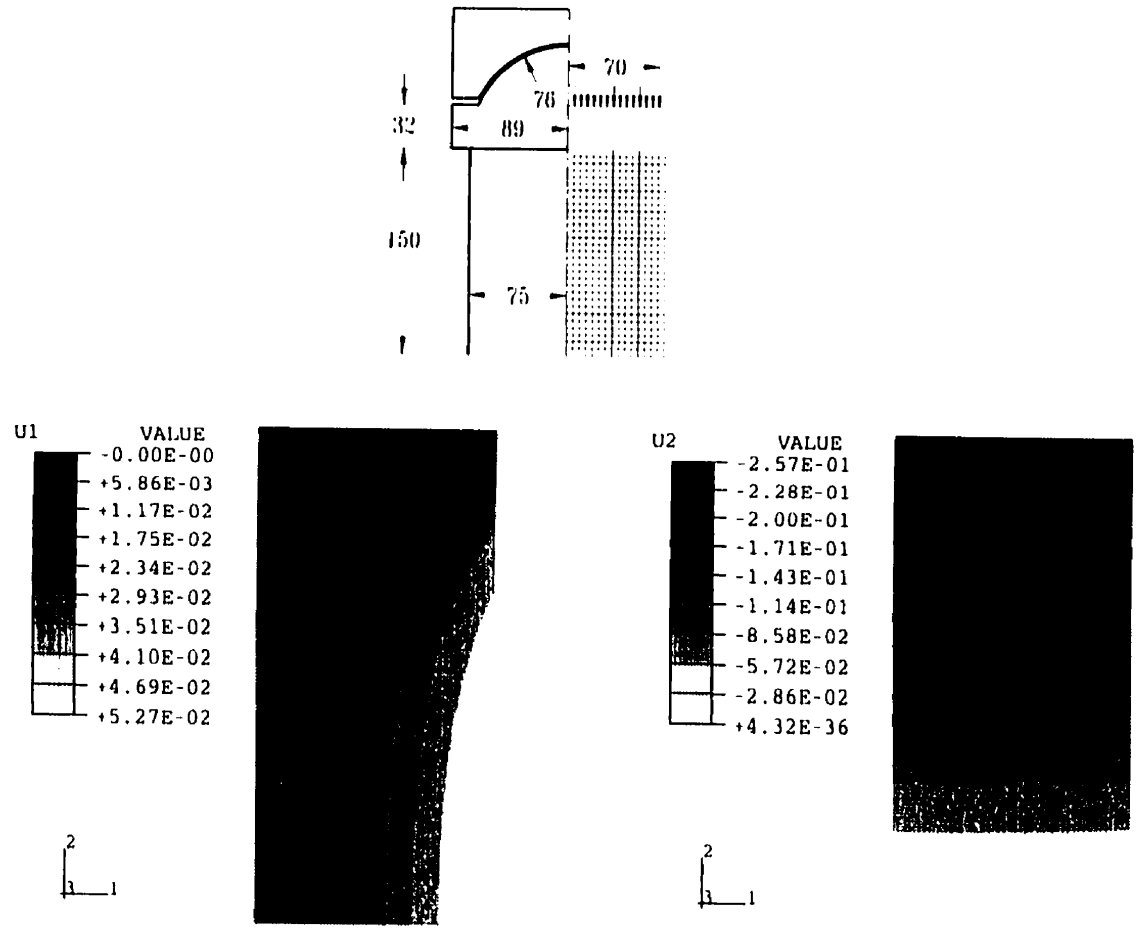

Figure 7.12: Displacement contours for a 150 × 300 mm cylinder, f'_c = 30 MPa, tested with a 152 mm bearing block at nominal axial stress = −30 MPa corresponding to 100 % loading and using interface element to simulate the interaction between the platen and the specimen: (a) lateral direction (U1); and (b) axial direction (U2)

strength of 70 and 100 MPa, respectively. The stresses in a 30 MPa cylinder were shown in Fig. 7.7. In general , the figures show that the minimum principal stresses (SP1) in the specimen, at the area under the platens, are smaller than the nominal applied stress. In addition there is a high stress concentration at the cylinder's corner. As the concrete compressive strength is increased, the area of low stresses decreases in size and the stress concentration at the specimen's corner slightly decreases. To facilitate the comparison between the different figures, the contour intervals of the axial stress are kept at a value of 2.0 % of f'_c, except for the last contour interval that reflects the stress concentrations at the cylinder's corners.

At the outer sides of the specimen there exists an area of low compressive stresses (Fig. 7.7(c). This area is extended down towards the cylinder's mid plane (for the 30 MP concrete specimen). As the specimen compressive strength is increased that region is decreased in size (Figs. 7.13(c) and 7.14(c). In addition, the state of stress near the middle of the cylinder becomes more uniform and closer to the nominal strength. This indicates that the state of stress in the middle of the cylinder becomes more homogeneous as the concrete compressive strength is increased.

The distributions of the maximum principal stresses (SP3), in a radial plane, are shown in Figures 7.7(c), 7.13(c), and 7.14(c) for the three grades of concrete (30, 70 and 100 MPa), respectively. For the 30 MPa concrete, the stresses in the middle plane of the cylinder, and towards the centre line of the specimen, are compressive and they change to tensile stresses towards the outer part of the cylinder. For the specimens with higher strength, the stresses in the middle plane of the cylinder are completely tensile.

Figures 7.7(a), 7.13(a), and 7.13(a) show the distribution of the circumferential stresses (S33), for the three grades of concrete (30, 70 and 100 MPa), respectively.

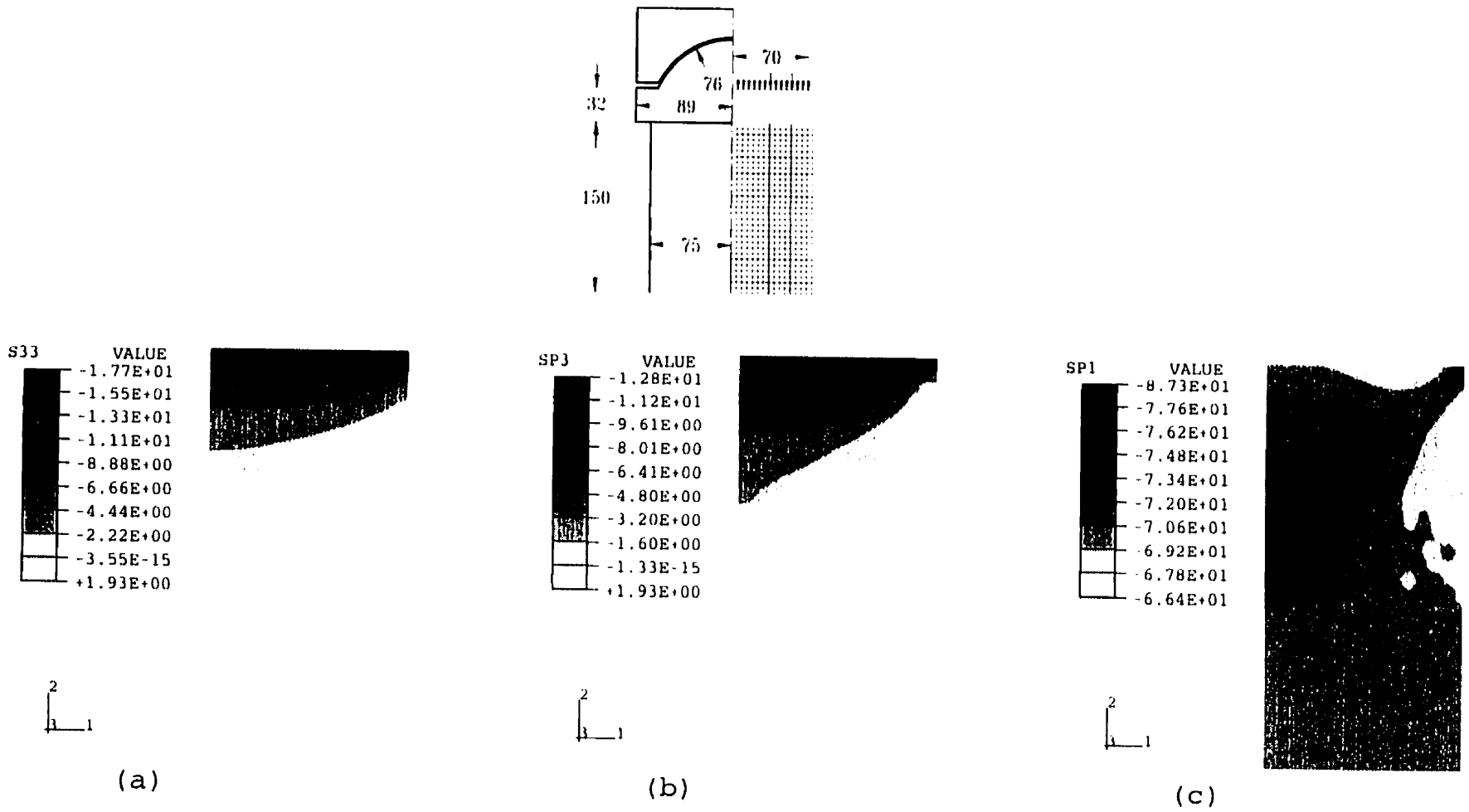

Figure 7.13: Principal stresses for a 150 × 300 mm cylinder, f'_c = 70 MPa, tested with a 152 mm bearing block at nominal axial stress = −70 MPa corresponding to 100 % loading: (a) circumferential stress (S33); (b) maximum principal stress (SP3) in a radial plane; and (c) minimum principal stress (SP1) in a radial plane

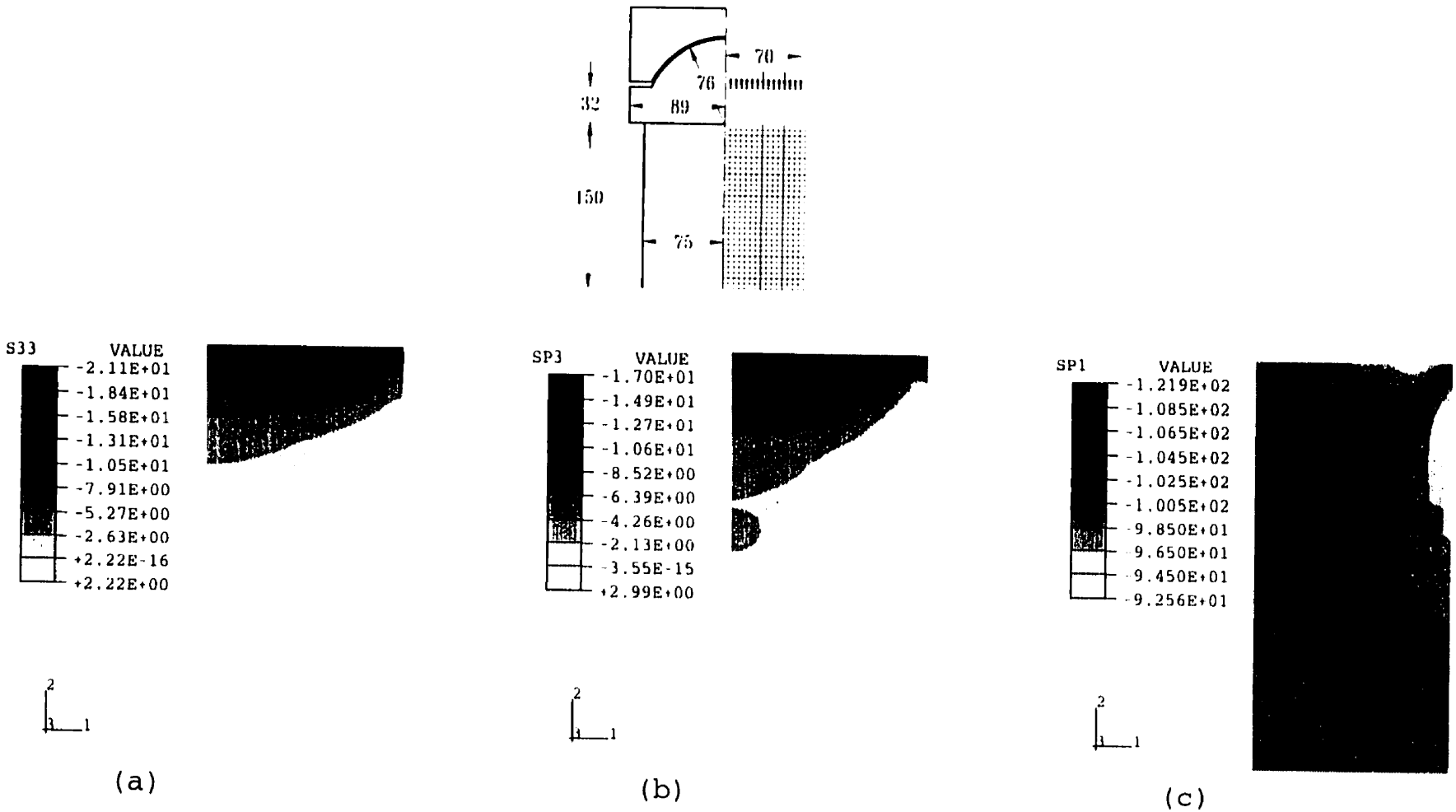

Figure 7.14: Principal stresses for a 150 × 300 mm cylinder, f'_c = 100 MPa, tested with a 152 mm bearing block at nominal axial stress = −100 MPa corresponding to 100 % loading: (a) circumferential stress (S33); (b) maximum principal stress (SP3) in a radial plane; and (c) minimum principal stress (SP1) in a radial plane

At the outer sides of the specimen's mid-plane, there is a region of low compressive stresses for the 30 MPa concrete specimen. The stresses change to tension near the centerline of the cylinder. As the compressive strength of the specimen increase, the stresses in the middle of the cylinder, at failure, become completely tensile. However, a small compression region appears at the centre of the specimen.

Figure 7.15 shows the shear stresses induced along the edge of the specimen (at failure) for the three grades of concrete: 30, 70 and 100 MPa. The figures show that the shear stresses at the interface varies very rapidly near the outside edge of the cylinder, rising very quickly and dying down more slowly towards the centre of the cylinder. The values of shear stress increase as the compressive strength increases. This is due to the higher failure loads of the specimen. However, the ratio of shear stresses to normal stresses decreases as the concrete compressive strength increases. Increasing the compressive strength from 30 MPa to 70 MPa changes the ratios of τ_{12}/σ_{22} from 31.2 % to 26.7 %. If the compressive strength for the specimens is increased from 70 MPa to 100 MPa, the ratios of τ_{12}/σ_{22} change from 26.7 % to 25.6 %. This could be interpreted by the reduction of the coefficient of friction between the steel loading platens and the concrete specimen as the required axial loads are increased (for cylinders with high compressive strength). Also, this finding could be considered to be in good agreement with previous analytical investigations [12] which concluded that as the ratio $(\nu/E)_{specimen}$ approaches the value of $(\nu/E)_{platen}$, the shear stresses induced in the specimen, at the specimen/platen interface, tend to decrease. Note that as the specimen's strength increases, its $(\nu/E)_{specimen}$ ratio tends to decrease.

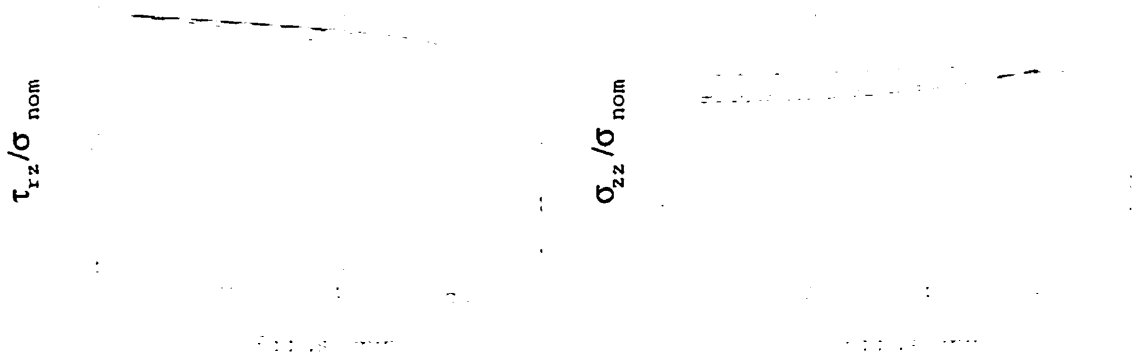

Figure 7.15: Shear stress induced in the specimen, along cylinder end, for different compressive strength. 150 × 300 mm cylinders that are tested with 150 mm bearing block: (- · - · -) f'_c = 30 MPa; and (- - -) f'_c = 70 MPa; (——) f'_c = 100 MPa

7.9.2 Specimen Size

The standard form of the common compression test for a concrete specimen (150 × 300 mm) was discussed in the previous section (Case 1 in Fig. 7.4). The 100 × 200 mm cylinder is popular, nowadays, for testing high strength concrete specimen. A 102 mm bearing block is required to test such a specimen (ASTM Test Method C 39-1993a). The 100 × 200 mm cylinder is discussed in this section (Case 4 in Fig. 7.4).

Figures 7.16, 7.17 and 7.18 show the stress distribution in a 100 × 200 mm specimen, tested by a 102 mm bearing block, with compressive strengths of 30, 70 and 100 MPa, respectively. A comparison of these figures with Figs. 7.7, 7.13, and 7.14 suggests that the stresses in the 100 × 200 mm specimen closely match those in the 150 × 300 mm specimen. This finding demonstrates that using the right dimensions of end blocks can replicate the stresses in the specimen with different sizes. However, some minor differences still exist. The stress concentration, at the specimen's corner, is lower for the 100 × 200 mm cylinders. Moreover, as the specimen's strength increases, the stress concentration becomes less for the small cylinders. The same tendency is also observed for the maximum principal stresses. In addition, the val-

ues of the tensile stresses, in a radial plane, are slightly lower for the case of small cylinders. Yet, the circumferential stresses assume the same trend for both cases with higher values for the 150 × 300 mm cylinders.

Figure 7.19 shows the shear and normal stress distribution at the interface between the specimen and the loading platens for the 100 × 300 mm specimens. The shear stresses rises from the centre of the cylinder to the outside edge. The stress distribution is similar to the 150 × 300 mm case (Fig. 7.15). However, the ratio of shear stress to normal stress is slightly lower in the small specimens. This indicates less restraining effect for the small specimen. The normal stress distribution is almost identical.

Although not presented here, the shapes of the displacement contours are almost identical for the 100 × 200 mm and the 150 × 300 mm cylinders. The values of the displacements the direction of loading (U2), and in the lateral direction (U1) are given in Table 7.3 at the ultimate load. From this table, it can be found that the ratio of the corresponding displacements, for the smaller and bigger cylinders, is almost 1.5. This demonstrates that both tests will lead to the same values of the measured intrinsic properties (E and ν).

The values of the failure loads were equal to the assumed compressive strength, for all cylinder grades, as in the case of the 150 × 300 mm cylinders. In the literature, different experimental investigations produced contradicting results for the strength ratio of the 100 × 200 mm cylinders to that of the 150 × 300 mm cylinders [reported in ref. [127]]. However, recent experimental investigations [127, 126] revealed that a factor of 1.03 - 1.05 exists. The current finite element results could not detect such a difference. The ultimate loads were almost matching in both cylinders. This factor could be attributed to other factors that are not included in the study such as the

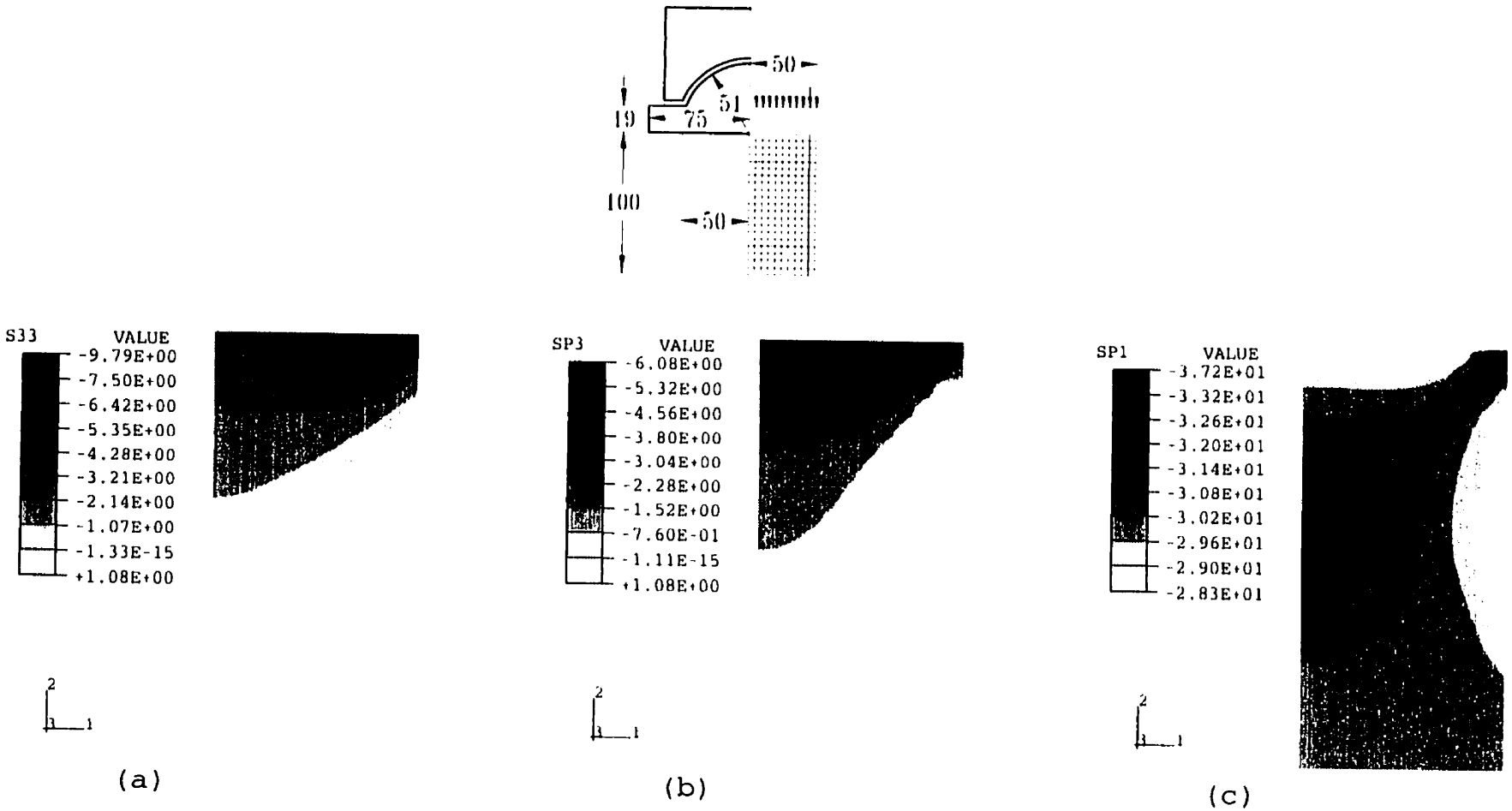

Figure 7.16: Principal stresses for a 100 × 200 mm cylinder, f'_c = 30 MPa, tested with a 102 mm bearing block at nominal axial stress = −30 MPa corresponding to 100 % loading: (a) circumferential stress (S33); (b) maximum principal stress (SP3) in a radial plane; and (c) minimum principal stress (SP1) in a radial plane

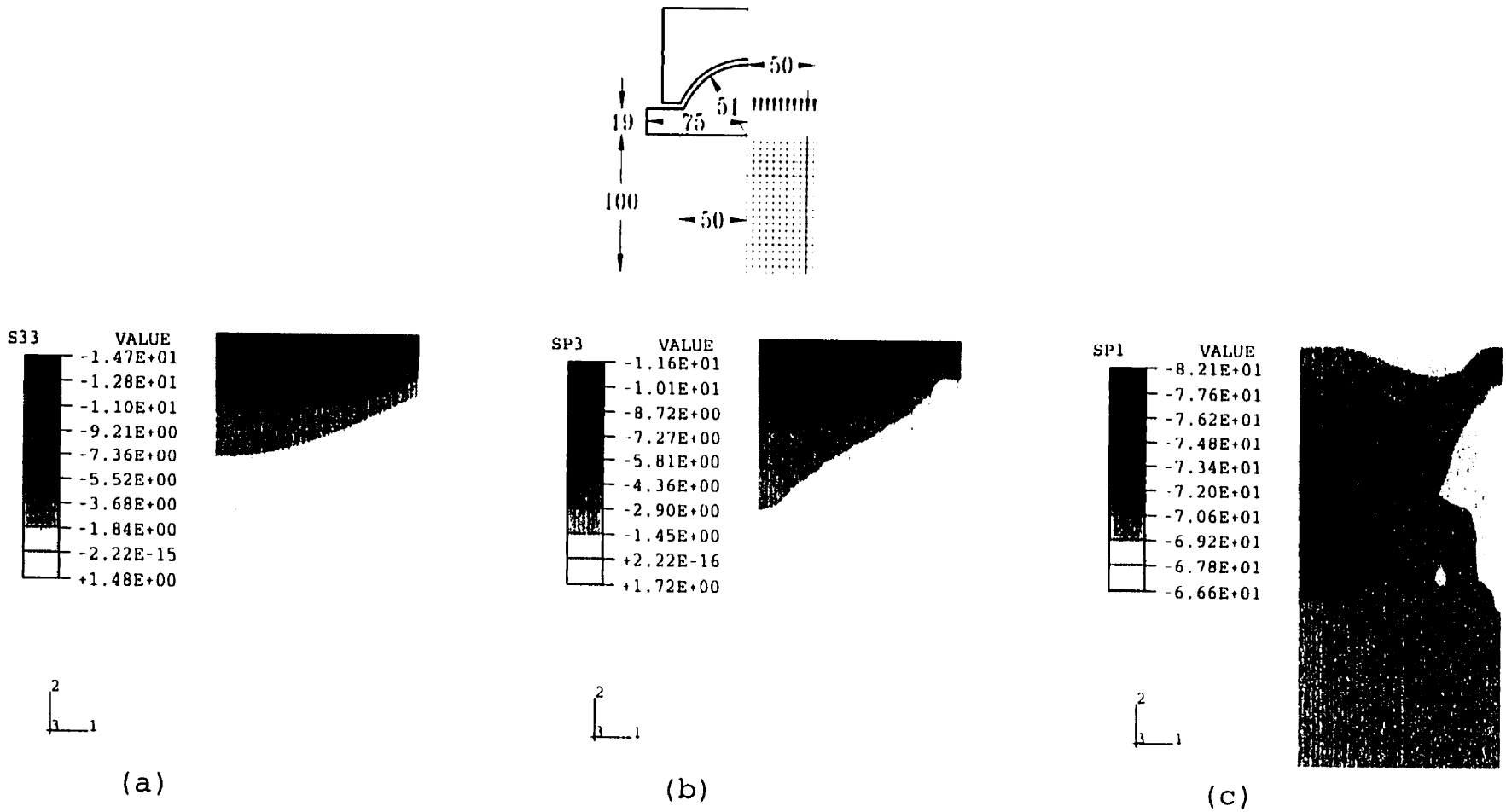

Figure 7.17: Principal stresses for a 100 × 200 mm cylinder, f'_c = 70 MPa, tested with a 102 mm bearing block at nominal axial stress = −70 MPa corresponding to 100 % loading: (a) circumferential stress (S33); (b) maximum principal stress (SP3) in a radial plane; and (c) minimum principal stress (SP1) in a radial plane

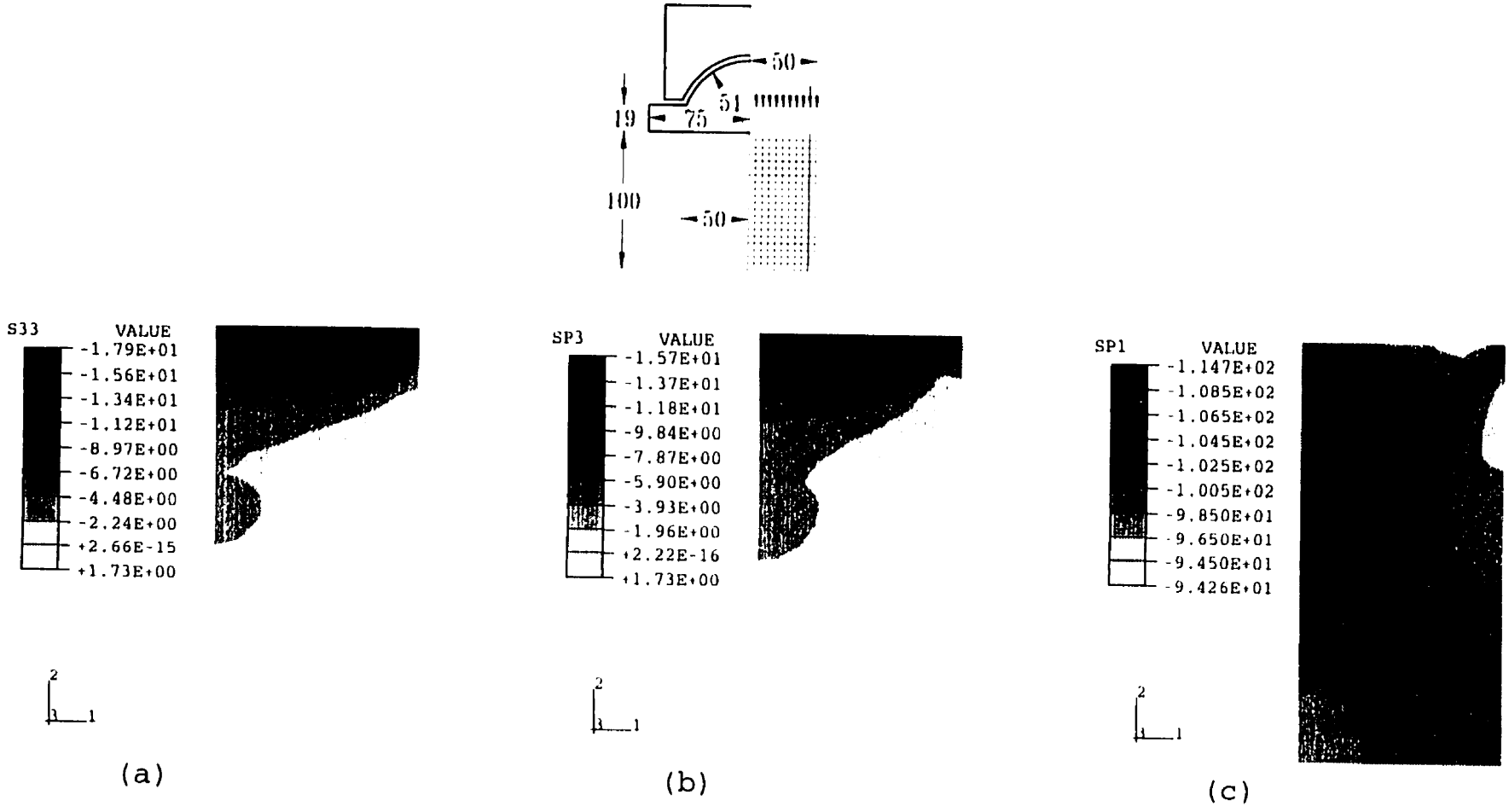

Figure 7.18: Principal stresses for a 100 × 200 mm cylinder, f'_c = 100 MPa, tested with a 102 mm bearing block at nominal axial stress = −100 MPa corresponding to 100 % loading: (a) circumferential stress (S33); (b) maximum principal stress (SP3) in a radial plane; and (c) minimum principal stress (SP1) in a radial plane

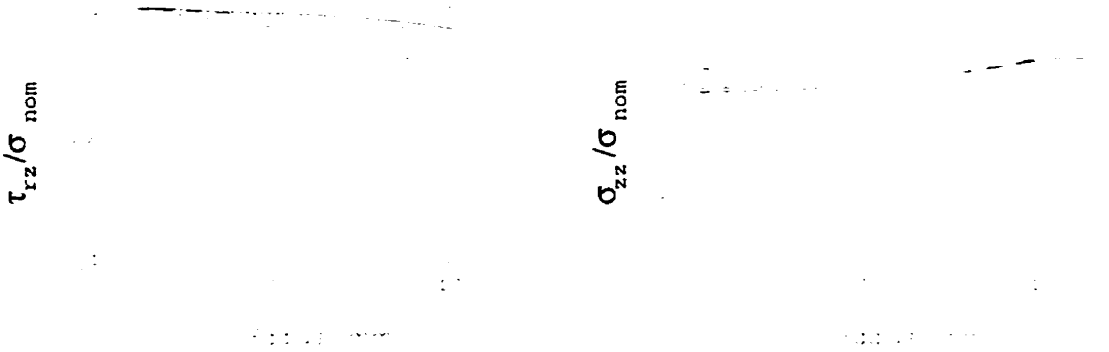

Figure 7.19: Shear stress induced in the specimen, along cylinder end, for different compressive strength. 100 × 200 mm cylinders that are tested with 102 mm bearing block: (- · - ·) f'_c = 30 MPa; (- - -) f'_c = 70 MPa; and (——) f'_c = 100 MPa

Table 7.3: Displacement values in the lateral direction (U1), and in the direction of loading (U2), at the ultimate load, for one-quarter of the test cylinder

Specimen size mm	f'_c MPa	U1 mm	U2 mm
150 × 300	30	5.23E-02	2.56E-01
	70	5.34E-02	3.39E-01
	100	5.45E-02	3.97E-01
100 × 200	30	3.21E-02	1.67E-01
	70	3.57E-02	2.26E-01
	100	3.77E-02	2.65E-01

effect of aggregate size and aggregate scaling (with respect to the specimen size) on the fracture process. Other factors could also contribute to the difference such as the lateral and longitudinal stiffness of the testing machines and their effect on the specimens with different sizes. However, these factors were not considered in the current study.

7.9.3 Bearing Block Dimensions

As previously described, ASTM Test Method C 39-1993a for standard compression test requires that a bearing block with a 152 mm block is used for testing 150 × 300 mm while a 102 mm block is used for testing 100 × 200 mm cylinders.

The two standard cases for the 100 × 200 mm and the 150 × 300 mm cylinders were discussed in the previous sections. In order to examine the influence of the bearing block on the compression test, two non-standard cases are considered. The first case portrays a 150 × 300 mm specimen tested with a 102 mm bearing block (Case 2 in Fig. 7.4). The second case represent a 100 × 200 mm tested with a 152 mm bearing block (Case 3 in Fig. 7.4). The selection of the first case is inspired by the experimental program conducted by the researchers at The Université de Sherbrooke [127]. The experimental results revealed a drop in strength of 20 % for high strength concrete (100 MPa) for this case. Also, a splitting type of failure occurred to the specimen.

Figure 7.20 shows the stress fields in a 150 × 300 mm test specimen $f'_c = 30$ MPa, and tested with a 102 mm diameter bearing block. Comparing Fig. 7.20 with Fig. 7.7 reveals that stress distribution in the specimen is completely different for the two cases. The circumferential stresses in the specimen, for the non-standard case considered here, are almost tensile except for a small area under the loading platens where the stresses are compressive. However, the stresses change from compressive to

tensile towards the specimen's corner. In addition, the values of the tensile stresses are much higher than the standard case. The same applies for the maximum principal stresses in a radial plane. The axial stresses are the highest under the platens and decrease towards the specimen's corner. This case is completely opposite to the standard case.

In addition, the ultimate loads for the specimens do not attain the value of the nominal compressive strength, f'_c, for the specimen. In fact the failure loads are 72.8, 57.1 and 53.7 % of the compressive strength for the 30, 70 and 100 MPa specimens, respectively. A most noteworthy finding here occurs when one observes the effect of the 102 mm bearing block on the 150 × 300 mm cylinder. As the specimen's compressive strength is increased, the specimen's failure load decreases drastically.

The failure loads, from the finite element simulation, are much lower than the experimental ones. Thus, based on the experimental results reported in [127], a possibility of slip between the specimen and the platens is considered. Interface elements are used to model the interaction between the platen and the specimen. The coefficient of friction is assumed to be 0.25. The simulation, using interface elements, revealed that the values of the obtained ultimate loads changed to 81.6, 64.2 and 59.2 % for the 30, 70 and 100 MPa specimens, respectively. Thus, it seems the analysis, assuming full bond between the specimen and the loading platens, may not be appropriate for such a case. However, no more attempts were made by assuming a lower coefficient of friction to improve the solution as this case is considered non-standard and should be prohibited.

The results of the simulation,using interface elements, are shown in Fig. 7.21. The significant finding from that figure is that the maximum principal stresses are lower (compared to Fig. 7.20), and the axial loads are higher (under the loading platens).

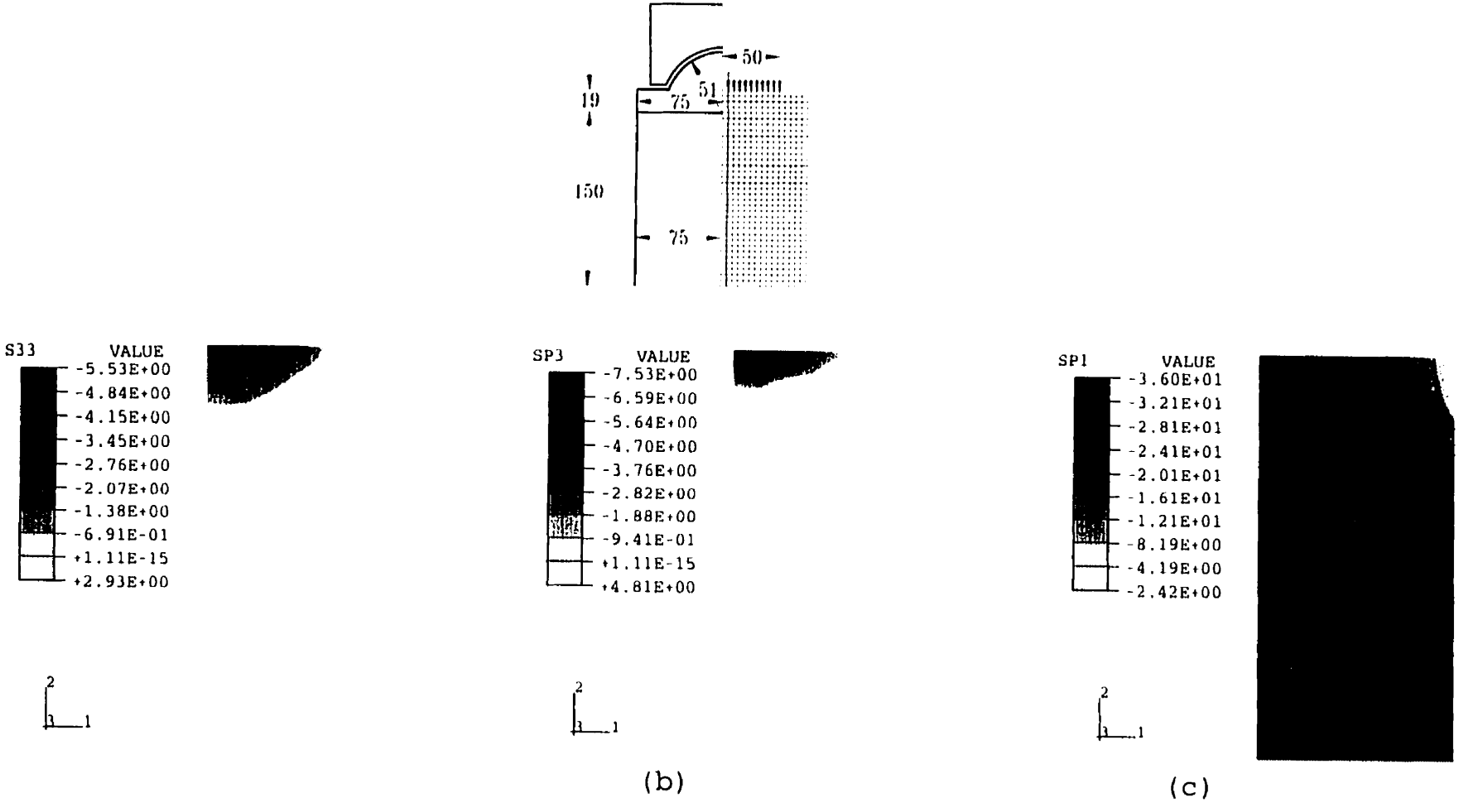

Figure 7.20: Principal stresses for a 150 × 300 mm cylinder, f'_c = 30 MPa, tested with a 102 mm bearing block at nominal axial stress = −30 MPa corresponding to 100 % loading: (a) circumferential stress (S33); (b) maximum principal stress (SP3) in a radial plane; and (c) minimum principal stress (SP1) in a radial plane

The circumferential stresses are almost the same.

The shear stress, τ_{rz}, and the normal stress, σ_{zz} along the cylinder's edge, at failure, are depicted in Fig. 7.22. At the interface the shear stresses changes direction, i.e., it produces a tensile force at the specimen. This leads to an apparent decrease of strength (as in the case of using weak lubricants to eliminate the friction between the specimen and the end blocks). In addition, due to the lack of confinement, the cup and cone failure will not be obtained; instead, a splitting type of failure will occur in the specimen. This is in good agrement with the experimental results [127]. The normal stress distribution along the edge is far from uniform with a value higher that the nominal stress under the platen (at the specimen edge's centre) and reaching a value close to zero at the specimen's corner.

Case 3 illustrates a cylinder with dimensions (100 × 200 mm) tested with a 150 mm end block (Fig. 7.4). The stresses in the cylinder (Fig 7.23) shows that the stresses are very disturbed in the cylinder. In addition, they are far more different than the standard case (Fig. 7.7). However, the failure loads, produced from this case, were almost identical to the standard case.

Figure 7.24 shows the shear stress distribution at the interface between the specimen and the loading platens. The shear stresses rise from the centre the of the cylinder to the outside edge. If this figure is compared with the standard case (Fig. 7.19), it is noticed that the gradients of the shear stresses varies very slowly. This means that the total shear force along the edges of 100 × 200 mm is higher if a 150 mm bearing block is used.

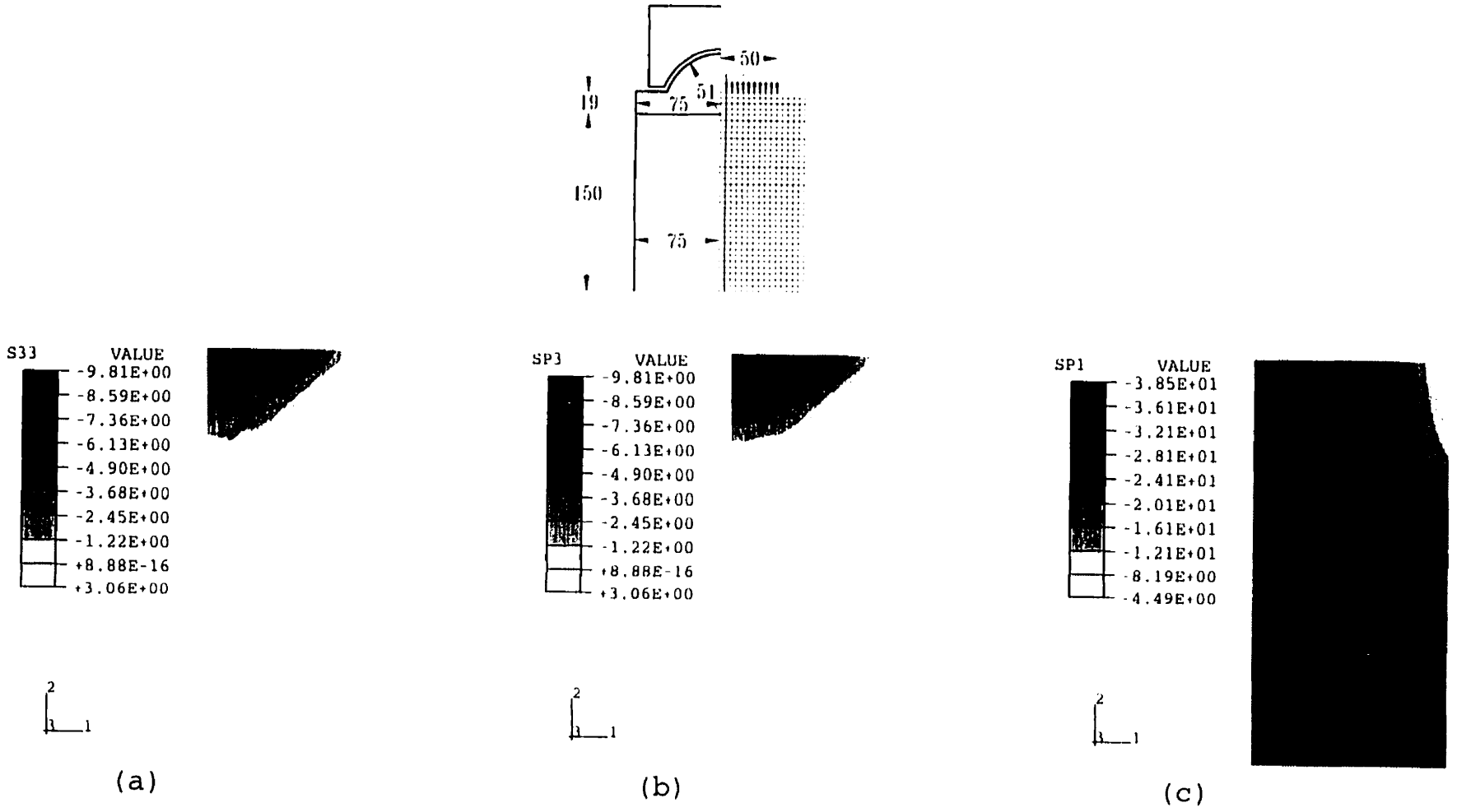

Figure 7.21: Principal stresses for a 150 × 300 mm cylinder, f'_c = 30 MPa, tested with a 102 mm bearing block at nominal axial stress = −30 MPa corresponding to 100 % loading and using interface element to simulate the interaction between the platen and the specimen: (a) circumferential stress (S33); (b) maximum principal stress (SP3) in a radial plane; and (c) minimum principal stress (SP1) in a radial plane

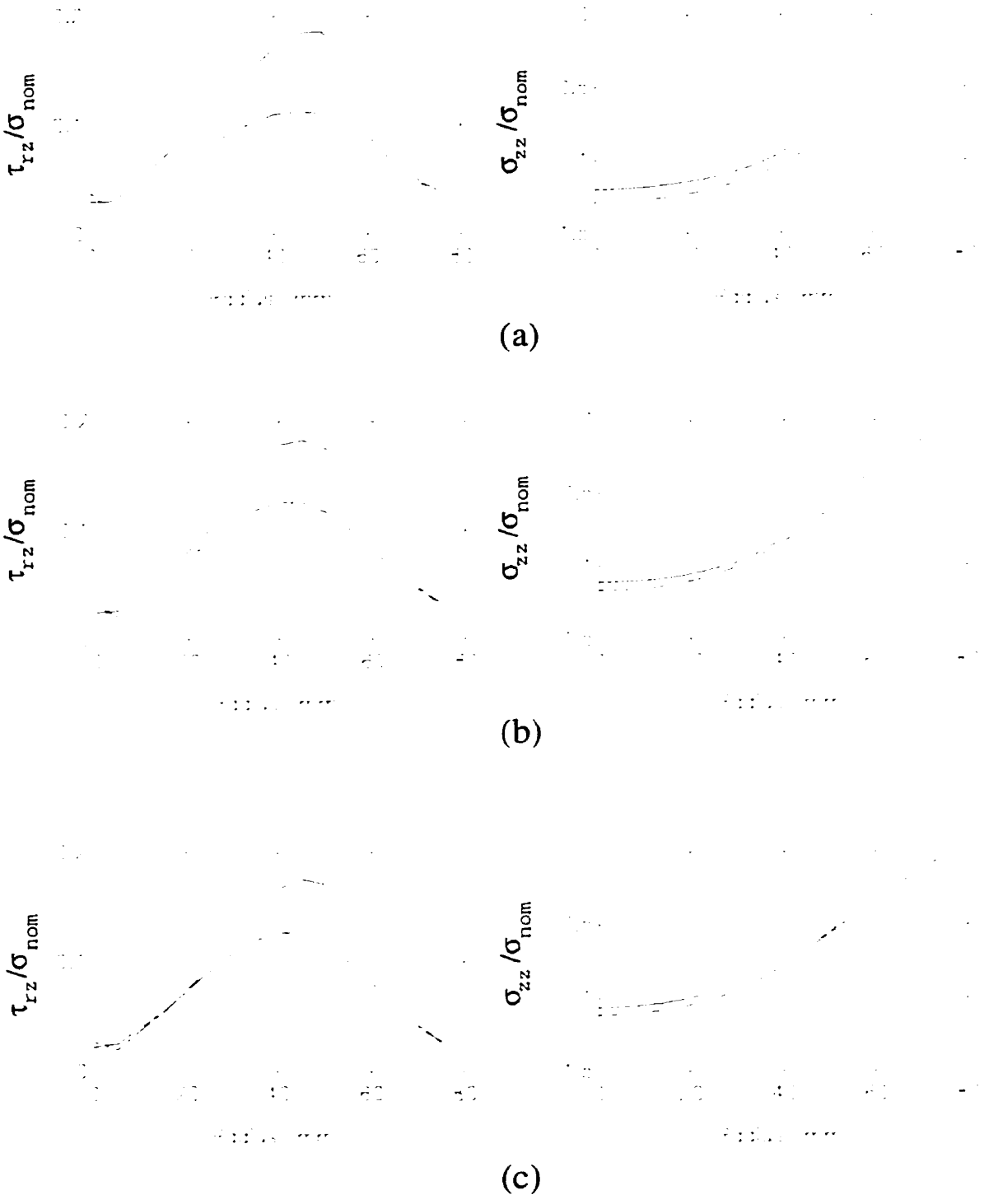

Figure 7.22: Shear stress induced in the specimen, along cylinder end, 150 × 300 mm cylinders that are tested with 102 mm bearing block, using different modelling assumptions: (——) assuming full bond between the platen and the specimen, (- - -) using interface elements: (a) f'_c = 30 MPa; (b) f'_c = 70 MPa and (c) f'_c = 100 MPa

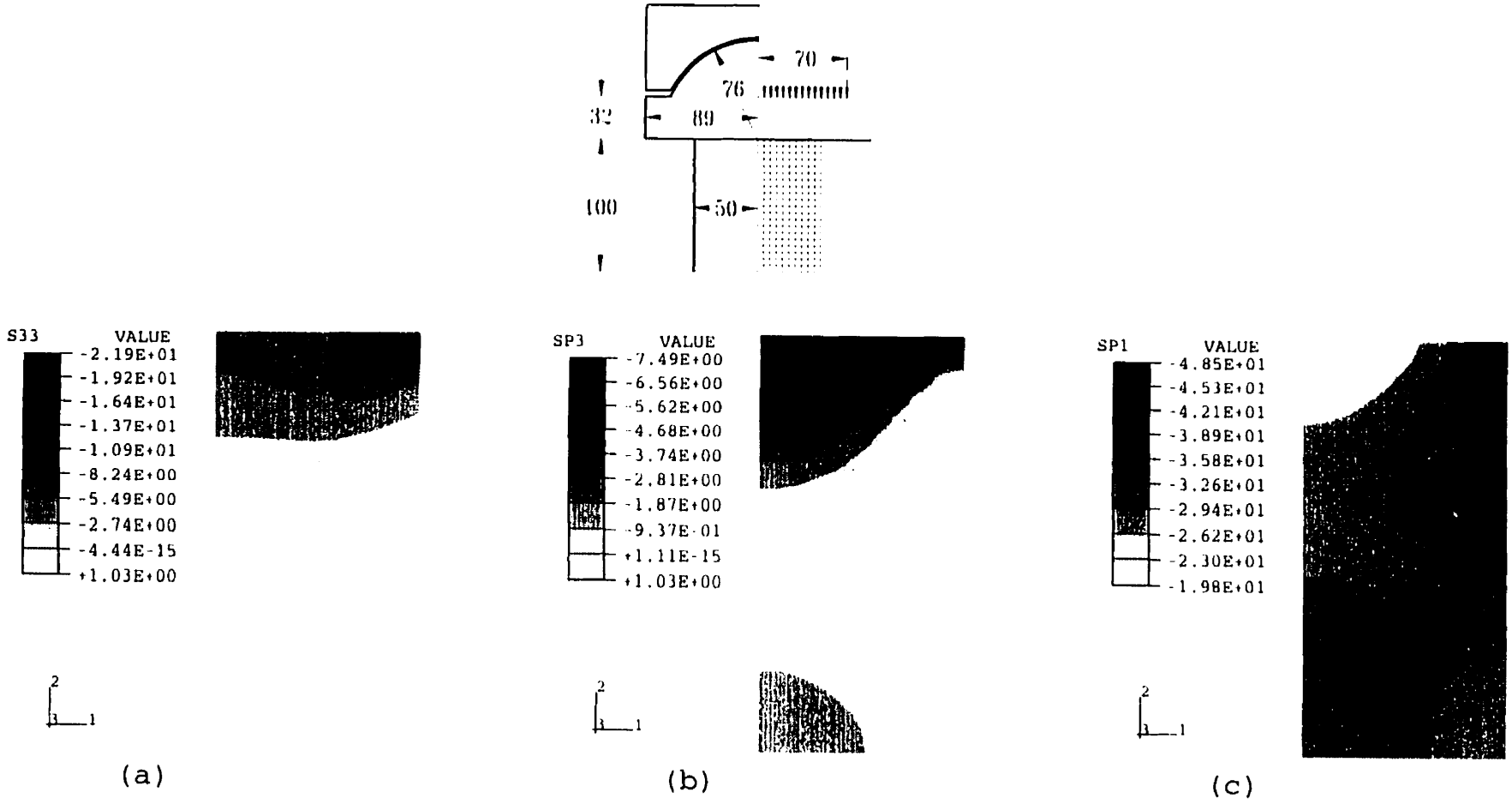

Figure 7.23: Principal stresses for a 100 × 200 mm cylinder, f'_c = 30 MPa, tested with a 152 mm bearing block at nominal axial stress = −30 MPa corresponding to 100 % loading: (a) circumferential stress (S33); (b) maximum principal stress (SP3) in a radial plane; and (c) minimum principal stress (SP1) in a radial plane

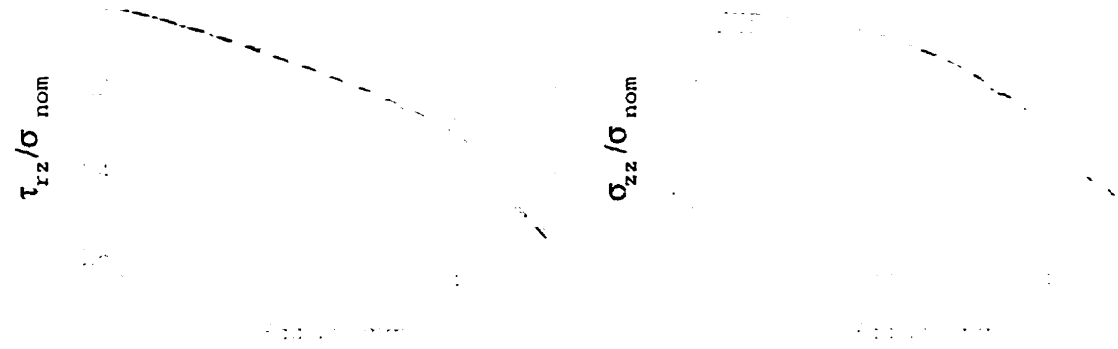

Figure 7.24: Shear stress induced in the specimen, along cylinder end, for different compressive strength, 100 × 200 mm cylinders that are tested with 150 mm bearing block: (- · - ·) f'_c = 30 MPa; (- - -) f'_c = 70 MPa; and (——) f'_c = 100 MPa

7.10 End Preparation of the Specimen

ASTM Practice C 617 [130] allows the use of either (a) neat cement paste, (b) high-strength gypsum plaster, or (c) sulphur mortar as capping materials. The strength requirements, although ambiguous, can be simply interpreted as the cap shall be at least as strong as the concrete. Also, the recommended cap thickness is 3 mm and should never be more than 8 mm. The current research on capping materials for high strength concrete includes the use of the traditional sulphur capping compound, grinding the specimen's end, and the use of unbounded caps and the sand box. A comprehensive, and up-to-date, literature review, regarding different capping methods, can be found in [126].

The previous results, presented in this chapter, can be considered to simulate a test specimen with ground ends. In this section, the effect of the capping material is examined. Two extreme cases are considered: (a) the use traditional sulphur caps, and (b) the use of a very soft material such as rubber. The unbounded caps and the sand box are not considered in this study.

In order to obtain accurate results from the finite element simulation, the mechanical properties of the capping materials should be identified properly. Unfortunately, there is no data available, in the literature, on the mechanical properties of the most commonly used capping material, sulphur compound. The only reported data about the modulus of elasticity using sonic readings [131] indicate that the modulus of elasticity of sulphur, used in that study, varies from 15 - 25 GPa. Consequently a modulus of elasticity of 25 GPa and Poisson's ratio of 0.15 can be considered a reasonable assumption. Such values are used in the study. The Young's modulus of elasticity for rubber is assumed 25 MPa while Poisson's ratio is taken as 0.45.

Four cases are considered: rubber capping with thicknesses of 1.5 and 3 mm, and sulphur capping with thicknesses of 3 and 6 mm. The capping is modelled with an eight-node axisymmetric element with 4 integration points. Full bond is assumed between the cap and the bearing block as well as between the cap and the specimen. Since the behaviour of the sulphur compound is not known, the material is assumed to be linear elastic. Also, for simplicity, a linear elastic model was used to simulate the rubber cap. Such an assumption may not be completely accurate, and it would greatly affect the results of the finite element simulation. Nevertheless, unless the behaviour of the capping materials is studied thoroughly, it will be very difficult for any simulation to produce accurate results. Thus, the results of the current finite element simulation, on the effect of the capping material, should only be considered as a rough guideline.

The results of the finite element simulation indicate that the use of rubber pads reduce the friction between the specimen and the bearing blocks. However, the use of rubber pads with a thickness of 3 mm resulted in lower failure loads. The failure loads are 57.9, 62.7, and 71 % for the 30, 70 and 100 MPa concrete, respectively. The

use of 1.5 mm rubber pads produced failure loads of 97.2, 95.5 and 93.8 % for the 30, 70 and 100 MPa concrete, respectively.

The stress fields, in a 30 MPa specimen using a 1.5 mm rubber pad, are shown in Fig. 7.25. The circumferential stresses are almost entirely tensile throughout the cylinder (comparing Fig. 7.25(c) with Fig. 7.7(c)). The axial stresses (Fig. 7.25(c)) are fairly uniform in the cylinder but they are below the cylinder nominal strength. The maximum principal stresses (SP3) are almost opposite to the standard case. Those stresses, at the top part of the cylinder, are entirely tensile whereas the stresses are completely compressive in the middle of the cylinder. This case shows clearly that the shear stresses are eliminated at the cylinder's edge. Two concerns arise from the case of using rubber pads. The first one is the drop of the cylinder's ultimate strength. Note that more proper simulation of the true behaviour of rubber will result in more deformation (in the cap) and the actual ultimate load should be even lower. A second concern is the measured E and ν as they will be completely different from those measured through the standard case.

The stress fields in a 30 MPa specimen tested using 3 and 6 mm sulphur caps are shown in Figs. 7.26 and 7.27, respectively. Those figures show that the stress fields in the specimen are essentially the same as the standard case (Fig. 7.7). However, the stress concentration in the specimen is reduced when sulphur cap is used. As the cap thickness is increased, the stress concentration is decreased. The failure loads for the 3 and 6 mm caps were equal to the nominal strength of the specimen.

The shear stress, τ_{rz}, and the normal stress, σ_{zz}, along the cylinder's edge, for the two different rubber pads are depicted in Fig. 7.28. The different stress distribution is presented for three different grades of concrete, namely 30, 70 and 100 MPa. The figure shows that the shear stress distribution is almost the same except near the

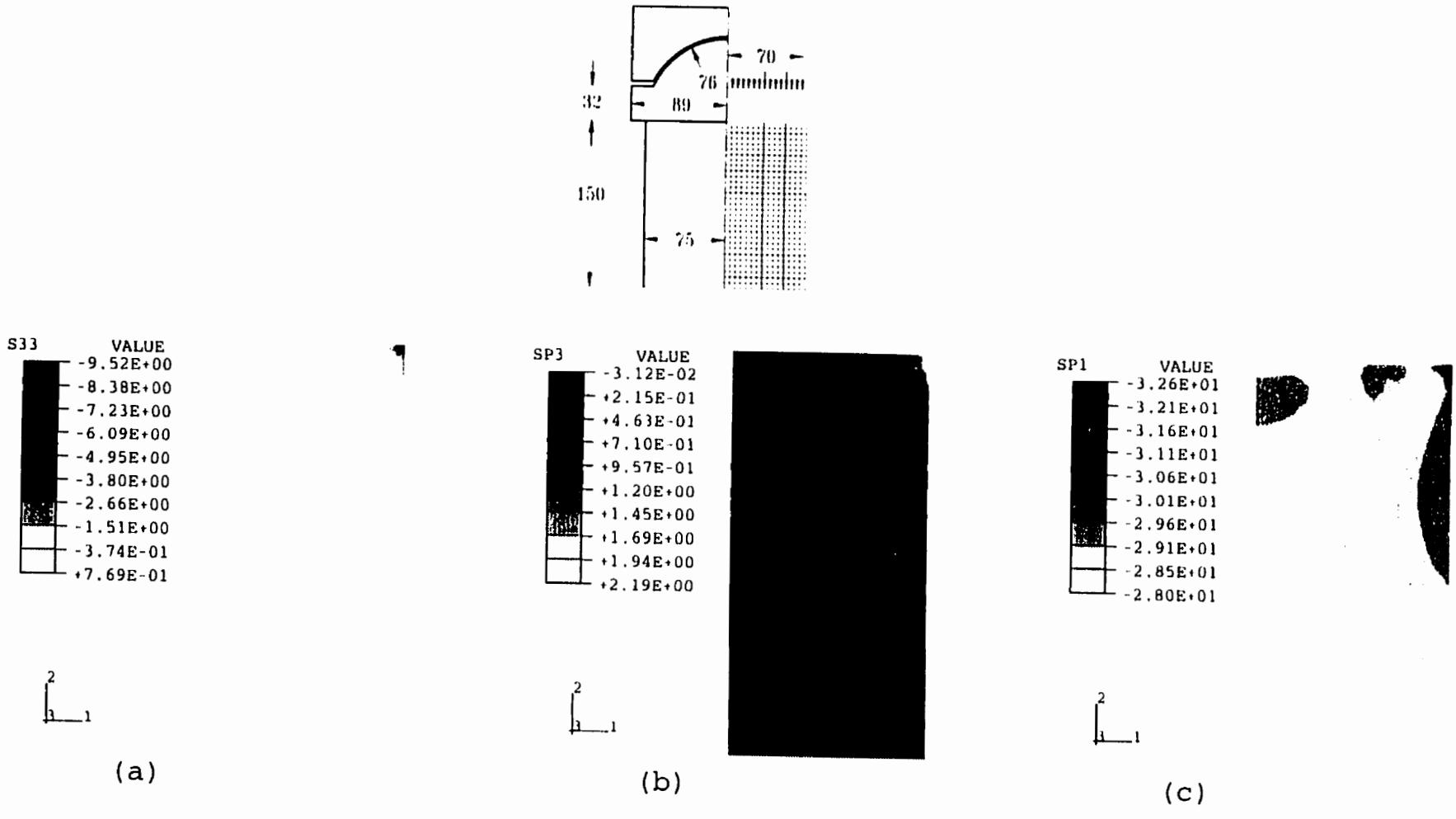

Figure 7.25: Principal stresses for a 150 × 300 mm cylinder, f'_c = 30 MPa, tested with a 152 mm bearing block at failure, specimen tested using a 1.5 mm rubber pad: (a) circumferential stress (S33); (b) maximum principal stress (SP3) in a radial plane; and (c) minimum principal stress (SP1) in a radial plane

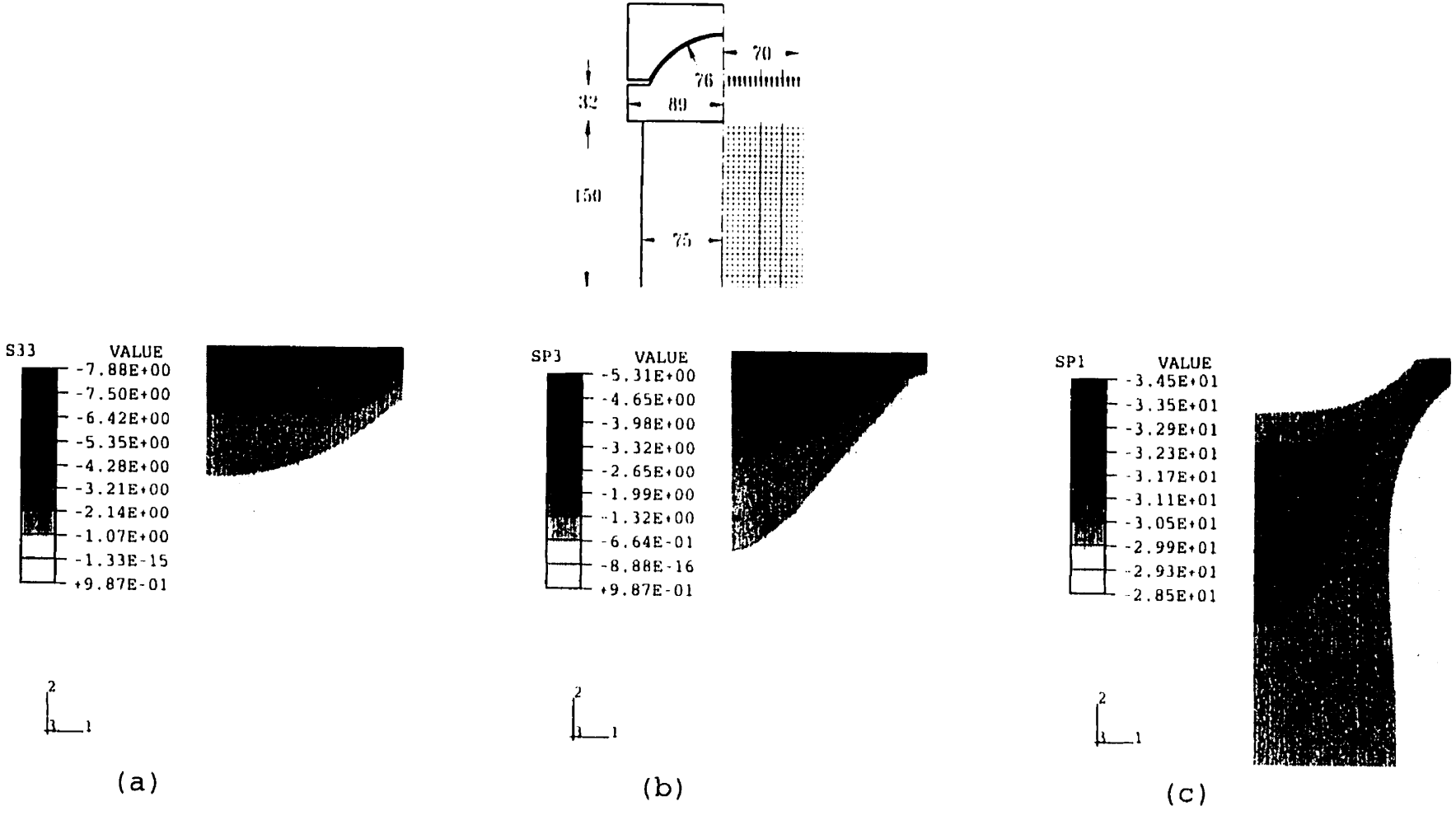

Figure 7.26: Principal stresses for a 150 × 300 mm cylinder, f'_c = 30 MPa, tested with a 152 mm bearing block at failure, specimen tested using a 3 mm sulphur capping compound: (a) circumferential stress (S33); (b) maximum principal stress (SP3) in a radial plane; and (c) minimum principal stress (SP1) in a radial plane

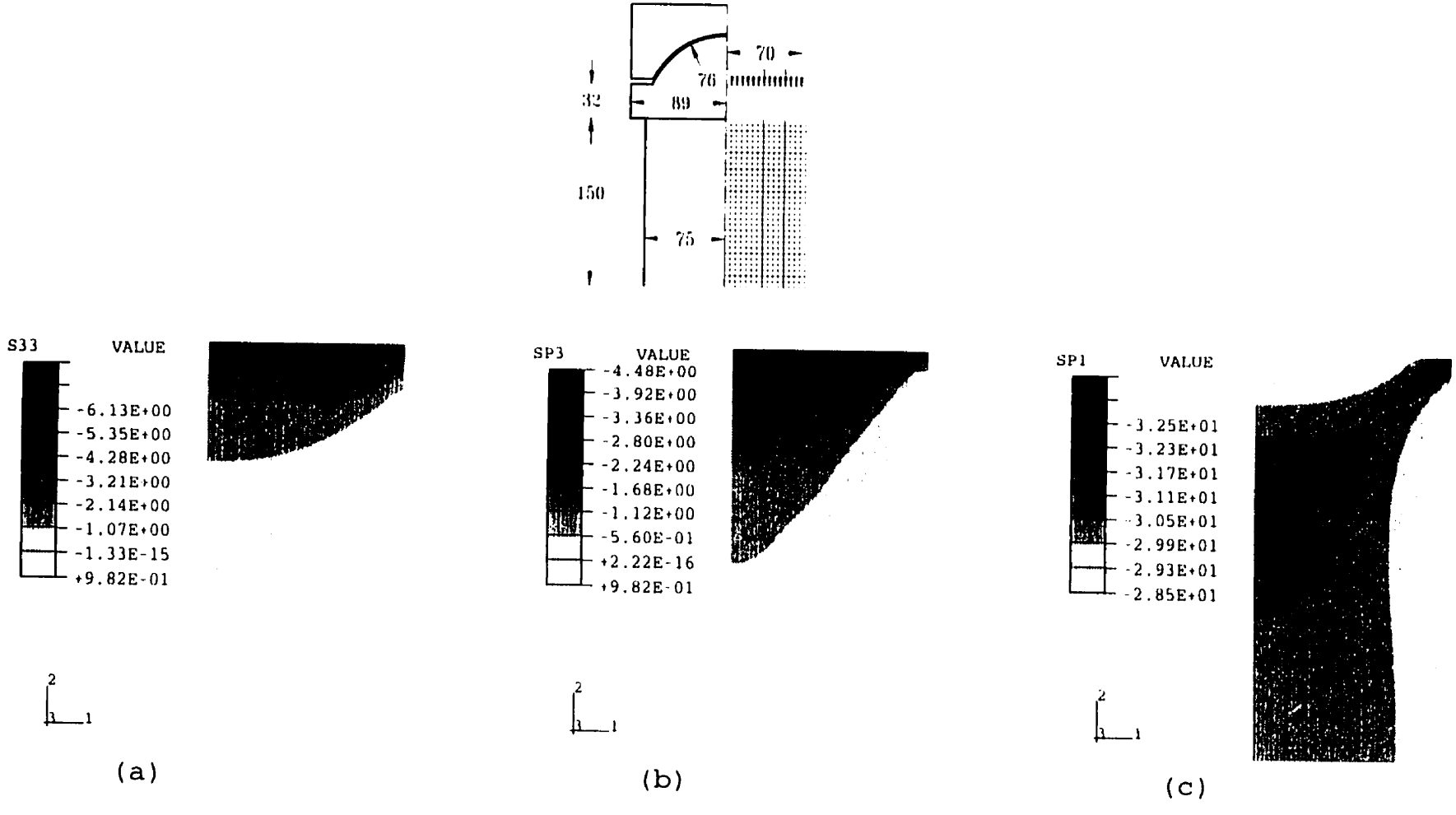

Figure 7.27: Principal stresses for a 150 × 300 mm cylinder, f'_c = 30 MPa, tested with a 152 mm bearing block at failure, specimen tested using a 6 mm sulphur capping compound: (a) circumferential stress (S33); (b) maximum principal stress (SP3) in a radial plane; and (c) minimum principal stress (SP1) in a radial plane

specimen's corner. The use of a sulphur cap results in lower values for shear. The axial stresses are also very similar. Again, one must be cautious with the results presented. A more proper simulation of the real behaviour of the sulphur capping compound may result in some different results. However, the margin of difference may be expected to be small.

7.11 Summary

In this chapter, a nonlinear finite element analysis of the standard uniaxial test of a concrete cylinder is conducted. The parameters investigated were the concrete compressive strength (30, 70 and 100 MPa), specimen dimensions (100 × 200 and 150 × 300 mm specimens), bearing block dimension (102 and 150 mm diameter bearing blocks), and the specimen's end preparation (sulphur capping and rubber pads).

Two different types of modelling the interaction between the specimen and the loading platens. The first assumption was that the specimen and the loading platen were fixed together, i.e. there is no relative slip between them. The second modelling method was carried out using an interface element and a Columnb friction model. The results showed that the shear stress distribution is almost the same, for the two modelling assumptions, except near the specimen's corner. The use of interface elements results in lower values for shear at the specimen's corners, thus, indicating that some slip may occur at this region. Therefore, it seems that the assumption of no slip, between the specimen and the loading platens, seems to be fait for cylindrical specimen with an aspect ratio of two.

The finite element results revealed that a triaxial compressive stress state exists at the cylinder end, and a large stress concentration occurs at the corner as the load is applied on the cylinder. The shear stresses at the interface varies very rapidly

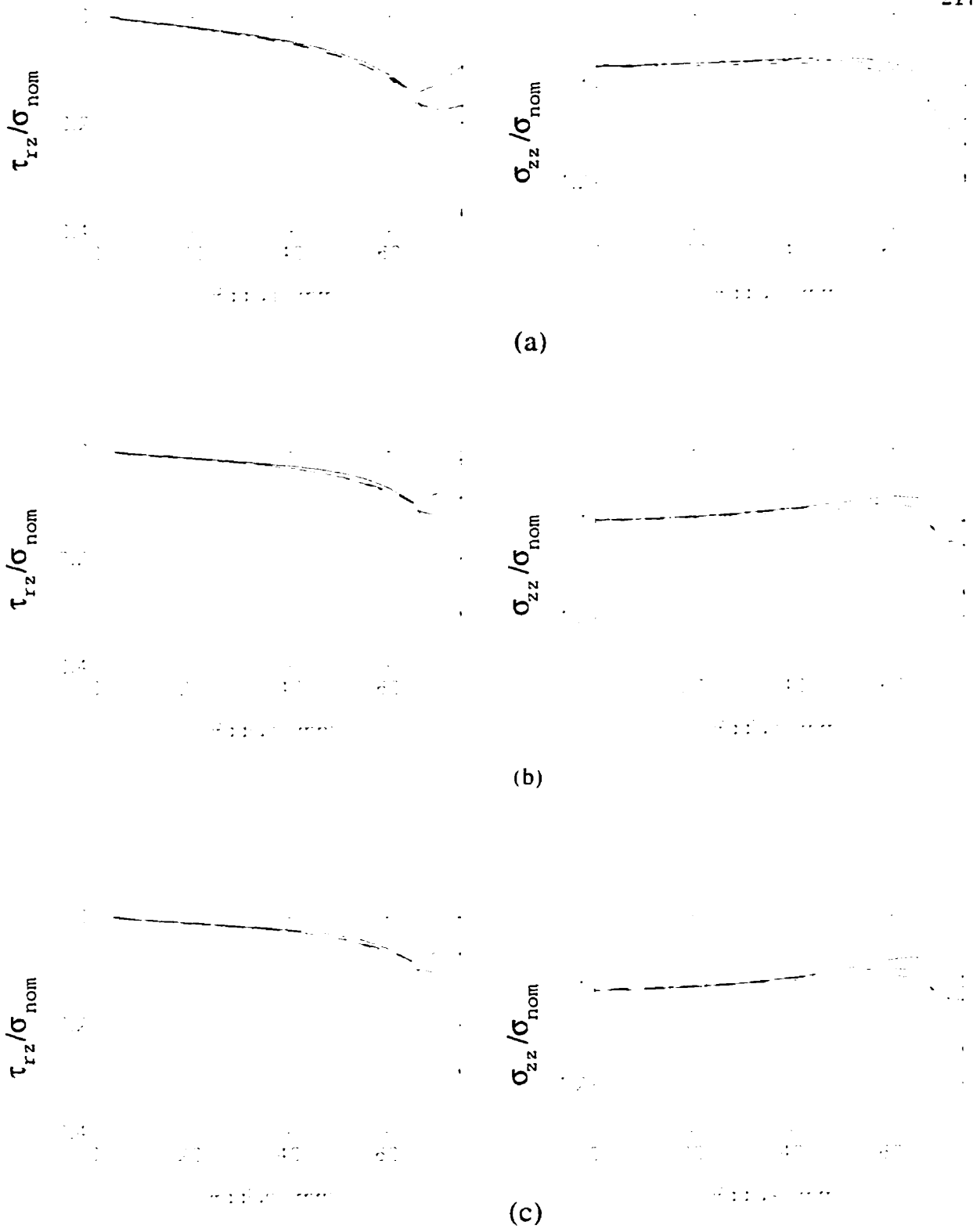

Figure 7.28: Shear stress induced in the specimen capped with sulphur compound for 150 × 300 mm cylinders that are tested with 150 mm bearing block: (- · · - ·) ground specimen, (- - -) using 3 mm sulphur cap, and (——) using 6 mm sulphur cap: (a) f'_c = 30 MPa; (b) f'_c = 70 MPa and (c) f'_c = 100 MPa

near the outside edge of the cylinder, rising very quickly and dying down more slowly towards the centre of the cylinder.

The stress distribution in the specimen, at the nominal applied load, becomes more uniform as the specimen's compressive strength is increased. The ratio of shear stresses to normal stresses decreases as the concrete compressive strength increases. Consequently, the confinement effects decreases as the specimen's compressive stress increases.

The results demonstrated that using the proper dimensions of end blocks can replicate the stresses in the specimen with different sizes (the 150 × 300 and the 10 × 200 mm specimen). However, the ratio of shear stress to normal stress is slightly lower in the small specimens. This produces less restraining effect for the small specimen.

The ultimate loads for the specimens do not attain the value of the nominal compressive strength if a 150 × 300 mm cylinder is tested with a 102 mm end block. The failure loads, from the finite element simulation, are lower than the experimental ones. The simulation provided an explanation for such a behaviour. The induced shear stresses reverses its direction and, as a result, the specimen's strength is reduced. Thus, a proper end block should always be used for testing.

In order to study the effects of end preparation of the specimen, four cases were considered: rubber capping with thicknesses of 1.5 and 3 mm, and sulphur capping with thicknesses of 3 and 6 mm. The simulation results demonstrated that the use of soft materials, as friction reducers, result in drastic change in the state of stress in the specimen as well as its compressive strength. The use of the traditional sulphur capping compound resulted only a light change in the shear forces, induced in the specimen, but did not change the overall stress distribution within the specimen. The use of soft materials should, therefore, be carried out with caution.

Chapter 8

Conclusions

8.1 Summary

In the current research, the behaviour of high-strength concrete under biaxial state of stress was studied carefully. For that regard, an experimental program was carried out. A test set-up was designed and manufactured. The selection of the loading platens was based on a finite element evaluation of some existing systems and a suitable selection was made. The test set-up was then manufactured. A suitable control scheme was adopted and a closed loop system was used to perform the experiments. Four different types of concrete were tested. Proportional loading was used for all the tests. The ratio of the two applied loads was kept constant throughout the test. All combinations of biaxial stress, compression-compression, compression-tension, and tension-tension, were investigated. For compression-compression, stress ratios were σ_1/σ_3 = 0 (uniaxial compression), 0.2, 0.5 and 1.0; for compression-tension, stress ratios were σ_1/σ_3 = -0.05, -01.0 and -0.25; and for tension-tension, stress ratios were σ_1/σ_2 = 1.0, 2.0 and ∞ (uniaxial tension). The strength data were collected and analyzed. The failure envelopes were then developed for each type of concrete. Concrete strains in the three principal directions are recorded. The principal stresses and strains at failure are also recorded and presented as functions of the stress ratios. Fi-

nally, the failure modes and crack patterns were observed and examined. The results of the experiments were then used to modify and calibrate an existing model by Etse and Willam (1994). The model was then implemented in a general finite element program. The modified finite element model was then used to evaluate the standard ASTM uniaxial compression test.

8.2 Evaluation of Different Loading Platens for Biaxial Testing of High-Strength Concrete

It was necessary to select a suitable loading platens for the experimental program. Appropriate platens should be used to reduce the friction forces induced in the specimen due to the specimen-platen interaction. A non-linear finite element analysis was carried out to evaluate three types of loading systems namely: dry solid platens, brush platens and the teflon pads. The following conclusions can be derived:

1. The shear stresses induced in the specimen were very high using dry solid platens. Using teflon pads decreases the induced shear stresses drastically. The induced shear stresses were the lowest for the case of brush platens. The ratios of the obtained values of the shear stresses to the normal stresses (at the interface) were 14 %, 2.5 % and 3.5 %, for the dry solid platens, brush platens and the teflon pads, respectively. The shear stress distribution was approximately linear from the centre of the specimen with some slight nonlinearity towards the corner. The observed irregularities in the shape of the shear stress distribution, due to the brush supports, could be present as a result of the gap between the rods.

2. For the biaxial loading cases, the shear stresses reached a value of 45 % of the normal stresses. For the case of the brush supports, the shear stresses are 8 %

of the normal stresses. The curve for shear stresses, in the case of teflon pads, changes its shape and become more distributed over the edge. This could be attributed to the effect of the lateral loading on the lubricated surface.

3. The effect of lateral confinement on the stress and displacement fields were examined for the three different loading systems. The results of the finite element study indicated that the most homogeneous stress and displacement fields were achieved for the brush platen case.

4. Buckling analysis of the brush rods indicated that a short brush can be safely used for testing high-strength concrete specimens with a compressive strength of 100 MPa.

5. As a result of the finite element investigation, a 150 × 150 mm brush was recommended. The width of the brush was selected as 40 mm and the filaments were 75 mm in length and with a 5 × 5 mm cross section. The brush was manufactured and it was successfully used in the experimental program.

8.3 Experimental Findings

Four different concrete mixtures were tested: a normal strength concrete (40 MPa), a high strength concrete mix (70 MPa), an ultra high strength concrete mix (100 MPa) and a high-strength light weight aggregate mix (67 MPa). The main findings of the experimental programs can be briefly summarized as follows:

1. The ultimate strength of concrete under biaxial compression is higher than under uniaxial compression. The maximum biaxial strength occurs at a biaxial stress ratio of 0.5, for all specimens tested. At this stress ratio, a strength

increase of about 31 % for the NSC specimen, 32 %, 35 % and 38 % for the HSC, UHSC and HSLWC, respectively, was observed.

2. At equal biaxial compression ($\sigma_2/\sigma_3 = 1.0$), the relative strength increase becomes smaller as the compressive strength is increased for all the normal weight mixes. The strength increase is 19, 14 and 9 % for the Normal strength, high strength, and ultra high strength concrete, respectively.

3. High strength light weight concrete have a higher strength gain, at all compression stress ratios, than the corresponding high strength normal weight concrete.

4. Test results confirmed that high strength concrete has a lower tensile to compressive strength ratio than normal strength concrete. The uniaxial tensile strength, f_t' was found to be 3.30, 4.15, 4.82 and 3.38 MPa for the NSC, HSC, UHSC and HSLWC, respectively, resulting in a ratio of f_t'/f_c' that is equal to 0.078, 0.056, 0.050, and 0.051.

5. In the biaxial compression-tension region, there is a significant difference in the behaviour between high strength and normal strength concrete. Introducing a small amount of tension decreases the compressive capacity more radically for high strength concrete than for normal strength concrete.

6. Under different biaxial compression loading combinations, the results show that the introduction of a second principal stress significantly affects the effective elastic modulus of concrete specimen in the direction of the first principal stress.

7. The average increase in stiffness under biaxial compression is higher for the HSC mix and less for the corresponding HSLWC specimen. This is due to the

higher modulus of elasticity of the granite, and the lower modulus of elasticity of the light weight aggregates.

8. The material constants obtained in the experimental study are somewhat different in uniaxial compression and uniaxial tension for all the mixes. The modulus of elasticity, in tension, was found to be slightly higher than that in compression.

9. High strength concrete showed a linear behaviour up to a higher stress than normal strength concrete.

10. The discontinuity limits were found to be 70, 85, 90 and 76 percent for the NSC, HSC, UHSC and HSLWC, respectively. Thus, as the compressive strength of concrete is increased, the discontinuity levels becomes higher. The discontinuity level for the high strength light weight concrete is lower than the corresponding high strength concrete.

11. There is no fundamental difference in the crack patterns and failure modes due to the increase in the compressive strength of the concrete or due to the use of light weight aggregates under different biaxial loading combinations.

8.4 Finite Element Model

A plasticity based model was adopted. The model is based on Etse and Willam [71]. It was implemented in the general purpose finite element program ABAQUS as a user defined subroutine in FORTRAN 77 language. The numerical implementation of plasticity was carried out through the elastic-predictor plastic-corrector method. The material model was calibrated for high strength concrete using the data obtained from the experiments. A finite element analysis using the calibrated constitutive model was conducted. The results were then compared to the experimental data. Results of the

verification indicated that the finite element model predicts a slightly softer response of the specimen. Nevertheless, the finite element model, generally speaking, is able to capture the stress-strain behaviour for test specimen.

8.5 Application of the Finite Element Model: Evaluation of the Standard Uniaxial Compression Test

The verified finite element model was then used to evaluate the standard uniaxial test of a concrete cylinder. The selection of this particular test was inspired by the ongoing discussion between the members of the ACI Committee 363 on high strength concrete [109]. The Committee is trying to establish a guide to inspection and testing of high strength concrete. Such a standard is vital to the high strength concrete industry. Issues have been raised concerning the specimen's size, end block size, the method of end preparation and the stiffness of the test machine. Currently there is an enormous amount of experimental work that is being carried out by different researchers. Among them is the excellent experimental work by Carino et al. [126]. Thus it was felt that a finite element analysis of such an important test can provide some insight and it could complement some of the experimental observations.

The parameters investigated were the concrete compressive strength, specimen dimensions, bearing block dimensions, and the specimen's end preparation (effect of mechanical properties of the capping material). These parameters are selected to simulate the actual ones used in the standard compression tests. The results of the finite element simulation can be briefly summarized as follows:

1. A triaxial compressive stress state exists at the cylinder end, and a large stress concentration occurs at the corner. However, at low loading levels the stresses

in the specimen are nearly uniform. At higher load levels the effect of the end restraint, due to specimen-platen interaction, becomes more significant and the stress state in the cylinder is far from uniform.

2. In order to simulate the interaction between the test specimen and the loading platens, two different modelling alternatives were examined. The first one was to assume that the platen and the specimen were glued together. The second one was carried out using interface element to simulate the friction that exist between the platen and the specimen. The results revealed that the use of interface elements resulted in lower values for shear near the specimen's corner. This would suggest that some slip may occur at this region. However, the results of the two different modelling assumptions, were fairly close except for that region.

3. The simulation results showed that the use of a standard bearing block is essential in testing high-strength concrete. The simulation confirmed that the stresses in the 100 × 200 mm specimen closely match those in the 150 × 300 mm specimen provided that a standard bearing block is used. The shear stress induced at the specimen's end is slightly lower for the small cylinders.

4. In some cases. the use of a non-standard bearing block can result in a lower strength, as was observed experimentally. The simulation provided an explanation for such a behaviour. The induced shear stresses reverses its direction and. as a result, the specimen's strength is reduced.

5. The simulation results demonstrated that the use of soft materials, as friction reducers, result in drastic changes in the state of stress in the specimen as well as its compressive strength. The use of the traditional sulphur capping compound

resulted only a slight change in the shear forces, induced in the specimen. but did not change the overall stress distribution within the specimen. The use of soft materials should, therefore, be carried out with caution.

8.6 Contribution

1. The design of the brush platens, using a nonlinear finite element. approach is carried out for the first time for uniaxial and biaxial loading. Although a similar simulation has been conduced in the past by [101], it was limited to uniaxial loading only using a linear elastic model, and the shear stresses induced in the specimen were not clearly identified.

2. In this study, it is the first time that the brush platens were designed and used to test a concrete strength for 100 MPa concrete.

3. To the author's knowledge, this is the first time that the behaviour of ultra high strength concrete (100 MPa) and high strength light weight concrete under biaxial state of stress have been examined. The thesis provides the failure envelopes and deformation characteristics of different types of concrete that are not available in the literature. Such data should prove useful for calibrating any type of constitutive model used in the finite element analysis.

4. The Etse and Willam model was implemented in the general finite element program ABAQUS. The implementation of this model is currently under development at MUN to improve the fracture mechanics aspect in it and to include the effect of reinforcement. This should enable the model to be used in the study of reinforced high strength concrete structures.

5. This thesis contains the first comprehensive study of the standard compression

test using the finite element approach. The previous studies in the literature were quiet limited [98]. Actual test parameters such as the standard loading platens. the effect of the specimen size and the effect of capping material for a concrete test specimen could not be found in the literature. This type of study can further our understanding of the standard compression test. In addition. it can help in evaluating new requirements for such a test

8.7 Recommendations for Further Research

1. The behaviour of light weight high strength concrete needs further experimental studies. The data reported in this thesis indicates that, under biaxial loading, the material behaves differently than normal strength concrete. Future studies should include higher concrete strength and different types of aggregates.

2. The softening of concrete is considered to be an important phenomena that needs future research. Currently, several researchers are trying to study the post peak behaviour of high strength concrete cylinders using different types of control to conduct the test. This issue has to be addressed more carefully for high strength concrete under biaxial loading. New control techniques have to be developed for such a test. Also, the effect of brush loading platens on the post peak behaviour warrants future studies, especially for high strength concrete specimen.

3. The current constitutive model that was implemented in the finite element program ABAQUS requires the inclusion of reinforcement elements so that it can be used in analyzing reinforced concrete structures.

4. The finite element method is a powerful tool that can be used to provide insight

into the behaviour of a test specimen in any type of standard testing. It also enables a better understanding of the interaction between the specimen and the test set-up can. Further studies should be conducted with actual test parameters. Experimental observations can also help in refining the used models so that they can accurately predict the behaviour of a test specimen.

References

[1] V. Randall and K. Foot. "High-Strength Concrete for Pacific First Center." *Concrete International.* Vol. 11. No. 4. April 1989. pp. 14-16.

[2] C. G. Hoff. "The Challenge of Offshore Concrete Structures." *Concrete International.* Vol. 7. No. 8. August 1985. pp. 12-22.

[3] A. K. Haug and M. Sandvik. "Mix Design and Strength Data for Concrete Platforms in the North Sea." *Concrete in Marine Environment. ACI SP-109.* American Concrete Institute. Detroit. 1988. pp. 896-906.

[4] C. G. Hoff. "The Challenge of Offshore Concrete Structures." *Concrete International.* Vol. 7. No. 8. August 1985. pp. 12-22.

[5] K. Gerstle. D. Linse. P. Bertacchi. M. Kotsovos. H. ko. J. Newman. P. Rossi. G. Schickert. M. Taylor. L. Traina. R. Zimmerman. and R. Bellotti. "Strength of Concrete Under Multi-axial Stress States." *Proc. McHenry Symp. Concr. Struct.*. Mexico City. American Concrete Institute. SP 55. 1976. pp. 103-131.

[6] P. G. Sheppard. "A Study of the Strength of Concrete Under Biaxial Compressive Stresses." *M.S. thesis.* New Mexico State University. 1967.

[7] B. Hugues and B. Baharamian. Reply to the Discussion by R. Zimmerman. to "Cube Tests and the Uniaxial Compressive Strength of Concrete." *Magazine of Concrete Research*. Vol. 18. No. 56. 1965. pp. 163-164.

[8] B. Hugues and B. Bahramian. "Cube Tests and the Uniaxial Compressive Strength of Concrete." *Magazine of Concrete Research*. Vol. 17. No. 53. pp. 177-182. 1965.

[9] G. Schickert. "On the Influence of Different Load Application Techniques on the Lateral Strain and Fracture of Concrete Specimens." *Cement and Concrete Research*. 1973. Vol. 3. No. 4. pp. 487-494.

[10] L. Mills and R. Zimmerman. "Compressive Strength of Plain Concrete Under Multiaxial Loading Conditions." *American Concrete Institute Journal. Proceedings*. Vol. 67. No. 10. October 1970. pp. 802-807.

[11] Y. Nojiri. K. Kotani. and Y. Abe. "Failure Envelope of Concrete Subjected to Multiaxial Compressive Stresses." *Proceedings of International Conference on Concrete Under Multiaxial Conditions*. (Toulouse). RILEM. 1984. pp. 141-148.

[12] J. Newman. "Concrete under Complex Stress." *Developments in Concrete Technology -1*." edited by Lydon. F.. Applied Science Publishers. London. 1979. pp. 151-220.

[13] H. Hilsdorf. "The Experimental Determination of the Biaxial Strength of Concrete: A Recapitulation and Criticism of Previous Experiments and a Suggestion for a New Method of Testing." *Bulletin* No. 173. Deutscher Ausschuss für Stahlbeton. Berlin. 1965.

[14] H. Kupfer, H. Hilsdorf, and H. Rusch, "Behaviour of Concrete Under Biaxial Stresses," *American Concrete Institute Journal, Proceedings*, Vol. 66, No. 8, August 1969, pp. 656–666.

[15] L. J. Nelissen, "Biaxial Testing of Normal Concrete," *Heron* (Delft), Vol. 18, No. 1, 1972, pp. 603–611.

[16] T. Liu, A. Nilson, and F. Slate, "Stress-Strain Response and Fracture of Concrete in Uniaxial and Biaxial Compression," *American Concrete Institute Journal, Proceedings*, Vol. 69, No. 5, May 1972, pp. 291–295.

[17] I. Tasuji, F. Slate, and A. Nilson, "Stress-Strain Response and Fracture of Concrete in Biaxial Loading," *American Concrete Institute Journal, Proceedings*, Vol. 75, No. 7, July 1978, pp. 306–312.

[18] J. G. M. van Mier, "Strain-Softening of Concrete Under Multiaxial Loading Conditions," *Ph.D. thesis*, Technisce Hogeschool Eindhoven, 1984, 349 p.

[19] G. Schickert, "On the Influence of Different Load Application Techniques on the Lateral Strain and Fracture of Concrete Specimens," *Proceedings of the Third International Conference on Fracture*, Munich, Vol. 8, No.2, April 1973, pp. 242–245.

[20] R. A. Vonk, H. S. Rutten, J. G. Van Mier, and H. J. Fijneman, "Influence of Boundary Conditions on the Softening of Concrete Loaded in Compression," *Fracture of Concrete and Rock-Recent Developments*, edited by S. P. Shah, S. E. Swartz and B. Barr, Elsevier Applied Science, London, 1990, pp. 711-720.

[21] J. G. Van Mier and R. A. Vonk. "Fracture of Concrete under Multiaxial Stress - Recent Developments." *Materials and Structures. RILEM.* Vol. 24. 1991. pp. 61-65.

[22] E. Andenaes. K. Gerstle. and H. Ko. "Response of Mortar and Concrete to Biaxial Compression." *Journal of the Engineering Mechanics Division. ASCE.* Vol. 103. No. EM4. August 1977. pp. 515-535.

[23] G. A. Hegemier and H. E. Read. "On Deformation and Failure of Brittle Solids: Some Outstanding Issues." *Mechanics of Materials.* North-Holland. Vol.4. 1985. pp. 215-259.

[24] H.-Y. Ko. R. Meier. and S. Sture. "Constitutive Properties of Steel Fiber Reinforced Concrete in Multiaxial Compression and Combined Tension and Compression." *Proceedings of International Conference on Concrete Under Multiaxial. Conditions.* (Toulouse). RILEM. 1984. pp. 157-165.

[25] K. T. Iyengar. K. T. Chandrashekhara. and K. T. Krishnaswamy. "Strength of Concrete Under Biaxial Compression." *American Concrete Institute Journal. Proceedings.* Vol. 62. No. 2. February 1965. pp. 239-249.

[26] G. W. Vile. "Strength of Concrete Under Short-Term Static Biaxial Stress." *Proceedings. International Conference on the Structure of Concrete and its Behaviour Under Load.* Imperial College. London. September 1965. pp. 275-288.

[27] J. C. Herrin. "Behaviour of High-Strength Concrete Model Subjected to Biaxial Compression." *MS Thesis.* University of Texas at Austin. May 1983. 148 pp.

[28] R. L. Chen. "Behaviour of High-Strength Concrete in Biaxial Compression." *PhD Dissertation.* University of Texas at Austin. December 1984. 298 pp.

[29] L. Traina and S. Mansour. "Biaxial Strength and Deformational Behaviour of Plain and Steel Fiber Concrete." *ACI Materials Journal. Proceedings.* Vol. 88. No. 4. July-August 1991. pp. 354–362.

[30] H. Marzouk and Z. Chen. "Fracture Energy and Tension Properties of High-Strength Concrete." *Journal of Materials in Civil Engineering.* ASCE. Vol .7. No. 2. May 1995. pp. 108–116.

[31] K. H. Gerstle. "Material Behaviour Under Various Types of Loading." *High Strength Concrete.* Proceedings of a Workshop Held at the University of Illinois at Chicago Circle. December 2–4. 1979. pp. 43–78.

[32] Y. Niwa. S. Kobayashi. and W. Koyanagi. "Failure Criterion of Lightweight Aggregate Concrete Subjected to Biaxial Compression." *Memoirs.* Faculty of Engineering. Kyoto University. Vol. 29. Part 2. April 1967. pp. 119–131.

[33] M. A. Taylor. A. K. Jain. and M. R. Ramey. "Path Dependent Biaxial Compressive Testing of an All-Lightweight Aggregate Concrete." *American Concrete Institute Journal. Proceedings.* Vol. 69. No. 12. December 1972. pp. 758–764.

[34] Y. Atan and F. Slate. "Strcutural Lightweight Concrete Under Biaxial Compression." *ACI Journal. Proceedings.* Vol. 70. No. 3. May 1973. pp. 182–186.

[35] M. Glavind and H. Stang. "Evaluation of the Complete Compressive Stress-Strain Curve for High Strength Concrete." *Fracture Process in Concrete. Rocks and Ceramics.* RILEM. J. G. M. van Mier. J. G. Rots. and A. Bakker. Editors. E & FN Spon. London. England. Vol. 2. 1991. pp. 749–759.

[36] M. D. Kotsovos. "Effect of Testing Techniques on the Post-Ultimate Behaviour of Concrete in Compression." *Magazine of Concrete Research*. Vol. 16. No. 91. 1983. pp. 3-12.

[37] S. P. Shah and R. Sankar. "Internal Cracking and Strain Softening Response of Concrete Under Uniaxial Compression." *ACI Materials Journal*. Vol. 84. No. 3. May-June 1987. pp. 200-212.

[38] L. Taerwe. "Influence of Steel Fibres on Strain-Softening of High-Strength Concrete." *ACI Structural Journal*. Vol. 89. No. 1. January-February 1992. pp. 54-60.

[39] S. P. Shah and D. C. Jansen. "Stable Feedback Signals for Obtaining Full Stress Strain Curves of High Strength Concrete." *Utilization of High Strength Concrete. Proceedings*. Lillehammer. Norway. June 1993. pp. 1130-1137.

[40] S. P. Shah. U. Gokoz. and F. Ansari. "An Experimental Technique for Obtaining Complete Stress-Strain Curves for High-Strength Concrete." *Cement. Concrete. and Aggregates*. CCAGDP. ASTM. Philadelphia. Pa.. Vol. 3. No. 1. Summer 1981. pp. 21-27.

[41] D. Jansen. S. Shah. and E. Rossow. "Stress-Strain Results of Concrete from Circumferential Strain Feedback Control Testing." *ACI Materials Journal*. Vol. 92. No. 4. July-August 1995. pp. 419-428.

[42] H. Dhal and R. Brincker. "Fracture Energy of High-Strength Concrete in Compression." *Fracture of Concrete and Rocks: Recent Developments*. S.P. Shah. S. E. Swartz. and B. Barr. Editors. Elsevier Applied Science. New York. England. 1989. pp. 523-536.

[43] F. de Larrad and Y. Mailer. "Engineering Properties of Very High Performance Concretes." *High Performance from Materials to Structures*. Y. Mailer. Editor. E & FN Spon. London. England. 1992. pp. 85–114.

[44] D. Jansen and S. Shah. "Effect of Length on Compressive Strain Softening of." *Journal of Engineering Mechanics*. Vol. 123. No. 1. January 1997. pp. 25–35.

[45] S. Okubo and Y. Nishimatsu. "Uniaxial Compression Testing Using a Linear Combination of Stress and Strain as the Control Variable." *International Journal of Rock Mechanics. Mining Sciences and Geomechanical Abstract*. Oxford. England. Vol. 22. No. 5. 1985. pp. 323–330.

[46] S. Choi. K. Thienel. and S. Shah. "Strain Softening of Concrete in Compression under Different End Constraint." *Magazine of Concrete Research*. Vol. 48. No. 75. 1996. pp. 103–115.

[47] M. A. Taylor and B. Patel. "The influence of Path Dependency and Moisture Conditions on the Biaxial Compression Envelope for Normal Weight Concrete." *American Concrete Institute Journal. Proceedings*. Vol. 71. No. 12. December 1974. pp. 627–633.

[48] W. F. Chen and A. F. Saleeb. *Constitutive Equations for Engineering Materials*. Volume 1: Elasticity and Modelling. John Wiley and Sons. 1982.

[49] W. F. Chen. *Plasticity in Concrete*. MacGraw-Hill. 1982.

[50] Committee on Finite Element Analysis of Reinforced Concrete Structure. "State-of-the-Art Report on Finite Element Analysis of Reinforced Concrete." *ASCE Structural Engineering Division*. 1982.

[51] Comité Euro-International Du Béton. "Concrete Under Multiaxial State of Stress Constitutive Equations for Practical Design." *Bulletin D'information No. 156.* Prague. 1983. 149 pp.

[52] H. Kupfer and K. Gerstle. "Behaviour of Concrete Under Biaxial Stresses." *Journal of the Engineering Mechanics Division. ASCE.* Vol. 99. No. EM4. August 1973. pp. 853–866.

[53] L. Cedolin. Y. Crutzen. and S. Dei Poli. "Triaxial Stress-Strain Relationship for Concrete." *Journal of the Engineering Mechanics Division. ASCE.* Vol. 103. No. EM3. June 1977. pp. 423–439.

[54] K. Gerstle. "Simple Formulation of Triaxial Concrete Behaviour." *American Concrete Institute Journal. Proceedings.* Vol. 78. No. 5. September-October 1981. pp. 382–387.

[55] D. Darwin and D. Pecknold. "Analysis of RC Shear Panels Under Cyclic Loading." *Journal of the Structural Division. ASCE.* Vol. 102. No. ST2. February 1976. pp. 355–369.

[56] D. Darwin and D. Pecknold. "Nonlinear Biaxial Stress-Strain Law for Concrete." *Journal of the Engineering Mechanics Division. ASCE.* Vol. 103. No. EM2. April 1977. pp. 229–241.

[57] A. Elwi and D. Murray. "A 3D Hypoelastic Concrete Constitutive Relationship." *Journal of the Engineering Mechanics Division. ASCE.* Vol. 105. No. EM4. October 1979. pp. 623–641.

[58] Z. Bažant . Discussion to "A 3D Hypoelastic Concrete Constitutive Relationship." by A. Elwi and D. Murray. *Journal of the Engineering Mechanics Division, ASCE*. Vol. 106. No. EM2. April 1980. pp. 422–424.

[59] R. A. Link and A. E. Elwi. "Finite Element Analysis of Composite Ice Resisting Walls." *Structural Engineering Report No. 180*. Department of Civil Engineering. University of Alberta. Edmonton. Alberta. June 1992. 232 pp.

[60] O. Buyukozturk. "Nonlinear Analysis of Reinforced Concrete Structures." *Computers and Structures*. Vol. 7. 1977. pp. 149–156.

[61] M. Suidan and W. Schnobrich. "Finite Element Analysis of Reinforced Concrete." *Journal of the Structural Division, ASCE*. Vol. 99. No. ST10. October 1973. pp. 2109–2123.

[62] A. C. Chen and W. F. Chen. "Constitutive Relations for Concrete." *Journal of the Engineering Mechanics Division, ASCE*. Vol. 101. No. EM4. August 1975. pp. 465–481.

[63] W. F. Chen and C. Ting. "Constitutive Models for Concrete Structures." *Journal of the Engineering Mechanics Division, ASCE*. Vol. 106. No. EM1. February 1980. pp. 1–19.

[64] R. Glemberg. M. Oldenburg. L. Nielsson. and A. Samuelson. "A general Constitutive Model for Concrete Structures." *Computational Modelling of Reinforced Concrete Structures*. E. Hinton and R. Owen. Editors. Pineridge Press. Swanson. Wales. 1986.

[65] C. Desai, S. Somasundaram, and G. Frantziskonis, "A Hierarchial Approach for Constitutive Modelling of Geologic Materials," *International Journal for Numerical and Analytical Methods in Geomechanics*, Vol. 10, No. 3, 1986, pp. 225–257.

[66] D. Han and W. F. Chen, "Constitutive Modelling in Analysis of Concrete Structures," *Journal Engineering Mechanics, ASCE*, Vol. 113, No. 4, 1987, pp. 577–593.

[67] S. Pietruszczak, J. Jiang, and F. A. Mirza, "An Elastoplastic Constitutive Model for Concrete," *International Journal of Solids and Structures*, Vol. 27, No. 7, 1988, pp. 705–722.

[68] J. Lubliner, J. Oliver, S. Oller, and E. Onate, "A Plastic- Damage Model for Concrete," *International Journal of Solids and Structures*, Vol. 25, No. 3, 1989, pp. 299–326.

[69] R. Meyer, H. Ahrens, and H. Duddeck, "Material Model for Concrete in Cracked and Uncracked States," *Journal Engineering Mechanics, ASCE*, Vol. 120, No. 9, September 1994, pp. 1877–1895.

[70] E. Pramono and K. Willam, "Fracture Energy-Based Plasticity Formulation of Plain Concrete," *Journal Engineering Mechanics, ASCE*, Vol. 115, No. 6, June 1989, pp. 1183–1204.

[71] G. Etse and K. Willam, "Fracture Energy Formulation for Inelastic Behaviour of Plain Concrete," *Journal Engineering Mechanics, ASCE*, Vol. 120, No. 9, September 1994, pp. 1983–2011.

[72] Z. Bažant and P. Bhat. "Endochronic Theory of Inelasticity and Failure of Concrete." *Journal of the Engineering Mechanics Division, ASCE*, Vol. 102, No. EM4, August 1976, pp. 701–722.

[73] Z. Bažant and C.-L. Shieh. "Endochronic Model for Nonlinear Triaxial behaviour of Concrete." *Nuclear Engineering and Design*, Vol. 74, 1978, pp. 305–315.

[74] A. Dragon and Z. Morz. "A Continuum Model for Plastic Brittle Behaviour of Rock and Concrete." *International Journal of Engineering Science*, Vol. 17, 1979, pp. 121–137.

[75] J. Lemaître and J. Mazars. "Application de la Théorie del l'Endommagement au Comportement Non Linàire et à la Rupture du Béton de Structure." *Annales de l'ITBTP*, 401, 1982.

[76] D. Krajcinovic. "Constitutive Equations for Damaging Materials." *Journal of Applied Mechanics, ASME*, Vol. 50, 1983, pp. 355–360.

[77] D. Krajcinovic and D. Fanella. "A Micromechanical Model for Concrete." *Engineering Fracture Mechanics*, Vol. 25 Nos. 5/6, 1986, pp. 585–596.

[78] J. Mazars and G. Pijaudier-Cabot. "Continuum Damage Theory – Application to Concrete." *Journal of the Engineering Mechanics Division, ASCE*, Vol. 115, No. 2, February 1989, pp. 345–365.

[79] D. Krajcinovic, "Continuous Damage Mechanics: Revisited." *Journal of Applied Mechanics, ASME*, Vol. 52, 1985, pp. 829–856.

[80] J. Lemaître and J. Mazars. "Local Approach of Fracture." *Engineering Fracture Mechanics*, Vol. 25 Nos. 5/6, 1986, pp. 523–537.

[81] D. Krajcinovic. "Damage Mechanics." *Mechanics of Materials*. Vol. 2. Nos. 2&3. December 1989. pp. 117-197.

[82] P. Léger. J. Venturelli. and S. Bhattacharjee. "Seasonal Temperature and Stress Distribution in Concrete Gravity Dams. Parts 1 and 2." *Canadian Journal of Civil Engineering*. Vol. 20. No. 6. pp. 999-1029.

[83] F. Ghrib and R. Tinawi. "Nonlinear Behaviour of Concrete Dams Using Damage Mechanics." *Journal of Engineering Mechanics. ASCE*. Vol. 121. No. 4. April 1995. pp. 513-527.

[84] Z. P. Bažant . "Microplane Model for Strain-Controlled Inelastic Behaviour." *Mechanics of Engineering Materials*. C. S. Desai and R. H. Gallager. Editors. John Wiley and Sons. New York. N.Y.. 1984. pp. 45-59.

[85] Z. Bažant and P. Prat. "Microplane Model for Brittle-Plastic Material - Parts I and II." *Journal of the Engineering Mechanics Division. ASCE*. Vol. 114. No. 10. October 1988. pp. 1672-1702.

[86] Z. Bažant and J. Ožbolt. "Nonlocal Microplane Model for Fracture. Damage. and Size Effect." *Journal of the Engineering Mechanics Division. ASCE*. Vol. 116. No. 11. November 1990. pp. 2485-2504.

[87] Z. Bažant and J. Ožbolt. "Microplane Model for Triaxial Cyclic Behaviour of Concrete." *Journal of the Engineering Mechanics Division. ASCE*. Vol. 118. No. 7. July 1992. pp. 1365-1386.

[88] M. Romano. "On Leon's Criterion." *Meccanica*. March 1969. pp. 48-66.

[89] K. Willam. B. Hurlbut. and S. Sture. "Experimental and Constitutive Aspects of Concrete failure." *Proceedings of US-Japan Seminar on Finite Element Analysis*

of Reinforced Concrete Structures. Tokyo. 1985. ASCE Special Publication. New York. N. Y., pp. 226–254.

[90] J. Xie. A. Elwi. and J. MacGregor. "Numerical Investigation of Eccentrically Loaded Tied High-Strength Concrete Columns." *Structural Engineering Report No. 204*. Department of Civil Engineering. University of Alberta. Alberta Canada. October 1994. 190. pp.

[91] N. G. Filon "On the Elastic Equilibrium of Circular Cylinders Under Certain Practical Systems of Load." *Philosophical Transactions of the Royal Society of London*. Series A. Vol. 198. 1902. pp. 147-233.

[92] G. Pickett. "Application of the Fourier Method to the Solution of Certain Boundary Problems in the Theory of Elasticity" *Transactions of the American Society for Mechanical Engineers*. Vol. 66. 1944. A176–A182.

[93] A. Balla. "Stress Conditions in Triaxial Compression." *Journal of Soil Mechanics and Foundation Engineering. ASCE*. 1960. pp. 57–84.

[94] B. T. Brady. "An Exact Solution to the Radially End-Constrained Circular Cylinder Under Triaxial Loading." *International Journal of Rock Mechanics and Mining Sciences*. Vol. 8. 1971. pp. 165-178.

[95] M. Al-Chalabi and C. L. Huang. "Stress Distribution within Circular Cylinder in Compression." *International Journal of Rock Mechanics and Mining Sciences and Geomechanical Abstracts*. Vol. 11. 1974. pp. 45-56.

[96] C. V. Girijavallabhan. "Stresses in Restrained Cylinder under Axial Compression." *Journal of Soil Mechanics and Foundations Division, ASCE*. Vol. 96. No. SM2. March 1970. pp. 783-787.

[97] N. G. Shrive. "Compression Testing and Cracking of Plain Concrete." *Magazine of Concrete research*. Vol. 35. No. 122. March 1983. pp. 27-39.

[98] N. S. Ottosen. "Evaluation of Concrete Cylinder Tests Using Finite Element." *Journal of the Engineering Mechanics Division. ASCE*. Vol. 110. No. 3. December 1980. pp. 465-481.

[99] ASTM C 39. "Test Method for Compressive Strength of Cylindrical Concrete Specimens." *Annual Book of ASTM Standards*. V. 04.02. 1993.

[100] B. Bakht. L. G. Jaeger. and A. A. Mufti. "Elastic Modulus of Concrete from Compression Tests." *ACI Materials Journal. Proceedings*. Vol. 86. No. 3. May-June 1989. pp. 220–224.

[101] J. M. Torrenti and P. Royis. "Etude numérique du dimensionnement d'un appui anti-frettage pour le béton." *Materials and Structures. RILEM*. Vol. 22. 1989. pp. 149–158.

[102] ABAQUS. "Theory Manual." Version 5.2. Hibbitt. Karlsson and Sorensen Inc.. Providence. R.I.. 1992.

[103] ABAQUS. "Users Manual." Version 5.2. Hibbitt. Karlsson and Sorensen Inc.. Providence. R.I.. 1992.

[104] A. Hillerborg. "Numerical Methods to Simulate softening and Fracture of Concrete." *Fracture Mechanics of Concrete*. G. Sih and A. Ditommaso. Editors. Martinus Nijhoff Publ. Dordrecht. The Netherlands. 1985. pp. 141-170.

[105] M. Criesfield. "Snap-through and Snap-back Response in Concrete Structures and the Dangers of Under-integration." *International Journal of Numerical Methods in Engineering*. Vol. 22. 1986. pp. 751–767.

[106] J. Oden and E. Piers, "Nonlocal and Nonlinear Friction Laws and Variational Principles for Contact Problems in Elasticity," *Journal of Applied Mechanics*, Vol. 50, 1983, pp. 67–73.

[107] H. Marzouk and Hussein, "Development of 70 MPa Concrete for the Nekton project Using Local Available Materials in Newfoundland," *Ocean Engineering Research Group*, Memorial University of Newfoundland, St. John's, Newfoundland, 146 pp.

[108] H. Marzouk and A. Hussein, "Properties of High-Strength Concrete at Low Temperatures," *ACI Materials Journal, Proceedings*, Vol. 87, No. 2, March-April 1990, pp. 167–171.

[109] ACI Committee 363, "State-of-the-Art Report on High-Strength Concrete," ACI 363R-92, American Concrete Institute, 1992, 55 p.

[110] H. Winkler, "Fundamental Investigations on the influence of Test Equipment on Multiaxial Test Results of Concrete," *International Conference on Concrete Under Multiaxial Conditions, Proceedings*, RIELM-CEB Symposium, Presses de l'Universit'e Paul Sabatier, INSA Toulouse, Vol. 1, 1984, pp. 9–18.

[111] W. Yin, E. Su, M. Mansour, and T. Hsu, "Biaxial Tests of Plain and Fibre Concrete," *ACI Materials Journal*, Vol. 86, No. 3, May-June 1989, pp. 236–243.

[112] M. Zhang and O Gjørv, "Mechanical Properties of High-Strength Lightweight Concrete," *ACI Material Journal*, Vol. 88, No. 3, May-June 1991, pp. 240–246.

[113] P. Daerga, M. Pettersson, and D. Pontinen, "Fracture Properties in Tension of a High Performance Concrete," *High-Strength Concrete 1993, Proceedings* Lillehammer, Norway, June 1993, pp. 1193-1200

[114] M. Zhang, T. Rønning, and O. Gjørv. "Mechanical Properties of High Strength Concrete." *High-Strength Concrete 1993, Proceedings* Lillehammer. Norway, June 1993, pp. 1271–1279.

[115] K. Newman, "Criteria for the Behaviour of Plain Concrete Under Complex State of Stress," *Proceedings, International Conference on the Structure of Concrete*, Cement and Concrete Association, London. 1968, pp. 255–274.

[116] K. Willam and E. Warnke, "Constitutive Models for Triaxial Behaviour of Concrete," *International Association for Bridge Structural Engineering, Proceedings*, Bergamo, Italy, Vol. 19, 1975, pp. 1–30.

[117] E. Hoek and E. Brown, "Empirical Strength Criterion for Rock Masses," *Journal of the Geotechnical Engineering Division, ASCE*, Vol. 106, No. GT9, 1980, pp. 1013–1035.

[118] B. Hurlbut, "Experimental and Computation investigation of Strain-Softening in Concrete," *Master's Thesis*, University of Colorado at Boulder, 1983, 128 pp.

[119] J. Lubliner, "Plasticity Theory," Macmillan Publishing Company, 1990.

[120] P. Vermeer and R. de Borst, "Non-Associated Plasticity for Soils, Concrete and Rock", *Heron*, Vol. 29, No.3, 1984. 64 p.

[121] Z. Bazant, "Stability of Structures", Oxford University Press, 1991.

[122] D. R. J. Owen and E. Hinton, "Finite Elements in Plasticity : Theory and Practice," Swansea, U.K., Pineridge Press, 1980.

[123] M. A. Crisfield, "Non-Linear Finite Element Analysis of Solids and Structures," Chichester, Toronto, Wiley, 1991.

[124] M. Ortiz and E. Popov, "Accuracy and Stability of Integration Algorithms for Elastoplastic Constitutive Relations," *International Journal for Numerical Methods in Engineering*, Vol. 21, No. 9, 1985, pp. 1561–1576.

[125] M. Ortiz and J. Simo, "An Analysis of a New Class of Integration Algorithms for Elastoplastic Constitutive Relations," *International Journal for Numerical Methods in Engineering*, Vol. 23, 1986, pp. 353–366.

[126] N. J. Carino, W. F. Guthrie, and E. S. Lagergren, "Effects of Testing Variables on the Measured Compressive Strength of High-Strength (90 MPa) Concrete," *National Institute of Standards and Technology (U.S.), NISTIR 5405*, Gaithersburg, Maryland, October 1994, 154 pp.

[127] M. Lessard, O. Chaallal, and P-C. Aitcin, "Testing High-Strength Concrete Compressive Strength," *ACI Materials Journal*, Vol. 90, No. 4, July-August 1993, pp. 303–308.

[128] J. Bickley, "Prequalification Requirements for Supply and Testing of Very High Strength Concrete, *Concrete International*." Vol. 15, No. 2, February 1993, pp. 62–64.

[129] S. Timoshenko and J. Goodier, "Theory of Elasticity," Second edition, McGraw-Hill Book Co., Inc., New York, N. Y., 1951.

[130] ASTM C 617, "Practice for Capping Cylindrical Concrete Specimens," *Annual Book of ASTM Standards, V.04.02*, 1993.

[131] G. Werner, "The Effect of Capping Material on the Compressive Strength of Concrete Cylinders," *ASTM Proceedings*, V. 58, 1958, pp. 1166-1186.

IMAGE EVALUATION
TEST TARGET (QA-3)

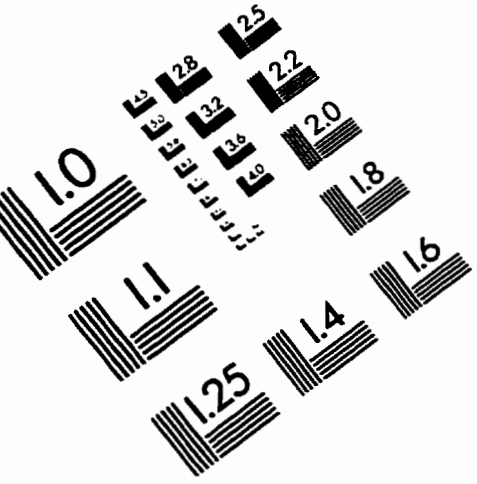

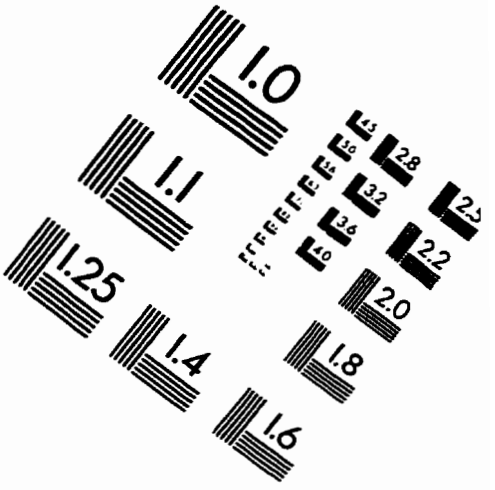

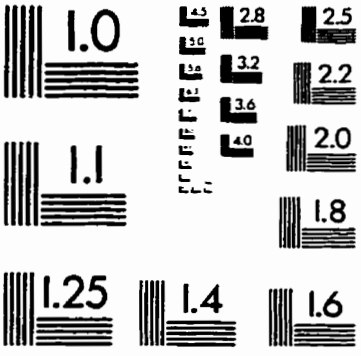

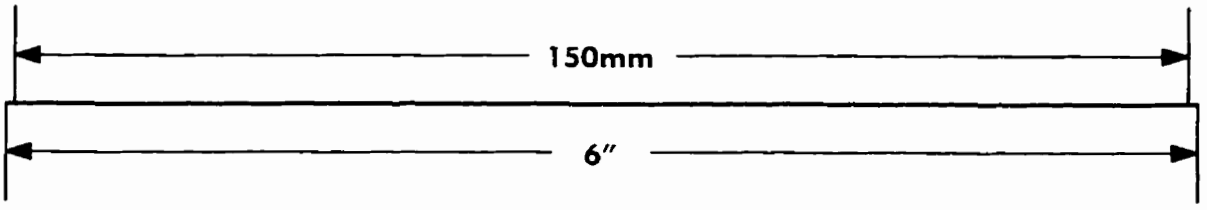

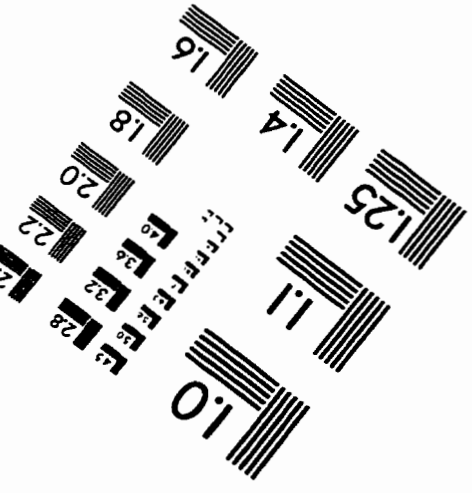

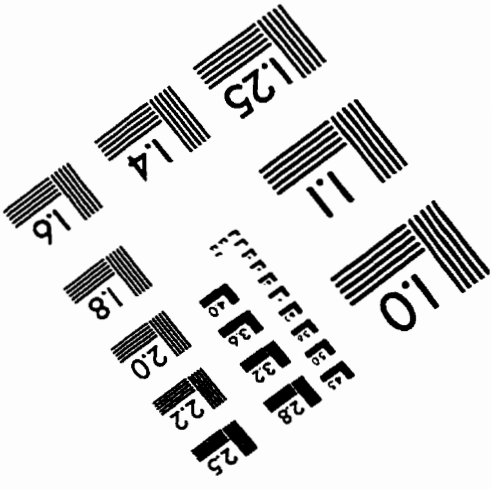

APPLIED IMAGE, Inc
1653 East Main Street
Rochester, NY 14609 USA
Phone: 716/482-0300
Fax: 716/288-5989

© 1993, Applied Image, Inc., All Rights Reserved